UNIVERSIDADE ESTADUAL DE CAMPINAS

FACULDADE DE ENGENHARIA MECÂNICA

DOUGLAS DANIEL DE CARVALHO

Non-equilibrium magnetization dynamics in ferrofluids subjected to quadratic flows

Dinâmica de magnetização de não equilíbrio em ferrofluidos sujeitos a escoamentos quadráticos

CAMPINAS
2020

DOUGLAS DANIEL DE CARVALHO

Non-equilibrium magnetization dynamics in ferrofluids subjected to quadratic flows

Dinâmica de magnetização de não equilíbrio em ferrofluidos sujeitos a escoamentos quadráticos

Dissertation presented to the School of Mechanical Engineering of the University of Campinas in partial fulfillment of the requirements for the degree of Master in Mechanical Engineering, in the area of Thermic and Fluids.

Dissertação apresentada à Faculdade de Engenharia Mecânica da Universidade Estadual de Campinas como parte dos requisitos exigidos para a obtenção do título de Mestre em Engenharia Mecânica, na Área de Térmica e Fluidos. .

Orientador: Prof. Dr. Rafael Gabler Gontijo

ESTE TRABALHO CORRESPONDE À VERSÃO FINAL DA DISSERTAÇÃO DEFENDIDA PELO ALUNO DOUGLAS DANIEL DE CARVALHO, E ORIENTADA PELO PROF. DR. RAFAEL GABLER GONTIJO

CAMPINAS
2020

Ficha catalográfica
Universidade Estadual de Campinas
Biblioteca da Área de Engenharia e Arquitetura
Rose Meire da Silva - CRB 8/5974

C253n

Carvalho, Douglas Daniel de, 1991-
Non-equilibrium magnetization dynamics in ferrofluids subjected to quadratic flows / Douglas Daniel de Carvalho. – Campinas, SP : [s.n.], 2020.

Orientador: Rafael Gabler Gontijo.
Dissertação (mestrado) – Universidade Estadual de Campinas, Faculdade de Engenharia Mecânica.

1. Fluidos magnéticos. 2. Magnetização. 3. Langevin, Dinâmica de. 4. Fluidodinâmica computacional. 5. Poiseuille, Fluxo de. I. Gontijo, Rafael Gabler, 1985-. II. Universidade Estadual de Campinas. Faculdade de Engenharia Mecânica. III. Título.

Informações para Biblioteca Digital

Título em outro idioma: Dinâmica de magnetização de não equilíbrio em ferrofluidos sujeitos a escoamentos quadráticos
Palavras-chave em inglês:
Magnetic fluids
Magnetization
Langevin dynamics
Computational fluid dynamics
Poiseuille flow
Área de concentração: Térmica e Fluídos
Titulação: Mestre em Engenharia Mecânica
Banca examinadora:
Rafael Gabler Gontijo [Orientador]
Yuri Dumaresq Sobral
William Roberto Wolf
Data de defesa: 14-09-2020
Programa de Pós-Graduação: Engenharia Mecânica

Identificação e informações acadêmicas do(a) aluno(a)
- ORCID do autor: https://orcid.org/0000-0003-2426-8928
- Currículo Lattes do autor: http://lattes.cnpq.br/6073161093351917

UNIVERSIDADE ESTADUAL DE CAMPINAS

FACULDADE DE ENGENHARIA MECÂNICA

DISSERTAÇÃO DE MESTRADO ACADÊMICO

Non-equilibrium magnetization dynamics in ferrofluids subjected to quadratic flows

Dinâmica de magnetização de não equilíbrio em ferrofluidos sujeitos a escoamentos quadráticos

Autor: Douglas Daniel de Carvalho

Orientador: Prof. Dr. Rafael Gabler Gontijo

A Banca Examinadora composta pelos membros abaixo aprovou esta Dissertação:

Prof. Dr. Rafael Gabler Gontijo, Presidente
Faculdade de Engenharia Mecânica – Universidade Estadual de Campinas

Prof. Dr. Yuri Dumaresq Sobral
Departamento de Matemática – Universidade de Brasília

Prof. Dr. William Roberto Wolf
Faculdade de Engenharia Mecânica – Universidade Estadual de Campinas

A Ata de Defesa com as respectivas assinaturas dos membros encontra-se no SIGA/Sistema de Fluxo de Dissertação/Tese e na Secretaria do Programa da Unidade.

Campinas, 14 de setembro de 2020.

Dedication

To my beloved parents, José and Wilma.

Acknowledgements

I would like to thank God for the gift of life and wisdom. Without the presence of a greater being, this work would not have been done.

To my eight strings: José, Wilma, Jhonie, Maycon, Raisa, Thaisa, Dácia and Alice.

To all the people who in one way or another helped me to walk this path, especially my family and friends.

To the artists and scientists who made this project less arduous.

To all professors who participated in my training process.

This study was financed in part by the Coordenação de Aperfeiçoamento de Pessoal de Nível Superior – Brasil (CAPES) – Finance Code 001.

To the funding agencies that made this project feasible, in particular: FAPESP, CNPq and PRP-Unicamp, respectively associated with the following grant numbers 2017/05643-8, 301467/2017-0 and 519.292-2400/19.

“Entre los pecados mayores que los hombres cometen, aunque algunos dicen que es la soberbia, yo digo que es el desagradecimiento…”

Miguel de Cervantes Saavedra in Don Quijote de la Mancha

Resumo

de Carvalho, Douglas Daniel. FEM - Dinâmica de magnetização de não equilíbrio em ferrofluidos sujeitos a escoamentos quadráticos. 2020. Dissertação (Mestrado). Faculdade de Engenharia Mecânica, Universidade Estadual de Campinas, Campinas.

Neste trabalho são realizadas simulações por Dinâmica de Fluidos Computacional (CFD) de um escoamento de Poiseuille plano de um ferrofluido sob a ação de um campo magnético uniforme aplicado. Uma metodologia numérica original para calcular campos magnéticos e hidrodinâmicos é proposta, incluindo uma discussão importante sobre uma região de entrada de magnetização identificada. Três modelos de magnetização diferentes são considerados para calcular o campo de magnetização. Esses modelos são implementados e validados por meio de diferentes abordagens, incluindo uma teoria assintótica desenvolvida neste manuscrito. As discrepâncias obtidas entre os resultados dados pelos diferentes modelos são fisicamente discutidas e interpretadas por meio das escalas de tempo do problema. Um intrincado equilíbrio entre diferentes mecanismos físicos é identificado e parece ser responsável por um comportamento difusivo do campo de magnetização. Esse equilíbrio é regido por uma competição entre a vorticidade do escoamento e os mecanismos de relaxação magnética, o que leva à proposição de um coeficiente difusivo de magnetização equivalente ν_{mag}. Além disso, mostra-se que a combinação de três diferentes escalas de tempo rege a dinâmica do desequilíbrio da magnetização: a escala de tempo difusiva Browniana, uma hidrodinâmica (convectiva) e uma escala de tempo magnética controlável associada à intensidade do campo magnético aplicado. Os resultados obtidos indicam a possibilidade de se controlar o desenvolvimento do campo de magnetização do fluxo por meio do campo magnético aplicado, da distribuição do tamanho das partículas, da concentração do fluido e da vazão. Inúmeros resultados relativos ao escoamento totalmente desenvolvido também são apresentados, incluindo perfis de magnetização e ângulos entre o campo aplicado $\boldsymbol{H}$ e o campo de magnetização $\boldsymbol{M}$. Além disso, um perfil de magnetização contínua para o fluxo totalmente desenvolvido é reconstruído usando uma abordagem de dinâmica de Langevin discreta para as partículas magnéticas. As simulações dinâmicas discretas de Langevin de uma coleção de partículas interagindo magneticamente leva em consideração as interações de longo alcance às quais as partículas estão sujeitas. Assim, as partículas interagem magneticamente com um campo magnético externo aplicado e com elas mesmas através de seus momentos dipolares magnéticos, além de estarem sujeitas a flutuações Brownianas devido ao seu pequeno tamanho. Nesta metodologia, os valores de vorticidade local extraídos das simulações CFD são usados como entrada para as simulações numéricas discretas,

que consideram uma suspensão coloidal submetida a um escoamento Couette local. Supõe-se que os momentos dipolares das partículas magnéticas são fixos a si mesmas, o que significa que giram ao longo da velocidade angular da partícula sem atraso. Para tanto, a rotação de partículas, promovida tanto por torques Brownianos quanto magnéticos, também é explorada nas simulações discretas, uma vez que a resposta de magnetização da suspensão está estritamente relacionada ao movimento rotacional das partículas. As equações que governam o movimento de partículas magnéticas suspensas em um fluido viscoso são resolvidas por simulações numéricas diretas em diferentes cenários físicos. Em geral, uma concordância muito boa entre os perfis de magnetização contínua e discreta foi obtida.

Palavras chave: Ferrofluidos, fluidos magnéticos, Dinâmica de Langevin, Região de entrada de magnetização, Escoamento plano de Poiseuille.

Abstract

de Carvalho, Douglas Daniel. FEM - Non-equilibrium magnetization dynamics of ferrofluids subjected to quadratic flows. 2020. Dissertação (Mestrado). Faculdade de Engenharia Mecânica, Universidade Estadual de Campinas, Campinas.

In this work, Computational Fluid Dynamics (CFD) simulations of a ferrofluid plane Poiseuille flow under the action of a uniform applied magnetic field are performed. An original numerical methodology to compute magnetic and hydrodynamic fields is proposed, including an important discussion regarding an identified magnetization entrance region. Three different magnetization models are considered in order to compute the magnetization field. These models are implemented and validated through different approaches, including an asymptotic theory developed in this manuscript. The obtained discrepancies between the results given by the different models are physically discussed and interpreted by means of the problem's timescales. An intricate balance between different physical mechanisms is identified and it seems to be responsible for a diffusive-like behavior of the magnetization field. This balance is ruled by a competition between the flow's vorticity and magnetic relaxation mechanisms, which leads to the proposition of an equivalent diffusive coefficient of magnetization ν_{mag}. In addition, it is shown that the combination of three different timescales rules magnetization non-equilibrium dynamics: the Brownian diffusive timescale, a (convective) hydrodynamic and a controllable magnetic timescale associated with the intensity of the applied magnetic field. The obtained results indicate towards the possibility of controlling the development of the flow's magnetization field by means of the applied magnetic field, size distribution of the particles, concentration of the fluid and flow rate. Numerous results regarding the fully developed flow are also presented, including magnetization profiles and angles between the applied field $\boldsymbol{H}$ and the magnetization field $\boldsymbol{M}$. In addition, a continuous magnetization profile for the fully developed flow is reconstructed by using a discrete Langevin dynamics approach for the magnetic particles. The discrete Langevin dynamics simulations of a collection of magnetically interacting particles takes into consideration long-range interactions to which the particles are subjected to. Hence, the particles interact magnetically with an external applied magnetic field and with themselves through their magnetic dipole moments, besides being subjected to Brownian fluctuations due to their small size. In this methodology, local vorticity values extracted from the CFD simulations are used as an input for the discrete numerical simulations, which consider a colloidal suspension subjected to a local Couette flow. It is assumed that the dipole moments of the magnetic particles are fixed to themselves, meaning they rotate

along the particle's angular velocity without delay. For this purpose, particle rotation, promoted both by Brownian and magnetic torques, is also explored in the discrete simulations, since the suspension's magnetization response is strictly related to the particles' rotational movement. The equations governing the motion of magnetic particles suspended in a viscous fluid are solved by direct numerical simulations under different physical scenarios. In general, a very good agreement between the continuous and discrete magnetization profiles was obtained.

Keywords: Ferrofluids, magnetic fluids, Langevin dynamics, Magnetization entrance region, Ferrofluid plane Poiseuille flow.

List of Figures

List of Tables

List of Abbreviations and Acronyms

Latin Letters

Chapter 1	-	-
$\boldsymbol{M}$	-	Magnetization field
$\boldsymbol{H}$	-	Applied magnetic field
M_0	-	Equilibrium magnetization
h	-	Spacing between plates
a	-	Half spacing between plates
$\hat{\boldsymbol{e}}_y$	-	Vertical direction vector
d	-	Particle's diameter
L	-	Duct's length
N, n	-	Number density of particles
T	-	Absolute temperature
$\boldsymbol{m}$	-	Magnetic moment
$\boldsymbol{d}_i$	-	Magnetic moment's direction
$\boldsymbol{g}$	-	Gravitational acceleration vector
M_s	-	Saturation magnetization
M_d	-	Bulk Magnetization
s	-	Coating layer thickness
S_t	-	Soret effect coefficient
r	-	Distance between particles
U_{aw}	-	van der Waals interaction potential
U_{ad}	-	Interaction energy between two magnetic dipoles
x	-	Distance between particles surfaces
U_r	-	Repulsive interaction between two particles
U_{st}	-	Steric repulsion between two particles
V	-	Volume
K_t	-	Thermal conductivity ratio

V_h	-	Hydrodynamic volume
f_0	-	Larmor frequency
$\boldsymbol{T}$	-	Magnetic torque
T_0	-	Reference temperature
a, b, c	-	Dimensionless curve fit parameters
M_H	-	Gain in viscosity parameter
m, n	-	Model constants
K	-	Magnetic anisotropy
Chapter 2	-	-
$\boldsymbol{B}$	-	Magnetic induction field
$\boldsymbol{F}$	-	Magnetic force
$\boldsymbol{L}$	-	External angular momentum
$\boldsymbol{S}$	-	Internal angular momentum
I	-	Volume density of the particle's moment of inertia
p	-	Pressure
M_i	-	Magnetization components
H_i	-	Field components
$\boldsymbol{E}$	-	Electric field
$\boldsymbol{v}, \boldsymbol{v}$	-	Velocity field, with components v_x and v_y
$\boldsymbol{H}_e$	-	Effective field
H_0	-	Reference field
U	-	Poiseuille mean velocity
$\boldsymbol{I}$	-	Identity tensor
D	-	Stokes-Einstein Brownian diffusion coefficient
Pe	-	Péclet number
Pe_r	-	Rotational Péclet number
Re	-	Reynolds number
St	-	Stokes number
St_r	-	Rotational Stokes number
k	-	Wavenumber
P_c	-	Contact parameter
$\boldsymbol{f}$	-	Force vector
$\boldsymbol{M}$	-	Mobility tensor
$\boldsymbol{x}$	-	Coordinates of the particles

$\boldsymbol{C}_N$	-	Set of vectors
$\boldsymbol{k}_\zeta$	-	Reciprocal lattice vectors
$\boldsymbol{x}_\gamma$	-	Lattice points
m_p	-	Particle's mass
J_p	-	Polar moment of inertia
$\boldsymbol{T}_B$	-	Brownian torque
$\boldsymbol{T}_m$	-	Magnetic torque
$\mathcal{L}$	-	Langevin function
$\mathcal{F}, \mathcal{G}, \mathcal{H}, \mathcal{C}, \mathcal{D}$	-	Modulation functions
$\boldsymbol{f}_b$	-	Brownian force
$\boldsymbol{f}_m$	-	Magnetic force
$\boldsymbol{f}_r$	-	Repulsive force
$\boldsymbol{f}_c$	-	Contact force
C_i	-	Constants
E	-	Young modulus
E_c	-	Material constant
Chapter 3	-	-
n_x	-	Number of grid points in the horizontal direction
n_y	-	Number of grid points in the vertical direction
$\boldsymbol{n}$	-	Normal vector
$\boldsymbol{T}$	-	Cauchy stress tensor
$\boldsymbol{v}_s$	-	Surface velocity
$\dot{Q}$	-	Flow rate
C	-	Constant
y	-	Vertical coordinate
Re_m	-	Magnetic Reynolds number
l_i	-	Length of each side of the cubic cell
$\boldsymbol{x}^{r,k}$	-	Position vectors in the physical and reciprocal spaces
Chapter 4	-	-
L_h	-	Hydrodynamic entrance length
L_m	-	Magnetic entrance length

Greek Letters

Chapter 1	-	-
ρ_s	-	Particle's density
ρ_f	-	Fluid's density
μ_B	-	Bohr magneton
μ_0	-	Magnetic permeability of free space
ϕ	-	Volume fraction of particles
ϵ	-	Electric permittivity of the carrier fluid
ψ_0	-	Surface potential
δ_{ip}	-	Relative distance between particle's surfaces
ϕ_h	-	Hydrodynamic volume fraction
μ_B	-	Bohr magneton
ξ	-	Density of particles
κ	-	Inverse of the Debye length; Carson model constant
κ_B	-	Boltzmann constant
$\Delta\rho$	-	Density difference
η	-	Viscosity
η_r	-	Rotational viscosity
η_0	-	Carrier fluid's viscosity; viscosity in the absence of a magnetic field
η_{eff}	-	Effective viscosity
η_{pl}	-	Plastic viscosity
η_H	-	Viscosity in the presence of a magnetic field
η_{zeta}	-	Virial coefficient
κ_H	-	Huggins coefficient
$\tilde{\phi}$	-	Volume concentration including surfactant
$\dot{\gamma}$	-	Shear rate
τ_B	-	Brownian relaxation time
τ_N	-	Néel relaxation time
τ	-	Total relaxation time; shear stress
τ_y	-	Yield stress
Ω	-	Angular velocity
χ	-	Magnetic susceptibility

λ	-	Dipole's coupling parameter
$\tilde{\lambda}$	-	Modified dipole's coupling parameter
Chapter 2	-	-
$\boldsymbol{\xi}$	-	Vorticity
∇	-	Nabla operator
$\boldsymbol{\omega}$	-	Particle's angular velocity
ζ	-	Vortex viscosity
α	-	Non-dimensional magnetic field
α_e	-	Non-dimensional effective magnetic field
$\boldsymbol{\sigma}$	-	Stress tensor
τs	-	Particle's relaxation time; Stokes timescale
λ'	-	Viscosity bulk coefficient
η'	-	Spin viscosity
θ	-	Angle between vectors $\boldsymbol{H}$ and $\boldsymbol{M}$
γ_H	-	Relaxation rate
λ_i	-	Model constants
ψ	-	Streamfunction
ψ_i, ψ_{ij}	-	Magnetic potentials
γ_w	-	Adjustable coefficient
$\boldsymbol{\omega}_s$	-	Angular velocity of the wall
U_s	-	Stokes velocity
ν	-	Poisson coefficient
τ_i	-	Modulation functions
$\boldsymbol{\beta}$	-	Random unitary vector
ξ	-	Convergence parameter
Chapter 3	-	-
β_i	-	Integers in an interval
Δt	-	Time step
γ_i	-	Integers in an interval
ζ_i	-	Components of the lattice enumeration vector
Chapter 4	-	-
ν_{mag}	-	Equivalent diffuse coefficient of magnetization
τ_{hydro}	-	Hydrodynamic timescale
τ_{mag}	-	Magnetic timescale

Abbreviations

CFD - Computational Fluid Dynamics
LD - Langevin Dynamics
pH - Power of Hydrogen
RES - Residue parameter

SUMMARY

1 Introduction

For centuries, researchers and scientists have been interested in some fascinating materials due to their extraordinary physical properties and applications. Magnetic fluids are some of these smart materials that can adaptively change their physical properties when in the presence of an external magnetic field [1]. They may be classified as ferrofluids and magnetorheological fluids [2]. Ferrofluids are stable colloidal suspensions of magnetic nanoparticles immersed in a Newtonian carrier liquid [3, 4]. Investigations of the flow, the rheological properties and the applications of ferrofluids are an extremely lively research field nowadays. Since the 1960's, they have been used in applications ranging from heat transfer enhancement [5, 6, 7, 8, 9] to separation processes [10] and biomedical applications (drug targeting or hyperthermia cancer treatments) [11, 12, 13], as well as in many other fields of scientific and technological interest [14, 15, 16, 17, 18, 19].

One of the most remarkable features of a magnetic fluid from a purely scientific perspective is the fact that the description of this material demands the coupled understanding of different branches of the physical sciences, such as hydrodynamics and electromagnetism [3, 4]. The equations of motion for a magnetic fluid consider the presence of additional forces that are not present in the classical set of Navier-Stokes equations [3, 4, 20, 21]. In the presence of a magnetic field gradient, magnetic forces and magnetic torques are developed to drive magnetic particles, which subsequently draw along the liquid solvent carrier. This allows continuous actuation and precise positioning of the ferrofluid using a magnetic field [22]. The appearance of an internal magnetic force acting on the dipolar matter due to the presence of a magnetic field gradient (*Kelvin forces*) in the inner structure of a magnetic fluid, demands additional modeling in order for a consistent closure of the mathematical description that governs the motion of a magnetic fluid [3, 4].

At the beginning of this century, an interesting study provided a rich discussion of whether such magnetic forces should arise from a modified stress-tensor (with additional terms from magnetic origin) or if they should be added in the form of volume forces by a source term in the equation of motion [23]. Indeed, this paper indicates different thoughts on the subject, presented by two different schools . While some physicists, used to study the behavior of matter in submolecular scales, often presents a way of thinking about these magnetic forces mostly in terms of energy [23, 24], classical fluid dynamicists tend to perceive these magnetic forces in the inner structure arising from the fluid's stress tensor [25]. Anyway, regardless the thought school around this subject, the fact is that additional terms of magnetic origin appear in the equation of motion

when it comes to the description of a magnetic fluid flow [3, 4].

It is known that in the presence of an external magnetic field, the magnetic particles suspended in the fluid tend to align their magnetic dipole moments in the direction of the applied field $\boldsymbol{H}$, resulting in a so-called fluid's bulk magnetization $\boldsymbol{M}$ [3, 4]. When it comes to the description of magnetic fluid's flow, the concept of internal rotation arises due to the relation between the magnetic and rotational degrees of freedom of the particles [26, 21], so that the fluid is subjected to an intense interplay between hydrodynamic and magnetic effects, whose intensity depends mostly on the particles internal magnetic relaxation timescale. In Néel regimes the particles dipole moments usually respond instantaneously to the presence of the field and hence the flow's vorticity has no influence on the magnetization field. However, when the particles internal relaxation is dominated by Brownian mechanisms the flow may substantially affect the magnetization response [27, 28]. This way, it seems the magnetization field is the main variable that connects magnetic manifestations with the hydrodynamic behavior of the fluid. Therefore, it is extremely important to properly understand this concept and its implications in hydrodynamics. Physically, one may interpret the fluid's magnetization as a local average (based on the continuum hypothesis) of the alignment of the magnetic dipoles in the direction of the applied field [29, 3, 30]. When the suspension is at rest, this property is referred as *equilibrium magnetization* $\boldsymbol{M_0}$ [3, 4]. This equilibrium scenario is well described by a Langevin model for dilute suspensions [3, 15, 14, 31, 32]. However, in more concentrated regimes, the role of particles' interactions produces a considerable deviation from this equilibrium relation. Under these circumstances, some models that capture with good precision the equilibrium magnetization of concentrated ferrofluids are known [33, 34].

In the equilibrium scenario, the physics of a magnetic suspension is well described by the competition of three mechanisms: field-particle interactions, interparticle interactions (i.e. dipolar and hydrodynamics long-range particle interactions) and particle-molecule interactions (Brownian motion). However, when the fluid is set to move, the vorticity field tends to misalign the magnetic particles from the direction of the field, producing a magnetic torque inside the material that breaks-up the symmetry of the fluid's stress tensor and leads to the so called *magnetoviscous effect* [35, 26, 36, 3, 37, 38, 39, 40, 15, 16]. If these magnetic torques are instantly balanced by viscous torques, the hypothesis of stress symmetry may be considered [40], but the appearance of extra stresses inside the material related to the additional energy that the local shear must impose in order to make the particles rotate in the direction of vorticity would still have to be dealt with.

Regarding hydrodynamics, in order to properly compute the velocity field of a ferrofluid flow-

ing under the presence of an applied magnetic field, the applied magnetic field $\boldsymbol{H}$ and the magnetization field $\boldsymbol{M}$ must be known in advance. While the applied field can be obtained from the solution of a Laplace equation through spherical harmonics (for the free space and depending on the type of boundaries) [41] and then jumped to the medium using properly boundary conditions arriving from Gauss and Ampère's laws of magnetism [3], a physical consistent computation of the magnetization field demands deeper thoughts and discussions [26, 42, 40, 43, 24], since in non-equilibrium regimes the magnetization field is no longer an exclusive function of the field [44].

The phenomenological equations describing non-equilibrium magnetic fluid's dynamics are based in the continuum hypothesis. Hence, details on microscopic long-range particle interactions are naturally filtered by this averaging process. Along these lines, an important unanswered question is: how to incorporate the role of particle's interactions in the non-equilibrium behavior of the magnetization field? Some authors argue that these should be incorporated in the equilibrium relaxation term in the magnetization equations by using higher-order asymptotic models [34], while others argue that these must be incorporated in the form of a configurational stress tensor that deals with the magnetoviscous effect directly [45], using hybrid models that mix Langevin Dynamics (LD) with classical Computational Fluid Dynamics (CFD) techniques [46]. This is a complex subject which will not be fully answered in this work. However, several physical discussions on this matter are presented, using as a case study a magnetic fluid flow between parallel plates under the action of a uniform applied field in order to physically understand the interplay between hydrodynamic and magnetic mechanisms in a framework that deals with this non-equilibrium magnetization dynamics.

It is important to mention that ferrofluid flows have been the subject of numerous scientific works in the past. For instance, many studies focused on the interesting effect of spin-up flow [47, 48, 49, 20, 50, 51], while others focused on the effect of oscillating fields on ferrofluid flow both in the presence [17, 52, 53, 54, 16] and in the absence [55] of pressure gradients. There are also theoretical studies of ferrofluid flow with applied fields [26, 17, 54] as well as experimental [35, 56, 57, 18] and numerical works [18, 16] in Poiseuille flow. Although ferrofluid's pipe flow has already been numerically, theoretically and experimentally studied, many studies focused on rotational viscosity (viscosity changes when in the presence of a magnetic field) [16, 56, 58, 57, 18, 17], however, none of them focused on effectively describing non-equilibrium magnetization dynamics, which is the center of attention of this present work.

In this work, by considering a continuum mathematical description, Computational Fluid Dy-

namics (CFD) simulations of a ferrofluid plane Poiseuille flow under the presence of a uniform applied field are performed. The behavior of a non-uniform magnetoviscous effect is identified. Spatial variations on the misalignment between the magnetization and the applied fields are explored and linked to vorticity profiles. In addition, the existence of a magnetic entrance length is identified, which leads to the postulation that the vorticity-magnetization interplay may be interpreted in terms of an equivalent diffusive coefficient of magnetization. This work aims at trying to contribute to the state of the art of this field, in order to enrich the discussion on how interparticle forces affect the non-equilibrium magnetization dynamics of ferrofluid flows.

One concern regarding a continuous description of ferrofluid's dynamics is that the phenomenological equations describing non-equilibrium magnetic fluid's dynamics do not necessarily capture all the details of the micro-structure of the material. By applying the continuum hypothesis in order to obtain the Eulerian hydrodynamic and magnetic fields, some information regarding the sub-continuum cause that leads to a perceivable consequence in the continuum representation is lost. This way, it is extremely important to understand the micro-structural behavior of the magnetic particles in order to comprehend the phenomenology of the suspension's magnetization dynamics. Up to these days, stochastic molecular dynamics have been used very timidly [2], with a few works regarding the equilibrium magnetization of a colloidal suspension formed by magnetically interacting particles [27, 28] and numerical simulations of rotational Brownian motion of ferromagnetic particles [59], to cite a few. Bearing this in mind, discrete Langevin dynamics (LD) simulations are performed in this work for the magnetic particles, which are subjected to long-range field-dipole and dipole-dipole magnetic interactions. It is intended that such investigations, done in the scale of the particles, lead to a better comprehension regarding the connection between the suspension microstructural behavior and its magnetization response, since hydrodynamic forces associated with stochastic molecular dynamics can lead to realistic predictions for magnetic fluids [2], leading to the prediction of properties and qualities of ferrofluids to be further tested in a laboratory. In the next section, the studied problem is presented.

1.1 Problem's description

A ferrofluid flow between parallel plates under the action of a uniform applied magnetic field in the perpendicular direction $\boldsymbol{H} = H\hat{\boldsymbol{e}}_{\boldsymbol{y}}$ in considered, as shown in Fig. (1.1). The plates are apart by a spacing of $h = 2a$. The length of the channel is $L = 400h$, in order to assure fully

developed flow for the studied physical scenarios. The flow entering the channel is considered to be uniform and demagnetized, in the absence of an applied magnetic field. The flow of an isothermal incompressible ferrofluid is considered, assuming a spatially uniform distribution of rigid spherical monodisperse magnetic particles with mean diameter d in the range $13nm \leq d \leq 15nm$.

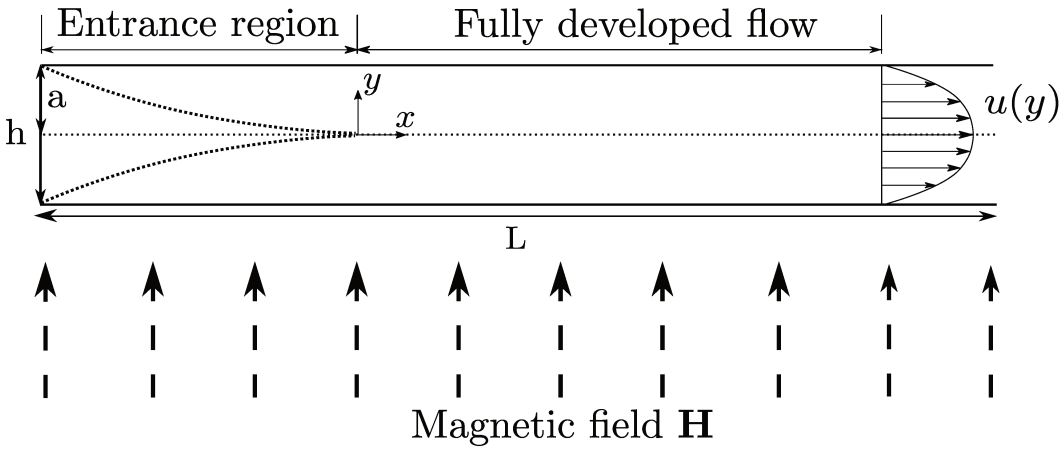

Figure. 1.1: Scheme of the geometry of the studied problem in the continuous approach. Image from de Carvalho and Gontijo [46].

The magnetic fluid flow is simulated through a two-dimensional CFD in-house code where the vorticity and magnetization fields are calculated. Afterwards, the calculation domain is divided into smaller cells called *local vorticity cells*. These cells are depicted in Fig. (1.2). These sub-regions are then simulated in another in-house code through a LD numerical scheme. The local vorticity obtained through the coupled solution of the vorticity and magnetization equations in the CFD code is used as an equivalent local shear-rate to be used as an input in the LD code, which simulates a local Couette flow.

The discrete simulations are carried out in a simulation box which performs the local Couette flows. A suspension of N magnetic spherical and monodisperse particles with diameter $d = 2a$ and density ρ_s immersed in a viscous fluid with viscosity η and density ρ_f at an absolute temperature T. The suspension is also subjected to the application of an external vertical homogeneous magnetic field $\boldsymbol{H}$. The localization of each one of the particles is described by a set of vectors $\boldsymbol{r}_N$ and their angular displacement by $\boldsymbol{d}_i$, where i refer to an index of the particles. The particle's magnetic dipole moments are described by $\boldsymbol{m}_i = m\boldsymbol{d}_i$. An initial simulation box in sketched in Fig. (1.3).

The idea is to use this approach in order to reconstruct a continuous magnetization profile without solving any partial differential equation based on the continuous hypothesis, but rather

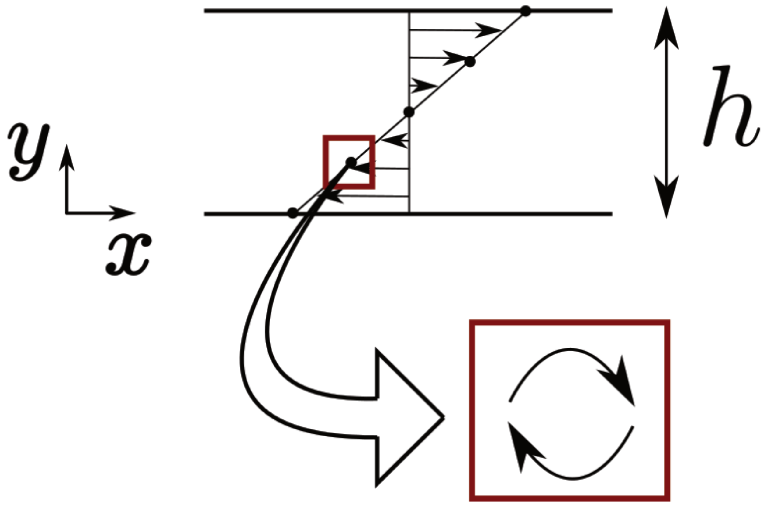

Figure. 1.2: Division of the flow into local vorticity cells. Image from de Carvalho and Gontijo [46].

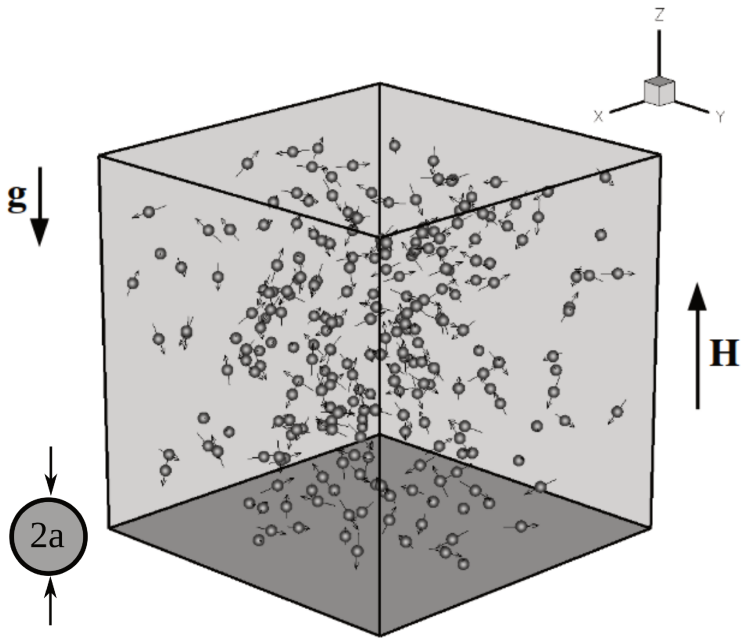

Figure. 1.3: Typical magnetic suspension simulated in this work. Image adapted from Gontijo and Cunha [27].

directly through the solution of the equations of motion for each individual magnetic particle. This tool could be used in future works in order to understand how particle interactions affect the magnetization of ferrofluid flows in non-equilibrium regimes. Nowadays, there is a discussion regarding if the inclusion of higher order equilibrium asymptotic magnetization models [34] in the evolutive magnetization equation are enough to capture this effect or if this should be considered

in a new constitutive formulation for the stress tensor of the ferrofluid by adding their contribution to a configurational tensor [45]. We hope that the ideas presented in this manuscript can be used in future works in order to understand how long-range dipolar interactions affect the non-equilibrium magnetization response of ferrofluids.

In this manuscript, a synthetic review regarding ferrofluids and particulate systems is firstly presented, with special attention to the magnetoviscous effect (viscosity variations under the action of a magnetic field). Afterwards, the mathematical description of the problem, both in its continuous and discrete approach is presented. In the next chapter, the numerical routines developed and used to obtain the results of this work are carefully described. Finally, the main results concerning the magnetization response of a ferrofluid plane Poiseuille flow are presented and discussed.

1.2 Ferrofluids: a synthetic review

Ferrofluids are stable colloidal suspensions of single domain (one single magnetic direction) magnetic nanoparticles that magnetize strongly in the presence of an external magnetic field [3, 15].

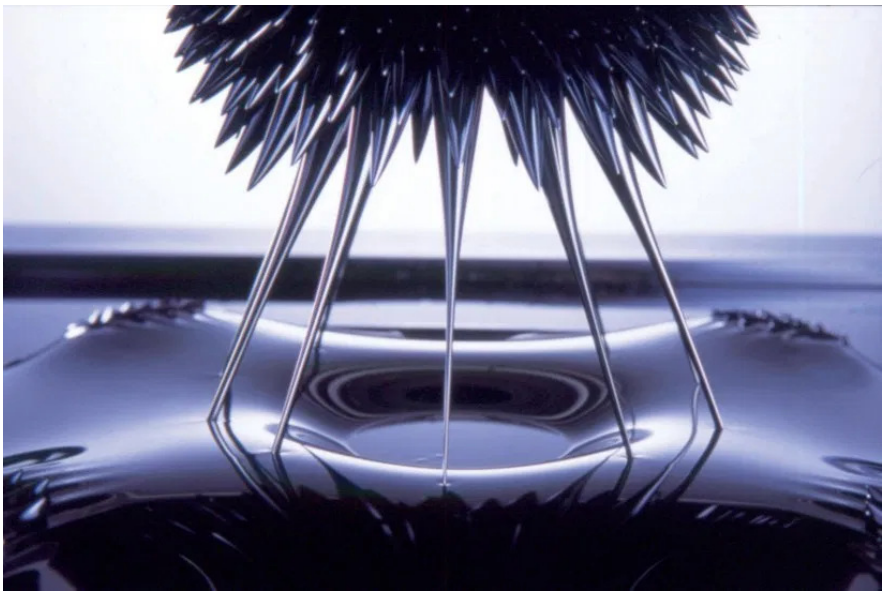

Figure. 1.4: Ferrofluid under the action of an applied magnetic field. Protrude, Flow by Sachiko Kodama and Minako Takeno [60] (Accessed on March 4, 2020).

These synthetic fluids were first produced in the early 1960's [3, 61]. The magnetic nanoparticles are usually made of iron oxides, most commonly magnetite (Fe_3O_4) [62] and maghemite ($\gamma - Fe_2O_3$) [63], however $MnZn$ ferrites [64] and ferrofluids containing cobalt particles have recently become available [65]. The particle's diameter are usually $d \approx 10nm$ (some references report $d \approx 3 - 15nm$ [3], others $d \approx 5 - 20nm$ [63] while others claim that "ideal" ferrofluids have $d \approx 5 - 10nm$ [1]) and the carrier liquid, which can be either polar or non-polar [2, 1], is usually a Newtonian fluid, like water, kerosene and various oils [62]. Most commercially available ferrofluids are synthesized with particles' diameter in the range $d \approx 5 - 15nm$ [1], however ferrofluids with particles' diameter $d = 24nm$ made of $CoNi$ and others composed of fiberlike $CoNi$ particles of $56nm$ in length and $6.6nm$ in width have already been reported in the literature [66]. It is important to mention that in the range $15nm \lessapprox d \lessapprox 40nm$, magnetic fluids are still considered ferrofluids, while above this limit they are considered magnetorheological fluids [1]. As mentioned above, ferrofluids differ from the usual magnetorheological fluids due to the size of the magnetic particles. In this case, the particles are larger (micron sized), usually non-stable magnetic particles, and such suspensions are used in dampers, brakes and clutches [2]. Figure (1.5) displays magnetic fluids classification due to the particle's diameter according to López-López et al. [66].

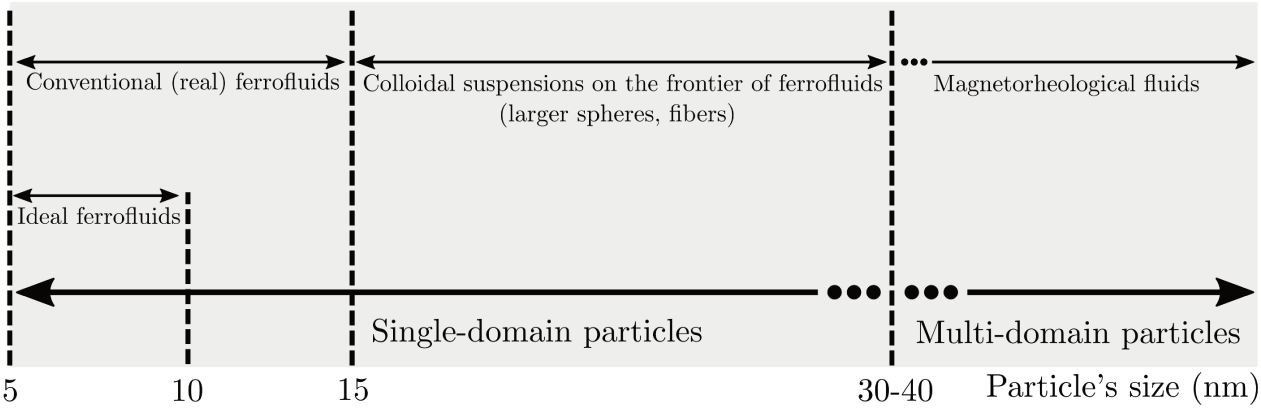

Figure. 1.5: Magnetic fluids classification due to particle's diameter according to López-López et al. [66]. Image adapted from López-López et al. [66].

Due to the small size of the magnetic particles, they undergo translational and rotational Brownian motion [63]. Brownian motion refers to the random movement of particles suspended in a fluid that occurs due to collision with molecules in the base fluid [67]. The particles do not sediment in the gravitational field or in moderate magnetic field gradients nor do they form agglomerates due to magnetic dipole's interactions [62]. Each particle, which must be sufficiently small to be considered a monodomain in a way to possess a non-zero magnetic moment $m \approx 10^4 \mu_B$, where μ_B is the Bohr magneton [62], is treated as a thermally agitated magnetic dipole, similar

to the molecules of a paramagnetic gas [63], so that the ferrofluid shows its magnetic properties [2]. In the absence of an applied magnetic field, the particles' dipole moments $\boldsymbol{m}$ are randomly oriented due to the thermal agitation, and in this configuration the fluid has no net magnetization [3, 63]

When a continuous body is placed in a magnetic field, the field in its vicinity can undergo significant changes. For instance, for ferromagnetic materials, the field at one point can increase by a tenfold factor [29], while for a dilute ferrofluid the magnetic field generated by the magnetization (demagnetizing field) is much smaller than the applied field and may be neglected [54]. This property depends on the microscopic interaction of the material's magnetic dipole moments with the external magnetic field. Every magnetic molecule or nanoparticle acquires an induced magnetic moment when subjected to a magnetic field. On the molecular scale, particles in a magnetic field are said to be magnetized, whereas on the macroscopic scale, magnetization measures the polarization state of a continuous magnetized material. For magnetic fluids, where each particle can be interpreted as a nanomagnet, the magnetization $\boldsymbol{M}$ represents a global measure of the degree of alignment of the magnetic moments in the direction of the applied field, being given by [3, 30, 29]:

$$\boldsymbol{M} = N\bar{\boldsymbol{m}} \tag{1.1}$$

In Equation (1.1), $\bar{\boldsymbol{m}}$ is the magnetic moments average and N is the density number of particles. Magnetization is, therefore, in the context of ferrofluids, a volumetric average of magnetic moments in the direction of the field per unit of volume. In the case of ferrofluids, when a magnetic field is applied the particles' magnetic moments tend to align in its direction, generating a net magnetization which increases with increasing magnetic field strength as more dipoles align, until a magnetization saturation value is reached (saturation magnetization M_s) [3, 63].

The magnetic particles are protected against agglomeration due to *van der Waals* interactions by a coating (with thickness $2nm \lessapprox s \lessapprox 8nm$) either with long chained organic molecules (surfacted ferrofluids) or an electric shell (ionic ferrofluids) [62, 2], as indicated in Fig. (1.6a). The coating generates repulsive forces that prevent the contact of the particles, suppressing the destabilizing effect of the *van der Waals* interaction [62]. This then creates a stable suspension which is stable over years [62], however particle agglomeration have been reported to occur as commercial

water-based ferrofluids age [51]. This coating also allows the fluidity of ferrofluids to be maintained under the action of high gradients of intense magnetic fields [68], as opposed to what is observed in magnetorheological fluids, which solidify in strong magnetic fields [15, 69]. Ferrofluids have a dark (almost black) color, being optically isotropic, but can exhibit an induced birefringence when in the presence of an external magnetic field [14], which can be used to examine some aspects of magnetic fluid rheology [70].

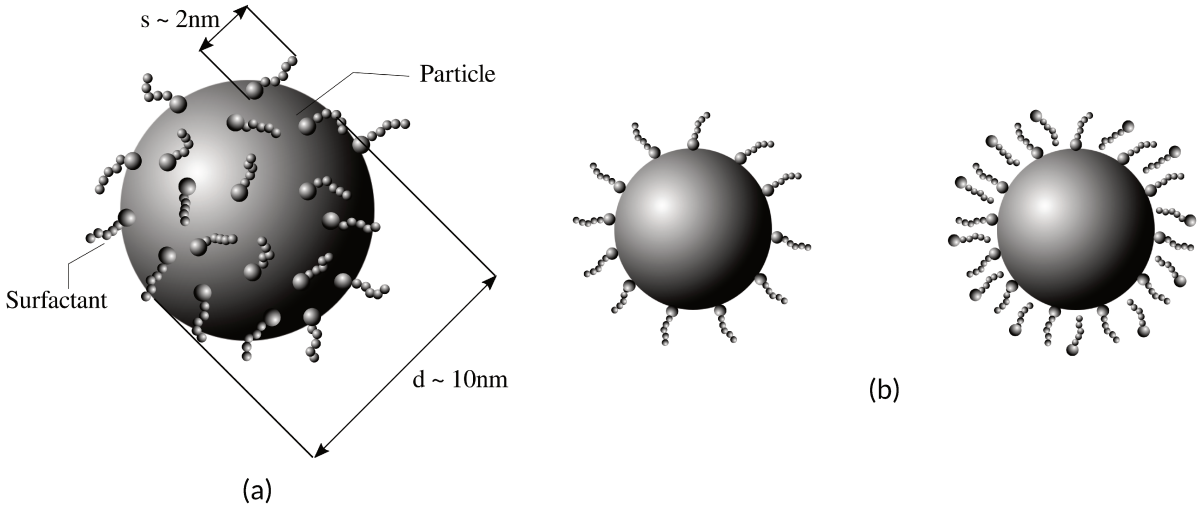

Figure. 1.6: (a) Schematic of the magnetic nanoparticles and their surfactant layer. (b) Type of surfactant layers: on the left, single-layered grain in an oil-based ferrofluid and on the right, double-layered grain in a water-based ferrofluid. Image adapted from that shown in Scherer and Figueiredo Neto [2]

.

The research interest in ferrofluids is justified due to the fact that such fluids combine the usual hydrodynamic properties of fluids with the possibility of controlling their flow and rheological properties with moderate magnetic fields [62, 29]. This incredible possibility arises from the fact that each of the thermally agitated particles is treated as a single domain with a magnetic moment ($m \approx 2.34 \times 10^{-19} Am^2$ for $d = 10nm$) that interacts with an applied magnetic field $\boldsymbol{H}$ [62], leading to the ferrofluid's magnetization, which may exist, though not for very long, even in the absence of $\boldsymbol{H}$ [16]. Since the force experienced by a magnetizable mass in the presence of a magnetic field gradient is proportional to the material's magnetization, strong magnetic forces can be generated for magnetic fluids with moderate magnetic fields [62]. In addition, in the presence of a non-homogeneous magnetic field, ferrofluids are attracted to the regions of maximum intensity of the field, as the magnetic moments $\boldsymbol{m}$ rotate towards the direction of minimum energy (parallel to the field), causing the fluid to be pulled towards the magnetic field's gradient [2].

Thermodiffusion phenomena (Soret effect), of which in an initial isotropic fluid without external forces a concentration gradient accumulates due to an applied temperature gradient [71], is also present in magnetic colloids, which in this case is strongly affected by the applied magnetic field [72, 73, 74, 75, 76, 77, 78, 79]. In this scenario, the originally homogeneous ferrofluid is subjected to a temperature gradient and a concentration current of magnetic nanoparticles is observed parallel to the direction of the thermal gradient [2]. The Soret effect is characterized by the Soret coefficient S_T, which represents the coupling between current of mass and temperature gradient [80]. If the particles tend to move away from the hottest region, the ferrofluid is called thermophobic ($S_T > 0$), however, if they tend to be concentrated in the warmest region, the colloid is called thermophilic ($S_T < 0$) [81]. Experiments performed in Luo et al. [82] demonstrated a diffusion of magnetic particles to colder regions, indicating a thermophobic behavior for the studied ferrofluid. Up to this day, a fully comprehensive theoretical picture of the different mechanisms that take place in the thermodiffusive behavior of these complex fluids is still lacking [2], however interesting phenomena have already been observed. For instance, positive and negative concentration gradients depending on the ferrofluid studied for the same temperature gradient have already been observed; dependences of the sign of S_T on the sign of the surface particles' charges have been reported in Alves et al. [83], Lenglet et al. [84]; the nature of the liquid carrier (i.e. polar or non polar) has been reported to be an important factor of the sign of S_T, but not the determinant one [2, 84, 81, 85], among others.

The large number of particles allows the spatial and temporal manipulation of small volumes of ferrofluids. Such controllability results in different types of flows and instabilities on their surfaces [63], so that they exhibit a wide range of very interesting lines, patterns and structures [86, 87, 88], as those shown in Rinaldi and Zahn [87]. This attribute of ferrofluids is also used by different artists worldwide to create different patterns and shapes in ferrofluids under the influence of magnetic fields [89], as the one presented in Fig. (1.4). Many astonishing images of ferrofluid control can be seen in Kodama [60]. The different types of instabilities that can arise at the air/fluid interface in ferrofluids are due to the balance between magnetic force, gravity and surface tension, depending on the size, confinement configuration and direction of application of the magnetic field [63]. One of the most common instabilities is the normal field instability of a ferrofluid layer in air interface, also called the Rosensweig instability [3, 90]. The observed peaks initiate in a hexagonal array when the magnetic surface force exceeds the stabilizing effects of fluid weight and surface tension, as observed in Rinaldi and Zahn [87]. In addition, a most unusual instability is the labyrinth instability, which appears when a ferrofluid layer confined between two parallel plates is subjected to a magnetic field normal to the surface [3, 87, 91, 63], also observed in Rinaldi

and Zahn [87].

The research field for magnetic fluids is enormously rich. They are the subject of study in many areas. For instance, chemists are interested in their synthesis and production processes; physicists study their physical properties and are constantly proposing theories to explain their interesting and, at times, somewhat strange behavior; engineers are more concerned with their applicability in various technological products; biologists and doctors study their biomedical possibilities and are currently using them in medicine applications and in research in the biological field; finally, due to the small size of the magnetic particles, ferrofluids have involved nanoscience and nanotechnology since its conception. In addition, due to their unique response to applied magnetic fields, which can deform their shapes and surfaces, direct their flow and exert forces and torques on wet surfaces and submerged objects [63], they find many real-life applications, which will be briefly described in section 1.2.2. For instance, ferrofluids are used to cool more than 50 million loudspeakers a year, almost all computer disk drives use a magnetic fluid rotary seal to exclude contaminants, and the semiconductor industry uses silicon crystal growing furnaces that uses ferrofluid rotary shaft seals [70].

Rosensweig [3] has given an authoritative introduction to research on ferrofluids in his monograph, and the interested reader is referred to such reference for more information on the fascinating world of magnetic fluids.

1.2.1 Synthesis and stability

Many aspects of the physics of ferrofluids and their content, such as the material and geometry of the magnetic particles, the viscosity and concentration of the suspension, the surfactants used in the particles, among others, affect their rheological properties, as well as their stability and redispersibility. Another important parameter which affects the magnetic properties of a ferrofluid is its temperature. If it is above the *Curie* temperature T_c the magnetic particles lose their magnetization [1]. A brief description of the synthesis and stability of these colloids is presented in the following sections.

Magnetic nanoparticles

Even though pure metals as $\mathrm{Fe}, \mathrm{Co}, \mathrm{Ni}$ possess the highest saturation magnetization (which is a very interesting attribute in ferrofluids' applications, since the magnetic body force acting on them is strongly related to the fluid's magnetization), they are extremely sensitive to oxidation, therefore magnetic particles are usually made of iron oxides [1]. Ferrites like magnetite ($\mathrm{Fe_3O_4}$) or maghemite ($\gamma - \mathrm{Fe_2O_3}$), or other materials with stoichiometric formula $\zeta\mathrm{O} \cdot \mathrm{Fe_2O_3}$, where ζ stands for divalent ions as $\mathrm{Mn}, \mathrm{Zn}, \mathrm{Ni}, \mathrm{Co}$ are commonly used in ferrofluids [1].

In order to synthesize such magnetic nanoparticles, two methods are usually employed: 1) the method of size reduction [61] and 2) the chemical precipitation method [92]. The latter is probably the most used method nowadays [2]. In size reduction, micron-sized magnetic powder is held in solution with a solvent and a dispersant in a ball mill. It will then grind for a long period, usually several weeks [2]. In the chemical precipitation method, the procedure usually starts with a mixture of iron(II) chloride $\mathrm{FeCl_2}$, iron(III) chloride $\mathrm{FeCl_3}$ and water. A process of co-precipitation then occurs after the addition of ammonium hydroxyde $\mathrm{NH_4OH}$. Later, different procedures are applied to the system (i.e. peptization, magnetic separation, filtration and finally dilution) [2]. The co-precipitation method is frequently used to prepare magnetic nanoparticles due to its low cost and simplicity [1, 93]. Apart from the aforementioned most common methods, others have been employed for magnetic particles synthesis and characterization [1], such as methods using sol-gel pyrolysys [94], thermal reductive decomposition [95, 96], mechanical alloying technique [97] and hydrothermal technique [98, 99].

Magnetic nanoparticles are coated with surfactant agents like amphiphilic molecules, such as oleic acid $\mathrm{C_{18}H_{34}O_2}$ and aerosol sodium di-2ethylhexyl-sulfosuccinate $\mathrm{C_{20}H_{36}Na_2O_7S}$ in the case of surfacted ferrofluids for preventing aggregations [2]. The magnetic grains are kept in solution due to steric repulsion between the particles which acts like a physical barrier [100], stabilizing the colloid [2]. Two different arrangements of surfactants are present depending on the polarity of the carrier liquid: 1) if the carrier medium is non polar, for instance oil, only one layer (left side Fig. 1.6b) of surfactant is needed to form a hydrophobic layer, and in this case the polar head of the surfactant is attached to the particles' surface and the carbonic "tail" is in contact with the fluid [2]; 2) if the particles are dispersed in a polar medium, for instance water, a hydrophilic layer around them is composed of two layers (right side Fig. 1.6b) [2]. The minimization in the particles' agglomeration as well as the increase in ferrofluid's stability due to dispersants is of great importance in

ferrofluids' applications. The additives must also match the dielectric properties of the carrier liquid [1]. Apart from the already mentioned, many surfactants as silica [101], chitosan [102], polyvinyl alcohol (PVA) [103] and ethylene glycol [104] are usually used [1]. Besides oleic acid, others acids as citric acid and tartaric acid are used to obtain stable ferrofluids over a large pH range $(3 - 11)$ [105]. Other classes of additives are sometimes used, such as anti-oxidation additives to prevent oxidation [1]. Surfacted ferrofluids are widely used in many applications as they are commercially available and easily found. One of the most well-known manufacturers is the company *Ferrotec* (*https://www.ferrotec.com/*).

In the case of ionic ferrofluids [106, 107], in order to keep the colloidal system stable and avoid aggregations, the nanoparticles are electrically charged, and in some cases both the steric and electrostatic repulsion are present [2]. In this scenario, an acid-alkaline reaction between the particles and the bulk keeps their surface electrically charged [2]. Such colloids usually make use of water as the carrier liquid [2]. The solution's pH is determined by the particle's charge, being acid ($pH < 7$) if the particles are positively charged and alkaline ($pH > 7$) if they are negatively charged [2].

The magnetic nanoparticles must be suspended in a carrier liquid. The choice of the carrier liquid is extremely important and depends mainly on the type of application in which the ferrofluid will be used. Theoretically, it should be possible to produce dispersion in any liquid, so that the adequacy of some requirements in different applications such as viscosity, surface tension, temperature and oxidative stability, vapor pressure, stability in hostile environments [72] and, in the case of transfer applications, high conductivity, high heat capacity, high thermal expansion coefficient, among others, could be obtained [67]. Many liquids have already been used in ferrofluids, such as water, mineral and silicone oils, kerosene, combinations of these in addition to other polar and non-polar liquids [108]. The main attribute of carrier liquids is that they must be non-reactive both with the magnetic phase and with the material of the device in which the ferrofluid will be in contact [1].

One of the most noble applications of ferrofluids are those related to biomedical applications. Table (1.1) provides a list of polymers and molecules that can be used to coat nanoparticles in biological applications [1, 109, 110].

Table. 1.1: Different polymers and molecules that can be used as nanoparticles coating to provide ferrofluid's stabilization with some biological applications [109, 110]. Adapted from Genc and Derin [1].

Polymers/molecules	Advantages
Polyethylene glycol (PEG)	Improves the biocompatibility
Dextran	Stabilizes the colloidal solution
Polyvinylpyrrolidone (PVP)	Stabilizes the colloidal solution
Fatty acids	Colloidal stability
Polyvinyl alcohol (PVA)	Prevents coagulation of particles, giving rise to monodisperse particles; Increases the stability and biocompatibility of the particles and helps in bioadhesion
Polyacrylic acid	Good for cell biology, for instance, cell targeting
Phosphorylcholine	Coagulation activation; Colloidal solution stabilizer
Chitosan	Used as a non-viral gene delivery system; Biocompatible and hydrophilic, used in medicine, biotechnology and water treatment
Gelatin	Hydrophilic emulsifier used as a gelling agent; Natural biocompatible polymer

Stability of the colloid

Many aspects of ferrofluids' physics affect their stability. It is worth noting that the magnetic nanoparticles are subjected to Brownian motion, interparticle interactions and particle-field interactions. The magnetic colloid stability depends on the thermal contribution and on the balance between attractive (van der Waals and dipole-dipole) and repulsive (steric and electrostatic) interactions [2].

Two main attractive interactions between magnetic nanoparticles in ferrofluids affect their stability, namely the van der Waals interaction and the magnetic dipole-dipole interaction. The short-range van der Waals interaction U_{Aw} (also known as van der Waals-London interaction), whose magnitude increases with particles' sizes is given, for the case between two spherical particles of diameter d separated by a distance r, by [111, 2]:

$$U_{Aw} = -\frac{A}{6}\left[\frac{d^2}{2(r^2-d^2)} + \frac{d^2}{2r^2} + \ln\left(1-\frac{d^2}{r^2}\right)\right] \tag{1.2}$$

In Equation (1.2), A is the Hamaker constant ($A \approx 10^{-19}J$ for ferrite particles $\mathrm{Fe}, \mathrm{Fe_2O_3}, \mathrm{Fe_3O_4}$ in hydrocarbon [2, 1]).

The other attractive interaction between the magnetic nanoparticles is that due to the magnetic dipole-dipole interaction. The interaction energy U_{Ad} between two magnetic dipole's $\boldsymbol{m_1}$ and $\boldsymbol{m_2}$ separated by a distance r is given by [3]:

$$U_{Ad} = \frac{\mu_0}{4\pi r^3}\left[\boldsymbol{m_1}\cdot\boldsymbol{m_2} - 3\left(\boldsymbol{m_1}\cdot\frac{\boldsymbol{r}}{r}\right)\left(\boldsymbol{m_2}\cdot\frac{\boldsymbol{r}}{r}\right)\right] \tag{1.3}$$

In Equation (1.3), $\boldsymbol{r}$ is the relative position of the particles. For larger particle's separation, the dipole-dipole interaction energy is similar to a Keesom interaction [112, 63]. The interacting force and torque between two permanent magnetic dipoles can be obtained from Eq. (1.3) [3].

Now, it is also important to briefly mention the large number of magnetic particles per unit volume in ferrofluids even at low volume fractions [63], since it is associated with the particle-particle interactions. The typical particle numerical density in a magnetic colloid is reported in Scherer and Figueiredo Neto [2] to be $\sim 10^{23}m^{-3}$. An estimate of the number density of particles n can be made by considering monodisperse nanoparticles arranged in a regular structure by neglecting Brownian motion, external shear stress and magnetic fields [63]. Results for the typical particle density are presented in Torres-Díaz and Rinaldi [63] for different particle diameters as a function of the hydrodynamic volume fraction ϕ_h, along with an estimate relative distance $\delta_{ip} = x/a$ between the particles' surfaces, where x is the distance between the particles' surfaces and a is the hydrodynamic particle radius. The estimated number density of particles n was estimated for a random distribution of particles [113].

The authors showed that ferrofluids have a large number of particles per unit volume along with very small distances between them, even though these results represented a rough estimate. This allows the control and manipulation of ferrofluids using the magnetic forces and torques which are generated by static or time varying magnetic fields [63]. In addition, they point out the relevance of magnetic and hydrodynamic interactions between the particles for volume fractions $\phi_h > 0.1\% v/v$, suggesting the possibility of cluster formation even in the absence of applied magnetic fields [114, 115], a subject that will be thoroughly covered in section 1.3.1.

The repulsive interaction between the magnetic particles is associated with the ferrofluid's nature (ionic or surfacted). In the case of ionic ferrofluids, repulsive interactions are due to the long-range electrostatic interactions between charged particles. On the other hand, in surfacted ferrofluids, the repulsive interactions are due to short-range steric repulsion forces [2]. In ionic ferrofluids, the interaction U_R between two electrically charged spherical particles of diameter d separated by a distance r is given by [116]:

$$U_R = \pi d \epsilon \psi_0 \exp[-\kappa(r-d)] \tag{1.4}$$

In Equation (1.4), ϵ is the electric permittivity of the carrier fluid, ψ_0 is the surface potential of the charged particle at the Helmholtz plane (typical values are of the order $\psi_0 < 50mV$) and κ is the inverse of the Debye length, which is defined as the distance, from the Helmholtz plane, at which the electrostatic potential is 37% smaller than the value at the plane [2]. For more details regarding repulsive forces on ionic ferrofluids, the reader is referred to Scherer and Figueiredo Neto [2].

For the case of surfacted ferrofluids, the steric repulsion U_{st} is linearly dependent on temperature and, for spherical particles of diameter d, with a surfactant shell of thickness s and density ξ molecules per nm^2, at temperature T, is given by [3]:

$$U_{st} = \pi d^2 \xi \kappa_B T \left\{ 1 - \frac{r}{2s} \left[\ln\left(\frac{d+2s}{r} \right) + 1 \right] + \frac{d}{2s} \right\} \tag{1.5}$$

For more details regarding repulsive forces on surfacted ferrofluids, the reader is referred to Rosensweig [3].

That said, the stability of ferrofluids can be assessed. Under a magnetic field, the magnetic particles are driven to regions where the magnetic energy is higher. However, due to their small size, they are forced to wander around the fluid due to Brownian motion (thermal agitation). This way, the stability against segregation is favored when the thermal energy is higher than the magnetic energy [3, 1], therefore:

$$\frac{\kappa_B T}{\mu_0 M V H} \geq 1 \quad \rightarrow \quad d \leq \left(\frac{6\kappa_B T}{\mu_0 \pi M} \right)^{1/3} \tag{1.6}$$

Also, when in the presence of a gravitational field, particles tend to settle in the direction of gravity. Therefore, to prevent settling and assure stability, the gravitational energy must be much smaller than the magnetic energy [3, 1]:

$$\frac{\Delta \rho g h}{\mu_0 M H} \ll 1 \tag{1.7}$$

In Equation (1.7), $\Delta\rho = \rho_{solid} - \rho_{liquid}$ is the difference of the phases' densities.

Now, taking into consideration the attractive dipole-dipole interaction between the particles, in order to avoid agglomeration the thermal energy must be greater than the dipole-dipole contact energy [3, 1]. This finally leads to an expression to calculate the typical particle diameter d to avoid magnetic agglomeration (right side of Eq. (1.8)).

$$\frac{12\kappa_B T}{\mu_0 M^2 V} \geq 1 \quad \rightarrow \quad d \lessapprox \left(\frac{72\kappa_B T}{\pi \mu_0 M^2} \right)^{\frac{1}{3}} \tag{1.8}$$

In Equation (1.8), $\kappa_B = 1.38 \times 10^{-23} N m K^{-1}$, T, μ_0 and M are the Boltzmann's constant, the absolute temperature, the permeability of free space and the intensity of magnetization, respectively. By plugging typical ferrofluid values in the expression for the right side of Eq. (1.8), one obtains $d \lessapprox 10nm$ [2] (other References report smaller values, i.e. $d \leq 7.8nm$ [1]), which is the typical particle diameter in ferrofluids. Therefore, typical ferrofluids are in the limits of agglomeration. The aforementioned stability criteria are summarized in Tab. (1.2).

In addition, to prevent the particle's contact, the application of coatings is another necessity to ensure stability in colloids [3], as stable ferrofluids cannot be synthesized with uncoated particles [117]. Despite the coating of the particles, over time the magnetic attraction causes the particles to regroup. This agglomeration process is more irreversible for particles with a larger size and greater

Table. 1.2: Forces acting on the magnetic nanoparticles and the ferrofluid's stability criteria. Adapted from Genc and Derin [1].

Interaction force	Expression	Stability
Magnetic field energy	$E_{mag} = \mu_0 MVH$	$\frac{\kappa_B T}{\mu_0 MVH} \geq 1;$ $d \leq \left(\frac{6\kappa_B T}{\pi \mu_0 M}\right)^{1/3}$
Gravitational field	$E_{grav} = \Delta\rho V g h$	$\frac{\Delta\rho g h}{\mu_0 MH} \ll 1$
Dipole-dipole contact energy	$E_{dip} = \left(\frac{\mu_0 M_0^2}{12}\right) V$	$\frac{12\kappa_B T}{\mu_0 M_0^2 V} \geq 1;$ $d \leq \left(\frac{72\kappa_B T}{\pi \mu_0 M^2}\right)^{1/3}$
van der Waals	$-\frac{A}{6}\left[\frac{2}{r^2+4r} + \frac{2}{(r+2)^2} + \ln\left(\frac{r^2+4r}{(r+2)^2}\right)\right]$	
Steric repulsion	Short ranged repulsive force	

magnetic moments [1]. For instance, particle agglomeration is reported to occur as commercial water-based ferrofluids age [51].

1.2.2 Applications

Many aspects of the increasingly interest in the research field of ferrofluids is due to their enormous range of applicability. A huge effort was made by physicists and chemists in the second half of the last century in order to synthesize stable magnetic fluids, motivated by the perspective of many and important technological uses [2].

Ferrofluids find numerous applications [14], some of them gaining high commercial value [62] and many of them being justified due to their following physical and chemical properties:

1. They have the ability to move to regions where the magnetic field is strongest and remain there;
2. They absorb electromagnetic energy at certain frequencies and, as a consequence, heat up;
3. Some of their physical properties may change when in the action of a magnetic field, for

instance, their viscosity (magnetoviscous effect, covered in section 1.3.1).

These very interesting properties make ferrofluids useful in many technological, biological and medical applications, in addition to being useful in materials science and engineering research [2]. For instance, they are used in shock absorbers, as heat transfer fluids in loudspeakers, in magnetocaloric pumps and heat pipes, in bearing lubricants [118, 119], in microfluidic pumps and valves [120, 121, 122], in microfluidic actuators and devices [123, 124], in stepper motors [125], in accelerometers and inclinometers in sensor applications [126, 127], in separation processes [128], in catalytic reaction supports [129, 130, 131, 132], and leak-proof seals [133], and are used in pneumatic and hydraulic micro-actuators [134, 135, 136] [63]. They are also used in many biomedical applications, such as contrast agents for magnetic resonance imaging, magnetically targeted and/or triggered drug delivery, hyperthermia treatment of cancer, magnetomechanical actuation of cell receptors, and biosensors [11, 12, 13] [63].

Not only ferrofluids are used in applications of fluid positioning and flow controlling, but also for the modification of fluid's properties, especially changes in their viscosity [62], which might be extremely useful in some industries. This particular feature will be covered in section 1.3.1.

In case these fluids are used in applications involving heat exchanges, the possibility of inducing and controlling the heat transfer and fluid flow processes through an applied external magnetic field has generated possibilities for applications in several sectors, including magnetically controlled thermosiphons, cooling of high-power electrical transformers and use in energy conversion systems [72]. Many of these applications are justified due to the possibility of flow induction in the absence of moving mechanical parts, as in common conversion and cooling devices, since the flow of ferrofluids can be generated by temperature and magnetic field gradients [137]. In addition, the thermomagnetic convection process (convection heat transfer process that uses the spatial gradient of magnetic susceptibility produced when in the presence of a temperature gradient [67, 30]) is much more intense than gravitational convection [137], besides the possibility of increasing thermophysical properties, such as thermal conductivity and viscosity, when ferrofluids are in the presence of an external magnetic field [15, 138]. Experimental investigations show that variations in the volume fraction of particles ϕ, in the particle size distribution, in the chemical composition of the magnetic particles, among others, change the thermal conductivity of ferrofluids in the absence of an applied magnetic field. For instance, it has been reported that the thermal conductivity of ferrofluids increases with its volume fraction ϕ [139, 140, 141, 142, 138, 143, 144]. Abareshi et al. [143]

reports an increase in the thermal conductivity ratio K_t (quotient of the thermal conductivity of the magnetic nanofluid to that of the carrier liquid [67]) of 11.5% at $\phi = 3\%$ in a water-based magnetite ferrofluid; Li et al. [139] observed an increase in the thermal conductivity in a water-based Fe ferrofluid with ϕ with and without a magnetic field; Yu et al. [144] reported a linear increase of K_t with ϕ with values reaching 34% at $\phi = 1\%$ in a kerosene-based magnetite ferrofluid while Hong et al. [145] reports a non-linear increase of K_t with ϕ in a ethylene glycon Fe ferrofluid; Philip et al. [142, 138] observed a highest K_t of 23% at $\phi = 7.8\%$; finally, the results obtained in Hong et al. [140] confirmed the enhancement of the thermal conductivity with the particle's volume fraction attributing it to the fact that ferrofluids with higher volume fractions tend to form clusters at higher rates (more on particle's aggregation in section 1.3.1). In addition to the changes in thermal conductivity caused by the parameters mentioned above, when in the presence of magnetic fields the thermal conductivity is also affected by the orientation and intensity of the applied field [72, 139]. For instance, Li et al. [139] reports an increase in the thermal conductivity of the ferrofluid with the strength of the applied magnetic field parallel to the temperature gradient and little change in fields applied perpendicular to the gradient. In addition, Philip et al. [142, 138] reports a huge enhancement of $K_t = 300\%$ under magnetic fields applied along the direction of heat flow and Gavili et al. [146] reports an enhancement of more than 200% in thermal conductivity in water-based ferrofluids with average diameter $d = 10nm$. Nkurikiyimfura et al. [147] also relates the thermal conductivity enhancement to magnetic fields parallel to temperature gradients. Li et al. [139], Nkurikiyimfura et al. [147] attributed this increase due to the chain-like structures formed under the influence of the magnetic field, which provided more effective bridges for energy transport along the direction of the temperature gradient. The most discussed mechanisms for interpreting experimental data on the increase in the thermal conductivity of ferrofluids, both in the absence and in the presence of a magnetic field, are the Brownian motion which the magnetic particles are subjected and the already mentioned particle's agglomeration/clustering [67, 142]. Brownian motion would make a direct contribution due to the diffusion of magnetic particles that carry heat and also through an indirect contribution due to the micro-convection of fluid surrounding the particles [67, 148].

That said, some ferrofluids' applications are now briefly presented. For more details regarding ferrofluids' applications, the reader is referred to Berkovski and Bashtovoy [14], Scherer and Figueiredo Neto [2], Torres-Díaz and Rinaldi [63].

Technological applications

These fluids have been used in dynamic sealings, heat dissipation and damping processes as well as in doping (intentional introduction of impurities) of technological materials.

For instance, ferrofluids are used as dynamic seals on computers' hard drives. In this case, hard drives must operate in hermetically sealed cases, as any impurity can damage the device and ruin its reading or writing processes. A hole is then made inside a magnet through which an axis made of a soft magnetic material is inserted. The ferrofluid is then placed in a groove on the shaft, being held in place by the applied magnetic field, thus blocking the passage of any impurities and also leaving the shaft free to rotate, as the obstructive material is obviously a liquid [2]. A schematic of this application can be found in Scherer and Figueiredo Neto [2].

Ferrofluids are also used as heat conductors in the process of removing heat from operating equipment. On a daily basis, they are used in loudspeakers, where they surround the speaker's coil, which heats up when it is working. In this case, contrary to what would happen if ordinary fluids were used for this application, as they would flow away from the place where they were supposed to operate, the ferrofluid is held in place by the application of a magnetic field applied by the magnet fixed on the loudspeakers' horn. A schematic of this application can be found in Odenbach [62]. In addition to heat dissipation, the presence of ferrofluid also improves the quality of the speaker, as it dampens unwanted resonances [2].

Apart from being used indirectly as dampers in loudspeakers, ferrofluids have a more direct use to dampen unwanted vibrations in inertial and viscous dampers in motors, mainly stepper motors. In this case, the oscillatory movement is opposite to a torque produced by a shear effect, causing the damper to absorb unwanted vibration. The damping has a non-magnetic housing connected to the motor shaft, the interior of which is filled with ferrofluid, where an inertial mass levitates. This clearly eliminates the need for bearings to support the mass [149]. In this scenario, the application is based on the unique property of ferrofluids to maintain a magnet, whose density is greater than that of ferrofluid, floating in it [2].

In the field of materials research, the doping of lyotropic liquid crystals with water-based surfacted ferrofluids is used to investigate different aspects of liquid crystal physics [150, 151, 2], for example the response of the nematic matrix to pulsed magnetic fields [152] and in the investi-

gation of elastic properties, such as the bend elastic constant and the anisotropy of diamagnetic susceptibility, which can be measured by comparing the relaxation behavior of liquid crystals with and without ferrofluid doping when subjected to different magnetic fields [153]. The introduction of anisotropic magnetic nanoparticles in a liquid crystalline matrix may also reduce the magnetic field needed to orient liquid crystals by a factor of 1000 [154, 2]. In addition, magnetic nanoparticles significantly increase the light absorption of lyotropic liquid crystals [2]. For instance, the non-linear refractive index of doped samples is 10 times higher than that of non-doped samples [155, 2], which makes ferrofluids particularly useful for investigating the nonlinear behavior of such complex fluids.

Biomedical applications

Of all the places and processes in which ferrofluids are used, biomedical applications are definitely the most noble of them. Magnetic nanoparticles have many attractions related to their physical properties that make them particularly useful in biomedical applications. First, its size may be smaller or in the range of that of biological entities, such as cells ($10 - 100\mu m$), viruses ($20 - 450nm$), proteins ($5 - 50nm$) or genes ($2nm$ wide and $10 - 100nm$ long). Not only can they be similar in size, but they can also be coated with biological molecules, making them biologically compatible, which makes them able to interact or connect to biological entities. Second is the fact that they are magnetic and can therefore be manipulated by external magnetic fields. This attribute combined with the intrinsic penetrability of magnetic fields in human tissues makes them useful in applications involving transport/immobilization of particles or biological entities, such as the delivery of anticancer drugs or a cohort of radionuclide atoms to a target region of the body, such as a tumor. Finally, magnetic nanoparticles can respond resonantly to time-varying magnetic fields, transferring energy from the exciting field to the nanoparticles, heating them up. This makes them hyperthermia agents, supplying energy to target bodies where moderate heating of tissue results in the destruction of malignant cells more effectively. [156]. In this section, the use of ferrofluids for magnetic drug targeting, cancer treatment, contrast enhancement for magnetic resonance imaging (MRI) and magnetic separation of cells will be briefly described.

The idea behind magnetic drug targeting is to use smaller amounts of drugs compared to traditional methods as well as applying it exclusively to particular cells or body tissues. The drug's distribution in the organism is done in such a way that its main fraction interacts exclusively with

the tissue to which it is intended to be applied at the cellular or subcellular level [157]. In magnetic drug targeting, the intended drug and a suitable magnetic component (a ferrofluid, for instance) are formulated in a pharmacologically stable formulation [157]. In the case of ferrofluid drug targeting, a ferrofluid bounded drug is locally injected into a cancerous tumor, being kept there by a properly (i.e. sufficient field strength and gradient [157]) applied magnetic field during a fixed period (approximately one hour). In addition to the smaller amount of medication used, as soon as the magnetic field is turned off the rest of the drug is soon dispersed in the body. However, as it is in small amounts, there are virtually no side effects [2]. Particles that are attached to magnetic fluids can be used to remove cells and molecules by applying magnetic fields and concentrating drugs in anatomical sites with restricted access [157]. Theoretically, in chemotherapy treatments, targeted drug delivery can significantly improve its outcome by allowing the maximum fraction of the administered drug to react exclusively with cancer cells, without side effects for normal cells, as well as the obvious preferential distribution of the drug for cancer cells [157]. Ferrofluid bounded drugs suitable for chemotherapy are already being used. An application of ferrofluid bound Mitoxantrone in 26 tumor-bearing rabbits is reported in Alexiou et al. [158], with outstanding success in curing the tumor without side effects. The reader is referred to Lübbe et al. [157], where a wide variety of possibilities with this technique is presented.

The ability of ferrofluids to absorb electromagnetic energy at certain frequencies is the key behind a cancer treatment known as magnetic fluid hyperthermia (MFH) [2]. Hyperthermia therapy is a treatment in which the temperature in a local region of the body is raised above the baseline to obtain a therapeutic effect. For example, an increase in local temperature to between $40°C$ and $44°C$ is sufficient to negatively impact cancer growth [159]. In magnetic fluid hyperthermia, while the ferrofluid absorbs electromagnetic energy provided by a magnetic field, it heats up. However, it absorbs electromagnetic energy at a different frequency than water absorbs it, thus allowing only the part of the body where the ferrofluid was injected (usually a tumor) to warm up, and not its surroundings. In this way, there is no compromise in the proper functioning of normal cells, the largest portion of which is composed of water (which makes up 70% to 90% of most tissues [160]), but only the functioning of cancer cells, due to the localized heating process by the application of a magnetic field, usually oscillatory [2]. This technique is already being used both in animals and human beings, with successful use for complete sarcoma tumor regression and life span increase in mice [161] as well as very good results in the treatment of glioblastomas in humans [2, 159].

Ferrofluids are also used to enhance the contrast in magnetic resonance imaging (MRI) [156].

MRI is a medical technique used to produce images of the body and its physiological processes by using magnetic fields and radio waves to generate these images [160]. Its operation is based on the differences between the relaxation times of the protons' magnetic moments when they are in different environments [2, 160]. In order to increase the contrast between the images produced by different tissues of the body, since, in some cases, the differences between the relaxation times are not strong enough to produce well resolved images, magnetic nanoparticles in biocompatible ferrofluids are used. These, in turn, are absorbed by different tissues of the body in different amounts, thus leading to different values in the relaxation time and, consequently, to clearly distinguishable images, since the magnetic particles are clearly visible by MRI [2]. For example, dextran coated iron oxides are biocompatible and absorbed by the mononuclear phagocyte system (also called reticuloendothelial system, which is a part of the immune system that consists of the phagocytic cells [162]). However, absorption occurs selectively, since cancer cells do not have an effective reticuloendothelial system like that of healthy cells. In this way, the relaxation time is not altered by the contrast agent, making the cancer cells easily differentiated from the surrounding healthy cells. In addition, dextran coated iron oxides are excreted by the liver after treatment [2].

Another common application in ferrofluids is the process of magnetic separation using biocompatible magnetic particles. This technique can be used to separate biological entities from a given environment, for several reasons, such as for the production of more concentrated samples of these biological entities. The process consists of fixing the magnetic particles to these entities and later removing them (which may be carrying a target), with the application of magnetic fields [2]. Common coatings for magnetic particles are dextran, polyvinyl alcohol, among others [156]. A prime example of application is the use of magnetic separation as a way to "clean" marrow samples infected with cancerous particles, aiming at implanting the clean sample in the same person, thus avoiding rejection, which is a common problem when implanted marrow comes from another patient [2]. In this case, the magnetic particles are coated with monoclonal antibodies that have an affinity for tumor cells, later removed by the magnetic separation process [14].

The interested reader is referred to Pankhurst et al. [156], Scherer and Figueiredo Neto [2] for more information regarding the biomedical applications of ferrofluids.

1.3 Ferrofluid flow phenomena

As indicated in section 1.2.2, ferrofluids are used on a daily basis in applications which require ferrofluid's flow. A ferrofluid flow in a magnetic field is accompanied with an interplay between hydrodynamic and magnetic effects, and it represents practically the only relevant case of flow with a continuum polarization, where the presence of body couples, internal angular momentum density and antisymmetric stresses are needed in order to provide its complete macroscopic description [63]. Ferrofluid's flows have been the subject of numerous scientific works. For instance, some studies focused on the effect of oscillating fields on ferrofluid flow both in the presence [17, 52, 53, 54, 16] and in the absence [55] of pressure gradients. Others consisted of theoretical studies of ferrofluid flow under the action of applied fields [26, 17, 54] as well as experimental [35, 56, 57, 18] and numerical studies [18, 16] on Poiseuille flow. In addition, many studies focused on predictions and measurements of ferrofluid's viscosity changes when in the presence of magnetic fields [16, 56, 58, 57, 18, 17]. Regardless the abundance of studies on ferrofluid's flow, there is a great lack of studies concerning the magnetization response of a ferrofluid when in the action of an applied magnetic field, which is the center of attention of the present work.

In addition to this lack of studies, since ferrofluids are opaque, direct unobtrusive measurements of ferrofluid flows are very difficult to achieve. Some works made use of ultrasonic techniques to work around this problem [163, 164, 165, 166, 51]. It is important to mention that it is well established, at this moment, that the speed of sound in a ferrofluid increases slightly with the strength of the magnetic field and the frequency of the ultrasound [167]. For instance, by using the ultrasonic velocity profile (UVP) method [168], which is based upon pulsed ultrasound echography, Chaves et al. [51] made use of low fractions of a polyamide powder tracer (since the magnetite particles suspended in a ferrofluid are too small to produce a UVP signal) in order to obtain velocity profiles for the bulk flow in the case of spin-up flow. Spin-up flow is a very interesting ferrofluid phenomena which occurs when a ferrofluid placed in a stationary cylindrical container is set to motion when in the action of a uniform rotating magnetic field [47, 51], having already been investigated in some works [47, 48, 49, 20, 50, 51]. In particular, Chaves et al. [51] showed that the induced flow behaves in a very interesting manner: a corotating bulk flow with the field, in a rigid-body-like rotation (i.e. linear dependence of the velocity with radial position) and a counter rotating flow at the surface [51]. Using tracers on the upper rotating surface, Rosensweig et al. [49] observed the velocity of the free surface of a ferrofluid under the action of a uniform magnetic field, noting that for situations where the meniscus (free surface) formed was concave the surface counter-rotated

with the applied magnetic field, while for convex menisci the ferrofluid surface co-rotated with the field. For flat surfaces, the ferrofluid proved to be stationary [49].

Another interesting and rather anomalous aspect of ferrofluid flow is the ferrofluid "pumping" effect [169, 52, 170, 22, 171, 55, 172], in which a time varying magnetic field is used to produce ferrofluid's motion [58]. In some cases, net flow is achieved in the absence of pressure gradients and the flow is driven mostly by the magnetic torque generated by the field, which acts on the particles whose rotational motion is converted to fluid motion by rotational friction and spin viscosity diffusion [55, 172]. However, in the presence of travelling wave magnetic fields, both the magnetic body force and torque pumping are developed [22]. In closed channel geometries, with the use of a travelling wave magnetic field, ferrofluid motion can be achieved both in the direction of the wave (forward pumping) or in the opposite one (backward pumping), depending on the field's frequency, amplitude and direction [58, 52, 170]. This change in behavior occurs at a critical magnetic field strength, which depends on the frequency, the concentration of the suspended magnetic particles and the fluid viscosity [52]. In the case of high magnetic field strengths, forward pumping has been reported, yet in low magnetic field strengths, backward pumping was observed [169]. Other magnetic field parameters such as the wavenumber and the frequency can also optimize the net flow rate, in cases of planar duct [55, 22] or circular tube [172] flows in the presence of running magnetic waves. Maximum pumping in planar ferrofluid layers is reported in Mao and Koser [22] when the excitation wave number is the inverse of the ferrofluid channel thickness, also, maximum flow velocity is achieved when the applied magnetic field frequency is close to the reciprocal of the relaxation time of the magnetic particles τ_B. Similarities are observed between induction motors and ferrohydrodynamic pumping with traveling waves. In induction motors, a stator creates a displacement excitation that moves the rotor and, where there is an ideal slip frequency associated with the rotor geometry, which is analogous to the particle relaxation time in the case of ferrohydrodynamic pumping [22]. The ferrofluid pumping effect is a promising method of fluid manipulation [55] as it has a great potential for practical applications. For instance, it could be used in precise positioning of ferrofluid's segment inside the body by using external magnetic fields [58, 22, 171].

As described in section 1.2.2, one of the main reasons behind the applications of ferrofluids is that their physical macroscopic properties may change when under the action of an applied magnetic field, specially their viscosity which varies accordingly to the intensity of the applied field, in a process known as the magnetoviscous effect, which is described below in section 1.3.1.

1.3.1 Magnetoviscous effect

The most important attribute of ferrofluids is that while they remain fluids ($\tau_y = 0$, where τ_y is the yield stress, which is a measure of the strength of solid materials [173]), they experience a change in their viscosity when in the presence of a magnetic field, achieving a wide range of viscosity in a fraction of millisecond [1]. When in the absence of a magnetic field, their viscosity can go up to $\eta = 0.002 - 7.5Pas$ - please refer to Tab. (4.1) - depending on the particle's concentration and carrier liquid, however, under the action of magnetic fields, viscosity enhancements of $\Delta\eta(B)/\eta(0) \sim 2$ have been reported [173]. This way, ferrofluids exhibit non-Newtonian behavior, as the field-dependent part of viscosity, which can be either positive or negative [17, 56, 174, 57, 175], depends on the flow's vorticity [16] and the applied magnetic field. Changes in the ferrofluid's viscous behavior by an increase in fluid viscosity with increasing magnetic fields were first reported in Rosensweig et al. [176] with concentrated ferrofluids made of magnetite nanoparticles, succeed by a different independent study [35] with highly diluted ferrofluids made of cobalt nanoparticles [62].

When it comes to ferrofluid flows, the net macroscopic effect of a magnetic field acting on the magnetic particles is manifested through this change in viscosity [18, 58], which has been the topic in numerous numerical, theoretical and experimental studies [35, 56, 57, 39, 54, 18, 16].

This effect [35, 26, 36, 3, 37, 38, 39, 40, 15, 16, 177] manifests due to hindering of the particle's rotation with the flow's vorticity due to the action of the magnetic field, which tends to fix the particle's magnetic moments in the direction of the field [16]. Under such conditions, the dissipation of fluid's kinetic energy is increased, leading to an additional - so-called rotational - viscosity [16].

In simple words, assuming that the particles' magnetic moments are fixed within the particles themselves (the rotation of a particle is directly followed by the rotation of its magnetic moment) and that they do not interact with each other, a shear flow will generate a rotation of the particles along the flow's vorticity direction. When a magnetic field is applied, the magnetic moment of the particles (and the particles themselves) will tend to align in the field's direction, as long as the relaxation process is governed by the Brownian mechanism, and not the Néel relaxation process (Rosensweig, 1985), a topic which will be covered below. The rotation due to the viscous friction will generate a misalignment between the particles' moments and the applied field, which gives rises to a magnetic torque which counteracts the mechanic torque due to the shear flow - Fig. (1.7)

-. This hinders the free rotation of the particles, macroscopically manifesting an increase in fluid's viscosity. If the field and the flow's vorticity are aligned, there will not be anything hindering the free rotation of the particles, and thus no increase in fluid's viscosity is observed [62].

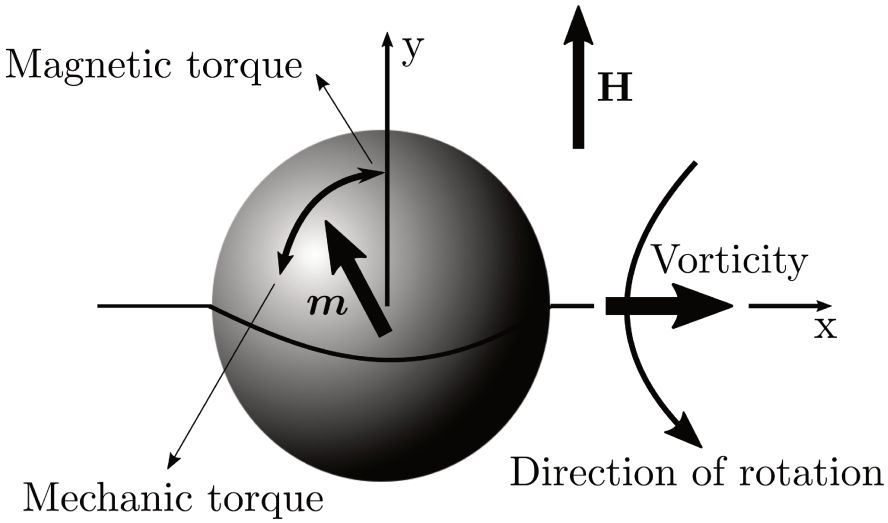

Figure. 1.7: Model of the origin of the magnetic field-dependent viscosity increase in ferrofluids, where $\boldsymbol{H}$ stands for the applied magnetic field and $\boldsymbol{m}$ for the particle's magnetic dipole moment. Image adapted from Odenbach [62].

In a pioneer work, Shliomis [26] derived a theoretical description of such phenomena that takes into account three physical mechanisms acting on the particles' dynamics: 1) the magnetic torque acting on the particles; 2) the mechanical torque acting on the particles and 3) the particle's Brownian motion. It has been shown that the rotational viscosity η_r increases as H^2 in weak fields and reaches a saturation value for large magnetic fields $\eta_r^{max} = \frac{3}{2}\eta\tilde{\phi}$, where η is the fluid's viscosity for vanishing magnetic fields and $\tilde{\phi}$ is the volume concentration of the magnetic particles including their surfactant [62]. For instance, considering a commercial standard ferrofluid with 7% of magnetic material, a mean particle diameter of $d \approx 10nm$ and a surfactant layer thickness of $2nm$, $\tilde{\phi} \approx 19.2\%$, which results in $\eta_r^{max}/\eta \approx 30\%$. This theoretical estimate is based upon the assumption that all magnetic particles contribute to the viscosity increase, however, only particles with a magnetic moment fixed inside them can contribute to the phenomenon [62]. This condition depends on the magnetic relaxation behavior of the particles. When the applied magnetic field $\boldsymbol{H}$ changes, the ferrofluid's magnetization $\boldsymbol{M}$ relaxes to a new equilibrium magnitude and direction [63]. In this case, two different relaxation behaviors are observed: 1) The particles with fixed magnetic moments align with the field by a rotation of the whole particles against the hydrodynamic resistance of the carrier fluid to align $\boldsymbol{m}$ and $\boldsymbol{H}$, in a process called Brownian relaxation or 2) the magnetic moment $\boldsymbol{m}$ inside the particle aligns with $\boldsymbol{H}$, due to flipping of atomic spins without par-

ticle rotation [70] (the magnetic moment $\boldsymbol{m}$ is quasi-free to rotate [2, 63]), in the so-called Néel relaxation process.

The Brownian relaxation mechanism is given by [3]:

$$\tau_B = \frac{3\eta V_h}{\kappa_B T} \tag{1.9}$$

In Equation (1.9), V_h is the particle's volume along with the surfactant or other surface coatings [70]. In a similar manner, the Néel relaxation mechanism is given by [3]:

$$\tau_N = \tau_0 \mathrm{e}^{\left(\frac{KV}{\kappa_B T}\right)} \tag{1.10}$$

The parameter K is the particle magnetic anisotropy and $\tau_0 = \frac{1}{f_0}$ is a constant where f_0 is the Larmor frequency [70, 2, 62]. Different values for the magnetic anisotropy K of magnetite can be found in the literature, over the range $15kJm^{-3} < K < 100kJm^{-3}$, while $f_0 \approx 10^9 s$ [70]. With the use of the *Mossbauer* spectroscopy, Lehlooh et al. [178] showed that the value of K is size dependent, increasing with the decrease in particle's diameter, and also presents a value of $K = 78kJm^{-3}$ magnetic nanoparticles with $d = 12.6nm$.

In rotating magnetic fields, the magnetization relaxation time processes of Eqs. (1.9) and (1.10) create a phase difference between the ferrofluid's magnetization $\boldsymbol{M}$ and the applied magnetic field $\boldsymbol{H}$, so that $\boldsymbol{M}$ and $\boldsymbol{H}$ are not in the same direction, which causes a magnetic torque [70]:

$$\boldsymbol{T} = \mu_0(\boldsymbol{M} \times \boldsymbol{H}) \tag{1.11}$$

The magnetic torque causes the magnetic particles and the surrounding fluid to spin. The joint action of approximately 10^{23} particles/m^3 can lead to fluid pumping [179, 16, 18] and to intricate microdrop behavior in Hele-Shaw cells [180, 181, 182], as depicted in the very interesting patterns observed in Rinaldi et al. [70], Lorenz and Zahn [180].

The total relaxation time scale τ represents the total magnetic time constant, which includes both the Brownian and Néel relaxation mechanisms, and is dominated by the smaller of τ_B and τ_N, as shown by Eq. (1.12) [70].

$$\frac{1}{\tau} = \frac{1}{\tau_B} + \frac{1}{\tau_N} \rightarrow \tau = \frac{\tau_B \tau_N}{\tau_B + \tau_N} \tag{1.12}$$

For instance, in a ferrofluid at temperature $T = 300K$ with representative suspending medium viscosity $\eta = 0.001Pas$, with magnetic nanoparticles with diameter $d = 12.6nm$ coated with a surfactant thickness of $s = 2nm$ with anisotropy constant $K = 78kJm^{-3}$, the relaxation times are given by $\tau_N \approx 368ms$ and $\tau_B \approx 1.7\mu s$ [70]. Therefore, for this particular configuration, we notice that the effective time constant is dominated by the Brownian mechanism. Direct torque measurements in spin-up flow [183] and in a cylindrical Couette geometry [184] for ferrofluids with diameter $d \sim 10nm$, have estimated, by comparison to theory, effective magnetic relaxation times of the same order of this computed Brownian relaxation time ($\tau_B \sim 10^{-5}s$).

The Brownian relaxation mechanism gets its name due to the fact that even in the absence of magnetic fields, the particles rotate due to Brownian torques, associated with the molecular collisions, which causes rotational Brownian motion [2]. If the Néel mechanism in the dominant one, the particle is said to be superparamagnetic [2]. Equations of motion for $\boldsymbol{m}$ to be used in cases of superparamagnetic particles, non-superparamagnetic particles and mixed situations can be widely found in the literature [185, 186].

From Equations (1.9) and (1.10), one notices that the Brownian mechanism scales linearly with the particle's volume, while the time for the Néel process grows exponentially with it. Since the particles' relaxation time is governed by the process with the shortest relaxation time, the small particles (magnetically weak particles) will follow the Néel process while the large ones (magnetically hard particles) will follow the Brownian manner [62]. Torres-Díaz and Rinaldi [63] gives the expected dependence of the Brownian and Néel relaxation times for magnetite ($\mathrm{FeO} \cdot \mathrm{Fe_2O_3}, K \sim 15kJm^{-3}$) and cobalt ferrite ($\mathrm{CoO} \cdot \mathrm{Fe_2O_3}, K \sim 180kJm^{-3}$) particles with different diameters of materials with different representative magnetocrystalline anisotropies is presented. The authors show that for a non-uniform particle size distribution, the particles' relaxation can be given by a combination of the two different mechanisms (Brownian and Néel) [63].

The critical diameter on which the relaxation behavior becomes Brownian is $d \approx 13nm$ [62] (it has already been presented that for particles with $d = 12.6nm$, the calculated relaxation times are $\tau_N \approx 368ms$ and $\tau_B \approx 1.7\mu s$). This way, only magnetically hard particles will contribute to the rotational viscosity effect [62]. For instance, by looking at a particle size distribution of a commercial standard ferrofluid made of magnetite nanoparticles $APG513A$, as depicted in Odenbach [62], one notices that particles with diameters $d > 13nm$ are present with a volume concentration of less than 1%, leading to a theoretical maximum increase in viscosity of less than $\eta_r/\eta < 2\%$.

The magnetic particles size distribution in ferrofluids is extremely important for several shear flows subjected to the action of a magnetic field. A magnetic field gradient causes larger particles to diffuse to regions where the intensity of the field is greater, while smaller particles suffer a milder effect [70]. Viscosity measurements made on rheometers show that larger particles and particle clusters have a strong magnetic field dependence on viscosity increase, which in turn depends on the shear rate, while ferrofluids with smaller particles experience only a small increase in viscosity and less dependence on the shear rate [187, 188].

In time varying magnetic fields, the magnetic weak particles (Néel relaxation time) will typically respond in phase with the field at most applied frequencies used in non-biomedical applications. However, the magnetic hard particles (Brownian relaxation time) response will depend on the applied frequency Ω_f. For frequencies used in non-biomedical applications, they behave in phase when $\Omega_f \tau \ll 1$, are significantly out of phase when $\Omega_f \tau = 1$ and have negligible magnetization when $\Omega_f \tau \gg 1$ [63].

The relaxation processes of the magnetic particles (Brownian time and Néel time) are processes that involve losses, which leads to energy dissipation, so that the complex magnetic susceptibility ($\chi = \chi' + i\chi''$, where χ' is real part of the magnetic susceptibility χ related to magnetic field energy storage and χ'' is the imaginary part which cases power dissipation) has an imaginary part [70]. Such losses lead to heat generation when the particles are subject to the action of time-varying magnetic fields, so that they can be used for the localized treatment of cancerous tumors [189, 190]. Magnetic hyperthermia has been briefly described in section 1.2.2.

It is important to mention that the rotational viscosity η_r is always positive in steady magnetic fields [16, 56] - in the case of Poiseuille flow a constant magnetic field balances vorticity and impedes the rotation of individual magnetic particles [56, 58] -, and the magnitude of this increase is dependent on field strength and its orientation [56]. Nevertheless, it can assume negative values

in certain conditions (i.e. in high oscillation frequency [58]) under oscillating magnetic fields, providing flow rate increases [16] - in the case of Poiseuille flow, an alternating magnetic field helps vorticity and favors this rotation, as a fast enough oscillating field forces the particles to rotate faster than the fluid [56] -. In this scenario, the oscillating magnetic field's energy is partially transformed into fluid's kinetic energy (angular momentum of the particles), accelerating it [16, 56], as if the particles acted like tiny motors that reduced the friction between adjacent fluid layers [57]. The decrease in rotational viscosity has been reported in both laminar [56, 57] and turbulent [18] ferrofluid flows. Even though the effect of viscosity reduction may appear odd, it is quite common with polymers where it is called shear thinning [18]. Physical conditions for the appearance of negative viscosity have been reported when $\Omega\tau_B \geq 1$ [56, 57] and in the case of planar Couette flow with a linear polarized oscillating magnetic field $\Omega\tau_B > 1$ [17]. Dependences of the reduced viscosity on flow rate, magnetic field and oscillation frequency have also been reported [18]. In the case of laminar pipe flow at a constant magnetic field the reduced viscosity decreases with increasing flow rate, yet for turbulent flow it remains relatively constant [18].

The increase in viscosity is also shear dependent. For instance, the change in viscosity of a magnetite based ferrofluid $APG513A$ in an oily carrier liquid, containing 7% of magnetic particles with a size distribution given in Odenbach [62], is presented in Odenbach [62] as a function of the magnetic field strength for various shear rates $\dot{\gamma}$. The author notes two main aspects: 1) a significant shear dependence of the increase of viscosity, which diminishes as the shear is increased and 2) the changes in viscosity can reach more than 100% in moderate magnetic fields of order $H = 30kA/m$, which is in contrast to the classical theory of rotational viscosity. Thus, this phenomenon is referred as the "magnetoviscous effect" [62].

The dynamics governing ferrofluid flow is mainly dictated by the competition of three physical mechanisms: the magnetic torque $(\boldsymbol{m} \times \boldsymbol{H})$, the Brownian torque $(\kappa_B T)$ and the viscous torque $(6\eta V\Omega)$. The magnetic torque acts in order to align the particle's magnetic moment $\boldsymbol{m}$ along the field's $\boldsymbol{H}$ direction. Such alignment is hindered by the random and the viscous torques [16]. When in low shear rates (i.e. $\Omega\tau_B \ll 1$), the system's behavior is only governed by the thermal - which in this case is the only mechanism preventing orientation of the magnetic particles - and magnetic mechanisms [16]. Under this scenario, the rotational viscosity η_r is a function only of the magnetic field, not depending on flow's vorticity [16]. In most commercially available ferrofluids, $\tau_B \ll 1$ (i.e. $\tau_B \sim 10^{-6}s$) due to the smallness of the particles (i.e. $d \approx 10nm$), in a way that the physical condition $\Omega\tau_B \ll 1$ is very often satisfied in practice, leading to Newtonian-like behavior of the fluid [16]. This would be the case for single particles, however, in many cases, ferrofluids are

composed by aggregates of magnetic grains, which is provided by magnetic dipole-dipole interparticle interactions [16], described by the dipole's coupling parameter λ, which must be sufficiently large to form long chains [16].

$$\lambda = \frac{\mu_0 m^2}{4\pi d^3 \kappa_B T} \tag{1.13}$$

When in the absence of a magnetic field, the particle's distribution in the ferrofluids is disordered leading to an isotropic thermal conductivity. However, when magnetic particles self-assemble, there is a tendency to align their magnetic dipole moments in the direction of the magnetic field due to neighboring particles or applied magnetic fields [15, 191, 192], resulting in anisotropy of the interactions, allowing the magnetic nanoparticles to form one-dimensional chains/wires, rings, two-dimensional aggregates or even three-dimensional super-lattices [67].

For a ferrofluid with coated particles a modified interaction parameter $\tilde{\lambda}$ must be used [193].

$$\tilde{\lambda} = \left(\frac{d}{d+2s}\right)^3 \lambda \tag{1.14}$$

In Equation (1.14), s denotes the thickness of the surfactant layer. For $s = 2nm$, this change means a reduction of λ by a factor of approximately 2 [62].

Many experiments and analysis show that forces of magnetic dipole-dipole interaction in strong magnetic fields cause large magnetic particles to form chains and aggregates (structures formed by the particles). These, in turn, can greatly affect the macroscopic properties of ferrofluids, such as their viscosity, even in physical scenarios of low particle concentration [194, 195, 196, 197]. The presence of aggregates is used as a macroscopic approach to understand the strong magnetoviscous effect displayed by ferrofluids. The ferrofluid is described as a bidisperse system, with a large fraction of small particles and a small fraction of large particles, however, as already mentioned, this small amount of magnetically hard particles cannot describe the observed behavior of viscosity increase [62]. So, one has to assume that the magnetic interparticle interactions lead to the formation of particles' aggregates. The excess of these strongly anisotropic interactions compared to the energy of thermal fluctuations leads to the formation of aligned magnetic dipole

chains [16], which in the easiest case the structures could be rigid straight chains [62]. A ferrofluid represents a set of these flexible chains [16, 195, 198], whose relaxation time, depending on its size, may reach values of $\tau_B \sim 10^{-4} - 10^{-2}s$, and, in such cases, $\Omega\tau_B$ is not small anymore, because the relaxation time - Eq. (1.9) - is directly proportional to the volume of the particles, and thus any agglomeration leads to larger relaxation times [18], which finally leads to non-Newtonian behavior of the fluid. It is important to mention that only big enough aggregates have perceptible contributions in this non-Newtonian behavior [16]. For the large particles with diameter $d \geq 13nm$ the magnetic dipole interaction is so strong that the parameter λ clearly exceeds 1, and thus these particles are able to form chain-like structures [62]. Based on the modified interaction parameter [193] - Eq. (1.14) - , particles should have diameter larger than $d > 16nm$ for magnetite and $d > 6.5nm$ for cobalt to able to form structures [199]. The strong increase in viscosity with magnetic field intensity has been assumed to be directly linked to the hindrance of rotation of these structures in the flow [62]. However, Krekhov et al. [16] points out that in the presence of high enough shear rates, these chains could be destroyed, which leads to reductions in the relaxation time τ_B and also provides an explanation for the reduction of the increasing viscosity effect with increasing shear rate, as the one presented in Odenbach [62]. In the case of pipe flows, Schumacher et al. [18] hypothesizes that in turbulent flow the particle agglomerates will be broken, however in laminar flows they could remain, considering that shear stresses are null at the pipe's center.

The formation of particles' clusters and chains is also reported in Butter et al. [115], whose experiments evidenced the important role of magnetic dipole-dipole interactions in ferrofluid dynamics. In this study, large particles tended to form clusters spontaneously even in the absence of an applied magnetic field [115]. Formation of linear dipole structures at small particles separations and particle chaining and clustering at constant magnetic fields were also observed, with disassembling of such structures due to thermal agitation after removing the field [63]. Reindl and Odenbach [200] also points out the importance of the way the magnetic material interacts at the microscopic level. In their *Taylor-Coette* experiments, a cobalt-based ferrofluid showing a high level of particle-particle interaction with 60 times less magnetic material compared to a magnetite-based ferrofluid without interacting magnetic particles showed much greater observed effects, evidencing the important role of particle-particle interaction in contrast to the role of the amount of magnetic material in a ferrofluid. The strong interactions in the cobalt-based ferrofluid led to enormous changes in the flow behavior, such as the decay in the number of vortices under axial magnetic fields and a greater stabilization of the circular *Couette* flow under transverse and axial fields.

Particles' clustering is also a mean of explaining the thermal conductivity enhancement in ferrofluids [142, 138, 201] and is regarded as the main mechanism of thermal conductivity [67, 202, 203, 204, 205, 148]. The presence of particle agglomerates in a ferrofluid leads to enlarged and highly conductive paths for the heat flow and, therefore, to a faster and more efficient heat transport over long distances, since the heat can be conducted much more quickly by solid particles compared to a carrier liquid [67, 202]. Philip et al. [138] claims that the enhancement in thermal conductivity in ferrofluids at higher volume fraction ($\phi > 2\%$) is due to the presence of dimmers and trimmers in the fluid and that the maximum enhancement was achieved when the chain-like aggregates were well-dispersed without clamping. The effect of particle clustering on thermal conductivity was also reported in Hong et al. [140], Zhu et al. [206], indicating that the size of the clusters [140] and the alignment of the particles [206] had major influences on thermal conductivity. Finally, Nkurikiyimfura et al. [207] indicates that the thermal conductivity component along the magnetic field parallel to the temperature gradient was significantly enhanced due to the chain-like aggregates.

It is clear that the formation and breakage of chains are the determining processes for the magnetoviscous effect, provided by the small amounts of large particles in magnetite ferrofluids [62]. Experimental studies [208, 193] have shown the dependence of the magnetoviscous effect on the content of large particles in the fluid, where it has been shown that fluids with an increased content of large particles show a strongly enhanced magnetoviscous effect yet fluids with a reduced fraction show a weak dependence of viscosity on magnetic field strength [62]. Finally, the model of chain formation of magnetic particles as an explanation for the magnetoviscous effect has also been confirmed in numerical studies [209, 210, 211], in neutron scattering experiments [212] and validations of a theoretical model [213] calculating the viscosity changes in a ferrofluid with chain formation [62].

In ferrofluid flow, the rotational viscosity effect is reported in many studies. In the cases of rigid rotation or Couette flow [214], as the vorticity field is constant so is the rotational viscosity η_r [16]. When a magnetic field is applied, the effective viscosity of the fluid is hence $\eta_{eff} = \eta + \eta_r$, which leads to alterations in the flow rate but not in the velocity profile, which remains linear [16]. Conversely, in the case of Poiseuille flow, vorticity is spatial coordinate dependent and so is η_r. Under such conditions, if the shear rate is significantly high, the values of rotational viscosity may vary significantly along the flow's section, which could generate velocity profiles that deviate from the parabolic Poiseuille analytical ones, as observed in Krekhov et al. [16]. Astonishing is also the fact that in time oscillating fields in sufficiently high frequencies the flow rate increases [17, 174, 54].

In addition, Krekhov et al. [16] reports the aforementioned increase in the flow rate when $\eta_r < 0$ and reductions when $\eta_r > 0$. The flow rate can also be altered depending on the magnitude of the magnetization and induction fields and on their phase relations [54]. In oscillating fields, besides the pressure gradient, there is an oscillating magnetic force density, accelerating the fluid, which, in low frequencies, its net effect acts against the pressure gradient, slowing the fluid down [54].

1.4 A brief discussion of the rheology of ferrofluids

The viscosity of ferrofluids is an important issue in its rheology. Many physical factors influence viscosity, such as the pH of the solution, the surfactants and the size of the magnetic particles, the content of solids and the temperature of the fluid [215]. Many models have been proposed to account for the presence of particles in solutions.

Albert Einstein proposed a model which predicts the viscosity of dilute particle suspensions [216]. This simple model relates the mixture viscosity η_{eff} to the carrier fluid's viscosity η_0 and the volume fraction of particles ϕ, which in this dilute model must be $\phi < 0.05$.

$$\frac{\eta_{eff}}{\eta_0} = 1 + \frac{5}{2}\phi \tag{1.15}$$

Following Einstein's model [216], many models were developed by different scientists to predict viscosity. Brinkman [217] extended Einstein's model [216] for the case of concentrated suspensions.

$$\frac{\eta_{eff}}{\eta_0} = \frac{1}{(1-\phi)^{2.5}} \tag{1.16}$$

By considering Brownian motion interactions of the particles with each other, Batchelor [218] extended Einstein's model [216] to include terms of order ϕ^2 in Eq. (1.15).

$$\frac{\eta_{eff}}{\eta_0} = 1 + 2.5\phi + 6.5\phi^2 \tag{1.17}$$

Later, Bicerano et al. [219] proposed an expression for the suspensions' viscosity that provides a smooth transition between dilute and concentrated regimes and is valid for low-shear, by examining the viscosity of suspensions of different hard bodies [1].

$$\frac{\eta_{eff}}{\eta_0} = 1 + \zeta\phi + \kappa_H\phi^2 \tag{1.18}$$

In Equation (1.18), ζ is the virial coefficient and κ_H is the Huggins coefficient.

All aforementioned models relate viscosity as a function of volume fraction, without taking into consideration temperature dependences. Viscosity is a strong function of temperature [220], as fluids near their freezing point increase their viscosity while they have relatively low viscosity near the boiling point [221]. A correlation for pure fluids between viscosity and temperature is presented in White and Corfield [222], where η_{ref}, T_0 are reference values and a, b and c are dimensionless curve-fit constants.

$$\frac{\ln\eta}{\eta_{ref}} \approx a + b\left(\frac{T_0}{T}\right) + c\left(\frac{T_0}{T}\right)^2 \tag{1.19}$$

In the particular case of ferrofluids, one has to account for changes in viscosity when in the presence of an applied magnetic field due to the magnetoviscous effect, carefully described in section 1.3.1. Einstein's formula for calculating the viscosity of a suspension works well in dilute suspensions of small particles. However, it does not consider the rotational motion of the particles in respect to the fluid [21]. When a difference between particle's and fluid's angular velocities arises, novel frictional forces will manifest themselves as an additional viscosity, called rotational viscosity η_r [21]. This way the viscosity of a suspension will be given by:

$$\eta_{eff} = \eta_0\left(1 + \frac{5}{2}\phi\right) + \eta_r \tag{1.20}$$

In this scenario, the rotational viscosity η_r represents the difference between the ferrofluid's effective viscosity and the viscosity given by the Einstein expression - Eq. (1.15) - [63], which would

then be the ferrofluid's viscosity in the absence of a magnetic field. More on rotational viscosity η_r will be presented in section 2.1.5.

Another important aspect affecting the rheological behavior of ferrofluids is the presence of particle-particle interactions when they are subjected to magnetic fields [15]. If it is assumed that the particles do not interact, the viscosity changes are solely due to the hindrance of the particle's free rotation caused by the magnetic torque exerted on the particles [26]. In this case, the magnetically hard particles are responsible for this effect, as described in section 1.3.1, even though the observed effects are comparatively small [223, 200]. Conversely, in ferrofluids with interacting particles, there are formations of particle's aggregations such as clusters and chains, and, as described in section 1.3.1, these structure's relaxation times are larger than that of single particles, in a way that the observed effects are also larger [200]. Some works have investigated the rheological response of ferrofluids with respect to the level of interparticle interactions [224, 193, 188, 199, 223, 200].

All models mentioned above are summarized in Tab. (1.3), along with Lundgren's model [225], under the form a Taylor expansion series.

Table. 1.3: Conventional models used for predicting suspensions' viscosity. Adapted from Hezaveh et al. [220].

Model	Expression	Description
[216]	$\frac{\eta_{eff}}{\eta_0} = 1 + 2.5\phi$	For low concentrations
[217]	$\frac{\eta_{eff}}{\eta_0} = \frac{1}{(1-\phi)^{2.5}}$	Concentrated suspensions
[225]	$\frac{\eta_{eff}}{\eta_0} = 1 + 2.5\phi + 6.25\phi^2 + \mathcal{O}(\phi^3)$	Under the form of a Taylor series
[218]	$\frac{\eta_{eff}}{\eta_0} = 1 + 2.5\phi + 6.5\phi^2$	Brownian motion's effect on bulk stress
[219]	$\frac{\eta_{eff}}{\eta_0} = 1 + \zeta\phi + \kappa_H\phi^2$	
[222]	$\frac{\ln \eta}{\eta_{ref}} \approx a + b\left(\frac{T_0}{T}\right) + c\left(\frac{T_0}{T}\right)^2$	

Although ferrofluids respond to the action of external magnetic fields with changes in viscosity, stable ferrofluids show a relatively small magnetorheological effect (MR effect), such as an increase yield strength [1, 173]. In a nutshell, the MR effect in magnetorheological fluids is associated with the property that, in the presence of a magnetic field, the magnetic particles are subject to a strong magnetostatic attraction, leading to the formation of structures which align in the field's direction. These structures impede the flow of the fluid and, as a consequence, the fluid's

rheological properties change to those of plastic materials, presenting high values of yield stress and viscosity, whose intensity depends on the strength of the applied magnetic field [66]. On the other hand, the effects of an applied magnetic field on the rheological properties of ideal ferrofluids (rigidly defined as colloidal suspensions of nanoparticles with $d \lessapprox 10nm$ to ensure stability, in which Brownian motion dominates over all other interaction forces) [66] are limited to small increments in viscosity, explained by the impediment of the free rotation of the particles with the vorticity due to their tendency of orientation in the direction of the field by the magnetic torque [36, 226, 227, 228], as carefully described in section 1.3.1. This would be the case for ideal ferrofluids, however, real ferrofluids are polydispersed and a part of the particles is large enough that the Brownian motion energy is overcome by the dipole-dipole interaction energy, in a way that these particles are grouped in the magnetic fields direction, which can generate high viscosity changes and even the appearance of yield stress τ_y [66].

The static yield stress is associated with the shear stress that must be overcome to dismantle the particle's structures formed under the influence of the field in order to induce the material's flow [66]. In simple words, when the shear stress is smaller than the yield stress there is no fluid motion [1]. The static yield stress is the first parameter used to assess the intensity of the MR effect in magnetorheology [69]. There is also the dynamic yield stress, which is generally greater than the static yield stress [66]. While the static yield stress is the shear stress necessary to induce the flow of a material, the dynamic yield stress is the one used to break up the aggregates that are formed in the presence of magnetostatic forces [229, 66]. In magnetic fluids, changes in the yield stress can be suitably described by some yield stress models, as the Bingham model [230, 231].

$$\tau = \tau_y + \dot{\gamma}\eta_{pl} \tag{1.21}$$

In Equation (1.21), τ is the shear stress, η_{pl} is the plastic viscosity and τ_y is the yield stress. Shear stress (τ) results at high shear rates ($\dot{\gamma}$) for ferrofluids with spherical CoNi particles and fiberlike CoNi particles presented in López-López et al. [66] were shown to be well-adjusted by the Bingham model - Eq. (1.21) -.

Models accounting for both yield stress and shear thinning behavior are also available [231], as the Carson model and the Herschel-Bulkley model. Shear thinning is characterized by the non-Newtonian behavior of fluids when their viscosity decreases with increased shear rate [232]. Car-

son's model, based on a structure model of the interactive behavior of the solid and liquid phases of a biphasic suspension [1], accounts for both the yield stress threshold and the shear thinning behavior, being given by [231]:

$$\sqrt{\tau} = \sqrt{\tau_y} + \sqrt{\kappa\dot{\gamma}} \tag{1.22}$$

In Equation (1.22), κ is a Carson model constant.

In a similar manner, the Herschel-Bulkley (H-B) model also takes the yield stress and shear thinning into consideration, being expressed in Eq. (1.23), where the constants m and n in are regarded as model factors [1].

$$\tau = \tau_y + m\dot{\gamma}^n \tag{1.23}$$

Results for water-based $\mathrm{Fe_3O_4}$ ferrofluids were correlated in Hong et al. [215] using the H-B model.

In diluted suspensions, the shear thinning behavior may be linked to changes caused by shearing in the structure and arrangement of particles [233, 1]. The effect generated by the shear can orient the particles in the flow's direction. The particle's structures, previously formed due to magnetostatic forces, can break due to shear gradients, leading to a decrease in the amount of carrier liquid immobilized by the particles, which ultimately generates a decrease in apparent viscosity [1]. This effect is clearly observed in the results presented in Fig. (4.9). Shear thinning behavior has been reported for water-based $\mathrm{Fe_3O_4}$ ferrofluids [215], paraffin-based $\mathrm{Fe_2O_3}$ ferrofluids [220], as well as in other various types of ferrofluids [234, 235], including cobalt-based ferrofluids [200], indicating a strong level of particle-particle interaction [15].

Although the magnetorheological response of ferrofluids may be assessed with the yield stress and viscosity models presented above, it is more common to quantify it through the magnetoviscous effect, since most ferrofluids applications must work in flow regimes, where yield stress is not relevant [1, 66]. The magnetoviscous effect was thoroughly described in section 1.3.1 and can be defined in mathematical notation as [15]:

$$M_H = \frac{\eta_H - \eta_0}{\eta_0} \tag{1.24}$$

In Equation (1.24), η_H and η_0 are the fluid's viscosity in the presence and in absence of a magnetic field, respectively. The dimensionless parameter M_H quantifies the gain in viscosity that can be reached at a shear rate when in the presence of a magnetic field [1].

1.5 A brief discussion of particulate systems

It is of extreme importance to understand the micro-structural behavior of magnetic particles in order to comprehend the phenomenology of the colloidal suspension's magnetization dynamics, since a continuous description of such materials may not capture all the details regarding their micro-structure. An important tool to understand their complex physical behavior is direct numerical simulations, aiming at proposing or better understanding constitutive equations for a continuous description of these fluids, with special interest in their stress tensor or evolutive magnetization equations. In the field of ferrohydrodynamics, these are still relatively controversial points, as evidenced when one compares the mathematical formulation presented in Jansons [33] for the stress tensor with that presented in Rosensweig [236], Rinaldi et al. [70], Odenbach [226] or the different magnetization models proposed in Shliomis [26], Martsenyuk et al. [42], Shliomis [40], Felderhof and Kroh [43], Müller and Liu [24], which will be better covered in section 2.1.3.

The study of particulate systems with long-range interactions is important in many scientific and industrial areas, since they appear in various practical situations in civil, chemical, mechanical and oil engineering, to cite a few. Usually, studies in this area are concerned with properties such as the mean sedimentation velocity or velocity fluctuations of particulate systems [237]. In the particular case of magnetic fluids, their complex physics involve different mechanisms and possibilities of particle interactions [28], which leads to a difficult task to properly model such fluids in the particle's scale. However, understanding their micro-structure behavior is an important step in order to quantify their transport properties (of special interest to this work is the fluid's magnetization) and also control their stability in a more precise way [70, 226, 238]. In this scenario, numerical simulations done on the particle scale are important tools for a deeper understanding of physical phenomena present in the suspension's microstructure, also helping to understand how such phenomena affect transport properties on a macroscopic scale. The behavior of diluted magnetic

suspensions with hydrodynamic and magnetic interactions has been investigated in some studies, considering the effect of rotational motion and, in some cases, particle inertia, with special interest in the analysis of the relative trajectory of particles in interaction as well as in formation of aggregates and self-diffusion of particles [239, 240, 241, 242, 243, 244, 27, 28].

This particular work aims at recovering continuous magnetization profiles obtained for the fully developed flow of a plane Poiseuille flow, as indicated in section 1.1, through simulations done in the scale of the magnetic particles. In order to model the dynamic behavior of a magnetic suspension of magnetically hard interacting spherical particles, the approach of Langevin dynamics simulations [226] was used. In few words, this approach solves the classical Langevin stochastic equation for each of the suspended particles in the fluid [27, 28]. This equation comes from Newton's second law of motion applied to dispersed particles subjected to random Brownian fluctuations. To date, few techniques that efficiently and accurately capture the temporal evolution of particle systems that interact magnetically have been developed [28], with few works investigating by direct numerical simulations transport properties or providing calculations of the bulk magnetization in both Brownian and non-Brownian magnetic suspensions [226, 27, 28]. On the other hand, several studies can be found in the literature regarding simulations of ferrofluids and dipolar fluids by means of Monte Carlo static simulations [245, 246, 247, 248] and others using a combination of other methods, such as the Fokker-Plank equation in conjunction with an approach of Monte Carlo with a Langevin dynamics scheme [249]. Brownian dynamics was also explored by some works, with some of them focusing on the influence of interactions between particle's dipole moments on ferrofluid magnetization [250] and others on direct numerical simulations of the rotational Brownian motion of ferromagnetic particles [59]. Such suspensions are not only studied through numerical techniques. For instance, some macroscopic properties of magnetic suspensions were predicted in some theoretical works based on a statistical physics approach [33, 251, 34, 252].

The central idea behind the discrete formulation of this problem is, as mentioned, the application of Newton's second law to each of the suspended particles, taking into account the translation and rotation movements. As the particles are considered hard magnetically interacting particles (those whose magnetic dipole moment is fixed and the rotation of its magnetic dipole is only possible with the rotation of the particle itself [3, 62, 70], as discussed in section 1.3.1), the calculation of its rotational movement is extremely important, because it is strictly related to the fluid's magnetization, which is precisely the physical property studied in this work. Much of the difficulty encountered comes from modeling the forces and torques that act on each particle. Most of these interactions decay in space, being instantaneous functions of the configuration of all particles in

the simulation space, which leads to an enormous computational effort for the calculation of such interactions. Since the magnetic particles are immersed in a carrier liquid, not only magnetic force and torque long-range interactions are modeled in our simulations, but also hydrodynamic forces due to the viscous flow induced by the motion of a single particle in the others. As a suspension contains many particles dispersed in the carrier liquid, the motion a single particle leads to disturbances in the velocity and pressure fields, which exerts an influence on the surrounding particles affecting their motion, inducing the so-called hydrodynamic interactions. At low Reynolds numbers, such disturbances are propagated by the fluid through the viscosity diffusion [28]. The hydrodynamic interactions between two rigid particles are classified in two main groups according to the distance between them: 1) far field interactions, which happen between two widely separated particles and 2) lubrication interactions, which happen in near contact particles [253, 254, 255].

Such interactions between magnetic particles depend on the way the particles are arranged and oriented in space (in the so-called hydrodynamic interaction network), in a way that the long-range interactions are fundamental to describe the movement of a single particle in the suspension. These interactions also lead to velocity fluctuations, which are also observed even in non-Brownian suspensions with very small particle Reynolds number [28]. Such fluctuations also lead to the so-called hydrodynamic self-dispersion, whose effect is important in describing mixing processes that inhibit separation [256, 257].

In general, hydrodynamic interactions are characterized by a "slow decay" of order $(1/r)$, where r is the distance between the center of two arbitrary particles [28]. Such slow decays lead to classical divergence problems when these interactions are numerically computed [258, 259, 260, 261, 262, 263, 264] in incompressible creeping flows (also known as Stokes flow or low Reynolds number $Re \ll 1$ hydrodynamics, referring to flows in which inertial effects are negligible when compared to viscous and pressure forces [265]), in which some important statistical properties such as the mean velocity and mean velocity variance depend on the size of the system [27]. This problem is directly associated with the far-reaching nature of hydrodynamic interactions between the particles under creeping flows [27]. For more information regarding these interactions and the aforementioned problem, the reader is referred to Guazzelli and Hinch [264].

To avoid this particular problem, in order to perform the sums of these interactions in suspensions with periodic boundary conditions ($\mathcal{O}(N^2)$ operations), a rather sophisticated technique is necessary, since the operations become lattice sums and the accurate, but expensive, method proposed in Ewald [266], known as the Ewald lattice summation technique [266, 267, 268, 269,

270, 271, 27, 28], must be applied to accelerate convergence [27]. The Ewald summing technique basically consists of calculating the sum of the interactions of all $(N-1)$ particles dispersed in the suspension with an arbitrary reference particle i, replicating the physical suspension periodically in space, in order to simulate an *infinite suspension* (that is, a suspension with periodic boundary conditions). In this way, the long-range particle-particle interactions that act on the reference particle i are computed for all particles in the physical cell, as well as for all periodic images replicated in the reciprocal space. In other words, this technique is an efficient although numerically expensive way of representing, as far as possible, a so-called infinite suspension in order to obtain the convergence of the physical properties of the suspension volume in numerical simulations [28]. Both magnetic and hydrodynamic interactions between the particles can be calculated in our numerical code using this technique, which has already been used in the works of Gontijo [272], Gontijo and Cunha [27], Gontijo et al. [273], Gontijo and Cunha [28]. Likewise, other works have also made use of Ewald sums in the simulation of particle systems subject only to hydrodynamic, not magnetic interactions [274, 262, 275, 276, 277]. The fact is that both periodic and non-periodic ways of carrying the summations while simulating suspensions of magnetically interacting particles have their own advantages and disadvantages. Both methods have already been employed in various works found in the literature. For instance, to cite a few, periodic summations were used to compute the dynamic behavior of magnetic suspensions in the works of McWhirter and Patey [278], Wang et al. [279], Berkov and Gorn [280], Usov and Grebenshchikov [281], Gontijo and Cunha [27, 28] while other works considered non-periodic ways (minimum image method) [282, 283, 284, 285].

Since this work deals with magnetic suspensions, other far-field interactions due to the magnetic interactions among the particles are considered. Such interactions decay like $(1/r^3)$ for magnetic force and $(1/r^4)$ for the magnetic torque, which are both faster decays than that of hydrodynamic interactions $(1/r)$ [28]. Since magnetically interacting suspensions account for new type of physical mechanisms, other issues impact on the numerical implementation of such suspensions. In particular, such suspensions tend to form particle's aggregates due to the induced magnetic dipole-dipole interactions, as discussed in section 1.3.1. These agglomeration effects require additional numerical control in order to prevent particle overlapping as the simulations progress in time, specially when the effect of particle inertia is considered [272, 27]. As shown in Gontijo and Cunha [27], a significant amount of computation time is saved when computing only the magnetic particle interactions induced by torque-dipole-dipole interactions through periodic boundary conditions in dilute suspensions where $\phi \sim 5\%$, leaving the magnetic force interactions to be computed directly with the minimum image method, since these interactions decay faster. This so-called *hybrid method* was effectively used to compute fluid's equilibrium magnetization and other

transport properties in Gontijo and Cunha [27, 28] and is also used in this particular work. In section 3.2, the numerical approach used in this work to simulate the behavior of the dynamics of a colloidal suspension of magnetically interacting particles is covered in detail.

2 Mathematical formulation

2.1 Ferrohydrodynamic equations - Continuous description

The classical set of ferrohydrodynamics equations consists of the phenomenologically derived equation of fluid motion, the Maxwell equations in the magnetostatic limit and a magnetization equation. The latter one gets revised from time to time [44].

2.1.1 Maxwell equations in the magnetostatic limit

Magnetic fluids are regarded as non-conducting fluids, therefore Maxwell equations [286, 287] are reduced to the classical Ampère's circuit law in the magnetostatic limit and Gauss's magnetism law [3].

$$\nabla \times \boldsymbol{H} = \mathbf{0}; \qquad \nabla \cdot \boldsymbol{B} = 0 \tag{2.1}$$

In Eq. (2.1), ∇ is the usual nabla operator, $\boldsymbol{H}$ is the applied magnetic field and $\boldsymbol{B}$ is the magnetic induction field.

2.1.2 Phenomenological equation of motion

A ferrofluid flow in a magnetic field is accompanied with an interplay between hydrodynamic and magnetic effects. When subjected to a magnetic field $\boldsymbol{H}$, ferrofluids magnetize and are subjected to magnetic force - Eq. (2.2) - and torque - Eq. (1.11) - densities [3].

$$\boldsymbol{F} = \mu_0 (\boldsymbol{M} \cdot \nabla) \boldsymbol{H} \tag{2.2}$$

$$\boldsymbol{T} = \mu_0(\boldsymbol{M} \times \boldsymbol{H}) \qquad \text{(1.11 revisited)}$$

In the above relations, $\boldsymbol{M}$ is the ferrofluid magnetization and $\mu_0 = 1.2566 \times 10^{-6}$kgm/s^{2}A^2 is the magnetic permeability of free space. The magnetic force density in Eq. (2.2) is extremely important and has been used for precise transportation and positioning of ferrofluids in damping, sealing, heat transfer and liquid distribution systems [288, 289, 290], as well as in experiments with possible zero gravity using the magnetic force to precisely balance gravity, so that bubbles float freely in the ferrofluid [291].

When it comes to magnetic fluids flow, the concept of internal rotation arises, due to the relation between the magnetic and rotational degrees of freedom of the magnetic particles of which the fluids are composed [26]. To model such fluids, the total volume density of angular momentum is composed not only by the visible (orbital) angular momentum $\boldsymbol{L}$, as in ordinary fluids, but also by a new contribution, regarded as the internal (spin) angular momentum $\boldsymbol{S}$. The prior is associated with the translational motion of magnetic grains and molecules of the solvent - Eq. (2.3) -, and the latter to the rotation of the particles themselves - Eq. (2.4) - [21].

$$\boldsymbol{L} = \rho(\boldsymbol{r} \times \boldsymbol{v}) \qquad (2.3)$$

$$\boldsymbol{S} = I\boldsymbol{\omega} \qquad (2.4)$$

Here, ρ is the fluid's density, $\boldsymbol{r}$ is the position vector of the infinitesimal fluid element, $\boldsymbol{v}$ is the element velocity, I is the volume density of the particle's moment of inertia, which depends on the shape and concentration of the particles [63], $\boldsymbol{\omega}$ is the macroscopic angular velocity of the particles averaged over a physically small magnetic fluid volume. For spherical particles with density ρ_s and diameter d, the volume density of moment of inertia is given by [21]:

$$I = \frac{\rho_s \phi d^2}{10} \qquad (2.5)$$

This way, a new appropriate thermodynamic coordinate arises, $(\boldsymbol{S} - I\boldsymbol{\Omega})$, where $\boldsymbol{\Omega} = \frac{1}{2}\boldsymbol{\xi}$ is the local angular velocity of the fluid and $\boldsymbol{\xi} = (\nabla \times \boldsymbol{v})$ is the flow's vorticity. Any deviation between $\boldsymbol{\omega}$ and $\boldsymbol{\Omega}$ causes additional dissipation processes due to the redistribution of angular momentum between the visible $\boldsymbol{L}$ and internal $\boldsymbol{S}$ forms [21], which is manifested by an increase in fluid's viscosity, defined as rotational viscosity η_r. This process will eventually contribute to the stresses on the fluid.

The stress tensor of an ordinary non-magnetic suspension, obtained from irreversible thermodynamics is given by [292]:

$$\sigma_{ij} = -p\delta_{ij} + \eta\left(\frac{\partial v_i}{\partial x_j} + \frac{\partial v_j}{\partial x_i}\right) + \frac{1}{2\tau_s}\left(S_{ij} - I\Omega_{ij}\right) \tag{2.6}$$

In Eq. (2.6), p is the hydrodynamic pressure, η is the usual shear viscosity, $\tau_s = I/6\eta\phi$ is the spin relaxation time, ϕ is the volume fraction of particles, δ_{ij} is the Kronecker delta operator, $S_{ij} = \epsilon_{ijk}S_k$, where ϵ_{ijk} is the anti symmetric unit tensor and $\Omega_{ij} = \frac{1}{2}\left(\frac{\partial v_j}{\partial x_i} - \frac{\partial v_i}{\partial x_j}\right)$.

It is easy to check that for spherical nanoparticles the difference $(\boldsymbol{\omega} - \boldsymbol{\Omega})$ instantly decays due to the smallness of τ_s (i.e. $\tau_s \approx 10^{-11}$s) reducing to ordinary hydrodynamics [21]. However, in ferrohydrodynamics, when in time transients or dynamic flow conditions, fluid viscosity causes the magnetization $\boldsymbol{M}$ to lag the magnetic field $\boldsymbol{H}$ with angle θ, making vectors $\boldsymbol{H}$ and $\boldsymbol{M}$ not collinear, giving rise to a magnetic torque density - Eq. (1.11) - that acts upon the particles making them and the surrounding fluid to spin, leading to novel flow phenomena [70], where the aforementioned difference $(\boldsymbol{\omega} - \boldsymbol{\Omega})$ can be held. In a two-dimensional problem, the angle between vectors $\boldsymbol{H}$ and $\boldsymbol{M}$ can be calculated through Eq. (2.7).

$$\theta = \sin^{-1}\left(\frac{|\boldsymbol{M} \times \boldsymbol{H}|}{MH}\right) = \sin^{-1}\left[\frac{|M_x H_y - M_y H_x|}{\sqrt{(M_x^2 + M_y^2)(H_x^2 + H_y^2)}}\right] \tag{2.7}$$

In Eq. (2.7), sin stands for the sine function, M and H stand for the magnitude of vectors $\boldsymbol{M}$ and $\boldsymbol{H}$, respectively, M_x and M_y are the horizontal and vertical magnetization components,

respectively, finally H_x and H_y are the horizontal and vertical applied field components. A visual representation of angle θ can be visualized in Fig. (4.8)-(a).

These internal rotation effects modify the stress tensor, leading to a new one for a magnetic suspension under the action of internal torques, shown in Eq. (2.8) [26, 36, 21].

$$\sigma_{ij} = -p\delta_{ij} + \eta\left(\frac{\partial v_i}{\partial x_j} + \frac{\partial v_j}{\partial x_i}\right) + 3\eta\phi\epsilon_{ijk}(\omega_k - \Omega_k) + \left(H_i B_j - \frac{\mu_0}{2}H^2\delta_{ij}\right) \tag{2.8}$$

The last tern in Eq. (2.8) represents the Maxwell tensor of magnetic stresses in magnetic fluids [40]. The magnetic induction field $\boldsymbol{B}$ is related to the applied magnetic field and the fluid magnetization by [286]:

$$\boldsymbol{B} = \mu_0(\boldsymbol{M} + \boldsymbol{H}) \tag{2.9}$$

The general torque equation for a magnetic fluid (internal angular momentum density) can be obtained by subtracting the moment of the linear momentum density equation of a ferrofluid from the total angular momentum density [63], given by [3, 15, 14, 31, 32, 70]:

$$I\left[\frac{\partial \boldsymbol{\omega}}{\partial t} + (\boldsymbol{v}\cdot\nabla)\boldsymbol{\omega}\right] = \mu_0(\boldsymbol{M}\times\boldsymbol{H}) + 2\zeta(\nabla\times\boldsymbol{v} - 2\boldsymbol{\omega}) + (\lambda' + \eta')\nabla(\nabla\cdot\boldsymbol{\omega}) + \eta'\nabla^2\boldsymbol{\omega} \tag{2.10}$$

The viscosity coefficients are the shear and bulk coefficients of spin viscosity η' and λ', respectively. The coefficient ζ is called the vortex viscosity (different than the rotational viscosity η_r discussed in Shliomis [36]) and from microscopic theory for dilute suspensions of non-interacting spheres it obeys the approximate relationship $\zeta = \frac{3}{2}\eta\phi$ [26, 293, 294, 70, 63]. This equation is valid in the limit of infinite dilution, in the absence of hydrodynamic and magnetic interactions [63]. It is important to notice that the antisymmetric part of the stress tensor provides a mechanism for conversion between internal angular momentum $\boldsymbol{S}$ and external angular momentum $\boldsymbol{L}$ [63]. Magnetic fluids flows are incompressible, so that $(\nabla\cdot\boldsymbol{v}) = 0$, and, as indicated in Rinaldi et al. [70],

flow geometry often results in ($\nabla \cdot \boldsymbol{\omega}$) = 0. In addition, dimensional analysis leads to $\eta' \sim \eta l^2 \phi^2$, where l is of the order of the distance between particles. In ordinary ferrofluids ϕ is small and l is comparable to particle diameters ($\sim$ 10nm) thus η' becomes very small and may be neglected [70]. Even though the spin viscosity is very small in magnitude, Felderhof [55, 172] report crucial dependence of the net flow rate on spin viscosity η' in the case of ferrofluid pumping by means of a running magnetic wave in the absence of a pressure gradient, both in planar duct [55] and circular tube [172] flows, indicating that it would vanish in the case of null η'. Differences in velocity profiles were also reported in such works [55, 172] under different η' conditions, which varied from a pluglike shape in small η' configuration to a nearly parabolic one in large η' configuration. The importance of spin viscosity is also reported in Zaitsev and Shliomis [48], Chaves et al. [295] for the case of spin-up flow [51], and its value has been experimentally [295] reported to be rather larger in comparison with earlier theoretical estimates [172]. Recent experimental evidences also support the role of the "spin viscosities" in describing/predicting certain classes of ferrofluid flows [296, 297, 298, 299].

In this work, the effects of spin viscosity are neglected due to its smallness, in a way that it is possible to rewrite Eq. (2.10), in the assumed physical limits, as:

$$\boldsymbol{\omega} \cong \frac{\mu_0}{6\eta\phi}(\boldsymbol{M} \times \boldsymbol{H}) + \frac{1}{2}\boldsymbol{\xi} - \tau_s \left[\frac{\partial \boldsymbol{\omega}}{\partial t} + (\boldsymbol{v} \cdot \nabla)\boldsymbol{\omega} \right] \tag{2.11}$$

By substituting Eq. (2.11) into Eq. (2.8) with the aid of Eq. (2.9), it is easy to check that the obtained stress tensor is asymmetric, as $(\sigma_{ij} - \sigma_{ji}) = I\epsilon_{ijk}\left[\frac{\partial \omega_k}{\partial t} + v_j \frac{\partial \omega_k}{\partial x_j}\right]$. The asymmetry of the stress tensor due to internal torques are better portrayed in Fig. (2.1), where two configurations are presented, one in the absence of internal angular momentum and other in its presence.

Due to the smallness of the magnetic particles, the spin relaxation time τ_s is much smaller than unity, and thus the inertial term in Eq. (2.11) may be neglected, in a way that the magnetic torque acting upon the particles is balanced by the viscous torques, leading to an algebraic equation for the macroscopic angular spin rate $\boldsymbol{\omega}$:

$$\boldsymbol{\omega} \sim \frac{\mu_0}{6\eta\phi}(\boldsymbol{M} \times \boldsymbol{H}) + \frac{1}{2}\boldsymbol{\xi} \tag{2.12}$$

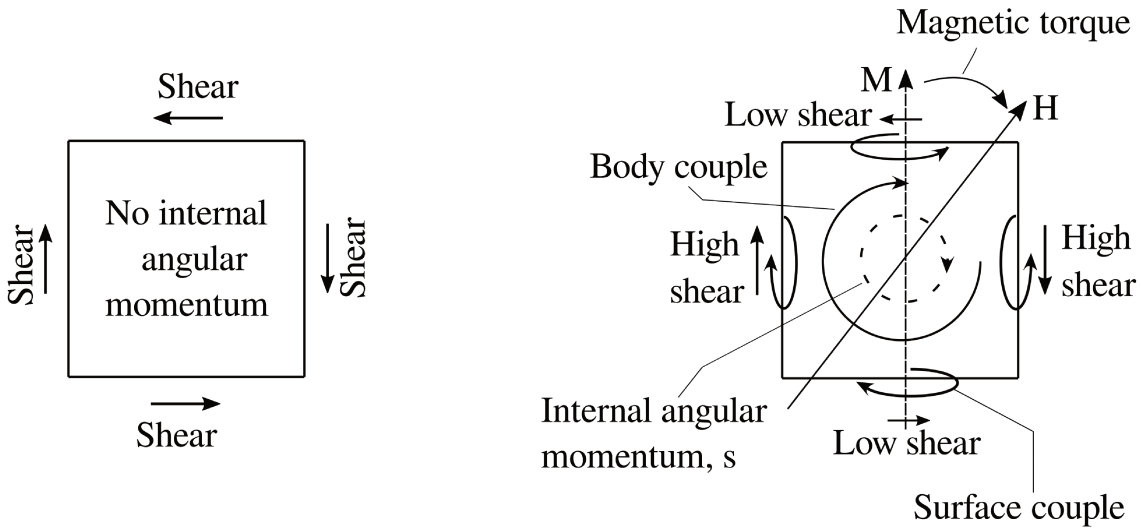

Figure. 2.1: Left: stress configuration in the absence of internal angular momentum. Right: stress configuration in the presence of internal angular momentum. Image adapted from Rosensweig [3].

When the macroscopic angular spin rate $\boldsymbol{\omega}$ is modeled with Eq. (2.12) and this relation is substituted into Eq. (2.8), one obtains [40]:

$$\sigma_{ij} = -\left(p + \frac{\mu_0}{2}H^2\right)\delta_{ij} + \eta\left(\frac{\partial v_i}{\partial x_j} + \frac{\partial v_j}{\partial x_i}\right) + H_i B_j + \frac{\mu_0}{2}\Big(M_i H_j - M_j H_i\Big) \tag{2.13}$$

By using Eq. (2.9) into Eq. (2.13), one notices that the stress tensor for a magnetic fluid takes now a symmetric form ($\sigma_{ij} = \sigma_{ji}$) [40], which is not an explicit function of the angular spin rate, but a function of the field variables $\boldsymbol{H}$ and $\boldsymbol{M}$.

$$\sigma_{ij} = -\left(p + \frac{\mu_0}{2}H^2\right)\delta_{ij} + \eta\left(\frac{\partial v_i}{\partial x_j} + \frac{\partial v_j}{\partial x_i}\right) + \mu_0 H_i H_j + \frac{\mu_0}{2}\Big(M_i H_j + M_j H_i\Big) \tag{2.14}$$

For the symmetric configuration under consideration [55], a uniform rotating magnetic field does not cause net flows [300]. With the stress tensor of a magnetic fluid defined, it is possible to obtain the equation of motion by using the momentum conservation law [301]:

$$\rho\left[\frac{\partial \boldsymbol{v}}{\partial t}+(\boldsymbol{v}\cdot\nabla)\boldsymbol{v}\right]=\nabla\cdot\boldsymbol{\sigma} \tag{2.15}$$

After carrying out the necessary algebra, the equation of motion for a magnetic fluid is obtained [21]:

$$\rho\left[\frac{\partial \boldsymbol{v}}{\partial t}+(\boldsymbol{v}\cdot\nabla)\boldsymbol{v}\right]=-\nabla p+\eta\nabla^2\boldsymbol{v}+\mu_0(\boldsymbol{M}\cdot\nabla)\boldsymbol{H}+\frac{\mu_0}{2}\nabla\times(\boldsymbol{M}\times\boldsymbol{H}) \tag{2.16}$$

It is interesting to notice in Eq. (2.16) the presence of the aforementioned magnetic force density - Eq. (2.2) -, and a term which is associated with the magnetic torque density - Eq. (1.11) -. The latter is referred as the rotation of the magnetic torque [58], which can be expressed as the divergence of an antisymmetric tensor [54, 55].

It is clear that fluid magnetization plays a major role in fluid motion, and, as will be shown, magnetization itself depends on the motion as well, due to the intertwinement between hydrodynamics and magnetism of which magnetic fluids are subjected to. A second way of presenting Eq. (2.16) is by taking its curl to obtain an evolutive equation for the flow's vorticity $\boldsymbol{\xi}$.

$$\rho\left[\frac{\partial \boldsymbol{\xi}}{\partial t}+(\boldsymbol{v}\cdot\nabla)\boldsymbol{\xi}\right]=\eta\nabla^2\boldsymbol{\xi}+(\boldsymbol{\xi}\cdot\nabla)\boldsymbol{v}+\mu_0\nabla\times\Big[(\boldsymbol{M}\cdot\nabla)\boldsymbol{H}\Big]+\frac{\mu_0}{2}\Big\{\nabla\Big[\nabla\cdot(\boldsymbol{M}\times\boldsymbol{H})\Big]-\nabla^2(\boldsymbol{M}\times\boldsymbol{H})\Big\} \tag{2.17}$$

In two-dimensional problems - Fig. (1.1) -, some terms presented in Eq. (2.17) vanish, resulting in the following two-dimensional vorticity equation:

$$\rho\left[\frac{\partial \boldsymbol{\xi}}{\partial t}+(\boldsymbol{v}\cdot\nabla)\boldsymbol{\xi}\right]=\eta\nabla^2\boldsymbol{\xi}+\mu_0\nabla\times\Big[(\boldsymbol{M}\cdot\nabla)\boldsymbol{H}\Big]-\frac{\mu_0}{2}\nabla^2(\boldsymbol{M}\times\boldsymbol{H}) \tag{2.18}$$

2.1.3 Magnetization equations

When in equilibrium, in the absence of a flow field, magnetic fluids' magnetization is called equilibrium magnetization $\boldsymbol{M_0}$, which is collinear to the applied magnetic field $\boldsymbol{H}$. In the case of a monodisperse collection of non-interacting particles, the equilibrium magnetization $\boldsymbol{M_0}$ in a ferrofluid is accurately described by the Langevin equation for paramagnetism [3, 15, 14, 31, 32, 70]:

$$\boldsymbol{M_0} = \boldsymbol{M_s}\left[\coth(\alpha) - \frac{1}{\alpha}\right] \tag{2.19}$$

The saturation magnetization $\boldsymbol{M_s}$ is defined as the magnetization value reached when all particles with volume V_p and bulk magnetization M_d have magnetic dipole moments m = $M_d V_p$ aligned with the applied magnetic field $\boldsymbol{H}$. It is defined as $M_s = Nm = \phi M_d$, where N is the number of magnetic dipoles per unit volume [70]. For the typically used magnetite nanoparticles with bulk magnetization $M_d = 4.46 \times 10^5 Am^{-1}$ in ferrofluids, with a representative volume fraction of $\phi = 4\%$ with particle's diameter $d = 10nm$ ($V = 5.236 \times 10^{-25} m^3$) one obtain a saturation magnetization $\mu_0 M_s = 0.0244T$ and $N = \frac{\phi}{V} \approx 7.64 \times 10^{22}$ magnetic nanoparticles/m^3. In Eq. (2.19) α is the Langevin parameter - Eq. (2.20) -, also named dimensionless magnetic field, being defined as a measurement of the relative intensity between magnetic and Brownian energies and $coth$ stands for the hyperbolic cotangent function, and

$$\alpha = \frac{\mu_0 m H}{\kappa_B T} \tag{2.20}$$

In Eq. (2.20), κ_B is the Boltzmann constant and T is the absolute temperature.

Langevin magnetization measurements may be used as a mean to estimate the magnetic particle's diameter [70]. In the linear low field region (i.e. $\alpha \ll 1$), estimates of the largest magnetic particles may be obtained, conversely, in the high field regime (i.e. $\alpha \gg 1$) an estimate of the smallest diameters may be obtained [3, 302].

$$\begin{aligned}\lim_{\alpha\gg 1}\frac{M_0}{M_s} &\approx 1-\frac{1}{\alpha}=1-\frac{6\kappa_B T}{\pi\mu_0 M_d H d^3}\\ \lim_{\alpha\ll 1}\frac{M_0}{M_s} &\approx \frac{\alpha}{3}=\frac{\pi\mu_0 M_d H d^3}{18\kappa_B T}\end{aligned} \tag{2.21}$$

With the use of a magnetometer, this method leads to estimates concerning the size range to which ferrofluid magnetic nanoparticles may belong [70], other methods such as transmission electron microscopy, atomic force microscopy and forced Rayleigh scattering of light can also be used [303, 70].

The prior model for describing magnetic fluids' equilibrium magnetization does not account for magnetic dipole-dipole interactions. In more concentrated regimes, the correct behavior of the suspension's equilibrium magnetization is predicted by higher-order asymptotic solutions, as the one proposed in Ivanov and Kuznetsova [34] that takes into consideration the interactions of dipole moments among triplets of particles. It corresponds to a second-order correction in ϕ of Langevin's equation.

$$\boldsymbol{M_0} = \boldsymbol{M_s}\Big[\mathcal{L} + E\lambda\phi + \big(F+G\big)\lambda^2\phi^2\Big] \tag{2.22}$$

In Eq. (2.22), $\mathcal{L}$, E, F and G are functions of α, where $\mathcal{L}$ is the well known Langevin function. The dipole's coupling parameter λ is a non-dimensional number responsible for accounting for the dipole-dipole interactions, calculated from the ratio of the interparticle interaction of two magnetic particles in contact to thermal energy, defined in Eq. (1.13). Typical values of λ range from 0.04 < λ < 4.5, depending on the particle's size and the fluid's temperature.

$$\mathcal{L}(\alpha) = \coth(\alpha) - \frac{1}{\alpha} \tag{2.23}$$

$$E(\alpha) = \left(\frac{8\pi}{\alpha}\right)\mathcal{L}(\alpha)\left[-\alpha\,\mathrm{csch}^2(\alpha) + \frac{1}{\alpha}\right] \tag{2.24}$$

$$F(\alpha) = \left(\frac{32\pi^2}{\alpha^2}\right)\mathcal{L}^2(\alpha)\left[2\alpha^2\,\mathrm{csch}^2(\alpha)\coth(\alpha) - \frac{2}{\alpha}\right] \tag{2.25}$$

$$G(\alpha) = \left(\frac{4\pi^2}{\alpha^2}\right)\mathcal{L}(\alpha)\left[-\alpha\,\mathrm{csch}^2(\alpha) + \frac{1}{\alpha}\right]^2 \tag{2.26}$$

$$\lambda = \frac{\mu_0 m^2}{4\pi d^3 \kappa_B T} \tag{1.13 revisited}$$

In Eqs. (2.24), (2.25) and (2.26), $csch$ stands for the hyperbolic cosecant function.

It is still up to debate a proper way of incorporating the role of particle's interactions in non-equilibrium magnetization dynamics. Some works argue that they should be incorporated in the equilibrium relaxation term in the magnetization equation by using higher-order asymptotic models [34], as the one presented in Eq. (2.22), while other works claim that thy must be incorporated in the form of a configurational stress tensor that deals with the magnetoviscous effect directly [45], using hybrid models that mix Langevin Dynamics with classical Computational Fluid Dynamics techniques [46]. Recently, de Carvalho and Gontijo [46] compared magnetization profiles obtained through CFD techniques and Langevin dynamics. Even though the shapes of the magnetization profiles were remarkably similar, the authors attributed the discrepancies among the results due to the non-prediction of the dipolar interactions effects by the studied magnetization models in non-equilibrium physical regimes, however, they indicated that further investigations needed to be done. In this particular work, the effects of the dipolar interactions are accounted by incorporating them into the predicted equilibrium magnetization [34], according to Eq. (2.22).

When magnetic fluids are not at rest and the magnetization is not in equilibrium due to time transients or time varying magnetic fields, a magnetization evolution equation is needed in order to fully describe the physics of the flow [70]. As there is no corresponding conservation law for magnetization, unlike energy and momentum, from the formal phenomenological thermodynamics the magnetization equations are ill defined [44]. In the scientific realm of ferrohydrodynamics, magnetization models have been the subject of several scientific publications. At least five models for the magnetization relaxation have been proposed in the literature [26, 42, 40, 43, 24]. These models have several differences in terms of accuracy and limitations in their validity [58]. They also

lead to drastically different predictions for the dependence of the magnetoviscosity on amplitude and frequency of an applied oscillating magnetic field [54].

In this work, three distinct models are used, which have proven to be capable of describing the magnetization dynamics of magnetic fluids in different regimes, two of them derived phenomenologically [26, 40] and the other one by using an effective-field method (EFM) [42]. Before presenting the aforementioned magnetization models, it is important to characterize the relaxation time τ it takes for each magnetic nanoparticle with magnetic moment $\boldsymbol{m}$ to align $\boldsymbol{m}$ with $\boldsymbol{H}$ when it experiences a torque $\mu_0 \boldsymbol{m} \times \boldsymbol{H}$. Since the particles' relaxation time is governed by the process with the shortest relaxation time, the small particles (magnetically weak particles) will follow the Néel process while the large ones (magnetically hard particles) will follow the Brownian manner [62]. The critical diameter on which the relaxation behavior becomes Brownian is $d \approx 13nm$, in a way that only magnetically hard particles will contribute to the rotational viscosity effect [62]. In the magnetization models presented below, the particles are assumed to be rigid magnetic dipoles whose reorientation is only possible with the rotation of the particles themselves [21], and therefore $\tau = \tau_B$. In addition, in this particular work, ferrofluids consisted of magnetite nanoparticles with average diameter $d = 13nm$ are considered.

The first presented model was derived phenomenologically in Shliomis [26] as a generalization of the Debye relaxation equation [304] in the case of spinning magnetic grains [21].

$$\frac{\partial \boldsymbol{M}}{\partial t} + (\boldsymbol{v} \cdot \nabla)\boldsymbol{M} = \frac{1}{2}\boldsymbol{\xi} \times \boldsymbol{M} - \frac{1}{\tau}(\boldsymbol{M} - \boldsymbol{M_0}) - \frac{\mu_0}{6\eta\phi}[\boldsymbol{M} \times (\boldsymbol{M} \times \boldsymbol{H})] \tag{2.27}$$

Equation (2.27) is valid in weakly non-equilibrium situations, when in small vorticities, for an arbitrary intensity of α and small values of $\Omega\tau$ [21]. Numerical and analytical solutions of the Fokker-Planck equation have corroborated the applicability of Eq. (2.27) for $\Omega\tau \ll 1$ [305, 306]. Apart from the presented validations of this model, Felderhof [307] claims that it does not apply in concentrated regimes and has limited validity in dilute regimes.

Using irreversible ferrofluid thermodynamics with hydrodynamics and the complete set of Maxwell's equations, a relaxation model for magnetization, which is closely related but not identical to the model of Eq. (2.27) [26], was proposed in Felderhof and Kroh [43], Felderhof [39]. However, it is presented here for illustrative purposes only, as this equation will not be used in our

studies, since Shliomis [21, 308] states that it leads to an incorrect rotational viscosity limit value when the non dimensional magnetic field α becomes too large. In addition, rotational measurements under the action of DC magnetic fields applied perpendicular to Poiseuille flow [309] are in line with the result of the first model - Eq. (2.27) - [26] and differ from that of Felderhof and Kroh [43] - Eq. (2.28) -. Similar measurements, however, with alternating magnetic fields [310] were in qualitative agreement with the rotational viscosity of the the first model - Eq. (2.27) - [26], although a frequency-dependent adjustment parameter was used to successfully fit theory and the experiment. This model is presented in Eq. (2.28).

$$\frac{\partial \boldsymbol{M}}{\partial t} + (\boldsymbol{v} \cdot \nabla)\boldsymbol{M} = \frac{1}{2}\boldsymbol{\xi} \times \boldsymbol{M} - \boldsymbol{M}(\nabla \cdot \boldsymbol{v}) + \gamma_H(\boldsymbol{B} - \boldsymbol{B'}) \tag{2.28}$$

In Equation (2.28), γ_H is a relaxation rate [39] and $\boldsymbol{B'} = \boldsymbol{B} - \frac{1}{c}(\boldsymbol{v} \times \boldsymbol{E})$ is in the local rest frame moving with velocity $\boldsymbol{v}$ with respect to the laboratory frame. $\boldsymbol{E}$ is the electric field and c is the speed of light [43].

The second model used in this work is a more precise magnetization equation that was derived microscopically from the Fokker-Planck equation by the implementation of an effective-field method (EFM) [42], derived for dilute ferrofluids in an effective field approximation for the orientational distribution function [54]. Out of equilibrium, the magnetization $\boldsymbol{M}$ is no longer a function of the field $\boldsymbol{H}$ [44], however, the model consists in considering an arbitrary magnetization $\boldsymbol{M}$ as an equilibrium one in a certain especially prepared effective field $\boldsymbol{H_e}$ [40]. The effective field $\boldsymbol{H_e}$ is related to the non-equilibrium magnetization $\boldsymbol{M}$ through the equilibrium relation [21]:

$$\boldsymbol{M} = M_s \mathcal{L}(\alpha_e)\frac{\boldsymbol{\alpha_e}}{\alpha_e} \tag{2.29}$$

The dimensionless effective field $\boldsymbol{\alpha_e}$ is determined by:

$$\boldsymbol{\alpha_e} = \frac{\mu_0 m \boldsymbol{H_e}}{\kappa T} \tag{2.30}$$

The dimensionless effective field $\boldsymbol{\alpha_e}$ tends to the dimensionless true field $\boldsymbol{\alpha}$ as the magneti-

zation $\boldsymbol{M}$ - Eq. (2.29) - relaxes to its equilibrium value $\boldsymbol{M_0}$ - Eq. (2.19) - [21], through the relaxation equation [42]:

$$\frac{\partial \boldsymbol{M}}{\partial t} + (\boldsymbol{v}\cdot\nabla)\boldsymbol{M} = \frac{1}{2}\boldsymbol{\xi}\times\boldsymbol{M} - \frac{\left[\alpha_e^2 - (\boldsymbol{\alpha}\cdot\boldsymbol{\alpha_e})\right]}{\tau\alpha_e^2}\boldsymbol{M} - \frac{\left[\alpha_e - \mathcal{L}(\alpha_e)\right]}{6\eta\phi\alpha_e\mathcal{L}^2(\alpha_e)}\boldsymbol{M}\times(\boldsymbol{M}\times\boldsymbol{H}) \quad (2.31)$$

For the calculation of the effective field, the $\mathcal{O}(\phi^2)$ asymptotic model of Ivanov and Kuznetsova [34] was considered using the following relation $\boldsymbol{H_e} = H_e\boldsymbol{M}/M_0$, which comes from Eq. (2.29), where $M_0(\alpha_e, \lambda, \phi)$ is the equilibrium magnetization analogous to the model proposed in Ivanov and Kuznetsova [34], since α_e can be defined as $\alpha_e = \alpha\frac{H_e}{H}$. This process is done iteratively from a numerical implementation perspective.

Equation (2.31) describes very well real magnetic fluids for any values of α and $\Omega\tau$ [40], and its use has been corroborated by experiments and direct numerical methods [20, 59, 32, 44]. It is clear that the potential of microscopic theory is much greater than that of macroscopic approach [44], as Eq. (2.31) guarantees the correct description of magnetization even far from equilibrium $\Omega\tau \gg 1$ [40]. Equation (2.31) also provides a very good approximation to the results of exact solution of the Fokker–Planck equation [306] and to the steady state magnetoviscosity in dilute ferrofluids [54], in addition to agreement to computer simulations of the Brownian dynamics of magnetic grains [311, 312]. However, according to Felderhof [54], this equation may not describe the relaxation behavior in dense ferrofluids correctly.

The last model used in this work consists of another phenomenological equation derived from irreversible thermodynamics [21].

$$\frac{\partial \boldsymbol{H_e}}{\partial t} + (\boldsymbol{v}\cdot\nabla)\boldsymbol{H_e} = \frac{1}{2}\boldsymbol{\xi}\times\boldsymbol{H_e} - \frac{(\boldsymbol{H_e}-\boldsymbol{H})}{\tau} - \frac{\mu_0}{6\eta\phi}[\boldsymbol{H_e}\times(\boldsymbol{M}\times\boldsymbol{H})] \quad (2.32)$$

Equation (2.32) along with Eq. (2.29) determines the magnetization $\boldsymbol{M}$ in an implicit form, with the effective field $\boldsymbol{H_e}$ as the parameter [21]. Equation (2.32) gives a correct quantitative description of magnetization even far from equilibrium, when $\Omega\tau \gg 1$. It also coincides with Eq. (2.27) in the limit of low field ($\alpha \ll 1$) when the true magnetization $\boldsymbol{M}$ and its equilibrium

value $\boldsymbol{M_0}$ can be written as [40]:

$$\boldsymbol{M} = \chi \boldsymbol{H_e}; \qquad \boldsymbol{M_0} = \chi \boldsymbol{H} \tag{2.33}$$

In Eq. (2.33), χ is the initial magnetic susceptibility. However, as the shear rate is increased, a discrepancy between Eqs. (2.32) and (2.27) arises [40]. So, in the low magnetic field limit, the magnetization is approximately linear with H. The magnetic susceptibility can then be written as [70]:

$$\frac{M_0}{H} = \chi; \qquad \chi = \frac{\mu_0 m^2 N}{3\kappa_B T} = \frac{\pi \phi \mu_0 M_d^2 d^3}{18\kappa_B T} \tag{2.34}$$

In Equation (2.34), the initial magnetic susceptibility χ is related to magnetic permeability as $\mu = \mu_0(1+\chi)$ [70]. By plugging some representative typical ferrofluid values, one obtain, at room temperature $T = 298K$ for magnetite nanoparticles with typical diameter $d = 10nm$ and volume fraction $\phi = 4\%$, $\chi \approx 0.424$, $\mu \approx 1.79 \times 10^{-6} N/A^2$ and relative permeability $\frac{\mu}{\mu_0} = 1.424$, which is larger than that of a neodymium magnet ($\frac{\mu}{\mu_0} = 1.05$ [313]).

When the initial magnetic permeability is large, the interaction between magnetic moments is quite appreciable in a way that Eq. (2.34) no longer holds [70]. For the case of monodispersed particles, Shliomis [36] uses a method similar to the used in the *Debye-Onsager* theory of polar fluids [70] to replace Eq. (2.34) with:

$$\frac{\chi(2\chi+3)}{\chi+1} = \frac{\mu_0 m^2 N}{\kappa_B T} = \frac{\pi \phi \mu_0 M_d^2 d^3}{6\kappa_B T} \tag{2.35}$$

Following the presentation of magnetization models, Eq. (2.32) is also in an excellent agreement in the low and high field limits with Eq.(2.31), and does not deviate much in the entire α region [40]. According to Krekhov et al. [16], the application of the first - Eq. (2.27) - and third - (Eq. 2.32) - models is limited to small amplitudes of an oscillating magnetic field and weak flow vorticities.

Finally, another important magnetization model but not used in this work is the one derived in Müller and Liu [24] with standard non-equilibrium thermodynamics with magneto-dissipative effects. The main advantage of this approach is that it does not need any microscopical assumptions about the fluid's structure, as the properties of the fluid are included in material parameters which have to be experimentally determined [62]. This equation, in a reduced form, is given by:

$$\frac{\partial \boldsymbol{M}}{\partial t} + (\boldsymbol{v} \cdot \nabla)\boldsymbol{M} = \frac{1}{2}(\boldsymbol{\xi} \times \boldsymbol{M}) + \frac{1}{\tau}(\boldsymbol{H} - \boldsymbol{H_{eq}}) - \lambda_1(\nabla \cdot \boldsymbol{v})\boldsymbol{M} - \lambda_2[(\nabla \boldsymbol{v}) + (\nabla \boldsymbol{v})^T] \quad (2.36)$$

First of all, the model presented in Eq. (2.36) contains the term associated with appearance of rotational viscosity (i.e. vector product of vorticity and magnetization) [62] which is also present in all models presented so far. In addition to that, two new terms appear, one associated to the divergence of the velocity field (sound propagation in ferrofluids) and other related to the the symmetric velocity gradient [62]. Experiments measuring the parameter λ_2 [314] had been conducted and the value $\lambda_2 = 0.2$ was found, contradicting the expected $\lambda_2 = 0$ value from the model presented in Eq. (2.27), giving a clear proof for the validity of the model presented in Eq. (2.36). Good results relating the found $\lambda_2 = 0.2$ parameter to mean particle chain length $\tilde{n}$ predicted in Zubarev et al. [213] were also reported [62]. Other experiments carried out with cobalt-based ferrofluid showed that fluids with a strong tendency to form chains show a λ_2 parameter that depends on the shear rate, corresponding well to the findings of rheological measurements [62]. Müller and Liu [24] claims that the models presented in Eqs. (2.27) and (2.31) are special cases of their model - Eq. (2.36).

Once again, it is important to emphasize that the magnetization models used in this work were those proposed in Shliomis [26], Martsenyuk et al. [42], Shliomis [40], given, respectively, by the Eqs. (2.27), (2.31) and (2.32).

A theoretical and quite satisfactory closed form solution for the particles' magnetization was obtained in Hatzikonstantinou and Vafeas [315], with the main assumption of immediate orientation of the magnetization vector $\boldsymbol{M}$ in a steady magnetic field with relatively small gradients [58] (i.e. negligible magnetic inertia $D\boldsymbol{M}/Dt$ in comparison to other terms in the magnetization equation), using the magnetization model proposed in Shliomis [26]. This solution was later confronted in Papadopoulos et al. [58] with direct numerical simulations of the governing equations,

where it has been shown that the model proposed is accurate for both magnetization components, and could be used in cases of non-uniform steady magnetic fields, especially for strong magnetic fields with weak gradients [58], as opposed to the steady and spatially uniform magnetic field that justifies the the null magnetic inertia hypothesis. In this case, estimations for the magnetization values could be made without the need for solving a magnetization equation [58]. However, in this particular, the whole set of ferrofluid's dynamics equations is solved.

The magnetization models used in this work are only valid for dilute regimes. In the case of dense ferrofluids, the equations describing magnetization relaxation are nor well established, as a detailed kinetic theory allowing for a macroscopic calculation of the magnetization relaxation is not available [54]. For more details regarding the differences among the magnetization models presented, please refer to Shliomis [40]. It is also important to mention that the described mathematical modeling behind ferrofluids' physics was discussed in detail in Rosensweig [3], Odenbach [4], Shliomis et al. [20], Shliomis [21].

2.1.4 Ferrohydrodynamic Bernoulli equation

A special case of the ferrohydrodynamic equations is that of incompressible Newtonian ferrofluids undergoing irrotational flow at constant temperature conditions. In this particular case, the equations are reduced to the so-called ferrohydrodynamic Bernoulli equation, which is analogous to the classical hydrodynamic Bernoulli equation however accounting for magnetic effects. In steady state it reads [3]:

$$p + \frac{1}{2}\rho v^2 + \rho g h - \mu_0 M H = constant \tag{2.37}$$

In Equation (2.37), h is the height above a reference plane and the magnetic term is the magnetic contribution to fluid pressure [299, 70]. Even though Eq. (2.37) is rather simple and simplified, it is a powerful weapon to describe simple yet practical phenomena, such as magnetic self-levitation in a ferrofluid, ferrofluid seals, magnetic nozzles, shape of ferrofluid meniscus, flow and instabilities of a ferrofluid jet and sink-float separations [3, 316, 14, 31].

2.1.5 Rotational viscosity

The phenomenon of rotational viscosity η_r, in which the viscosity of the ferrofluid changes when in the presence of a magnetic field due to the impediment of particle rotation along vorticity by magnetic torques, has been widely described in section 1.3.1. It represents the difference between the ferrofluid's effective viscosity when in the presence of a magnetic field and the viscosity given by the Einstein expression - Eq. (1.15) - [63]. In Poiseuille or Couette flow subjected to a transversal magnetic field H - Fig. (1.1) -, rotational viscosity η_r may be expressed as [40]:

$$\eta_r = \frac{M_x H}{4\Omega} \tag{2.38}$$

For small values of $\Omega\tau$, M_x is also small and η_r does not depend on flow vorticity [40]. According to all magnetization models presented in Eqs. (2.27), (2.31) and (2.32), M_x is proportional to $\Omega\tau$ [40].

In the configuration where $\boldsymbol{H}$ is perpendicular to the flow, Eqs. (2.31) and (2.32) admit steady solutions in which the effective field $\boldsymbol{\alpha_e}$ tracks the true field $\boldsymbol{\alpha}$ with lag angle β. In an analogous way, Eq. (2.27) admits a steady solution but considering a special created variable $\boldsymbol{\alpha'_e} = \frac{\alpha \boldsymbol{M}}{M_s \mathcal{L}(\alpha)}$ [40]. These considerations lead us to the following relations for the rotational viscosity in all models presented [40]:

- First model [26]:

$$\eta_r = \frac{3}{2}\eta\phi\frac{\alpha_e'^2\mathcal{L}(\alpha)}{2\alpha + \alpha_e'^2\mathcal{L}(\alpha)}; \quad \sqrt{\alpha^2 - \alpha_e'^2} = \frac{2\Omega\tau\alpha\alpha_e'}{2\alpha + \alpha_e'^2\mathcal{L}(\alpha)} \tag{2.39}$$

- Second model [42]:

$$\eta_r = \frac{3}{2}\eta\phi\frac{\alpha_e\mathcal{L}^2(\alpha_e)}{\alpha_e - \mathcal{L}(\alpha_e)}; \quad \sqrt{\alpha^2 - \alpha_e^2} = \frac{2\Omega\tau\alpha_e\mathcal{L}(\alpha_e)}{\alpha_e - \mathcal{L}(\alpha_e)} \tag{2.40}$$

- Third model [21]:

$$\eta_r = \frac{3}{2}\eta\phi\frac{\alpha_e\mathcal{L}(\alpha_e)}{2 + \alpha_e\mathcal{L}(\alpha_e)}; \quad \sqrt{\alpha^2 - \alpha_e^2} = \frac{2\Omega\tau\alpha_e}{2 + \alpha_e\mathcal{L}(\alpha_e)} \tag{2.41}$$

Due to the small size of the particles, the relaxation time τ is $\tau < 10^{-4}$ even for high viscous magnetic fluids, in a way that the condition $\Omega\tau \ll 1$ is usually satisfied [40]. Having that in mind, it is easy to see that in such cases $\alpha_e = \alpha$ or $\alpha'_e = \alpha$, leading to the following relations for rotational viscosity as a function of the dimensionless field α when in the limit $\Omega\tau \ll 1$ [40]:

- First and third models (phenomenological equations):

$$\eta_r(\alpha) = \frac{3}{2}\eta\phi\left(\frac{\alpha - tanh(\alpha)}{\alpha + tanh(\alpha)}\right) \tag{2.42}$$

- Second model (EFM equation):

$$\eta_r(\alpha) = \frac{3}{2}\eta\phi\left(\frac{\alpha\mathcal{L}^2(\alpha)}{\alpha - \mathcal{L}(\alpha)}\right) \tag{2.43}$$

In Eq. (2.42), $tanh$ stands for the hyperbolic tangent function. A quick analysis of Eqs. (2.42) and (2.43) shows that in the absence of a magnetic field, when an individual particle is able to roll freely along the flow, in a torque free configuration ($\boldsymbol{\omega} = \boldsymbol{\Omega}$), the rotational viscosity is zero $\eta_r(0) = 0$ [21], as expected. In a similar manner, when the field is sufficiently large ($\alpha \gg 1$) that it guarantees the constancy of particle's orientation, the rolling of the particle is substituted by slipping, and the rotational viscosity reaches a saturation value $\eta_r(\infty) = \frac{3}{2}\eta\phi$ [21].

Together, Eqs. (2.1), (2.16) and one among equations (2.27), (2.31) or (2.32) describe the physics of magnetic fluids flow under conditions of null spin viscosity (η').

2.1.6 Vorticity-streamfunction formulation in two-dimensional flows

In the present work, the aforementioned governing equations were solved through the well-known vorticity-streamfunction formulation [317, 318]. As it deals with a two-dimensional flow confined in two parallel plates - Fig. (1.1) -, it is possible to define a streamfunction ψ as a direct function of the velocity field $\boldsymbol{v} = v_x\boldsymbol{e_x} + v_y\boldsymbol{e_y}$, where [301]:

$$v_x = \frac{\partial \psi}{\partial y}; \qquad v_y = -\frac{\partial \psi}{\partial x} \tag{2.44}$$

In Equation (2.44), v_x and v_y are the horizontal and vertical components of the velocity field, respectively. From the definition of flow's vorticity ($\boldsymbol{\xi} = \nabla \times \boldsymbol{v}$), a Poisson equation for the stream-function is readily obtained, as $\xi = \left(\frac{\partial v_y}{\partial x} - \frac{\partial v_x}{\partial y}\right)$ [301]:

$$\nabla^2 \psi = -\xi \tag{2.45}$$

2.1.7 Non-dimensional equations

The governing equations have been made non-dimensional with the use of some reference scales, shown in Eq. (2.46):

$$\begin{gathered} \tilde{x} = \frac{x}{h}; \quad \tilde{y} = \frac{y}{h}; \quad \tilde{t} = \frac{t}{h/U}; \quad \tilde{p} = \frac{p}{\rho U^2}; \quad \tilde{\boldsymbol{M}} = \frac{\boldsymbol{M}}{M_s}; \\ \tilde{\boldsymbol{u}} = \frac{\boldsymbol{u}}{U}; \quad \tilde{\nabla} = h\nabla; \quad \tilde{\boldsymbol{H}} = \frac{\boldsymbol{H}}{H_0}; \quad \tilde{\boldsymbol{\xi}} = \frac{h}{U}\boldsymbol{\xi}; \quad \tilde{\boldsymbol{H}}_{\boldsymbol{e}} = \frac{\boldsymbol{H_e}}{H_0} \end{gathered} \tag{2.46}$$

In Equation (2.46), $h = 2a$ is the spacing between the parallel plates, H_0 is a reference field with the same magnitude as the applied magnetic field and U is the mean Poiseuille velocity. For clarity in presenting the non-dimensional equations, the tildes $\sim$ were omitted and the obtained non-dimensional governing equations are presented below.

Linear momentum equation

$$\frac{\partial \boldsymbol{v}}{\partial t} + (\boldsymbol{v} \cdot \nabla)\boldsymbol{v} = -\nabla p + \frac{1}{Re}\nabla^2 \boldsymbol{v} + \frac{3\phi\alpha}{PeRe}\Big[(\boldsymbol{M} \cdot \nabla \boldsymbol{H})\Big] + \frac{3}{2}\frac{\phi\alpha}{PeRe}\Big[\nabla \times (\boldsymbol{M} \times \boldsymbol{H})\Big] \tag{2.47}$$

Vorticity equation for a two-dimensional problem

$$\frac{\partial \boldsymbol{\xi}}{\partial t} + (\boldsymbol{v} \cdot \nabla)\boldsymbol{\xi} = \frac{1}{Re}\nabla^2 \boldsymbol{\xi} + \frac{3\phi\alpha}{PeRe}\Big\{\nabla \times \big[(\boldsymbol{M} \cdot \nabla)\boldsymbol{H}\big]\Big\} - \frac{3}{2}\frac{\phi\alpha}{PeRe}\Big[\nabla^2(\boldsymbol{M} \times \boldsymbol{H})\Big] \tag{2.48}$$

Relaxation magnetization equations

- First model - Phenomenological equation:

$$\frac{\partial \boldsymbol{M}}{\partial t} + (\boldsymbol{v} \cdot \nabla)\boldsymbol{M} = \frac{1}{2}\boldsymbol{\xi} \times \boldsymbol{M} - \frac{1}{Pe}(\boldsymbol{M} - \boldsymbol{M_0}) - \frac{1}{2}\frac{\alpha}{Pe}[\boldsymbol{M} \times (\boldsymbol{M} \times \boldsymbol{H})] \tag{2.49}$$

- Second model - EFM equation:

$$\frac{\partial \boldsymbol{M}}{\partial t} + (\boldsymbol{v} \cdot \nabla)\boldsymbol{M} = \frac{1}{2}\boldsymbol{\xi} \times \boldsymbol{M} - \frac{1}{Pe}\frac{\Big[\alpha_e^2 - (\boldsymbol{\alpha} \cdot \boldsymbol{\alpha_e})\Big]}{\alpha_e^2}\boldsymbol{M} - \frac{1}{2}\frac{\alpha}{Pe}\frac{\Big[\alpha_e - \mathcal{L}(\alpha_e)\Big]}{\alpha_e \mathcal{L}^2(\alpha_e)}\boldsymbol{M} \times (\boldsymbol{M} \times \boldsymbol{H}) \tag{2.50}$$

- Third model - Phenomenological equation:

$$\frac{\partial \boldsymbol{H_e}}{\partial t} + (\boldsymbol{v} \cdot \nabla)\boldsymbol{H_e} = \frac{1}{2}\boldsymbol{\xi} \times \boldsymbol{H_e} - \frac{1}{Pe}(\boldsymbol{H_e} - \boldsymbol{H}) - \frac{1}{2}\frac{\alpha}{Pe}[\boldsymbol{H_e} \times (\boldsymbol{M} \times \boldsymbol{H})] \tag{2.51}$$

In Eqs. (2.47), (2.48), (2.49), (2.50) and (2.51) one notices the presence of non-dimensional physical parameters, defined as follows:

$$Re = \frac{\rho U h}{\eta}; \quad Pe = \frac{\tau_B}{\tau_{flow}} = \frac{\tau_B U}{h}; \tag{2.52}$$

The classical Reynolds number Re is a measurement between the relative intensities of inertial and viscous effects and the Péclet number Pe represents the relative importance of particles and flow time scales.

2.1.8 The case of non-zero spin viscosity

As described, the effect of spin viscosity, even though small, has been reported to have influence in ferrofluid dynamics in Felderhof [55, 172], Zaitsev and Shliomis [48], Chaves et al. [295, 296], Torres-Díaz and Rinaldi [297], Torres-Diaz and Rinaldi [298], Torres-Diaz et al. [299]. Therefore, the interested reader who wants to simulate ferrofluid flow dynamics considering the effects of the spin viscosity (the antisymmetric part of the stress tensor), is briefly referred to the presented below set of ferrohydrodynamic equations along with the most common boundary condition used for the spin velocity.

1. Continuity equation:

$$\nabla \cdot \boldsymbol{v} = 0 \tag{2.53}$$

2. Linear momentum equation [63]

$$\rho\left(\frac{\partial \boldsymbol{v}}{\partial t}+\boldsymbol{v}\cdot\nabla\boldsymbol{v}\right) = -\nabla p+\rho\boldsymbol{g}+\mu_0(\boldsymbol{M}\cdot\nabla)\boldsymbol{H}+2\zeta(\nabla\times\boldsymbol{\omega})+(\lambda+\eta-\zeta)\nabla(\nabla\cdot\boldsymbol{v})+(\eta+\zeta)\nabla^2\boldsymbol{v} \tag{2.54}$$

   Here, λ is the usual bulk viscosity.

3. Internal angular momentum

$$I\left[\frac{\partial \boldsymbol{\omega}}{\partial t}+(\boldsymbol{v}\cdot\nabla)\boldsymbol{\omega}\right] = \mu_0(\boldsymbol{M}\times\boldsymbol{H})+2\zeta(\nabla\times\boldsymbol{v}-2\boldsymbol{\omega})+(\lambda'+\eta')\nabla(\nabla\cdot\boldsymbol{\omega})+\eta'\nabla^2\boldsymbol{\omega} \tag{2.10 revisited}$$

4. Magnetization relaxation equation

   Phenomenological equation from Shliomis [26]

$$\frac{\partial \boldsymbol{M}}{\partial t}+(\boldsymbol{v}\cdot\nabla)\boldsymbol{M} = \frac{1}{2}\boldsymbol{\xi}\times\boldsymbol{M}-\frac{1}{\tau}(\boldsymbol{M}-\boldsymbol{M_0})-\frac{\mu_0}{6\eta\phi}[\boldsymbol{M}\times(\boldsymbol{M}\times\boldsymbol{H})] \tag{2.27 revisited}$$

Irreversible thermodynamics model from Felderhof and Kroh [43]

$$\frac{\partial \boldsymbol{M}}{\partial t} + (\boldsymbol{v} \cdot \nabla)\boldsymbol{M} = \frac{1}{2}\boldsymbol{\xi} \times \boldsymbol{M} - \boldsymbol{M}(\nabla \cdot \boldsymbol{v}) + \gamma_H(\boldsymbol{B} - \boldsymbol{B'}) \quad \text{(2.28 revisited)}$$

Effective field model from Martsenyuk et al. [42]

$$\frac{\partial \boldsymbol{M}}{\partial t} + (\boldsymbol{v} \cdot \nabla)\boldsymbol{M} = \frac{1}{2}\boldsymbol{\xi} \times \boldsymbol{M} - \frac{\left[\alpha_e^2 - (\boldsymbol{\alpha} \cdot \boldsymbol{\alpha_e})\right]}{\tau \alpha_e^2}\boldsymbol{M} - \frac{\left[\alpha_e - \mathcal{L}(\alpha_e)\right]}{6\eta\phi\alpha_e\mathcal{L}^2(\alpha_e)}\boldsymbol{M} \times (\boldsymbol{M} \times \boldsymbol{H}) \quad \text{(2.31 revisited)}$$

Phenomenological equation from Shliomis [40]

$$\frac{\partial \boldsymbol{H_e}}{\partial t} + (\boldsymbol{v} \cdot \nabla)\boldsymbol{H_e} = \frac{1}{2}\boldsymbol{\xi} \times \boldsymbol{H_e} - \frac{(\boldsymbol{H_e} - \boldsymbol{H})}{\tau} - \frac{\mu_0}{6\eta\phi}[\boldsymbol{H_e} \times (\boldsymbol{M} \times \boldsymbol{H})] \quad \text{(2.32 revisited)}$$

Irreversible thermodynamics model from Müller and Liu [24], here not presented in its fully form

$$\frac{\partial \boldsymbol{M}}{\partial t} + (\boldsymbol{v} \cdot \nabla)\boldsymbol{M} = \frac{1}{2}(\boldsymbol{\xi} \times \boldsymbol{M}) + \frac{1}{\tau}(\boldsymbol{H} - \boldsymbol{H_{eq}}) - \lambda_1(\nabla \cdot \boldsymbol{v})\boldsymbol{M} - \lambda_2[(\nabla \boldsymbol{v}) + (\nabla \boldsymbol{v})^T] \quad \text{(2.36 revisited)}$$

Even though the correct choice of boundary conditions for the spin velocity is still up to debate [319, 298, 320, 321, 322, 323, 324, 325, 326], the most common is:

$$\boldsymbol{\omega} - \boldsymbol{\omega_s} = \frac{\gamma_\omega}{2}(\nabla \times \boldsymbol{v})_b \quad (2.55)$$

In Equation (2.55), γ_ω is an adjustable coefficient and $\boldsymbol{\omega_s}$ represents the angular velocity of the wall. Here, two cases are considered: 1) that of strong interactions between the wall surface and the subcontinuum units and 2) that of weak interactions between the wall surface and the fluid. The first case is represented by the no-spin-slip condition ($\gamma_\omega = 0$). The second case is expressed by the vanishing antisymmetric stress at the wall surface ($\gamma_\omega = 1$) [63].

2.2 Discrete approach

In the discrete approach of the problem, Langevin dynamics is used to solve for each particle suspended in the magnetic fluid its linear and angular momentum balance equations, which are based on the Langevin stochastic equation that comes from Newton's second law of motion applied to colloidal particles subjected to Brownian motion [27]. The suspension under consideration is also subject to a local Couette flow. Once again, it is important to note that the discrete simulations are used in order to recover a continuous magnetization profile obtained through the numerical solution of the ferrohydrodynamic equations presented in the previous section by means of CFD techniques, covered in section 3.1. After the continuous simulations are performed, the flow field is divided into local vorticity cells and these are simulated under the Langevin dynamics scheme, as previously described in section 1.1.

A monodisperse suspension of N spherical magnetic particles with radius $a = d/2$ and density ρ_s dispersed in a Newtonian viscous fluid of viscosity η and density ρ_f at an absolute temperature T is studied, as indicated in Fig. (1.3). All particles are large enough to be considered magnetically hard particles [62], in a way that they will follow the Brownian relaxation process τ_B, in which the particle's magnetic dipole moment $\boldsymbol{m}$ is fixed in the particle and rotates along with it in the surrounding fluid to align vectors $\boldsymbol{m}$ and $\boldsymbol{H}$ [62, 70]. Under this scenario, the intrinsic magnetic timescale for the particle's dipole moment to rotate τ_N (Néel relaxation time) can be much larger than the Brownian τ_B, defined in Eq. (2.56), and the Stokes timescale τ_S [28], defined in Eq. (2.56).

$$\tau_B = \frac{a^2}{D}; \qquad D = \frac{\kappa_B T}{6\pi\eta a}; \qquad \tau_S = \frac{a}{U_s}; \qquad U_s = \frac{2a^2\Delta\rho g}{9\eta} \tag{2.56}$$

In Equation (2.56), D is the Stokes-Einstein Brownian diffusion coefficient [216], U_s is the Stokes velocity, $\Delta\rho = (\rho_s - \rho_f)$ is the density difference between the particle and the fluid and g is the gravitational acceleration [28].

Under the assumed conditions that $\tau_N \gg \tau_B$, the effect of magnetic field moment rotation relative to the particle as a consequence of particle anisotropy is neglected and, since the dipole is assumed to be fixed with respect to the particles, the only magnetic interactions are those between

the particles themselves and with the external applied field $\boldsymbol{H}$ [28]. It is of extreme importance to compute the rotational motion of the particles, since it is related to the fluid's magnetization. Therefore, the rotational movement, induced by Brownian fluctuations, magnetic dipole-dipole interactions and by the action of the applied magnetic field, which tends to magnetize the suspension, is considered in this work. Relevant physical properties, such as fluid magnetization, are calculated based on the particle's dipolar orientation throughout the time evolution process [27].

In addition, the particles are immersed in a viscous fluid, which brings to mind the quite small scales involved in the problem. The velocities the particles acquire combined with the viscosity of the carrier liquid and their extremely small sizes ($d \sim 10nm$) will usually generate a low Reynolds number ($Re << 1$) flow (creeping flow) when they move. In this particular case, Re is the particle's Reynolds number defined as $Re = \rho_f a U_s/\eta$. Therefore, the particles are subjected to the creeping flow properties, as instantaneity and time-reversibility [254]. The particle's inertial relaxation time is defined as $\tau_i = m_p/(6\pi\eta a)$, where m_p is the particle's mass [28]. For a typical magnetite spherical particle with diameter $d = 13nm$ and $\rho_s \approx 7874Kg/m^3$ the particle's mass is extremely low ($m_p = 9.06 \times 10^{-21}Kg$). This is associated with the low Stokes number St configurations to which the particles are subjected to, since the Stokes number is defined as $St = \tau_i/\tau_s = m_p U_s/(6\pi\eta a^2)$. For instance, the same particle immersed in water with $\rho_f \approx 1000Kg/m^3$ and $\eta = 8.9\times10^{-4}Pa.s$, under $g = 9.81m/s^2$ reads $St \approx 9.09 \times 10^{-12}$. For this reason, in this work particle inertia is neglected. It is important to briefly mention that a small amount of inertia is inserted in the numerical routine when hydrodynamic interactions are neglected in the simulations. This topic is covered in section 3.2.6.

Under low Reynolds conditions, when each particle moves, it induces a flow that will reach other suspended particles. The configuration resembles the presence of several microflows being generated, producing different local disturbances in each particle. The hydrodynamic interactions between the particles are then calculated taking into account all these velocity disturbances produced by the movement of the surrounding particles at the velocity of a single reference particle. If the particle is adhered to the fluid (i.e. there is no slip), it will move along with the fluid induced by the other particles. Therefore, the particles are connected on a microscale in a hydrodynamic network, usually called the hydrodynamic interaction network. The flow induced by such movements is, as already mentioned, a creeping flow, in which $Re \ll 1$. Since the density ratio is usually of first order $\rho_s/\rho_f = \mathcal{O}(1)$ (for instance, for magnetite and water it reads $\rho_s/\rho_f \approx 7.87$), the Stokes number St will also be much smaller than unity, since $St = (2/9)Re(\rho_s/\rho_f) \rightarrow St \sim Re(\rho_s/\rho_f) \ll 1$ [28]. Therefore, the flow is then governed by Stokes' equations, which, for an incompressible New-

tonian fluid, the lack of inertia of the fluid leads to a physical balance between pressure gradients and viscous velocity diffusion, which are the physical mechanisms that govern flow dynamics induced by each of the suspended particles. Stokes' equations are shown below.

$$\nabla \cdot \boldsymbol{v} = 0 \tag{2.53 revisited}$$

$$\nabla p = \eta \nabla^2 \boldsymbol{v} \tag{2.57}$$

Stokes' equations are linear and the forces induced in the fluid by the movement of the particles are proportional to the velocity induced by the particles. To solve these equations, it is then assumed the presence of a point particle (null volume) immersed in an infinite fluid. Afterwards, a concentrated force accompanied by a Dirac $\delta(r)$ function is applied in the system, meaning the nullity of the force in all the extension of the fluid, except at the point where the particle is located, in a way that there is a singularity of force due to the presence of the particle. In this scenario, Eq. (2.57) yields:

$$\boldsymbol{f}\delta(r) = -\nabla p + \eta \nabla^2 \boldsymbol{v} \tag{2.58}$$

Equation (2.58) is analytically solved in conjunction with Eq. (2.53) using Fourier transform techniques, leading to the calculation of both pressure and velocity fields for the entire fluid in the context of a point particle. It is observed in such expressions that both pressure and velocity, in any part of the fluid, are functions of the forces located on top of a particle that will be multiplying tensors of disturbance propagation, known as Green tensors. In other words, the disturbance generated by a particle when it moves at a certain point is given by the product of the force at the position where the particle is by tensors that depend on the decay of the space that connects the cause (particle's movement) with the consequence (disturbance generated). Therefore, by knowing the force acting on each particle and the position occupied by the others, one is able to calculate all the velocities on the surface of each particle. The information regarding the configuration of the system as a whole is placed in such tensors, leading to the computation of the long-range interactions between the particles. In this point it is important to mention that, as

discussed in section 1.5, the computation of hydrodynamic interactions by using Green's functions of incompressible creeping flows [327] leads to well known divergence problems [27], but this will be covered later in section 2.2.1.

The linearity of the Stokes equations lead to two formulations used to compute the velocities or forces induced by the interparticle hydrodynamic interactions: 1) mobility formulation - Eq. (2.59) - and 2) resistance formulation - Eq. (2.60) -. The first is more indicated in the context of non-massive particles and the later when inertial effects are considered [28]. So to speak, by using a multipole expansion, the grand resistance matrix relating force, torque and stresslet between two interacting spherical particles was obtained in Jeffrey and Onishi [328] for low Reynolds number [63]. For the case of lubrication interactions (in near contact particles), forces and torques were assessed in different physical scenarios, such as relative shearing motion, both translational and rotational, and relative squeezing flow, all of them depending on the relative distance between the particles' surfaces [254].

$$\boldsymbol{u} = \boldsymbol{M} \cdot \boldsymbol{f} \tag{2.59}$$

$$\boldsymbol{f} = \boldsymbol{M}^{-1} \cdot \boldsymbol{u} \tag{2.60}$$

In Equations (2.59) and (2.60), $\boldsymbol{u}$ denotes the velocities of the particles, $\boldsymbol{M}$ the Green tensors, $\boldsymbol{M}^{-1}$ the inverted Green tensors and $\boldsymbol{f}$ the forces acting on the particles.

As already mentioned, in this study the particles are considered to be non-massive, since $m_p \sim 10^{-21} Kg$. Therefore, the mobility formulation is used. The mobility representation when one groups together the velocities induced by N spherical magnetic particles is given in Eq. (2.61).

$$\begin{pmatrix} u_1 \\ u_2 \\ \vdots \\ u_N \end{pmatrix} = \begin{pmatrix} M_{1,1} & M_{1,2} & \cdots & M_{1,N} \\ M_{2,1} & M_{2,2} & \cdots & M_{2,N} \\ \vdots & \vdots & \ddots & \vdots \\ M_{N,1} & M_{N,2} & \cdots & M_{N,N} \end{pmatrix} \cdot \begin{pmatrix} f_1 \\ f_2 \\ \vdots \\ f_N \end{pmatrix} \tag{2.61}$$

In Equation (2.61), $\boldsymbol{u}_1, \boldsymbol{u}_2, \ldots, \boldsymbol{u}_N$ represent the velocities of particles $1, 2, \ldots, N$, respectively. As already mentioned, the second rank mobility tensor $\boldsymbol{M}_{ij}$, for $i = 1, \ldots, N$ and $j = 1, \ldots, N$ depends on the suspension spacial configuration. In simple words, these tensors connect the way the particles move, based on how the forces acting on a particle j change the velocities of a different particle i. Also, $\boldsymbol{f}_i$ represents the sum of all non-hydrodynamic forces acting on the reference particle i.

2.2.1 Periodic hydrodynamic interactions

In the previous section, it was shown that in order to obtain the solutions for the Stokes equations - Eq. (2.53) and (2.57) - a point particle (null volume) was considered to be immersed in an infinite fluid. To incorporate the effects of a finite sized particle in such solutions, a multipole expansion (Taylor series expansion around the center of the particle) is applied in the Green tensor, leading to the so-called Rotne-Prager tensor [268]. The tensor proposed in Rotne and Prager [268] is used for computing the long-range hydrodynamic interactions between solid spherical particles in a particulate system, given by:

$$\boldsymbol{M}_{ij} = \frac{1}{8\pi\eta}\left[\frac{1}{r}(\boldsymbol{I} + \hat{\boldsymbol{r}}\hat{\boldsymbol{r}}) + \frac{2a^2}{3r^3}(\boldsymbol{I} - 3\hat{\boldsymbol{r}}\hat{\boldsymbol{r}})\right] \tag{2.62}$$

In Equation (2.62), $\boldsymbol{I}$ is the identity tensor, $r = \left[(x_j - x_i)^2 + (y_j - y_i)^2 + (z_j - z_i)^2\right]$ is the relative spacing between particle i whose center is located in the coordinates $\boldsymbol{x}_i = (\boldsymbol{x}_{i,x}, \boldsymbol{x}_{i,y}, \boldsymbol{x}_{i,z})$ and particle j, whose center is located in the coordinates $\boldsymbol{x}_j = (\boldsymbol{x}_{j,x}, \boldsymbol{x}_{j,y}, \boldsymbol{x}_{j,z})$. Also, the unit vector $\hat{\boldsymbol{r}} = \boldsymbol{r}/r$ points out in the centerline direction of two independent suspended particles.

It is important to mention that, due to the far-reaching nature of hydrodynamic interactions, which decay spatially in the form $(1/r)$, the calculation of the sums of these interactions in a direct way, using the Rotne-Prager tensor - Eq. (2.62) -, leads to divergent numerical results for the mean transport properties of the suspension. These divergences are associated with the relatively small sizes of the numerical suspension. This is a classic problem found in the study of particulate systems that take into account long-range interactions, which in turn slowly decay as the separation distance is increased. Therefore, in order to compute the hydrodynamic interactions as accurately

as possible, the so-called Ewald sum technique applied to the Rotne-Prager tensor [266, 268, 269] is used, which takes into account the suspension with periodic boundary conditions, so that it is replicated in all spaces. In a nutshell, in order to reduce the N number of particles necessary for a reliable computation of suspension properties and in order to accelerate the convergence of the sum of the interactions between the particles, a finite number of particles N is used and they are replicated periodically within a finite volume V. This periodic sum, in turn, is efficiently calculated using a well-known technique, proposed by Ewald-Beenakker [266, 269]. In this way, the particles considered are distributed in a periodic system composed of a lattice structure. For the problem under analysis, a central physical cell is considered and another 124 image cells are arranged around the central cell to form the computational network. The surrounding cells (124 in this case) contain replicated images of the particles contained in the central cell. Through this approach, it is possible to accelerate the convergence of the sums of long-range interactions between the particles across the computational network, which, in the case of this particular problem, interact both magnetically and hydrodynamically. In this way, it is possible to carry out dynamic simulations that, besides being accurate, are also computationally efficient. By this approach, the numerical simulations performed do not require the presence of physical walls [28].

In order to better illustrate the concept of the periodic cells, it is presented in Fig. (2.2) a three-dimensional perspective view of an initial arbitrary simulation volume of the suspension under analysis as well as a side view of one of the typical periodic structures.

It is important to note that the central cell is the physical cell that contains the reference particles, the number of which may vary in the simulations. All other cells shown are periodic and exactly identical images of the central physical cell, containing the same number of particles. Thus, to calculate the velocity disturbances induced in each of the i particles within the central reference cell, it is necessary to calculate not only the interactions between these and other particles located in the reference cell, but also the interactions among them with all the particles inserted in the image cells along the entire periodic spatial network. Even though the interactions must be computed between the particles of the central cell with all others of the periodic cells, when using this technique there is no need to calculate the interactions that occur between the particles inserted in the images. For this reason, when considering N particles in the central cell and N_c in the imaging cells, the computational cost will not be $\mathcal{O}[(N \times Nc)^2]$, but $\mathcal{O}[(N \times N \times Nc)]$ [28].

To model the simulation box, the center positions of N particles within a unit cell denoted by the set of vectors $\boldsymbol{C}_N = (\boldsymbol{x}_1, \ldots, \boldsymbol{x}_N)$ are considered [269, 262, 271, 28]. It is assumed

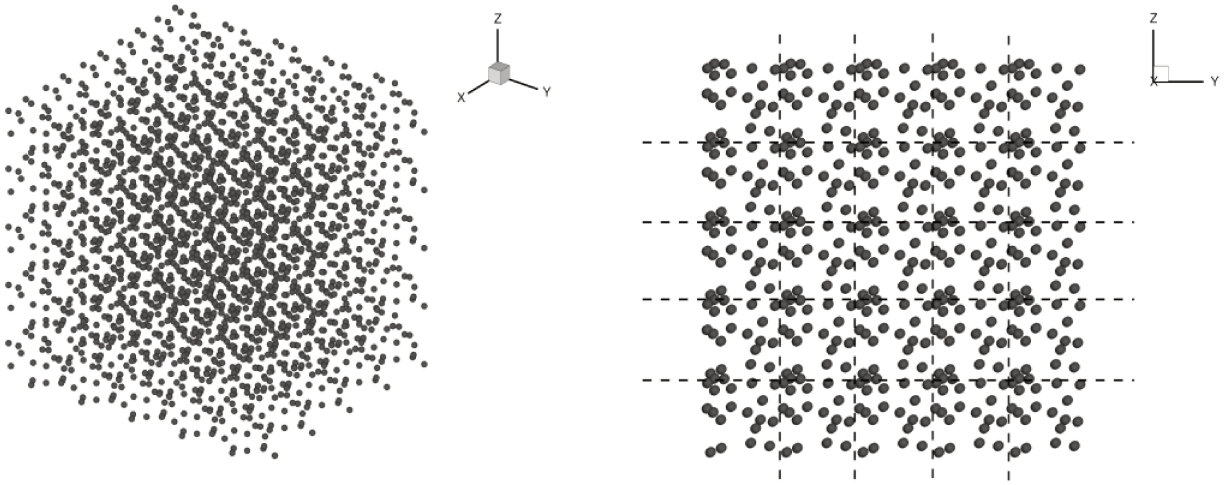

Figure. 2.2: Left: typical representation of a three-dimensional simulation box of a suspension with periodic boundary conditions. Right: side view of one of the typical periodic structures. In this particular image, each cell has 20 particles, of which, considering the total amount of 125 cells (1 physical + 124 periodic), lead to the representation of an infinite suspension with 2500 particles. Images kindly provided by Dr. Rafael Gontijo, from Gontijo [272].

the existence of a periodic lattice $\mathcal{L} = (\boldsymbol{x}_{\gamma 1}, \ldots, \boldsymbol{x}_{\gamma N}) = (\boldsymbol{x}_1 + \boldsymbol{x}_\gamma, \ldots, \boldsymbol{x}_N + \boldsymbol{x}_\gamma)$, where $\boldsymbol{x}_\gamma = (\gamma_1 d, \gamma_2 l, \gamma_3 h)$ and $(\gamma_1, \gamma_2, \gamma_3 = 0, \pm 1, \pm 2, \ldots)$ denotes the lattice points, which are obtained through a linear combination of the base orthogonal vectors $d\boldsymbol{e}_1$, $l\boldsymbol{e}_2$ and $h\boldsymbol{e}_3$. In these relations, d, l and h correspond to the lengths of the edges of each of the cubic lattice cells, also $\gamma = \{\gamma_1, \gamma_2, \gamma_3\}$ denotes the set of integer coefficients named as cell indices and finally, the set of vectors $\{\boldsymbol{e}_1, \boldsymbol{e}_2, \boldsymbol{e}_3\}$ is the canonical base. In this technique, not only lattices $\mathcal{L}$ in the physical space are considered, but also numerical lattices $\hat{\mathcal{L}}$ in the reciprocal (wavenumber) space. In this context, the reciprocal lattice vectors $\boldsymbol{k}_\zeta$ are written in the manner $\boldsymbol{k}_\zeta = 2\pi(\zeta_1/d, \zeta_2/l, \zeta_3/h)$, where the cell index in the reciprocal space $\zeta = \{\zeta_1, \zeta_2, \zeta_3\}$ is denoted as $(\zeta_1, \zeta_2, \zeta_3 = 0, \pm 1, \pm 2, \ldots)$.

That being said, one is able to calculate the time evolution of the velocity of each of the suspended non-massive particles periodically distributed in space and subjected to long-range hydrodynamic and magnetic interactions as:

$$\boldsymbol{u}_i = \boldsymbol{M}_s \cdot \boldsymbol{f}_i + \sum_{j \neq i} \boldsymbol{M}_{ij} \cdot \boldsymbol{f}_j \tag{2.63}$$

In Equation (2.63), $\boldsymbol{M}_s$ stands for the self-mobility matrix (i.e. $\boldsymbol{M}_s \cdot \boldsymbol{f}_i$ represents the velocity self-induced in a particle by its own periodic images) and $\boldsymbol{M}_{ij}$ is the pair mobility matrix, given, respectively by Eqs. (2.64) and (2.65).

$$\boldsymbol{M}_s = \left(\frac{1}{6\pi\eta a} - \frac{1}{\eta}\xi\pi^{-\frac{3}{2}} + \frac{20}{9\eta}\xi^3\pi^{-\frac{3}{2}}a^2 \right)\boldsymbol{I} \tag{2.64}$$

$$\boldsymbol{M}_{ij} = \sum_{x\in\mathcal{L}} \boldsymbol{M}_1(r) + \frac{1}{L^{*3}} \sum_{k\in\hat{\mathcal{L}},k\neq 0} \boldsymbol{M}_2(k)\cos(\boldsymbol{k}\cdot\boldsymbol{r}) \tag{2.65}$$

In the above relation, $\boldsymbol{M}_1(r)$ and $\boldsymbol{M}_2(r)$ are given by:

$$\boldsymbol{M}_1(r) = \mathcal{F}(r)\boldsymbol{I} + \mathcal{G}(r)\hat{\boldsymbol{r}}\hat{\boldsymbol{r}} \tag{2.66}$$

$$\boldsymbol{M}_2(k) = \mathcal{H}(k)(\boldsymbol{I} - \hat{\boldsymbol{k}}\hat{\boldsymbol{k}}) \tag{2.67}$$

In Equations (2.66) and (2.67), one notices the presence of the scalar functions $\mathcal{F}(r)$, $\mathcal{G}(r)$ and $\mathcal{H}(k)$, which are respectively given by the relations:

$$\mathcal{F}(r) = \left(\frac{3}{4r} + \frac{1}{2r^3} \right)\operatorname{erfc}(\xi r) + \left(4\xi^7 r^4 + 3\xi^3 r^2 - 20\xi^5 r^2 - \frac{9}{2}\xi + 14\xi^3 + \frac{\xi}{r^2} \right)\frac{\mathrm{e}^{-\xi^2 r^2}}{\sqrt{\pi}} \tag{2.68}$$

$$\mathcal{G}(r) = \left(\frac{3}{4r} - \frac{3}{2r^3} \right)\operatorname{erfc}(\xi r) - \left(4\xi^7 r^4 + 3\xi^3 r^2 - 16\xi^5 r^2 - \frac{3}{2}\xi + 2\xi^3 + \frac{3\xi}{r^2} \right)\frac{\mathrm{e}^{-\xi^2 r^2}}{\sqrt{\pi}} \tag{2.69}$$

$$\mathcal{H}(k) = \frac{6\pi}{k^2}\left(1 - \frac{k^2}{3}\right)\left(1 + \frac{k^2}{4\xi^2} + \frac{k^4}{8\xi^4}\right)\mathrm{e}^{-\frac{k^2}{4\xi^2}} \tag{2.70}$$

In Equations (2.68), (2.69) and ((2.70)), r represents the distance between the center of two individual distinct particles, $\hat{\boldsymbol{k}} = \boldsymbol{k}/k$ denotes the normalized wavenumber vector (reciprocal space coordinate), $\xi = \pi^{1/2}V^{-1/3}$ is the convergence parameter of the lattice sums proposed in Beenakker [269], where V is the volume of the central lattice and, finally, erfc is the complementary error function, defined as [329]:

$$\mathrm{erfc}(x) = 1 - \mathrm{erf}(x); \qquad \mathrm{erf}(x) = \frac{2}{\sqrt{\pi}}\int_0^x \mathrm{e}^{-t}dt \tag{2.71}$$

If the reader is interested in a more instructive description of the used lattice summation technique, he or she is referred to Cunha et al. [262] and to some extent to Gontijo and Cunha [27, 28].

In the next section, a modeling of the forces to which the magnetic particles are subjected to and that are considered in this work is presented.

2.2.2 Forces modulation

In this section, the modulation of the forces involved in the discrete simulations behind the dynamics of magnetic suspensions is presented.

In the case of non-massive particles (absence of inertial effects), the balance of forces acting on a particle i is given by:

$$\boldsymbol{f}_i = \Delta\rho\boldsymbol{g}\frac{4}{3}\pi a^3 + \boldsymbol{f_B}^i + \boldsymbol{f_m}^i + \boldsymbol{f_r}^i + \boldsymbol{f_c}^i \tag{2.72}$$

In Equation (2.72), $\boldsymbol{g}$ is the gravitational acceleration vector and $\boldsymbol{f_B}, \boldsymbol{f_m}^i, \boldsymbol{f_r}^i$ and $\boldsymbol{f_c}^i$ corre-

spond to the Brownian, magnetic, repulsive and contact forces acting on an arbitrary particle i, respectively. The first term in the right-hand side of Eq. (2.72) denotes the net gravitational force, due to the difference between the particle and the fluid densities ($\Delta\rho$). For a mobility problem, the trajectories of the particles are simply obtained from the integration of kinematic Eq. (2.73).

$$\frac{D\boldsymbol{x}_i}{Dt} = \boldsymbol{u}_i; \qquad \boldsymbol{x}_i(0) = \boldsymbol{x}_0^i \tag{2.73}$$

As an addendum, if one considered massive particles, the formulation would be slightly different than that presented in Eq. (2.72). Under this scenario, it would not be necessary to take into account hydrodynamic interactions, since ferrofluids usually consist of dilute suspensions with volume fraction of particles of approximately $\phi \approx 5\%$ and ϕ is usually treated as the parameter responsible for measuring the influence of hydrodynamic interactions [27]. In addition, when considering particle inertia, the influence of hydrodynamic interactions is smaller than it would be in the approaching limit of non-massive particles [27]. That said, the translational motion of a particle i inside a monodisperse solution of N particles would be given by:

$$m_p \frac{d\boldsymbol{u}^i}{dt} = -6\pi\eta a\boldsymbol{u}^i + \Delta\rho\boldsymbol{g}\frac{4}{3}\pi a^3 + \boldsymbol{f_B}^i + \boldsymbol{f_m}^i + \boldsymbol{f_r} + \boldsymbol{f_c}^i \tag{2.74}$$

The first term on the right-hand side of Eq. (2.74) is defined as the Stokes viscous drag, which is purely produced by the motion of the particles that occurs in low Reynolds number regimes, which would also be the only hydrodynamic force considered. One could also consider other hydrodynamic forces such as virtual mass or Oseen [330] and Basset [331] drags, however, as shown in Sobral et al. [332], in regimes of low Reynolds number combined with non-null Stokes number, the dominant hydrodynamic force on the particles is the Stokes hydrodynamic drag.

Still considering the scenario of massive particles, the rotational motion of the particles would take into account the promotion of particle rotation by torques due to hydrodynamic drag, Brownian and magnetic forces. In particular, the torque generated due to magnetic interactions is due to magnetic dipole-external field interactions and to magnetic dipole-dipoles interactions. This would read:

$$J_p \frac{d\boldsymbol{\omega}^i}{dt} = -8\pi\eta a^3 \boldsymbol{\omega}^i + \boldsymbol{T_B}^i + \boldsymbol{T_m}^i \tag{2.75}$$

In Equation (2.75), J_p is the polar moment of inertia and $\boldsymbol{T_B}^i$ and $\boldsymbol{T_m}^i$ are the non-hydrodynamic torques due to Brownian and magnetic forces, respectively, defined in Eqs. (2.80) and (2.86). The first term on the right-hand side of Eq. (2.75) is the torque produced due to the viscous Stokes drag [27].

Now, each of the forces presented in Eq. (2.72) is modeled.

Brownian interactions

The first force that appears in Eq. (2.72) other than the net thrust is the Brownian force $\boldsymbol{f_B}^i$. The stochastic Brownian force comes from a subroutine of generation of random numbers which have a uniform distribution in the interval $[-1, +1]$. A well-known model [333] of the stochastic Brownian force comes from the solution of the stochastic Langevin's differential equation, assuming that Brownian fluctuations are isotropic, have no memory and by using the dissipation-fluctuation theorem. Under such conditions, a random force $\boldsymbol{f_B}(t)$ is considered to be a stationary white noise with non-correlated random fluctuations on the timescale of the particle's motion. Such condition is expressed as [27]:

$$\langle \boldsymbol{f_B}(t) \rangle = \mathbf{0}; \qquad \langle \boldsymbol{f_B}(t) \boldsymbol{f_B}(t') \rangle = \boldsymbol{F_B} \delta(t - t') \tag{2.76}$$

In Equation (2.76), δ is the Dirac delta distribution and $\boldsymbol{F_B} = 12\pi\eta a \kappa_B T \boldsymbol{\delta}$ relates the intensity of the Brownian force with viscous forces which act in order to dissipate the thermal fluctuations of the suspended particles [333].

After taking the trace of Eq. (2.76), one arrives at the fluctuation and dissipation theorems for force and torque, which reads, respectively:

$$\langle \boldsymbol{f_B}(t) \cdot \boldsymbol{f_B}(t') \rangle = (6\pi\eta a)(6\kappa_B T)\delta(t - t') \tag{2.77}$$

$$\langle \boldsymbol{T_B}(t) \cdot \boldsymbol{T_B}(t') \rangle = (8\pi\eta a^3)(6\kappa_B T)\delta(t - t') \tag{2.78}$$

With the aid of Eqs. (2.77) and (2.78), one is able to model both stochastic Brownian force $\boldsymbol{f_B}$ and stochastic Brownian torque $\boldsymbol{T_B}$, which are respectively given by:

$$\boldsymbol{f_B}^i = 6\pi\eta a \left(\frac{6D_t}{\delta\tau} \right)^{\frac{1}{2}} \boldsymbol{\beta} \tag{2.79}$$

$$\boldsymbol{T_B}^i = 8\pi\eta a^3 \left(\frac{6D_r}{\delta\tau} \right)^{\frac{1}{2}} \boldsymbol{\beta} \tag{2.80}$$

In Eqs. (2.79) and (2.80), D_t and $D_r = \kappa T / 8\pi\eta a^3$ are the translational and rotational Brownian diffusion coefficient of Stokes-Einstein [216], respectively, $\delta\tau$ is a typical time step related to Brownian thermal fluctuations and $\boldsymbol{\beta}$ is a random unitary vector associated with the stochastic Brownian fluctuations, where β_x, β_y and β_z are three different random numbers with uniform probability in $[-1, +1]$ and $\boldsymbol{\beta} = |\boldsymbol{\beta}|^{-1}(\beta_x \hat{\boldsymbol{e}}_x, \beta_y \hat{\boldsymbol{e}}_y, \beta_z \hat{\boldsymbol{e}}_z)$ [27, 28].

Magnetic interactions

When it comes to magnetic interactions, the forces experienced by the particles are closely linked to magnetic interaction potentials. Generally, the mathematical expressions for such forces are calculated through the appliance of gradients to the potentials. The interaction potential between particles depends on how they are arranged in space. Therefore, one must have precise control of mapping the positions and the orientations (since this work deals with magnetic particles which are also subject to rotate) of the particles over time (evolutionary process), which consumes a great deal of computational time. Magnetic interactions between magnetic particles

come from two different sources: 1) magnetic interactions between dipole-dipole moments and 2) magnetic interactions between the particle's dipole moment and the external applied magnetic field. The magnetic particle interaction potentials for the dipole-dipole interactions and external field-dipole interactions are given below, respectively [3, 226]:

$$\psi_{ij} = \sum_{i \neq j} \frac{\mu_0 m_i m_j}{4\pi r^3} [\boldsymbol{d}_i \cdot \boldsymbol{d}_j - 3(\boldsymbol{d}_i \cdot \hat{\boldsymbol{r}}_{ij})(\boldsymbol{d}_j \cdot \hat{\boldsymbol{r}}_{ij})] \tag{2.81}$$

$$\psi_i = -\mu_0 m_i H(\boldsymbol{d}_i \cdot \hat{\boldsymbol{h}}) \tag{2.82}$$

In Equations (2.81) and (2.82), the lower indexes i and j denote particles i and j, respectively, m_i and m_j represent the magnitude of the magnetic dipole moment of particles i and j with directions $\boldsymbol{d}_i$ and $\boldsymbol{d}_j$, respectively. Also, $\hat{\boldsymbol{r}}_{\boldsymbol{ij}}$ is the unitary vector in the direction that links particle i to particle j and H is the intensity of an applied external magnetic field with direction $\hat{\boldsymbol{h}}$. Therefore, the magnetic force acting on each of the suspended particles in given by:

$$\boldsymbol{f_m}^i = -(\nabla \psi_{ij} + \nabla \psi_i) \tag{2.83}$$

Since particles are able to rotate with an angular velocity different than that of the surrounding fluid (particles are not considered torque-free), it is of extreme importance to compute the magnetic torque acting on each of the suspended particles, which is calculated through Eq. (2.84).

$$\boldsymbol{T_m}^i = -\boldsymbol{d}_i \times (\nabla_{\boldsymbol{d}_i} \psi_{ij} + \nabla_{\boldsymbol{d}_i} \psi_i) \tag{2.84}$$

In Equation (2.84), $\nabla_{\boldsymbol{d}_i}$ is a vector operator that accounts for the derivatives with respect to the orientation of the magnetic dipole moments of the i_{th} particle [27, 28]. After carrying out the necessary algebra (presented in detail in Gontijo [272]) to deduce expressions for both the magnetic force and torque from Eqs. (2.83) and (2.84) using Eqs.(2.81) and (2.82), one obtains:

$$\boldsymbol{f_m}^i = \sum_{i \neq j} \frac{3\mu_0 m_i m_j}{4\pi r^4} \Big[(\boldsymbol{d}_i \cdot \boldsymbol{d}_j)\hat{\boldsymbol{r}}_{ij} + (\boldsymbol{d}_i \cdot \hat{\boldsymbol{r}}_{ij})\boldsymbol{d}_j + (\boldsymbol{d}_j \cdot \hat{\boldsymbol{r}}_{ij})\boldsymbol{d}_i - 5(\boldsymbol{d}_i \cdot \hat{\boldsymbol{r}}_{ij})(\boldsymbol{d}_j \cdot \hat{\boldsymbol{r}}_{ij})\hat{\boldsymbol{r}}_{ij} \Big] + \Big[\mu_0 m_i H (\boldsymbol{d}_i \cdot \nabla)\hat{\boldsymbol{h}} \Big] \tag{2.85}$$

$$\boldsymbol{T_m}^i = \sum_{i \neq j} \frac{3\mu_0 m_i m_j}{4\pi r^3} \left[-\frac{1}{3}(\boldsymbol{d}_i \times \boldsymbol{d}_j) + (\boldsymbol{d}_j \cdot \hat{\boldsymbol{r}}_{ij})(\boldsymbol{d}_i \times \hat{\boldsymbol{r}}_{ij}) \right] + \Big[\mu_0 m_i H (\boldsymbol{d}_i \times \hat{\boldsymbol{h}}) \Big] \tag{2.86}$$

Since this work deals with a uniform (homogeneous) applied magnetic field ($\nabla(H\hat{\boldsymbol{h}}) = \boldsymbol{0}$), as indicated in Fig. (1.3), the last term in Eq. (2.85) is null, leading to:

$$\boldsymbol{f_m}^i = \sum_{i \neq j} \frac{3\mu_0 m_i m_j}{4\pi r^4} \Big[(\boldsymbol{d}_i \cdot \boldsymbol{d}_j)\hat{\boldsymbol{r}}_{ij} + (\boldsymbol{d}_i \cdot \hat{\boldsymbol{r}}_{ij})\boldsymbol{d}_j + (\boldsymbol{d}_j \cdot \hat{\boldsymbol{r}}_{ij})\boldsymbol{d}_i - 5(\boldsymbol{d}_i \cdot \hat{\boldsymbol{r}}_{ij})(\boldsymbol{d}_j \cdot \hat{\boldsymbol{r}}_{ij})\hat{\boldsymbol{r}}_{ij} \Big] \tag{2.87}$$

Periodic magnetic interactions

The magnetic interactions in this work can be calculated through the same technique of periodic particle-particle interactions described in Beenakker [269], Cunha et al. [262], Abade and Cunha [271], Gontijo and Cunha [27, 28]. When one applies Ewald's summation technique [266] to Eqs. (2.87) and (2.86), one obtains expressions for the periodic magnetic force and torques acting on a particle i. The expression for the magnetic force reads:

$$\boldsymbol{f_m}^i = \mu_0 m_i m_j \left\{ \sum_{x \in \mathcal{L}} \Big[\boldsymbol{\mathcal{T}_1}(r) + \boldsymbol{\mathcal{T}_2}(r) \Big] + \frac{2\pi}{L^4} \sum_{k \in \hat{\mathcal{L}}, k \neq 0} \boldsymbol{\mathcal{T}_3}(k) \right\} \tag{2.88}$$

In Equation (2.88), L denotes the length of the primary lattice cell. Also, one identifies the presence of vector functions $\boldsymbol{\mathcal{T}_1}(r)$, $\boldsymbol{\mathcal{T}_2}(r)$ and $\boldsymbol{\mathcal{T}_3}(k)$, given, respectively, by:

$$\boldsymbol{\mathcal{T}_1}(r) = \Big[(\boldsymbol{d}_i \cdot \boldsymbol{d}_j)\hat{\boldsymbol{r}}_{ij} + (\boldsymbol{d}_i \cdot \hat{\boldsymbol{r}}_{ij})\boldsymbol{d}_j + (\boldsymbol{d}_j \cdot \hat{\boldsymbol{r}}_{ij})\boldsymbol{d}_i\Big]\mathcal{C}(r) \tag{2.89}$$

$$\boldsymbol{\mathcal{T}_2}(r) = -\Big[(\boldsymbol{d}_i \cdot \hat{\boldsymbol{r}}_{ij})(\boldsymbol{d}_j \cdot \hat{\boldsymbol{r}}_{ij})\hat{\boldsymbol{r}}_{ij}\Big]\mathcal{D}(r) \tag{2.90}$$

$$\boldsymbol{\mathcal{T}_3}(k) = 4\pi\hat{\boldsymbol{k}}(\boldsymbol{d}_i \cdot \hat{\boldsymbol{k}})(\boldsymbol{d}_j \cdot \hat{\boldsymbol{k}})\mathrm{e}^{-\left(\frac{\pi k}{\xi}\right)^2}\sin\Big(2\pi\hat{\boldsymbol{k}} \cdot \hat{\boldsymbol{r}}_{ij}\Big) \tag{2.91}$$

The scalar functions $\mathcal{C}(r)$ and $\mathcal{D}(r)$ that appear in Eqs. (2.89) and (2.90), are given by:

$$\mathcal{C}(r) = \left[3\,\mathrm{erfc}(\xi r) + \left(\frac{2\xi r}{\sqrt{\pi}}\right)(3 + 2\xi^2 r^2)\mathrm{e}^{-\xi^2 r^2}\right] r^{-4} \tag{2.92}$$

$$\mathcal{D}(r) = \left[15\,\mathrm{erfc}(\xi r) + \left(\frac{2\xi r}{\sqrt{\pi}}\right)(15 + 10\xi^2 r^2 + 4\xi^4 r^4)\mathrm{e}^{-\xi^2 r^2}\right] r^{-4} \tag{2.93}$$

In the same manner, the periodic magnetic torque acting on a particle i due to magnetic interactions between the suspended particles dispersed in the lattice system reads:

$$\boldsymbol{T_m}^i = \mu_0 m_i m_j \left[-\sum_{x \in \mathcal{L}} \boldsymbol{\mathcal{T}_4}(r) + \frac{1}{L^3}\sum_{k \in \hat{\mathcal{L}}, k \neq 0} \boldsymbol{\mathcal{T}_5}(k)\right] + \mu_0 m_i H\big(\boldsymbol{d}_i \times \hat{\boldsymbol{h}}\big) \tag{2.94}$$

In the above relation, one identify the presence of vector functions $\boldsymbol{\mathcal{T}_4}(r)$ and $\boldsymbol{\mathcal{T}_5}(k)$, which are respectively denoted as:

$$\boldsymbol{\mathcal{T}_4}(r) = (\boldsymbol{d}_i \times \boldsymbol{d}_j)\mathcal{B}(r) - (\boldsymbol{d}_i \times \hat{\boldsymbol{r}}_{ij})(\boldsymbol{d}_j \cdot \hat{\boldsymbol{r}}_{ij})\mathcal{C}(r) \tag{2.95}$$

$$\boldsymbol{\mathcal{T}_5}(k) = 4\pi(\boldsymbol{d}_i \times \hat{\boldsymbol{k}})(\boldsymbol{d}_j \cdot \hat{\boldsymbol{k}})\mathrm{e}^{-\left(\frac{\pi k}{L\xi}\right)^2}\cos\left(\hat{\boldsymbol{k}} \cdot \hat{\boldsymbol{r}}_{ij}\right) \tag{2.96}$$

Finally, the scalar function $\mathcal{B}(r)$ in Eq. (2.95) is given by:

$$\mathcal{B}(r) = \left[\mathrm{erfc}(\xi r) + \left(\frac{2\xi r}{\sqrt{\pi}}\right)\mathrm{e}^{-\xi^2 r^2}\right] r^{-3} \tag{2.97}$$

Repulsion forces $\boldsymbol{f_r}^i$

It is well known that along numerical simulations, particles may somehow overlap [27, 28]. One way of avoiding such overlaps is to incorporate a pairwise repulsive force acting on near-contact particles [27, 28]. The use of fictitious repulsive forces is much cheaper computationally than the numerical implementation of near-field lubrication forces, since it does not require resistance matrix inversions - Eq. (2.60) - at each time-step (as commonly treated in Stokesian dynamics simulations [334]) nor $\mathcal{O}(N^3)$ calculations [27] and very small time steps [28, 256] to compute the near-field particle interactions. This way, as to emulate a lubrication-like force, as proposed in Cunha [256], this work considers:

$$\boldsymbol{f_r}^i = C_1(6\pi\eta a)u_i\mathrm{e}^{\left(-\frac{\epsilon_{ij}}{C_2}\right)}\hat{\boldsymbol{e}}_{\boldsymbol{r}} \tag{2.98}$$

In Equation (2.98), C_1 and C_2 are calibration constants related to the intensity and range of the repulsive force based on the behavior of two approaching particles [272, 27, 28], u_i represents the velocity of the i_{th} particle, $\epsilon_{ij} = r_{ij} - 2a$ denotes the distance between the surfaces of two near-contact particles i and j and $\hat{\boldsymbol{e}}_{\boldsymbol{r}}$ denotes the unit vector in the repulsion direction and depends only on the configuration of the particles. These quantities are better visualized in Fig. (2.3), which presents a scheme of the near-field particle interaction configurations.

The approach proposed in Cunha [256] has been successfully adopted in Nitsche and Batchelor [335] in investigations of the motion of sedimenting blob of rigid particles at low Reynolds number, also in Gontijo and Cunha [27, 28] for simulating colloidal suspensions of magnetically

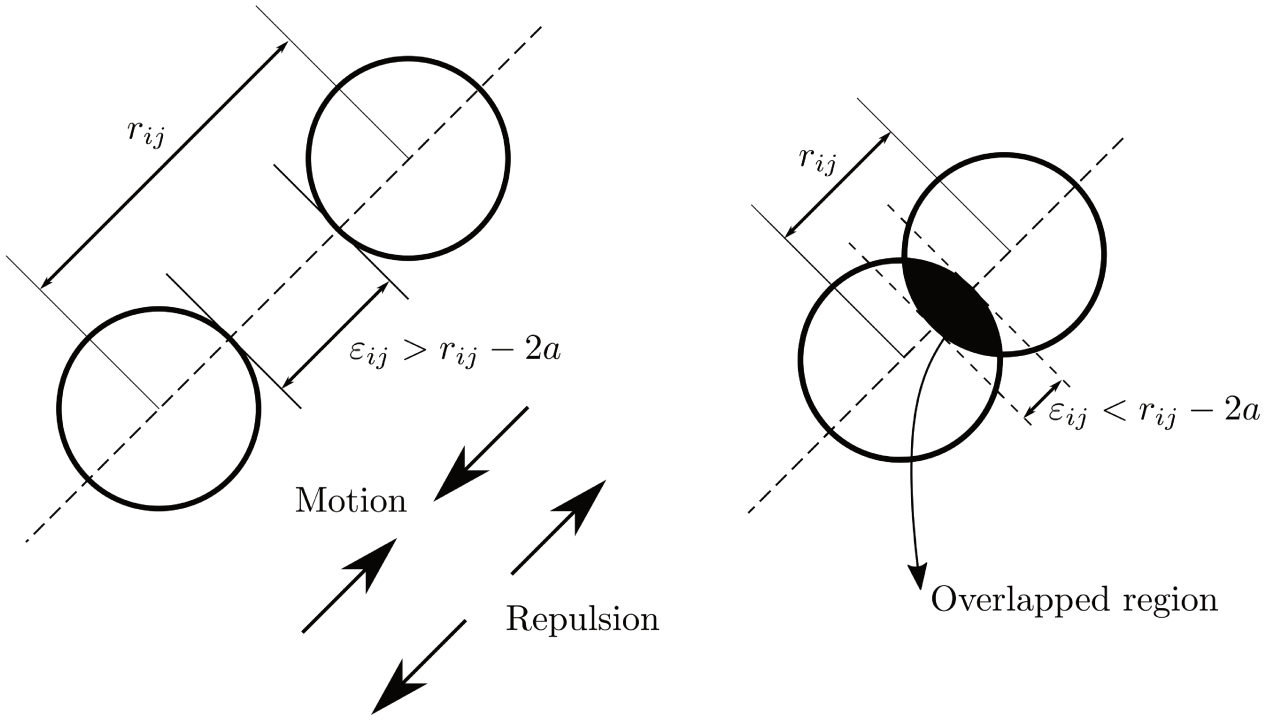

Figure. 2.3: Schematic of the near-field interactions. Left: Repulsive configuration. Right: Hertz contact configuration. Image adapted from Gontijo and Cunha [28].

interacting particles. A similar repulsive force to this one, known as the screened-Coulomb type, was used in Berkov et al. [252].

Contact forces $\boldsymbol{f_c}^i$

In magnetic suspension simulations, along the numerical time evolution, magnetic attractive forces may become very strong depending on many factors as the dipole's coupling parameter λ, and, in some cases, the repulsive force $\boldsymbol{f_r}^i$ of Eq. (2.98) may not be strong enough to avoid particle's collisions or overlaps [27, 28]. This problem is also observed when particles are considered to be massive. Under this scenario, due to the particle inertia, an intrinsic particle relaxation time associated with the moment a particle receives the influence of a force and the moment it responds to it is present. So, in order to avoid such problem, a nonlinear contact force is proposed and modeled using a Hertz tension that depends on the mechanical properties of the surfaces in contact and the materials which the particles are made of [27, 28]. Thus, this is a pseudophysical methodology used in order to avoid particle's overlap.

$$\boldsymbol{f_c}^i = C_3 E_c b^{1/2} \epsilon_{ij}^{3/2} \hat{\boldsymbol{e}}_{\boldsymbol{r}} \tag{2.99}$$

In Equation (2.99), C_3 is a calibration constant of the model, E_c is a material constant that depends on the particles elastic modulus (E represent the Young modulus and ν denotes the Poisson coefficient). For a monodisperse solution, $b = a/2$, however, E_c and b changes for polydisperse suspensions [27].

$$E_c = \frac{E}{2(1-\nu)} \tag{2.100}$$

This effect is better visualized in Fig. (2.3).

Non-dimensional equations

The governing equations of the discrete approach have been made non-dimensional with the use of some reference scales, shown in Eq. (2.101):

$$\tilde{\boldsymbol{u}} = \frac{\boldsymbol{u}}{U_s}; \qquad \tilde{t} = \frac{tU_s}{a}; \qquad \tilde{\boldsymbol{\omega}} = \frac{\boldsymbol{\omega} a}{U_s}; \qquad \tilde{r} = \frac{r}{a} \tag{2.101}$$

In order to make the presentation as clear as possible, the tildes $\sim$ are removed from the non-dimensional variables and the resulting equations are presented below. For the forces which compose the vector $\boldsymbol{f}_i$ in Eq. (2.72), it reads:

$$\boldsymbol{f_g}^i = -\hat{\boldsymbol{e}}_z \tag{2.102}$$

$$\boldsymbol{f_B}^i = \left(\frac{6}{Pe\delta\tau} \right)^{\frac{1}{2}} \boldsymbol{\beta} \tag{2.103}$$

$$\boldsymbol{f_r}^i = C_1 u_i e^{\left(-\frac{\epsilon_{ij}}{C_2}\right)} \hat{\boldsymbol{e}}_{\boldsymbol{r}} \tag{2.104}$$

$$\boldsymbol{f_c}^i = P_c \epsilon_{ij}^{3/2} \hat{\boldsymbol{e}}_{\boldsymbol{r}} \tag{2.105}$$

In Equation (2.105), P_c is a contact parameter related to the elastic properties of the particle material defined in Eq. (2.111). In all simulations, P_c was set to $P_c = 100$.

The magnetic force acting on a particle i takes the following non-dimensional form:

$$\boldsymbol{f_m}^i = \frac{24\pi\lambda}{Pe} \left\{ \sum_{x \in \mathcal{L}} \left[\boldsymbol{\mathcal{T}_1}(r) + \boldsymbol{\mathcal{T}_2}(r) \right] + \frac{2\pi}{L^4} \sum_{k \in \hat{\mathcal{L}}, k \neq 0} \boldsymbol{\mathcal{T}_3}(k) \right\} \tag{2.106}$$

Since the magnetic interactions for the force have a faster decay like $(1/r^4)$, as seen in Eq. (2.87), the sums of magnetic interactions via induced forces may not be calculated by lattice sums [27]. On the other hand, due to the slower decay of the magnetic torques $(1/r^3)$, as seen in Eq. (2.86), torque interactions must be carried out in a periodic way, as indicated in McWhirter and Patey [278], Wang et al. [279], Berkov and Gorn [280], Usov and Grebenshchikov [281], Gontijo and Cunha [27, 28], otherwise the summations may lead to divergent suspension transport properties that depend strictly on rotational dynamics, as the fluid's magnetization. That being said, if one desires to calculate the magnetic force in a non-periodic manner, making use of a hybrid method, as clearly explained in Gontijo and Cunha [27], this force will take the non-dimensional form:

$$\boldsymbol{f_m}^i = \frac{24\lambda}{Pe} \sum_{i \neq j} \frac{1}{r_{ij}^4} \left[\left(\boldsymbol{d}_i \cdot \boldsymbol{d}_j\right) \hat{\boldsymbol{r}}_{ij} + \left(\boldsymbol{d}_i \cdot \hat{\boldsymbol{r}}_{ij}\right) \boldsymbol{d}_j + \left(\boldsymbol{d}_j \cdot \hat{\boldsymbol{r}}_{ij}\right) \boldsymbol{d}_i - 5 \left(\boldsymbol{d}_i \cdot \hat{\boldsymbol{r}}_{ij}\right) \left(\boldsymbol{d}_j \cdot \hat{\boldsymbol{r}}_{ij}\right) \hat{\boldsymbol{r}}_{ij} \right] + \frac{\alpha}{Pe} \left(\boldsymbol{d}_i \cdot \nabla\right) \hat{\boldsymbol{h}} \tag{2.107}$$

The relations presented above accounted for the translational motion of a particle i. As for the rotational motion of a particle i, one obtains:

$$\boldsymbol{\omega}_i = \boldsymbol{T_m}^i + \boldsymbol{T_B}^i \tag{2.108}$$

In Equation (2.108), $\boldsymbol{T_m}^i$ and $\boldsymbol{T_B}^i$ denote the magnetic and Brownian torques acting on particle i, respectively. The non-dimensional form of such torques are given by:

$$\boldsymbol{T_m}^i = \frac{24\pi\lambda}{Pe}\left[-\sum_{x\in\mathcal{L}} \boldsymbol{\mathcal{T}_4}(r) + \frac{1}{L^{*3}} \sum_{k\in\hat{\mathcal{L}},k\neq 0} \boldsymbol{\mathcal{T}_5}(k)\right] + \frac{3\alpha}{4Pe}(\boldsymbol{d}_i \times \hat{\boldsymbol{h}}) \tag{2.109}$$

$$\boldsymbol{T_B}^i = \left(\frac{6}{Pe_r\delta\tau}\right)^{\frac{1}{2}} \boldsymbol{\beta} \tag{2.110}$$

In Equations (2.106), (2.107), (2.109) and (2.110), one notices the presence of the non-dimensional physical parameters Pe, Pe_r, λ and α. The Péclet number Pe, the non-dimensional field α and the dipole's coupling parameter λ have already appeared in the formulation of the continuous part, but are again depicted in Eq. (2.111). The new parameter Pe_r corresponds to the rotational Péclet number, also defined in Eq. (2.111).

$$Pe = \frac{U_s a}{D}; \qquad Pe_r = \frac{U_s}{D_r a}; \qquad \lambda = \frac{\mu_0 m^2}{4\pi\kappa_B T(2a)^3}; \qquad \alpha = \frac{\mu_0 m H}{\kappa_B T}; \qquad P_c = \frac{C\epsilon a^2}{6\pi\eta a U_s} \tag{2.111}$$

As an addendum, in the case of massive particles, the non-dimensional equations, which come from Eqs. (2.74) and (2.75) would read, for the translational and rotational motion, respectively:

$$St\frac{d\boldsymbol{u}^i}{dt} = -\boldsymbol{u}^i + \hat{\boldsymbol{g}} + \boldsymbol{f_B}^i + \boldsymbol{F_m}^i + \boldsymbol{f_r}^i + \boldsymbol{f_c}^i \tag{2.112}$$

$$St_r \frac{d\boldsymbol{\omega}^i}{dt} = -\boldsymbol{\omega}^i + \boldsymbol{T_B}^i + \boldsymbol{T_m}^i \tag{2.113}$$

In Equation (2.113), St_r is the rotational Stokes number, defined as $St_r = J_p U_s/(8\pi\eta a^4)$.

The interested reader in this discrete formulation, is referred to Gontijo and Cunha [27] for a more complete mathematical modulation of this problem in the case of massive particles in the absence of hydrodynamic interactions and to Gontijo and Cunha [28] for the case of non-massive particles subjected to hydrodynamic interactions.

3 Numerical solutions and code validation approaches

3.1 Continuous approach

The classical vorticity-streamfunction ($\xi - \psi$) formulation [317, 318], which leads to the solution of the two-dimensional vorticity equation - Eq. (2.48) -, the Poisson equation for the streamfunctions - Eq. (2.45) - and one of the magnetization equations - Eqs. (2.49), (2.50) or (2.51) - was used in this work. The velocity field is then recovered with the aid of the relations in Eq. (2.44).

Three distinct non-commercial Fortran based numerical routines were developed, which incorporates each of the magnetization models. These codes were fully programmed by the author and account for the results which will be shown in section 4.1. The post-processing of the obtained data was performed with *Tecplot 360*, allowing the presentation in graphical form of the obtained results.

The governing equations were discretized using a finite-difference method and solved in a coupled manner through a first-order, explicit forward-time central-space scheme (FTCS), which is based on central differences in space and the classical forward in time Euler method [318]. The discretized equations can be found in Appendix A. The oscillations associated with the FTCS method were treated by applying a first-order upwind difference to model the convective terms in the governing equations [318].

3.1.1 Computational domain

A uniform grid with distinct dimensionless steps in vertical and horizontal directions was used to model the channel, whose dimensions were obtained by means of a simple grid analysis in plane Poiseuille flow. In the vertical direction, they were made sufficiently small to be able to capture the high gradients close to the walls. The procedure consisted in taking a determined number of grid points that after being changed would not be able to perturb the final solution anymore, as if it had reached a saturation value or oscillated through a particular value after a fixed number of grid points. Figure (3.1a) displays the obtained results for the maximum velocity in Poiseuille plane flow.

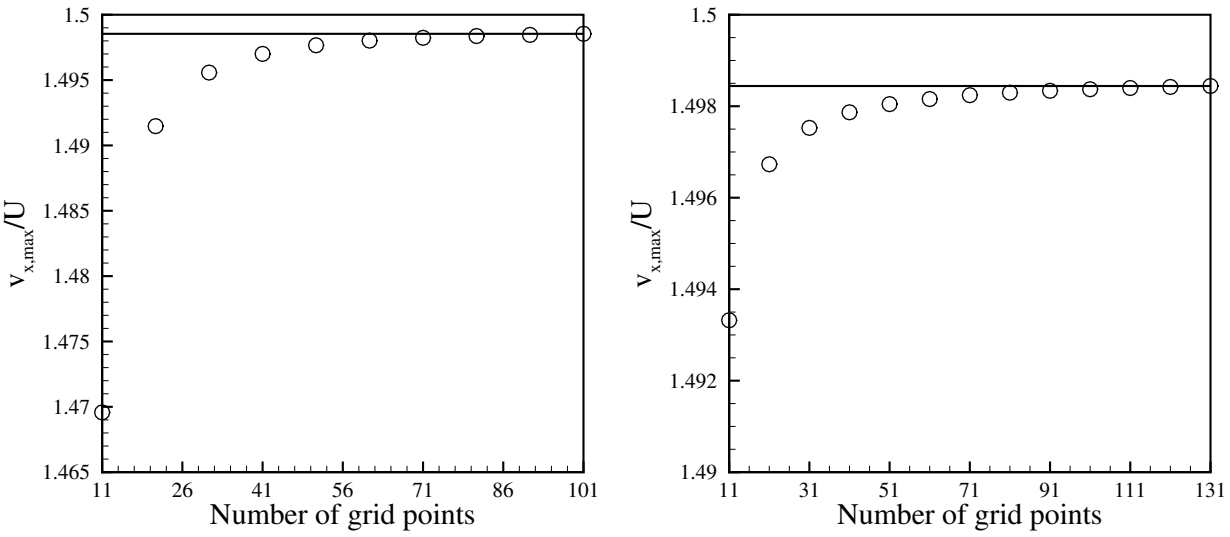

Figure. 3.1: Number of grid points as a function of the maximum streamwise velocity. (a) Vertical direction with $n_x = 101$. (b) Horizontal direction with $n_y = 81$. In both figures $Re = 5000$.

From Fig. (3.1a) it is clear that after a determined number of grid points, the obtained solution is not altered anymore. In this case, the saturation velocity was $v_x/U = 1.4985$, which corresponds to 99.9% of the analytical Poiseuille non-dimensional velocity $v_x/U = 1.5$. However, $n_y = 81$ grid points were employed in the vertical direction, where the maximum velocity reached $v_x/U = 1.4984$, which corresponds to 99.89% of the analytical Poiseuille velocity. This choice was based on the significant smaller time the grid with $n_y = 81$ took for the numerical simulation to take place compared to that with $n_y = 101$, bearing almost exactly the same result in both cases. A similar procedure was done in the horizontal direction, aiming to determine the length of the channel necessary to obtain a fully developed flow under the studied Reynolds number condition. By doing this, the dimensionless horizontal step was fixed and the number of grid points was varied. These results are presented in Fig. (3.1b).

After completing this process, $n_x = 101$ grid points were used in the horizontal direction. In this case, the saturation velocity was $v_x/U = 1.4984$, which corresponds to 99.89% of the analytical Poiseuille non-dimensional velocity $v_x/U = 1.5$. It is important to mention that this number of grids points was used when analyzing the fully developed flow. For the analysis of the flow's entrance region, a more refined grid was employed. In this case, the chosen number of grid points was: $n_x = 801$ and $n_y = 81$.

Additional tests were carried out for the strictly magnetic case. In this scenario, the value of magnetization on the wall was the variable chosen to verify the existence of variations under changes in the number of grid points. Similar to that performed in the non-magnetic case, when the wall magnetization reached a saturation value for a certain number of grid points, these were then chosen to define the mesh. Therefore, in both cases, the number of grid points chosen was sufficient to guarantee no variations in the test variables (velocity in the center and wall magnetization).

3.1.2 Boundary conditions

In this section we present the boundary conditions used in order to numerically solve the discretized equations presented in Appendix A.

The solution of Eqs. (A.4), (A.5), (A.6), (A.7), (A.8), (A.9), (A.10), (A.11) and (A.12) requires that appropriate vorticity, streamfunction, magnetization and velocity boundary conditions are specified at the boundaries of the problem. The specification of the boundary conditions is extremely important, as it directly affects the stability and precision of the solution [336].

Regarding hydrodynamics, in order to properly compute the velocity field of a ferrofluid flowing under the presence of an applied magnetic field, the applied magnetic field $\boldsymbol{H}$ and the magnetization field $\boldsymbol{M}$ must be known. While the applied field can be obtained from the solution of a Laplace equation through spherical harmonics (for the free space) [41], and then jumped to the medium using properly boundary conditions arriving from Gauss and Ampère's laws of magnetism [3], a physical consistent computation of the magnetization field demands deeper thoughts and discussions [26, 42, 40, 43, 24], since in non-equilibrium regimes the magnetization field $\boldsymbol{M}$ is no longer an exclusive function of the field $\boldsymbol{H}$ [44]. The magnetic boundary conditions between two distinct media state that, in two-dimensional conditions, the horizontal components of the applied magnetic field $\boldsymbol{H}$ and the normal components of the magnetic induction field $\boldsymbol{B}$ are conserved, in a way that, between medias 1 and 2, $H_{2t} = H_{1t}$ and $B_{1n} = B_{2n}$. The demonstration of these boundary conditions are presented in Appendix B.

For the hydrodynamic problem, many different sets of boundary conditions have already been employed [319, 298, 320, 321, 322, 323, 324, 325, 326]. However, in this work, a model for

the simulation of ferrofluid flows is proposed, which leads to assumptions in boundary conditions, especially with regard to magnetization.

For the translational velocity, Lamb [337] suggests that:

$$\boldsymbol{v} - \boldsymbol{v_s} = \frac{1}{\beta}[\boldsymbol{n} \times (\boldsymbol{n} \cdot \boldsymbol{T} \times \boldsymbol{n})] \tag{3.1}$$

In Equation (3.1), β is a friction coefficient, $\boldsymbol{v_s}$ is the surface velocity, $\boldsymbol{n}$ is the unit vector outward to the surface and $\boldsymbol{T}$ is the Cauchy stress tensor. However, β is inversely proportional to the particles' radius r [320], which makes it extremely large, since $r \sim 10^{-9} \rightarrow \beta \sim 10^{9}$, in a way that the slip effects can be considered negligible in macroscopic ferrofluid flows [63]. Then, for the translational velocity, one gets:

$$\boldsymbol{n} \cdot (\boldsymbol{v_2} - \boldsymbol{v_2}) = 0; \qquad \boldsymbol{n} \times (\boldsymbol{v_2} - \boldsymbol{v_2}) = \boldsymbol{0}; \tag{3.2}$$

That said, the boundary conditions used to solve the problem's ferrohydrodynamic governing equations were:

1. Solid walls

   The classical no-slip condition of ordinary fluids on the walls was conventionally used, which leads to null velocities at solid boundaries. The no slip condition has an uncertain status in the present context of magnetic fluids [3], however, it was retained since its use has proven to produce physically consistent results, even though there is no assertive that this simple condition is physically sound in all instances [3]. Solid boundaries and symmetry planes are surfaces of constant streamfunction [336]. As the flow is parallel to the duct walls, they were treated as streamlines with a constant streamfunction value. The difference between two streamlines corresponds to the volume flow rate per unit depth normal to the paper [336] between them, so the values of the streamfunctions have been set to maintain a difference equal to the flow rate $\dot{Q}$. By expanding the streamfunction ψ at the wall point using a Taylor series, it is possible to obtain boundary conditions for the vorticity [317, 318, 336]. A first-order approximation was used, as it often provides better results than higher-order expres-

Table. 3.1: Problem's boundary conditions.

Variable	Lower wall	Upper wall	Entrance	Exit
ξ	$\xi_{(i,1)} = \frac{2}{\Delta y^2}\left[\psi_{(i,1)} - \psi_{(i,2)}\right]$	$\xi_{(i,ny)} = \frac{2}{\Delta y^2}\left[\psi_{(i,ny)} - \psi_{(i,ny-1)}\right]$	0	$\frac{\partial \xi}{\partial x} = 0$
ψ	$\psi_{(i,1)} = 0$	$\psi_{(i,ny)} = \dot{Q}$	$\psi_{(1,j)} = \int v_{x(1,j)} dy$	$\frac{\partial \psi}{\partial x} = 0$
M_x	$M_{x(i,1)} = 2M_{x(i,2)} - M_{x(i,3)}$	$M_{x(i,ny)} = 2M_{x(i,ny-1)} - M_{x(i,ny-2)}$	0	$\frac{\partial M_x}{\partial x} = 0$
M_y	$M_{y(i,1)} = 2M_{y(i,2)} - M_{y(i,3)}$	$M_{y(i,ny)} = 2M_{y(i,ny-1)} - M_{y(i,ny-2)}$	0	$\frac{\partial M_y}{\partial x} = 0$

sions, susceptible to instabilities in higher Reynolds numbers [318]. To avoid an imprudent assumption about the boundary conditions of the magnetization, a simple approximation of the values on the walls was used using a Taylor series expansion. In this case, the magnetization profile smoothly approaches the wall, with no clear discontinuities between the value calculated at the first point of the grid above the wall and the value imposed on the wall. A similar approach was used in Schumacher et al. [18] for calculations of the spin boundary conditions when it comes to the smoothness of the profiles. The approach used in this work is different than that used in Papadopoulos et al. [58], where the magnetization at the boundaries was obtained from the numerical solution of the magnetization equation after neglecting the term of magnetic inertia $(\boldsymbol{v} \cdot \nabla \boldsymbol{M})$.

2. Inlet boundary conditions:

   The flow that enters the duct is uniform and demagnetized, causing both magnetization components to be null and the irrotationality of the flow. As for the streamfunctions, the boundary values are obtained from a simple numerical integration of the first relation in Eq. (2.44).

3. Outlet boundary conditions:

   Sufficiently away from the entrance, the solution of the governing equations must approach a fully developed flow between parallel plates, so that the derivatives of the quantities in relation to the horizontal direction x, with the exception of pressure, are all null.

The boundary conditions used to solve the governing equations are best seen in Tab. (3.1).

3.1.3 Stability and stop criteria

The dimensionless time step Δt used in the simulations was based on the well-known condition of stability for the (FTCS) method in the non-magnetic case multiplied by an arbitrary constant C. In Equation (3.3), min represents the minimum value.

$$C\left[\frac{\Delta t}{Re \times min(\Delta x,\Delta y)^2}\right] \leq \frac{1}{2} \tag{3.3}$$

As for stopping criteria, a process similar to that presented in Erturk [338] was adopted. During the calculations, the residual parameter RES was used as a measure of the solution's convergence to steady state. This residue is defined as the maximum absolute difference between two iteration steps in the streamfunction, vorticity and magnetization, which is an indication if the solution has converged to a steady state.

$$\begin{aligned} RES_{\psi} &= max\Big(|\psi^{n+1} - \psi^{n}|\Big); \\ RES_{\xi} &= max\Big(|\xi^{n+1} - \xi^{n}|\Big); \\ RES_{M_x} &= max\Big(|M_x^{n+1} - M_x^{n}|\Big); \\ RES_{M_y} &= max\Big(|M_y^{n+1} - M_y^{n}|\Big); \end{aligned} \tag{3.4}$$

In Equation (3.4), max represents the maximum value. In the calculations, convergence was achieved when RES_{ψ}, RES_{M_x}, $RES_{M_y} \leq 10^{-6}$ and $RES_{\xi} \leq \Delta t \times 10^{-6}$. These low values were chosen to guarantee the accuracy of the obtained solution. At these convergence levels, RES_{ξ} was always in the order of $RES_{\xi} \sim 10^{-9}$.

A schematic algorithm of the numerical routine developed by the authors is presented below:

1. Input computational domain;

2. Input Re, Pe, α, ϕ, λ and tol = 10^{-6};
3. Input initial conditions for $\boldsymbol{v}$, $\boldsymbol{H}$, ξ, ψ, $\boldsymbol{M}$, $\boldsymbol{H_e}$ and p;
4. Calculate Δt and $\boldsymbol{M_0}$;
5. Solve Poisson streamfunction equation - Eq. (A.4) -;
6. Boundary conditions for ψ;
7. Compute velocity field $\boldsymbol{v}$ - Eq. (A.12) -;
8. Boundary conditions for ξ;
9. Solve vorticity transport equation - Eq. (A.5) -;
10. Solve magnetization equations - Eqs. (A.6) and (A.7); or (A.8) and (A.9); or (A.10) and (A.11) -;
11. Boundary conditions for M_x and M_y;
12. Calculate residue RES between time steps;
13. If RES$_\xi \leq \Delta$t $\times$ tol $\rightarrow$ END (go to step [16])
14. Actualize properties values from new time step
15. Get back to item [5]
16. Generate data files.

3.1.4 Numerical code validation

Three different approaches were used to validate the numerical codes: one at the limit of non-magnetic fluid flow and two in the context of magnetic fluid flow. For the case of non-magnetic fluid flow, the simulated conditions were simply adjusted to consider the absence of a magnetic field (i.e. $\alpha = 1.0 \times 10^{-7}$), which led to completely non-magnetic conditions. Under this condition, the analytical velocity profile predicted by simple hydrodynamic plane Poiseuille flow [301] was completely recovered in the simulations. As for the magnetic approaches, an asymptotic solution for the velocity profile was developed using a regular perturbation method - see Appendix C -, in addition to comparing the calculated rotational viscosity with that given by the analytical expressions presented in section 2.1.5.

Non-magnetic Poiseuille flow

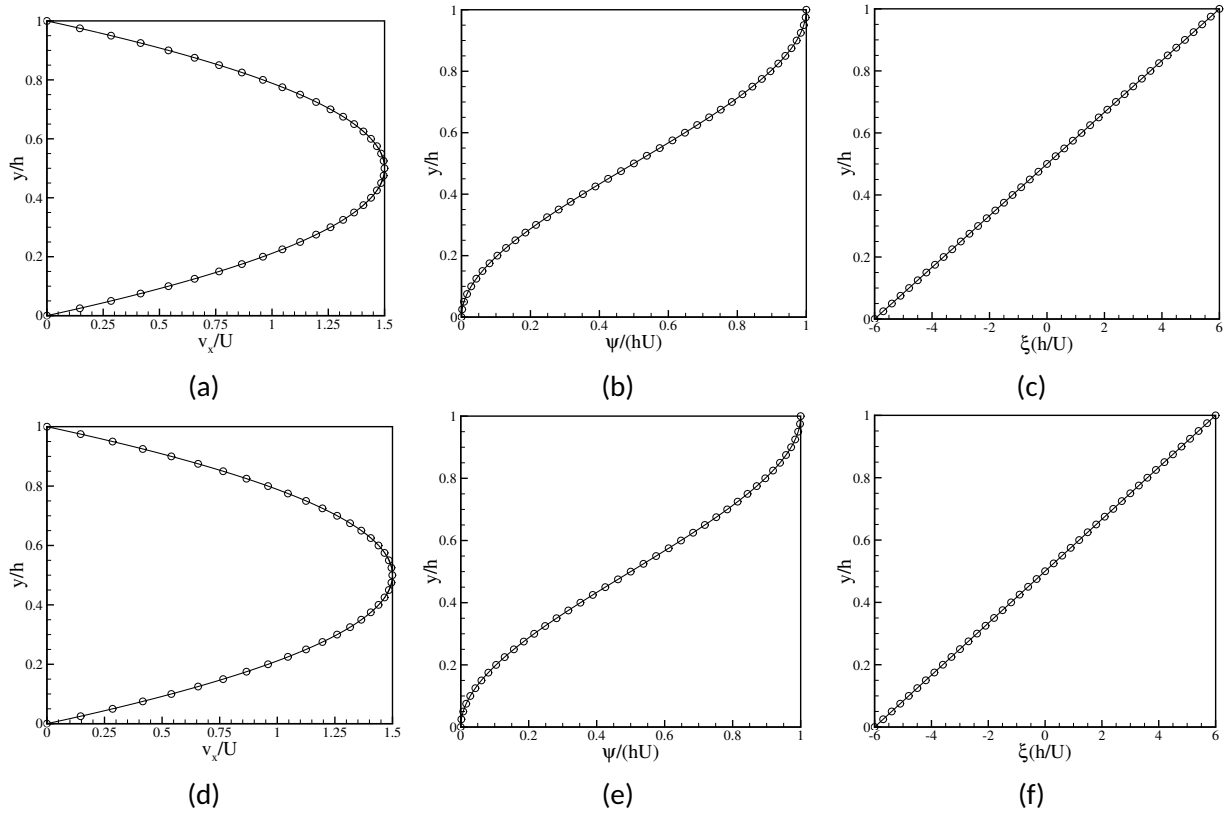

Figure. 3.2: (a) and (c) Horizontal velocity; (b) and (d) stream-function and (c) and (f) vorticity profiles obtained for the fully developed flow in non-magnetic conditions. ○ and — represent the numerical and Poiseuille analytical results - Eqs. (3.5), (3.6) and (3.7) -, respectively. For (a), (b) and (c): $Re = 50$. For (d), (e) and (f): $Re = 5000$.

.

The first approach used to validate the numerical routines was to compare the numerical results obtained for the velocity, streamfunction and vorticity profiles for the flow fully developed at the limit of the non-magnetic Poiseuille flow with the analytical equations for such quantities known in the literature [301], in two distinct conditions of Reynolds number. The velocity profile for the fully developed Poiseuille flow is easily obtained through the Navier-Stokes equations after some simplifications and application of boundary conditions on the walls. The equations for the streamfunction and vorticity profiles are easily obtained by integrating and differentiating the velocity equation with respect to y, respectively, which leads to the following non-dimensional equations:

$$v_x(y) = 6\dot{Q}(y - y^2) \tag{3.5}$$

$$\psi(y) = \dot{Q}(3y^2 - 2y^3) \tag{3.6}$$

$$\xi(y) = 6\dot{Q}(2y - 1) \tag{3.7}$$

In the above relations, $\dot{Q}$ stands for the non-dimensional flow rate.

To simulate the limit of non-magnetic Poiseuille flow in the numerical routines, a magnetic fluid was simulated in the absence of a magnetic field ($\alpha = 1.0 \times 10^{-7}$) , which led to completely non-magnetic conditions. The results obtained are shown in graphical form in Fig. (3.2).

From Figure (3.2), it is clear that the obtained numerical results are in excellent agreement with the analytical results proposed in Eqs. (3.5), (3.6) and (3.7) for both Reynolds number conditions simulated: $Re = 50$ and $Re = 5000$.

Asymptotic solution

An asymptotic solution for the fluid velocity was derived to be used as a means to validate the numerical code. This solution takes into account the coupling between magnetization and hydrodynamics, however, it is assumed that the fluid is symmetrical, which leads to the nullity of the magnetic torque, since the vectors $\boldsymbol{H}$ and $\boldsymbol{M}$ are collinear in such a physical scenario. The magnetization model used for its development was that presented in Eq. (2.27) proposed in Shliomis [26]. In addition, the variations produced in magnetization M due to its advective transport were considered much smaller than those produced by the flow's vorticity. Such simplifications lead to a system of linear differential equations which are solved asymptotically to obtain a solution for the flow's velocity in the fully developed region. This solution was developed taking inspiration from the pioneer work of Rosa et al. [339], where the authors presented an asymptotic solution for a magnetic fluid laminar pipe flow undergoing pressure and magnetic field gradients. In the present

context, a ferrofluid laminar flow is held between two horizontal flat plates with unitary spacing $h = 2a$ and aspect ratio $L/h = 100$. The flow is subjected to a stationary magnetic field gradient with linear decay applied in the horizontal direction as well as a pressure gradient. The complete mathematical development of the asymptotic solution is presented in Appendix C and the final solution is given by Eq. (3.8).

$$v_x(y) = \frac{\gamma}{2}\left(y - y^2\right) + \epsilon\frac{\gamma^2}{24}\left(2y^4 - 4y^3 + 3y^2 - y\right) + \epsilon^2\frac{\gamma^3}{6}\left(\frac{-2}{15}y^6 + \frac{2}{5}y^5 - \frac{1}{2}y^4 + \frac{1}{3}y^3 - \frac{1}{8}y^2 + \frac{1}{40}y\right) \quad (3.8)$$

In Equation (3.8), the perturbation parameter ϵ is defined as:

$$\epsilon = \frac{Pe^2 Re M_{0x}\frac{dH}{dx}}{8Re_m} \quad (3.9)$$

One identifies in Eq. (3.9) the presence of the Péclet number Pe, the Reynolds number Re, the magnetic Reynolds number Re_m, the horizontal component of the equilibrium magnetization M_{0x} and the magnetic field gradient $\frac{dH}{dx}$, all of which are thoroughly defined in Appendix C.

For the validation of the numerical code, the velocity obtained in the center of the duct for the fully developed flow in the context of a magnetic fluid was compared with that proposed by Eq. (3.8). The obtained results are presented in Fig. (3.3) and Tab. (3.2).

For a given ϵ, a magnetic Reynolds number Re_m was defined through relations (C.20) and the simulations were carried out.

Two different sets of asymptotic results are presented in Fig. (3.3). One is associated with a first-order correction in ϵ and the other with a second-order correction in ϵ. One is associated with a first order correction in ϵ and the other with a second order correction. One notices the non-linearity of the first order solution, which happens due to the correction performed in the solution due to the γ parameter - Eq. (C.20) -, which is associated with the pressure gradient. As expected, the second order solution presents better results when compared to the first order. The numerical results agreed very well up to $\epsilon \approx 0.05$ with the first-order solution and up to $\epsilon \approx 0.35$

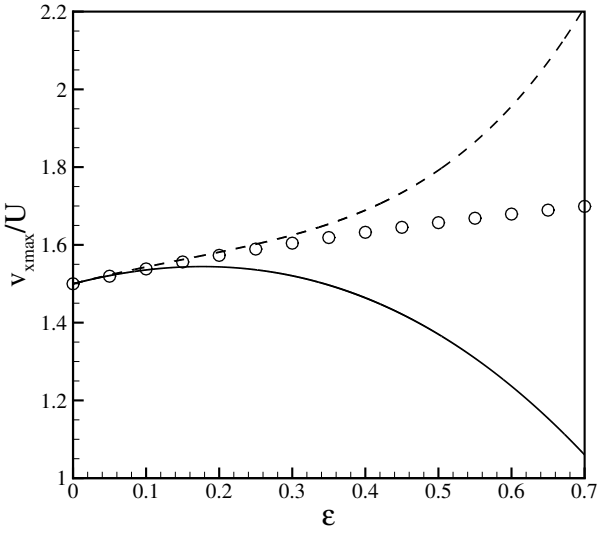

Figure. 3.3: Velocity at $y/h = 0$ as a function of ϵ. ○ accounts for the numerical and —— , - - - for the $\mathcal{O}(1)$ and $\mathcal{O}(2)$ analytical solutions, respectively. Here: $Re = 50$, $Pe = 0.9$, $\alpha = 10$ and $\phi = 0.03$.

Table. 3.2: Associated percentage errors between numerical and analytical solutions.

ϵ	1^{st} order	2^{nd} order
1.0E-06	0.00%	0.00%
1.0E-05	0.00%	0.00%
1.0E-04	0.00%	0.00%
1.0E-03	0.01%	0.01%
1.0E-02	0.56%	0.06%
1.0E-01	5.25%	0.32%
0.2	9.95%	0.52%
0.3	14.21%	1.27%
0.4	18.13%	3.36%
0.5	21.73%	7.52%
0.6	25.05%	14.17%
0.7	28.13%	23.16%

with the second-order solution. Overall, the numerical results were in excellent agreement with the analytical solution for $\epsilon \ll 1$. As the analytical solution was developed under such conditions, the numerical results are then validated.

Rotational viscosity

Another approach used to validate the numerical schemes was to compare the obtained numerical rotational viscosity, calculated through - Eq. (2.38) -, with the analytical relations presented in section 2.1.5 - Eqs. (2.39), (2.40) and (2.41) -. For that, thirty different simulations were carried out for thirty different dimensionless fields α, for each of the three numerical codes. Six local vorticity values were extracted from a fully developed vorticity profile, and, at points analogous to those in which the vorticity values were extracted, local magnetization values in the horizontal direction were also collected. With these values, it is possible to calculate the rotational viscosity using Eq. (2.38). It is important to keep in mind that the calculations refer to non-dimensional rotational viscosity, therefore $\Omega\tau = \frac{1}{2}\xi Pe$. The six points selected to calculate the rotational viscosity represent one point on the duct's wall - $\Omega\tau = 3$ -, one in the center of the duct - $\Omega\tau = 0.0001$ -, and the four others are linearly distributed between the aforementioned two. These points are associated

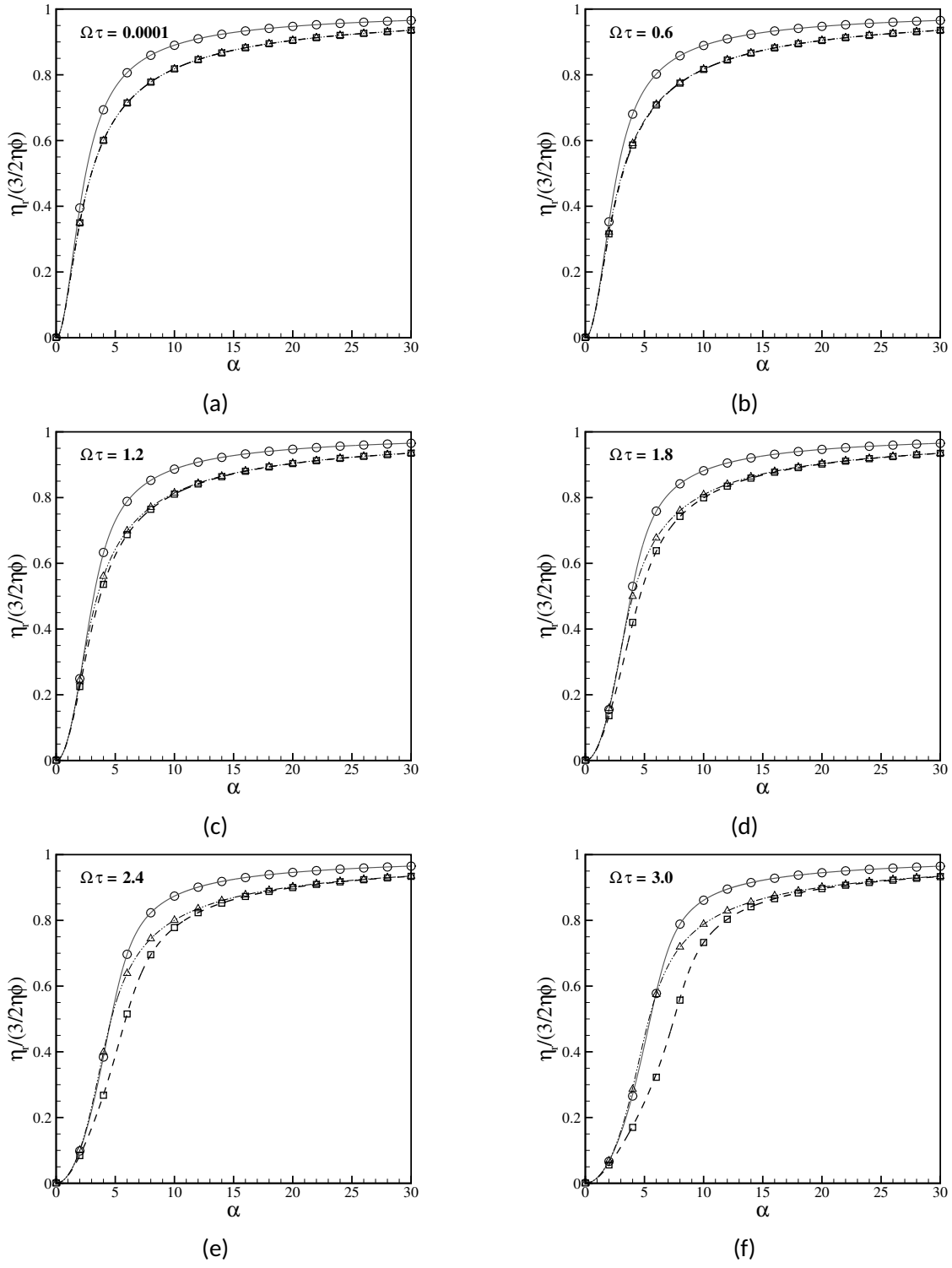

Figure. 3.4: Non-dimensional rotational viscosity as a function of α for various $\Omega\tau$ configurations. Symbols represent numerical and lines represent analytical - Eqs. (2.39), (2.40) and (2.41) - results. □ and - - - for the model of Shliomis [26]; ○ and —— for the model of Martsenyuk et al. [42], and ▫ and -···- for the model of Shliomis [40]. In all figures: $Pe = 1$ and $\phi = 0.05$.

with the highest, lowest and intermediaries vorticity values of the flow. The results for rotational viscosity, normalized by its saturation value $\frac{3}{2}\eta\phi$, are presented in Fig. (3.4), for six different $\Omega\tau$ configurations.

It is clear in Fig. (3.4) that, across the simulated range of vorticity and dimensionless field α, the numerical results are in excellent agreement with the analytical ones, in the three magnetization models.

In addition, the numerical code is capable of correctly capturing the expected trend of an increase in rotational viscosity when α is increased. Due to the increased intensity of the magnetic field, the magnetic particles are subjected to more intense magnetic torques, which act to align them in the direction of the field, making them less free to rotate along the flow's vorticity, which leads to an increase in energy dissipation. This physical effect is manifested by increasing the viscosity of the fluid, as discussed in section 2.1.5. The numerical code also captures the expected saturation value of the rotational viscosity, as $\eta_r \to \frac{3}{2}\eta\phi$ as $\alpha \to \infty$.

In this way, the numerical results were validated using three different approaches. The next section deals with the description of the numerical code used in the discrete approach of this work.

3.2 Discrete modulation

In this section, a brief description of the numerical code used to simulate the colloidal suspensions of magnetically interacting particles under the perspective of Langevin dynamics is described. Since the numerical routine is very similar to that presented in Gontijo and Cunha [27, 28], the reader is deprived from all its details. If the reader is interested in more details regarding this numerical modeling process, he/she is referred to such References.

As previously mentioned in sections 1.5 and 2.2, the mobility matrix is a function of the configuration and the decay of particle's interactions, which happen to be a very slow one when describing hydrodynamic interactions ($1/r$). The tendency to obtain a statistical divergence when computing average transport properties of particulate systems that are subject to very slow decays is quite general, appearing in many systems that involve numerous interacting bodies (magnetic, purely hydrodynamic, charges that interact over long distances . . .). To achieve convergent statistics of the

system's properties, a large system should be considered, since the interactions disturbances, due to their slow decay, are felt over long distances. This results in an impractical situation when one considers how far one should simulate in order to generate convergent statistics. To work around this problem, the well known periodic summation technique [266] should be considered. In few words, this technique consists in the simulation of an infinite system (from the point of view of a statistical thermodynamic limit) with viable computational cost. Ewald's summation technique [266] arose from his studies on crystals (geometric structures with periodic structures that replicate in space). He proposed a lattice theory to compute crystal properties by looking at its periodic repetitions. Under the condition of periodic interactions, a number of boxes surrounding the main box defines a lattice system where the number of particles is replicated periodically in the wholly space, and these periodic boxes are Incorporated in the accounting of the particle's interactions sums [27]. Not only the summation technique was proposed but also a procedure to accelerate its convergence when simulating "infinite" spaces in not very large systems. Under this technique, analysis in both physical and reciprocal (Fourier) spaces are performed in order to accelerate the convergence of the properties over time. This way, two lattice structures are considered, one in the physical space r and the other in the wavenumber Fourier space k.

Much later, Beenakker [269] used Ewald's technique [266] to compute summations of the Rotne-Prager Tensor tensor (associated with hydrodynamic interactions under low Reynolds number regimes, considering particles with finite volume, originating from Green's tensors) when simulating infinite systems. Beenakker [269] expressions are used in this numerical routine to simulate hydrodynamic interactions.

In the case of magnetic interactions, as proposed in Gontijo and Cunha [27], a *hybrid model* is considered, which combines the computation of interactions using periodic and non-periodic approaches. As shown in Eqs. (2.85) and (2.86), magnetic forces decay spatially with $(1/r^4)$, which correspond to a fast decay, while magnetic torques decay spatially with $(1/r^3)$, which correspond to a relatively slow decay. Since the magnetic interactions for the force have a faster decay, the sums of magnetic interactions via induced forces may not be calculated by lattice sums [27]. On the other hand, due to the slower decay of the magnetic torques, torque interactions must be carried out in a periodic way, as indicated in McWhirter and Patey [278], Wang et al. [279], Berkov and Gorn [280], Usov and Grebenshchikov [281], otherwise the summations may lead to divergent suspension transport properties that depend strictly on rotational dynamics, as the fluid's magnetization. This has also been demonstrated in Gontijo and Cunha [27], with the analysis of numerical stability and convergence applied to simulations of colloidal suspensions of magneti-

cally interacting particles, where it has been shown that the computation of magnetic forces can be done in a non-periodic manner, since their faster decay allows for non-periodic calculations in order to achieve convergent statistics, particularly in the prediction of the suspension's equilibrium magnetization M_0. On the other hand, Gontijo and Cunha [27] pointed out that magnetic torque interactions, due to their slower decay, should be computed through periodic spaces. The authors demonstrated that computations of magnetic torques in a non-periodic manner lead to large discrepancies from the predicted values (asymptotic theories) of the equilibrium magnetization, specially when considering concentrated magnetic fluids ($\phi \sim 10\%$). To work around this problem, the authors proposed a so-called *hybrid method*, in which magnetic forces are computed directly, through the minimum image method, while magnetic torques are computed periodically (with the use of lattice imaginary structures, in which the central cell structure is replicated). This hybrid technique is applied in this particular work, since it enables accurate calculations of transport properties with statistical convergence, as indicated in the works of Gontijo and Cunha [27, 28].

That said, to simulate a colloidal suspension of particles interacting magnetically, a non-commercial numerical code was developed by the author's advisor, undergoing minor changes to be used in this work. It is written in Fortran language and uses Langevin dynamics to compute interactions between the particles subjected to a local Couette flow through a Lagrangean perspective, calculating for each suspended particle its translational and rotational motions. This code accounts for all the results which involve discrete simulations in section 4.2. It uses a non-commercial Intel Fortran compiler to produce an executable file that reads an entrance text file which contains all the information regarding the physical parameters to be simulated (i.e. α, Pe, λ, ϕ ...) along with the simulations characteristics (i.e. periodicity in computing torques or magnetic forces ...). The numerical code makes all the required statistics of the suspension based on an ensemble average through several simultaneous numerical experiments, providing the wanted transport properties, which, in the case of this particular work, correspond solely to the suspension's magnetization. As already mentioned, a hybrid method is used to compute the magnetic interactions, where particle interactions induced by force-dipole are accounted without periodic sums while interactions induced by torque-dipole are accounted using the periodic approach, where a number of image boxes surrounding the main cell will define the so-called lattice system, in which the periodic boxes will be incorporated for accounting the images particle contributions to the particle's interacting sums [27]. As indicated in Gontijo and Cunha [27, 28], this procedure enhances the computational cost. The numerical code used in this work is very similar to that presented in Gontijo and Cunha [27, 28], therefore, one is referred to such References for more details regarding this numerical modeling process. Some of the steps used to compute both magnetic and hydrodynamic periodic

interactions are briefly described in this section.

3.2.1 Initialization of the process and generation of the lattice network

To initialize the numerical process, all simulation variables must be declared. These include the number of particles N, the number of lattice boxes in the simulating network (125 in this work), the number of particle's realizations, as well as the non-dimensional physical parameters involved in the problem's physics, namely: the non-dimensional magnetic field α, the dipole's coupling parameter λ, the Péclet number Pe, the rotational Péclet number Pe_r and the volume fraction of particles ϕ. It is important to mention that although ϕ do not appear explicitly in the discrete modeling of the problem, it determines implicitly the size of the simulation boxes. One must also bear in mind that α, ϕ, λ and Pe also appear explicitly in the ferrohydrodynamic equations in the continuous formulation. The suspension's initial condition is generated without the presence of particle overlaps in all realizations [28]. At each realization of the dynamical simulation - all numerical realizations are computed simultaneously -, there is an initial particle distribution with random and independent position of the particles inside the simulation box. This generates an initial condition as close as possible to a spatially statistical homogeneous particle distribution in the absence of particle's clusters or any heterogeneity [27]. It is then checked if the smallest distance between the center of two interacting particles is greater than a particle's diameter $d = 2a$. If this is not the case for any pair of interacting particles, a small Brownian random displacement is numerically provided to ensure the absence of particle's overlapping [28]. A similar procedure is used for the initial configurations of the particles' dipole moments, which are generated with a procedure of random and independent orientations [27]. As soon as the physical simulation box is created, respecting the imposed spatial restrictions, the imaginary lattice cells are replicated and distributed around the central cell, as indicated in Fig. (3.5) [262, 271, 28].

For the construction of the numerical lattice network, one procedure is adopted for the lattice physical space and other for the lattice reciprocal space [28]. For the lattice physical space, a vector $\boldsymbol{x}^R$ is added to the position of each particle located in the central cell, according to Eq. (3.10) and Fig. (3.6).

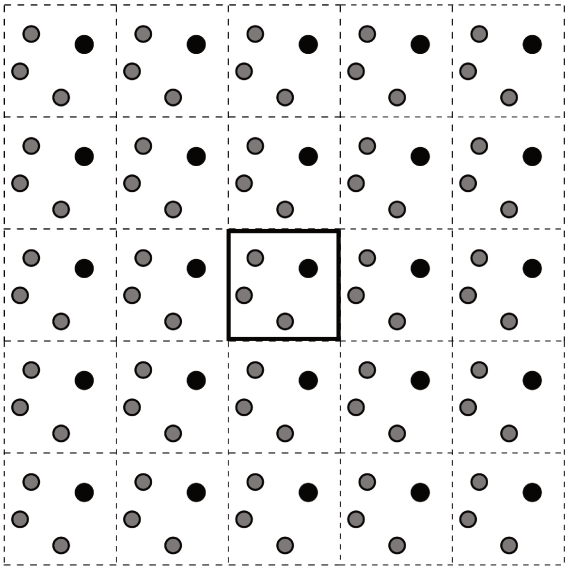

(2,-2)	(2,-1)	(2,0)	(2,1)	(2,2)
(1,-2)	(1,-1)	(1,0)	(1,1)	(1,2)
(0,-2)	(0,-1)	(0,0)	(0,1)	(0,2)
(-1,-2)	(-1,-1)	(-1,0)	(-1,1)	(-1,2)
(-2,-2)	(-2,-1)	(-2,0)	(-2,1)	(-2,2)

Figure. 3.5: Lattices simulating network. Left: the central cell, surrounded by the image cells, is shown highlighted in the center. Right: example of a two-dimensional domain, in which the cell (0,0) represents the so-called physical lattice cell, while all the surrounding ones are the imaginary periodic cells. Image adapted from Gontijo and Cunha [28].

$$\boldsymbol{x}^R = \sum_{i=1}^{3} \gamma_i l_i \hat{e}_i, \qquad \gamma_i \in \mathbb{Z} \tag{3.10}$$

In Equation (3.10), $\gamma_i = \gamma_1, \gamma_2, \gamma_3$ are integers contained in the interval $[-2, +2]$, representing the lattice vectors and $l_i = l_1, l_2, l_3$ denote the lengths of each side of the central cubic cell [28]. The procedure presented in Eq. (3.10) is depicted in Fig. (3.6).

It is easily verified that, when accounting for all the combinations, it reaches $5^3 = 125$ lattice cells, in a way that each of the γ_i coefficients represent a different cell. For instance, the central cell would be described as $\gamma_1 = \gamma_2 = \gamma_3 = 0$. As for the reciprocal space sums, associated with the Ewald summation technique [266], a vector $\boldsymbol{x}_k$ is added to the position of each particle, in accordance to Eq. (3.11) [28].

$$\boldsymbol{x}^k = \sum_{i=1}^{3} \frac{2\pi\beta_i}{l_i} \hat{e}_i, \qquad \beta_i \in \mathbb{Z} \tag{3.11}$$

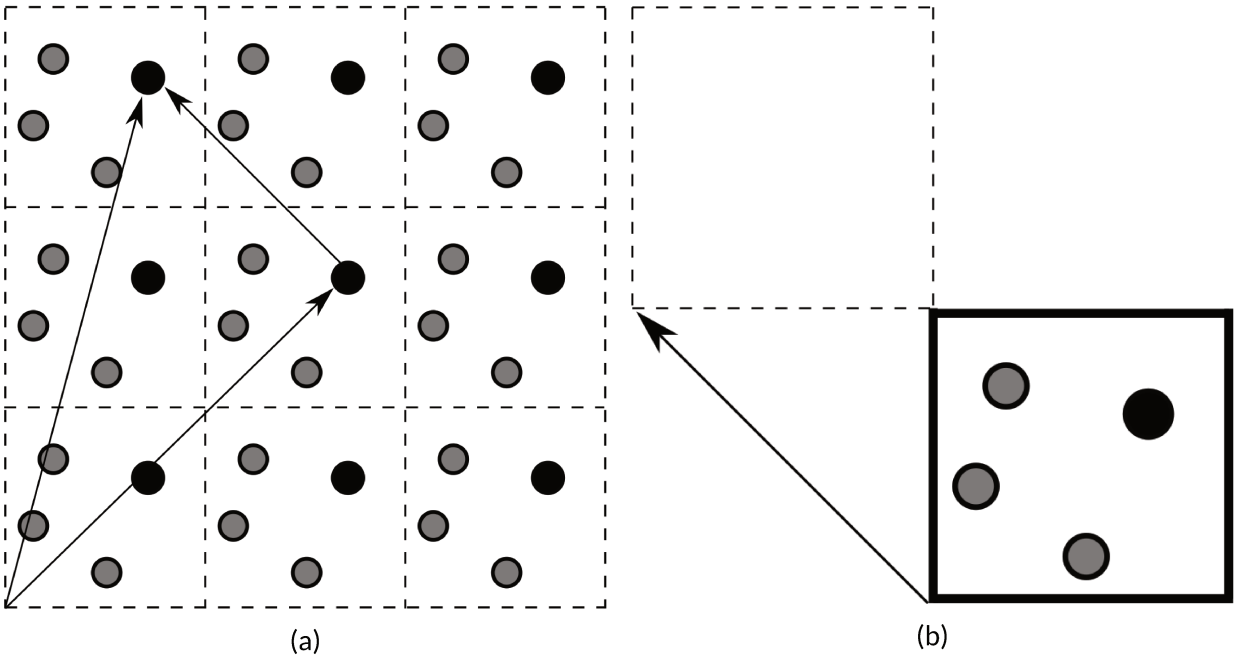

Figure. 3.6: (a) distance of an arbitrary particle in the central cell to its correspondent particle in one of the imaginary surrounding cells. (b) Construction of lattice vectors. Image adapted from Gontijo and Cunha [28].

In Equation (3.11), $\beta_i = \beta_1, \beta_2, \beta_3$ denote integers contained in the interval $[-2, +2]$. The procedure described in Eq. (3.11) is used for creating reciprocal lattice cells with different wavenumbers [28]. Each of these cells are enumerated in accordance to the algorithm presented in Eq. (3.12) and visually presented in Fig. (3.7).

$$L_n = \zeta_1 + \zeta_2 + \zeta_3 \tag{3.12}$$

In Equation (3.12), ζ_1, ζ_2, ζ_3 denote the components of the lattice enumeration vector, all defined in Eq. (3.13), and L_n is the lattice number.

$$\begin{aligned} \zeta_1 &= \big(\gamma_1 + \max|\gamma_i|\big) N_l^{\frac{2}{3}} \\ \zeta_2 &= \big(\gamma_2 + \max|\gamma_i|\big) N_l^{\frac{1}{3}} \\ \zeta_3 &= \gamma_3 + \max|\gamma_i| + 1 \end{aligned} \tag{3.13}$$

Plane x = -1

30	35	40	45	50
29	34	39	44	49
28	33	38	43	48
27	32	37	42	47
26	31	36	41	46

Plane x = 1

80	85	90	95	100
79	84	89	94	99
78	83	88	93	98
77	82	87	92	97
76	81	86	91	96

Plane x = 0

55	60	65	70	75
54	59	64	69	74
53	58	63	68	73
52	57	62	67	72
51	56	61	66	71

Plane x = -2

5	10	15	20	25
4	9	14	19	24
3	8	13	18	23
2	7	12	17	22
1	6	11	16	21

Plane x = 2

105	110	115	120	125
104	109	114	119	124
103	108	113	118	123
102	107	112	117	122
101	106	111	116	121

.

Figure. 3.7: Enumeration of each of the 125 lattice cells in different planes for the three-dimensional typical configuration depicted in Fig. (2.2). Image adapted from Gontijo and Cunha [28].

To illustrate the algorithm presented in Eq. (3.12), if one considers the central cell in which $\gamma_i = (\gamma_1,\gamma_2,\gamma_3) = (0,0,0)$ and for a periodic system composed of 125 lattice cells where $\gamma_i \in [-2, +2]$ and $\max|\gamma_i| = 2$, by taking $\zeta_1 = 50$, $\zeta_2 = 10$ and $\zeta_3 = 3$ the number of central cell according to Eq. (3.12) would be $L_n = 63$, as illustrated in plane $x = 0$ in Fig. (3.7).

Although tedious, the process of enumerating each of the lattice cells is extremely important, since interactions between all the particles in the imaginary cells and those in the real lattice cell are computed in order to describe their motions influenced by magnetic and hydrodynamic

interactions. This procedure is performed in a loop which considers all of the 125 lattice cells, and it accounts for the effects of the imaginary particles on their counterparts in the central lattice-cell, but not between the imaginary particles themselves [28].

As previously discussed, the sum of the hydrodynamic interactions of the particles results in divergence problems in the statistical properties of the suspension due to the slow decay of these interactions ($1/r$) [340, 341, 262, 27, 28], which is avoided by the application of a periodic system with periodic boundary conditions [27, 28]. However, this approach is accompanied with a significant increase in the computational cost in dynamic simulations [27]. It is important to mention that, in the context of magnetic interactions, dipole–dipole interactions spatially decay considerably faster then hydrodynamic interactions, like ($1/r^4$) for the force-dipole interactions and ($1/r^3$) for torque-dipole interactions. It has been shown in Gontijo and Cunha [27] that a hybrid method, in which periodicity for particle interaction in a periodic box is considered only when computing the torque-dipole interactions, is both accurate and much less expensive when it comes to computational cost. This hybrid method is used in the present work for computing the magnetic interactions.

3.2.2 Computation of the functions present in the discrete equations

After the initialization process described in section 3.2.1 is completed, several tables containing the values of the scalar functions (section 2.2) used to module the suspension's discrete dynamics are computed. Scalar functions $\mathcal{F}(r)$, $\mathcal{G}(r)$ and $\mathcal{H}(k)$ presented in Eqs. (2.68), (2.69) and (2.70) respectively, used to compute matrices $\boldsymbol{M}_1(r)$ and $\boldsymbol{M}_2(k)$ of Eqs. (2.66) and (2.67), are computed along with scalar functions $\mathcal{B}(r)$, $\mathcal{C}(r)$ and $\mathcal{D}(r)$ of Eqs. (2.97), (2.92) and (2.93), respectively, used to compute functions $\boldsymbol{\mathcal{T}_1}(r)$, $\boldsymbol{\mathcal{T}_2}(\boldsymbol{r})$, $\boldsymbol{\mathcal{T}_4}(r)$ and $\boldsymbol{\mathcal{T}_5}(k)$ of Eqs. (2.89), (2.90), (2.95) and (2.96) modeling the long-range periodic magnetic interactions. As easily seen in their own definitions, these functions depend only on the distance between the particles r and on the different wavelengths k used in the computation of the reciprocal sums, therefore, these functions are calculated beforehand for all possible particle configurations and these values are then interpolated from the pre-tabulated mobility functions [28]. According to Gontijo and Cunha [28], this procedure is quite accurate and computationally effective, since it avoids the expensive computation of the mobility functions in all timesteps, drastically decreasing the $\mathcal{O}(N^2 \times N_c)$ computational cost of these simulations.

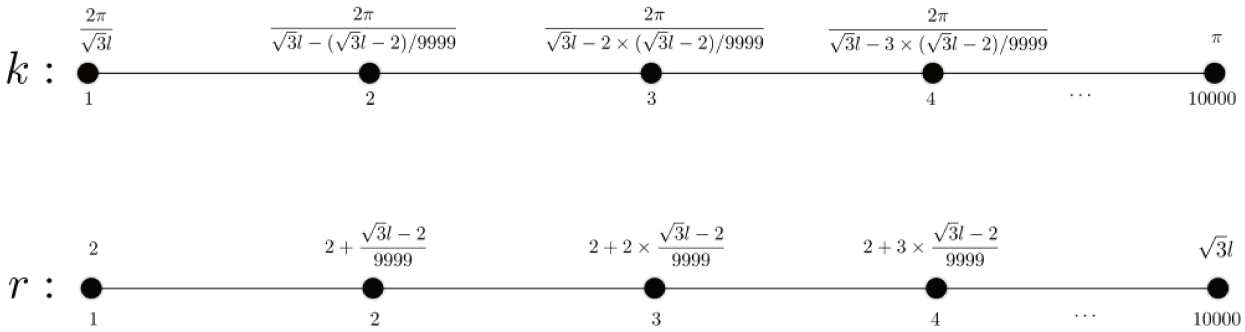

Figure. 3.8: One-dimensional meshes used to pre-tabulate the mobility functions for hydrodynamic and magnetic interactions in both physical and reciprocal spaces in the periodic lattices configurations. Image adapted from Gontijo and Cunha [28].

The aforementioned pre-calculated tables are better interpreted as one-dimensional meshes with 10^4 nodes, as depicted in Fig. (3.8). As soon as the suspension geometrical parameters (number of particles N and volume fraction of particles ϕ) are defined, the largest and shortest distances between two interaction particles should be defined, in the same manner as all possible wavelengths [28]. This way, the one-dimensional mesh of pre-tabulated functions is constructed, in accordance to Fig. (3.8).

As indicated in Fig. (3.8), the possible distances will lie in the interval $[2,\sqrt{3}l]$, where l corresponds to the length of an edge of the central lattice cell. Similarly, wavenumbers will lie in the interval $[2\pi/\sqrt{3}l,\pi]$ [28].

3.2.3 Evolution process

The forces and torques acting on each of the suspended magnetic particles are computed along with their velocities and positions in space. A fourth-order Runge-Kutta scheme [318, 342] is used to solve the time developing of the suspension's dynamics. As soon as the velocities are calculated, the particles' positions are evaluated from a current iteration n to the next $n+1$ through [28]:

$$\boldsymbol{x}^{n+1} = \boldsymbol{x}^{n} + \boldsymbol{u}^{n}\Delta t \tag{3.14}$$

In Equation (3.14), Δt corresponds to the numerical time-step. The non-dimensional physical parameters presented in Eq. (2.111) represent ratios between different time-scales of the problem. Therefore, the numerical time-step Δt used in the Langevin dynamics simulations is defined based upon these parameters. In addition, 0.01 is considered, which works as a numerical filter in order to avoid large numerical time-steps [28].

$$\Delta t = \min\left(\frac{Pe}{10}, \frac{\alpha}{10}, \frac{\lambda}{10}, 0.01\right) \tag{3.15}$$

With the information obtained from the torques acting on each particle, their angular velocities are then computed, assuming that the magnetic dipole moments will rotate without delay with their angular velocities, since this work deals with magnetically hard particles [62]. After doing so, the particles' velocities evolve in time with the next time step. The evolution of the dipole moments $\boldsymbol{d}_i$ of the particles follow:

$$\boldsymbol{d}_i^{n+1} = \boldsymbol{d}_i^n + (\boldsymbol{\omega} \times \boldsymbol{d}_i^n)\Delta t \tag{3.16}$$

This procedure is carried out until the desired magnetization value reaches a statistical steady state behavior.

3.2.4 Computing magnetization

One of the most important properties of a suspension of magnetic particles is its magnetization $\boldsymbol{M}$, and, in the absence of a flow, its equilibrium magnetization $\boldsymbol{M}_0$. Such macroscopic property is strictly related to the particle's rotational motion when it is subjected to an external applied magnetic field. In the absence of a magnetic field, the particle's dipole moments are randomly oriented in space. When in the presence of a field, a magnetic torque ($\boldsymbol{T_m} = \boldsymbol{m} \times \boldsymbol{H}$) is exerted in each magnetic particle due to the interaction between the particle's dipole moment and the external field. This torque tends to orient the dipole moments in the direction of the field, resulting in a net magnetization. In the simulations considered in this work, the assumption that the particle's Néel relaxation time τ_N is greater than the Brownian relaxation time τ_B is assumed,

in a way that the rotation of the particle's dipole moment due to magnetic torques is followed by the rotation of the particle itself. When all particles are aligned in the field's direction, the suspension's equilibrium magnetization reaches a saturation value $\boldsymbol{M_s}$. In this particular condition, the suspension's magnetization is simply given by the volume average ϕM_d, where M_d is the magnetization of the solid material which composes the magnetic particles. That said, the procedure used in this work for calculating magnetization is based upon its own definition. Magnetization is a macroscopic physical property defined as the average orientation of the particle's dipole moments with respect to the direction of an applied external field, being calculated in this work as [27]:

$$\frac{M}{\phi M_d} = \left(\frac{1}{N}\frac{1}{N_{rea}}\right)\langle\cos(\theta)\rangle_i^j \tag{3.17}$$

In Equation (3.17), N is the number of particles in the simulating box, N_{rea} is the number of realizations and θ is the angle between the direction of the dipole moment of particle i in realization j at a given time step and an applied field direction [27].

3.2.5 Local Couette flow

As discussed in section 1.1, Langevin dynamics simulations are used in order to reconstruct a continuous magnetization profile of a plane Poiseuille ferrofluid flow. The magnetization and vorticity profiles are obtained through a two-dimensional CFD in-house code. After the continuous simulations are carried out, the numerical domain is divided into smaller so-called *local vorticity cells*, in accordance to Fig. (1.2). These small flow field sub-regions are precisely the domains simulated in the discrete approach. In order to do so, the local vorticity obtained in the continuous approach is used as an equivalent local shear-rate to feed a local Couette flow simulated through the LD numerical code. Since this specific part is responsible for differentiating this numerical code to the ones used in Gontijo and Cunha [27, 28], it is important to explain how the implementation of the aforementioned local Couette flow is performed.

The vorticity ξ obtained through the CFD approach is used as an input in the discrete simulations, as an equivalent local shear-rate $\dot{\gamma}$ ($\dot{\gamma} = -\xi$). From kinematics of fluids [301], a linear velocity profile associated with the Couette flow, where $\boldsymbol{v} = \dot{\gamma} y \hat{\boldsymbol{e}}_x$, is locally created in the domain central

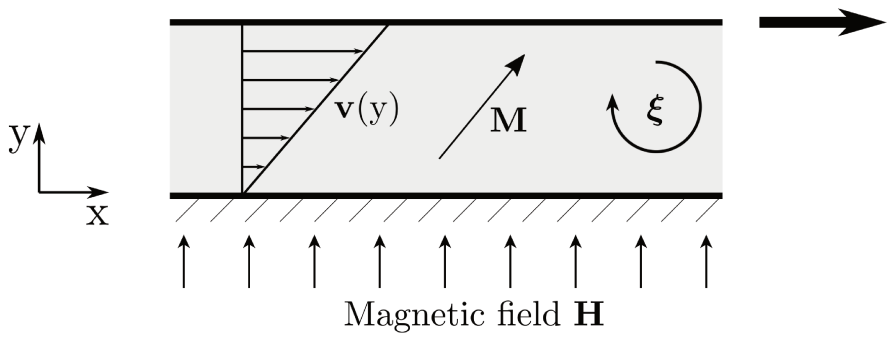

Figure. 3.9: Scheme representing a local Couette ferrofluid flow in the presence of a magnetic field. Image adapted from Rosa [343].

cell (physical box subject to periodic boundary conditions), as indicates the scheme of Fig. (3.9).

Afterwards, this deterministic velocity in the direction of the shear ($\boldsymbol{v} = \dot{\gamma} y \hat{\boldsymbol{e}}_x$), which in turn varies according to the height y, is added to the pre-calculated translational velocity of the particles, which results from the interactions between the particles.

In addition to increments in the translational velocity, an angular velocity, associated to the fluid's vorticity $\boldsymbol{\xi}$, is also added to the angular velocity of the particles. From kinematics of fluids [301], the angular velocity of an infinitesimal particle is associated with the fluid's vorticity ($\boldsymbol{\Omega} = \frac{1}{2}\boldsymbol{\xi} = \frac{1}{2}\nabla \times \boldsymbol{v}$). In the present case, the velocity field is known a priori (Couette flow's velocity field), being given by $\boldsymbol{v} = \dot{\gamma} y \hat{\boldsymbol{e}}_x$. By taking the curl of this velocity field, vorticity ξ is obtained, given by $\xi = -\dot{\gamma}$. This way, $-\frac{1}{2}\dot{\gamma}$ is added to the angular velocity of each of the suspended particles. It is important to mention that this increase promoted in the angular movement of the particles does not depend on their position in space, therefore all particles present in the central cell will have their angular velocities modified in the same way, since the increase by the deterministic angular velocity (in vorticity's direction) is the same throughout the simulation box, in contrast to the increase in the deterministic translational velocity, which depends on the position of the particles.

These modifications in both translational and rotational velocities of the particles are made in those suspended in the central cell. It is important to remember that the particles are subjected to long-range interactions, which in order to be computed, a periodic cells scheme must be applied. Under this approach, the central domain (cell) is replicated periodically in all directions. To avoid wall effects, a particle which leaves the domain through any of the surrounding walls, enters the

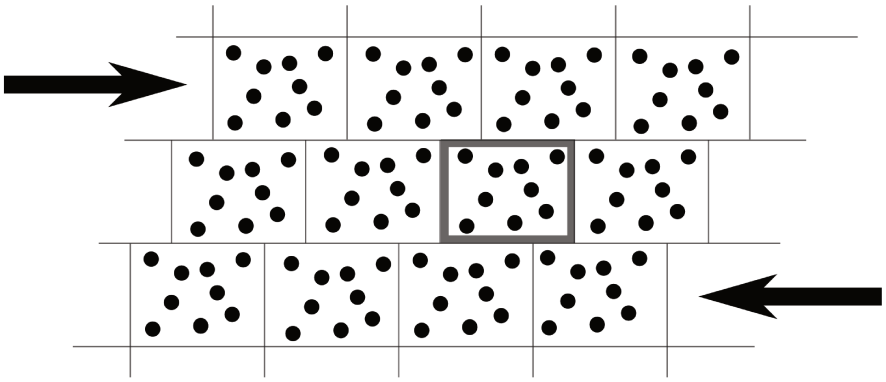

Figure. 3.10: Scheme of the movement of the upper and lower domains, in the presence of shear, according to the scheme of Lees and Edwards [344]. Image adapted from Rosa [343].

very opposite wall again, in a way that the number of particles inside the box remains constant throughout the simulation. In order for the discontinuities in particle velocities to be minimized, the condition proposed by Lees and Edwards [344] is used, in which the domains above and below the central domain move with velocities proportional to the shear rate [343]. This way, a distortion in the position of the imaginary lattices is generated, as if they were being sheared, generating a change in the relative position of the particles that occupy the imaginary cells in relation to the particles that are in the physical central box. Figure (3.10) shows a schematic of this method. Under this scheme, it is interesting to notice that a particle which leaves the domain through the lower wall, will enter the upper wall with its velocity added to the product of the shear rate by the size of the simulation domain y [343].

3.2.6 Should hydrodynamic interactions be computed?

It is well-known that the computation of hydrodynamic interactions significantly increases the computational cost of dynamic simulations [28]. The important issue is whether hydrodynamic interactions substantially affect ferrofluid dynamics or not. In case such interactions could be neglected in dynamic simulations, a substantial economy of simulating time would be achieved. Surprisingly, it has become known in ferrohydrodynamics that the effect of hydrodynamic interactions can be neglected to first order in dilute ferrofluids [63]. For instance, Torres-Díaz and Rinaldi [63] compares the magnitude of hydrodynamic interactions with that of magnetic interactions in a typical water-based ferrofluid whose particles have radius $a = 10nm$ and bulk magnetization $M_d = 425kAm^{-1}$. The authors show that is in both cases of large and small separations between

the particles, the magnetic interactions clearly exceed the magnitude of the hydrodynamic interactions. Therefore, as already stated, hydrodynamic interactions can be neglected to first order in dilute ferrofluids [63], leading to less computational cost in dynamic simulations.

In addition, Gontijo and Cunha [28] has demonstrated that hydrodynamic interactions tends to attenuate the frequency in which particle agglomerates are formed, modifying their overall behavior, however only when considering *dense* ferrofluids with volume fraction of particles up to $\phi = 15\%$, which is clearly not the case in this work, since it deals with *dilute* ferrofluids with $\phi \sim 5\%$, confirming that hydrodynamic interactions may be neglected under such conditions.

That said, it is important to mention that in this work, although the calculation of hydrodynamic interactions is already programmed in the discrete numerical routine, they are not considered in its dynamical simulations. It is also important to mention that, in practical terms, the magnetic particles are not massive, so that the Stokes number is practically null ($St \sim 10^{-11}$). However, in the absence of hydrodynamic interactions and when considering $St = 0$, the only hydrodynamic force considered in the problem's modulation is the Stokes drag ($\boldsymbol{F}_{drag} = -6\pi\eta a\boldsymbol{u}$), in a way that the particle's velocity is algebraically resolved, since $\sum \boldsymbol{F} = \boldsymbol{0}$ and that the Stokes drag depends linearly on velocity. Nevertheless, when this modeling is considered in the absence of hydrodynamic interactions, the numerical code becomes unstable, leading to several noise generated in part by the presence of Brownian interactions. Thus, a numerical subterfuge for the purpose of controlling numerical stability is used when hydrodynamic interactions are not computed, in which the presence of little inertia (a very small but not null Stokes number) is considered, which leads to an attenuation/stabilization of code instabilities, attenuating stochastic noises, which come from the fictitious modeling of Brownian forces and torques, leading to statistically convergent results. Nonetheless, when in the presence of hydrodynamic interactions, this numerical subterfuge is not necessary, since the mitigating role is exercised by the mobility matrix itself, since it is associated with viscous dissipation strictly associated with hydrodynamic interactions.

3.2.7 Code validation and computational cost

It has been established in Gontijo and Cunha [27, 28] that periodic particle interactions drastically increase the computational cost involved in performing dynamic simulations. Such References also demonstrated that depending on the volume fraction of particle's ϕ and on the intensity of

the dipole's coupling parameter λ, a hybrid method, which involves computations of interactions in a periodic way for interactions with slower decays and in a non-periodic manner for interactions with faster decays can be used. Since the computational cost of these particular simulations is $\mathcal{O}(N^2 \times N_c)$, it rapidly increases when all interactions are calculated periodically by using the lattice system [28]. For instance, Gontijo and Cunha [28] shows that when performing particle-particle interactions using $N = 1500$ particles in the central cell ($N_c = 186000$) with full periodicity, the numerical cost is 200% larger if compared to the case when only magnetic-torque interactions are calculated periodically. Bearing that in mind, and considering that the hybrid method has proved to be accurate in Gontijo and Cunha [27, 28] for physical regimes where $\phi \sim 5\%$, it is applied in this particular work.

The numerical routine used in this work was extensively validated in Gontijo and Cunha [27, 28] by comparing the values obtained numerically for transport properties of the suspension with those theoretically predicted in the literature. Properties such as mean sedimentation velocity and equilibrium magnetization were used in such validations. The latter is directly associated with the scope of this work and, therefore, the numerical validation of the code in relation to the calculation of the equilibrium magnetization M_0 will be briefly presented below, in accordance with that presented in Gontijo and Cunha [27, 28].

Equilibrium magnetization is the suspension's magnetization in the absence of flow. Its simplest theoretical model, used in very dilute magnetic fluids with non-interacting magnetic dipoles, is the well-known Langevin model [3], presented in Eq. (2.19), which is a $\mathcal{O}(\phi)$ model. However, in more concentrated regimes and in the presence of interacting particles, more robust ($\mathcal{O}(\phi^2,\phi^3)$) models [33, 34] must be used, as the one presented in Ivanov and Kuznetsova [34] - Eq. (2.22) - which is a $\mathcal{O}(\phi^3,\lambda^2)$ along with the model of Jansons [33].

Gontijo and Cunha [27] shows a very good agreement between the first [3] order and second [33] order models with their obtained numerical results. They note that under high α regimes, where field effects dominates both Brownian thermal fluctuations and dipole-dipole interactions, all curves collapse to the same prediction of magnetization. It is also shown that the numerical values tend to underestimate the higher order asymptotic models, which is an indicative that non-periodic dipole-dipole magnetic interactions are valid only for small values of ϕ and λ [27]. The biggest discrepancies between the models lie when $\alpha \sim 1$, since under these regime the energy of the external field is compared with that of the Brownian fluctuations. In addition, they show the behavior of the suspension's magnetization when $\alpha = 1$, calculated considering both periodic and

non-periodic interactions for the dipole-dipole-magnetic torque interactions. They state that when $\phi \sim 0.01$, all theoretical results and numerical simulations give very similar results. Up to a point where $\phi = 0.03$, the results were very close to each other. However, when $\phi \geq 5\%$, the results seemed to deviate. In this dilute regime, when considering $\lambda \sim 1$, the dipole–dipole magnetic interactions are not as significant as the other interactions that govern the suspension's dynamics. However, when the volume fraction of particles ϕ is increased, the dipole–dipole magnetic interactions tend to become much more important on the suspension's dynamics. Under these regimes, they note that the numerical results computing particle interactions without periodic sums tend to underestimate significantly the asymptotic $\mathcal{O}(\phi^3)$ model [34]. Thus, it is demonstrated that the computation of dipole–dipole magnetic interactions in a non-periodic way tend to underestimate the equilibrium magnetization values for more concentrated regimes (i.e. $\phi > 0.05$ for $\lambda \sim 1$). On the other hand, when using periodic computations for magnetic torques due to dipole–dipole interactions (using the hybrid model), the numerical results produced by the authors were in excellent agreement with the theoretical $\mathcal{O}(\phi^3)$ model [34] for values of ϕ up to $\phi = 0.1$ [27]. This way, the authors not only validated the numerical routine in terms of computing magnetization, but also established the limits where the hybrid method can be applied, which occurs when $\phi \sim 10\%$. Considering that this particular work deals with dilute suspensions of $\phi \sim 5\%$, the hybrid method is clearly applicable and the results obtained through the dynamic numerical simulations can be considered accurate. That said, the discrete numerical routine is validated and the results obtained through the numerical approach described in section 3.2 are presented in section 4.2.

Numerical convergence of the suspension's magnetization was also evaluated in Gontijo and Cunha [27, 28] when considering the number of particles N and number of realizations N_{rea}, where it has been shown that for $N \sim 500$ particles and $N_{rea} \sim 50$ realizations convergent statistical properties of the suspension can be obtained.

4 Results and discussions

4.1 Results and discussions

This section is concerned with the presentation of the numerical results obtained through the coupled numerical solution of the non-dimensional vorticity equation - Eq. (2.48) -, one of the non-dimensional magnetization equations - Eqs. (2.49), (2.50) or (2.51) - and the Poisson equation - (2.45) - in different physical situations. The results presented cover both the entrance region and the fully developed region of the flow. These results are published in de Carvalho and Gontijo [345].

4.1.1 Considerations

A brief discussion about the choice of the magnitude of physical parameters

Before presenting the results, a brief discussion is made about the choice of the magnitude of the problem's physical parameters. Some of them are physically limited due to the very nature of problem. As in this study a laminar flow is considered, the Reynolds number Re must be less than $Re < 5772$ in order to guarantee laminar flow [346, 347]. Thus, the simulations are performed with $Re = 5000$ so that a laminar flow is maintained. The physical parameters related to the composition of the analyzed ferrofluid, such as the volume fraction of particles ϕ and the dipole's coupling parameter λ are also physically limited. Ferrofluid's magnetic particles have diameter in the range $3nm < d < 15nm$ [3], therefore λ, according to Eq. (1.13), lies in the range $0.036 < \lambda < 4.474$. As for ϕ, this paper deals with diluted ferrofluids. Therefore, values of $\phi \sim 0.05$ and $\lambda \approx 2.9$ are used in the simulations, for particle's diameter $d \approx 13nm$. When it comes to the magnitude of α, it is strictly related to the temperature of the ferrofluid, the composition and geometry of the particles, as well as the applied magnetic field. All simulations were performed considering ferrofluids with magnetite nanoparticles with domain magnetization M_d = 4.46 $\times 10^5 A/m$ [70] at $T = 298K$. Different values of α were simulated through changes in the intensity of the applied magnetic field. Normally, in all simulations, α is in the range $1 < \alpha < 15$.

The main issue regarding the choice of physical parameters was the choice of physically con-

sistent Péclet numbers Pe. As discussed in de Carvalho and Gontijo [46], typical values of Péclet number for ferrofluid applications are generally $Pe \ll 1$, due to the small nature of the Brownian timescale τ_B. However, under these conditions, magnetization cannot be effectively disturbed by the vorticity field and, therefore, hydrodynamics has little influence on the magnetization field. As this work is concerned with understanding the nature of the hydrodynamic-magnetic coupling through the action of vorticity, it is interesting to analyze scenarios in which $Pe \approx 1$. Péclet numbers of this order can lead to non-physical consequences, as they can be outside of realistic configurations in which magnetic fluids exist and have stable properties. To ensure physically applicable scenarios, the properties of commercially available ferrofluids taken from Rosensweig [3] were considered in the pressure gradient $\frac{dP}{dx}$ calculations necessary to maintain the flow for fixed Reynolds and Péclet numbers. Calculations of the Brownian timescale τ_B - Eq. (1.9) - of the magnetic particles were performed using commercially available ferrofluids data from Rosensweig [3]. For a typical particle's diameter $d = 13nm$, Tab. (4.1) presents the calculated values for τ_B.

Table. 4.1: Brownian timescale of different commercially available ferrofluids with diameter $d = 13nm$ taken from Rosensweig [3] at 298K.

Carrier liquid	ρ (Kg/m^3)	η (Pa.s)	τ_B (s)
Diester	1185	0.075	6.29E-05
Hydrocarbon	1050	0.003	2.52E-06
Hydrocarbon	1250	0.006	5.03E-06
Fluorocarbon	2050	2.5	2.10E-03
Ester	1150	0.014	1.17E-05
Ester	1300	0.03	2.52E-05
Ester	1400	0.035	2.94E-05
Water	1180	0.007	5.87E-06
Water	1380	0.01	8.39E-06
Polyphenylether	2050	7.5	6.29E-03

A huge variation in the typical Brownian timescale τ_B is observed for different carrier liquids. This timescale has a major impact on the estimate of the Péclet number. For fixed Péclet and Reynolds numbers scenarios, such as the cases studied in this work, it is possible to calculate the typical velocity and spacing between the plates using Eq. (2.52). The pressure gradient required to maintain these flows can also be estimated using Eq. (4.1).

$$\frac{dP}{dx} = \frac{12\eta U}{h^2} \tag{4.1}$$

The greater the Péclet number, the greater the hydrodynamic impact on magnetization dynamics, leading to non-equilibrium results. However, as already mentioned, it is necessary to define Pe with caution, in order to guarantee physically applicable situations, without jeopardizing the important physical consequences of non-equilibrium scenarios. That said, the Péclet number was fixed as $Pe = 0.5$ in the simulations, as it guarantees applicability in order to maintain consistent physical values for at least some of the aforementioned ferrofluids. The calculated values are shown in Tab. (4.2).

Table. 4.2: Pressure gradient in order to maintain the channel flow of different commercially available ferrofluids with diameter $d = 13nm$ taken from Rosensweig [3] at 298K. In this table: $Re = 5000$ and $Pe = 0.5$.

Carrier liquid	U (m/s)	h (m)	dP/dx (atm/m)
Diester	50.15	6.31E-03	11.19
Hydrocarbon	53.28	2.68E-04	263.27
Hydrocarbon	48.83	4.92E-04	143.63
Fluorocarbon	38.13	1.60E-01	0.44
Ester	50.91	1.20E-03	59.04
Ester	47.88	2.41E-03	29.29
Ester	46.14	2.71E-03	26.06
Water	50.26	5.90E-04	119.61
Water	46.47	7.80E-04	90.55
Polyphenylether	38.13	4.80E-01	0.15

From the data obtained in Tab. (4.2), it is possible to see that, for part of the presented ferrofluids, the chosen values of Péclet and Reynolds numbers ($Pe = 0.5$ and $Re = 5000$) would lead to realistic physical scenarios, as is the case of ferrofluids with carrier liquids of diester, fluorocarbon, ester and polyphenylether. In this way, physical applicability is guaranteed in relation to the choice of physical parameters used in the numerical simulations ($\phi \sim 5\%$, $\lambda = 2.9$, $Re = 5000$ and $Pe = 0.5$).

From a different perspective, we decided to explore what the particle's diameter d should be so that physical scenarios with higher Péclet number configurations, which would generate strongly non-equilibrium results, were physically "possible". Table (4.3) presents results on values of d necessary to obtain consistent physical pressure gradients for all ferrofluids present on Tab. (4.1) under conditions of $Re = 5000$ and $Pe = 1$. For this, the velocity U was fixed at $U = 15m/s$ and the diameter d was obtained through Eq. (4.2).

$$d = \left(\frac{2\kappa_B T Re Pe}{\pi \rho U^2} \right)^{\frac{1}{3}} \tag{4.2}$$

Table. 4.3: Typical diameters d in order to maintain conditions of $Re = 5000$, $Pe = 1$ and $U = 15m/s$.

Ferrofluid	d (m)	dP/dx (atm/m)
Diester	3.66E-08	0.30
Hydrocarbon	3.81E-08	5.88
Hydrocarbon	3.60E-08	4.16
Fluorocarbon	3.05E-08	0.03
Ester	3.70E-08	1.51
Ester	3.55E-08	0.90
Ester	3.46E-08	0.90
Water	3.67E-08	3.18
Water	3.48E-08	3.04
Polyphenylether	3.05E-08	0.01

All results presented in Tab. (4.3) are physically applicable. However, it would be necessary to employ a synthesized ferrofluid with an average particles diameter of $d \approx 35nm$. These ferrofluids would be suitable for a higher hydrodynamic-magnetic coupling, which could lead to other possibilities in terms of ferrofluid flow control and to strongly non-equilibrium configurations. Unfortunately, this ferrofluid cannot exist, since the dipole's coupling parameter would reach $\lambda \approx 58$. In the range $\lambda \approx 5 - 7$, the interparticle magnetic attraction forms – in a sufficiently strong external field – long and almost linear particle chains. In a weak magnetic field, the chains collapse into dense globules. Therefore, these fluids could not exist. These physical scenarios would approach those of magneto-rheological suspensions (MRS), as suspensions of magnetic globules (i.e. big aggregates of single-domain particles) represent a variety of MRS, but having little in common with ferrofluids. This would obviously be outside the scope of this work.

Although particles with diameter $d \sim 35nm$ seem unrealistic, ferrofluids with larger particle's diameter of $d = 24nm$ made of CoNi and others composed of fiberlike CoNi particles of $56nm$ in length and $6.6nm$ in width have been reported in the literature [66]. Such ferrofluids have greater intensity of the magnetorheological (MR) effect [1], which results in the development of a larger yield stress and viscosity upon magnetic field application. However, they are less stable than conventional ferrofluids, as magnetostatic forces dominate Brownian motion [1]. Although less stable, they have properties between the conventional ferrofluids and magnetorheological

fluids, making them good candidates for applications that require stability and moderate MR effect [1].

A brief discussion about the choice of magnetization model

Figure (4.1) displays total magnetization $M = \sqrt{M_x^2 + M_y^2}$ profiles for the fully developed flow obtained by the three magnetization models presented in section 2.1.3. Two different configurations of the Péclet number are shown. In both cases, the hydrodynamic timescale is greater than the magnetic relaxation time of the particles; however, in one case, the former is ten times greater than the latter ($Pe = 0.1$) and in the second case, twice as large ($Pe = 0.5$).

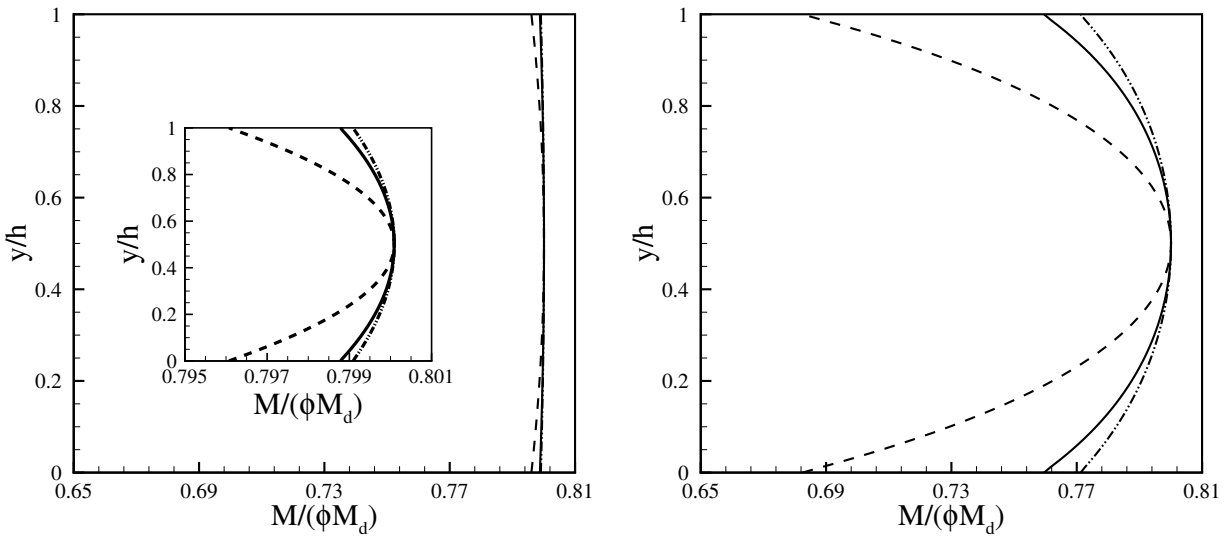

Figure. 4.1: Total magnetization profiles obtained for the fully developed flow. - - - represent the first magnetization model (Eq. (2.27)); — represent the second magnetization model (Eq. (2.31)) and -··- represent the third magnetization model (Eq. (2.32)). In all figures, Re = 5000, α = 5 and ϕ = 0.05. In (a) Pe = 0.1 and (b) Pe = 0.5.

Lower Péclet number configurations are associated with a more magnetic state in which hydrodynamics is not able to significantly disturb the magnetization field. This occurs due to higher relative magnitudes between the hydrodynamic timescale, when compared to the magnetic relaxation time of the particles, leading to weakly non-equilibrium states. In the case of configurations with a larger Péclet number, the hydrodynamic effects become more prominent and lead to non-equilibrium states. In simple words, the Péclet number measures the relative importance between

Brownian and hydrodynamic convective timescales. Configuring numerical settings of the Péclet number is a way of interacting with the timescales of the problem. However, it is important to restrict the range of variations, as very high Péclet numbers can lead to non-physical consequences, as they may be outside of realistic configurations in which magnetic fluids exist and have stable properties.

A first glance in Fig. (4.1) reveals different magnetization profiles produced by the three different models in the two different Péclet number configurations. All models recover the equilibrium magnetization value $M_0 = 0.8$, predicted by Langevin's model - Eq. (2.19) -, in the center (where vorticity is null - check Fig. (4.10b) -). However, they diverge differently from equilibrium along the cross section.

Under the weakly non-equilibrium configuration ($Pe = 0.1$), a more detailed inspection in Fig. (4.1a) shows that deviations between models occur only in third decimal places. In weakly non-equilibrium states, the models predict very similar results in the studied dimensionless field α configuration, as discussed in section 2.1.3. Thus, any of the three models is suitable for use. As the first model is the easiest to implement numerically, this model should be implemented to simulate weakly non-equilibrium situations.

On the other hand, in the higher Péclet number configurations, as shown in Fig. (4.1b), the second - Eq. (2.31) [42] - and third - Eq. (2.32) [40] - models predict similar results, however, there is a large discrepancy between these models and the first - Eq. (2.27) [26] -, mainly in the magnetization close to the walls. Right on the walls, the deviations reach $\approx 10.1\%$ between the first [26] and second [42] models and $\approx 11.5\%$ between the first [26] and third [40] models. Likewise, it reaches only $\approx 1.5\%$ between the second [42] and third [40] models. The higher the shear rate, the greater the discrepancy between the first [26] and third [40] models, according to Shliomis [40]. It is interesting to note that the deviations increase as one approaches the walls. On the other hand, they decrease towards the center, where all models collapse to the same predicted value of equilibrium magnetization M_0.

In short, for weakly non-equilibrium situations, the first [26] magnetization model should be used, as it is much simpler to implement than the others. The second [42] model, however, guarantees the correct description of the magnetization field, even if the equilibrium deviation is large [40]. However, as the third [40] model is simpler than the second [42] and is also valid for describing non-equilibrium situations, it should be used for a wide range of applications [21].

Regarding the time that the simulations took to be carried out in each case, after some tests, it was observed that $t_{first} < t_{second} < t_{third}$, where $t_{second} \approx 1.21 t_{first}$ and $t_{third} \approx 1.33 t_{first}$. In this analysis, t_{first}, t_{second} and t_{third} corresponds to the time the simulations took complete when applying the first [26], second [42] and third [40] magnetization models, respectively. That said, the second model - Eq. (2.31) [42] - was used in the following results, as it describes very well real magnetic fluids for any values of α and $\Omega\tau$ configurations [40].

A brief discussion about the problem's timescales

In this section, the timescales responsible for governing the dynamics of the problem are presented. Three different physical timescales have been identified: the Brownian relaxation time of the particles τ_B; the magnetic timescale τ_{mag} associated with the applied magnetic field and the hydrodynamic timescale τ_{hydro} associated with the characteristics and geometry of the flow. In simple words, the magnetic timescale τ_{mag} is associated with an intrinsic timescale related to viscosity, such as how the dissipation of momentum is altered when in the presence of a magnetic field.

Table. 4.4: Typical timescales of the problem.

Time scales	Mathematical expression
Brownian	$\tau_B = \frac{3\eta V_p}{\kappa_B T}$
Magnetic	$\tau_{mag} = \frac{3\eta V_p}{\mu_0 m H}$
Hydrodynamic	$\tau_{hydro} = \frac{h}{U}$

It is important to note that the particle's diameter play an important role in both the Brownian and the magnetic timescales. In addition, the duct's geometry is strictly related to the hydrodynamic timescale. The magnetic timescale is confined to typical intervals, as its value depends on the magnitude of the applied magnetic field. It is a balance between these timescales that will govern all physical phenomena observed in the simulations; therefore, it is of great importance to estimate the order of magnitude of each individual timescale. It is important to highlight that these timescales depend on the properties of the ferrofluids, being, therefore, different for each ferrofluid present in Tab. (4.1). The estimates of these timescales are presented in Tab. (4.5) for

all ferrofluids presented in Tab. (4.1). For the magnetic timescale, magnetic fields were considered stronger than the Earth's magnetic induction field on its surface ($B_{Earth} \approx 5 \times 10^{-5}$T) [348] and smaller than $1T$.

Table. 4.5: Timescales of different commercially available ferrofluids with diameter $d = 13nm$ taken from Rosensweig [3] at 298K, $Re = 5000$ and $Pe = 0.5$.

Carrier liquid	τ_{mag} (s) $[5 \times 10^{-5}T < \mu_0 H < 1T]$	τ_{hydro} (s)	τ_B (s)
Diester	1.01E-02 < τ_{mag} < 5.04E-07	1.26E-04	6.29E-05
Hydrocarbon	4.04E-04 < τ_{mag} < 2.02E-08	5.03E-06	2.52E-06
Hydrocarbon	8.07E-04 < τ_{mag} < 4.04E-08	1.01E-05	5.03E-06
Fluorocarbon	3.36E-01 < τ_{mag} < 1.68E-05	4.19E-03	2.10E-03
Ester	1.88E-03 < τ_{mag} < 9.42E-08	2.35E-05	1.17E-05
Ester	4.04E-03 < τ_{mag} < 2.02E-07	5.03E-05	2.52E-05
Ester	4.71E-03 < τ_{mag} < 2.35E-07	5.87E-05	2.94E-05
Water	9.42E-04 < τ_{mag} < 4.71E-08	1.17E-05	5.87E-06
Water	1.35E-03 < τ_{mag} < 6.73E-08	1.68E-05	8.39E-06
Polyphenylether	1.01E+00 < τ_{mag} < 5.04E-05	1.26E-02	6.29E-03

Beforehand, it is noted that, in all cases, the hydrodynamic timescale τ_{hydro} is greater than the relaxation time of the particles τ_B, which means that the hydrodynamic effects will take longer to manifest when compared to the Brownian's. A relation between the magnitudes of the magnetic timescale τ_{mag} and the others depends on the strength of the applied magnetic field. However, assuming commonly applied magnetic fields ($\alpha \geq 1$), in all cases the magnetic timescale is less than or equal (i.e. $\tau_{mag} = \tau_B$ when $\alpha = 1$) to the Brownian and hydrodynamic timescales. Therefore, it must be borne in mind that magnetic effects will always occur faster than hydrodynamic and Brownian effects. This "timescale dance" is responsible for governing the complex nature of this problem.

The timescales presented in Tab. (4.4) were used to compose two important physical parameters of the problem, that is, α and Pe, as they will be used to interpret the results.

$$\alpha = \frac{\tau_B}{\tau_{mag}}; \quad Pe = \frac{\tau_B}{\tau_{hydro}} \quad \rightarrow \quad \frac{\alpha}{Pe} = \frac{\tau_{hydro}}{\tau_{mag}} \tag{4.3}$$

From Equation (4.3), it is possible to see that the non-dimensional magnetic field α is given by a ratio between the Brownian and magnetic timescales, that is, the larger the applied magnetic

field, the faster the magnetic effects are manifested, because the value of the magnetic timescale τ_{mag} is decreased under such conditions.

As already mentioned, a ferrofluid flow in a magnetic field is accompanied by a coupling between hydrodynamic and magnetic effects. From Equation (4.3), it is noted that the combination of physical parameters responsible for pointing out a possible interplay between the magnetic and hydrodynamic timescales will be a combination of the parameters (α, Pe), since their ratio α/Pe is a relation between these timescales ($\alpha/Pe = \tau_{hydro}/\tau_{mag}$).

The terms associated with hydrodynamics in the magnetization models are linked to the Péclet number, since this number has the hydrodynamic timescale in its own definition. One notes the presence of the Péclet number associated with the mechanisms related to the deviation from equilibrium magnetization, as well as the precession restoring mechanism in the magnetization models. The relation α/Pe appears explicitly in all magnetization models multiplying the precession terms. In common applied magnetic fields under the simulated hydrodynamic physical condition, this relation will always be a positive number larger than 1, since $\tau_{mag} < \tau_{hydro}$, evidencing the importance of the restorative precession mechanism in non-equilibrium magnetization dynamics. In addition, in Eqs. (2.49), (2.50) and (2.51), the presence of $Pe^{-1} = \tau_{hydro}/\tau_B$ is noted. In this case, since $\tau_{hydro} > \tau_B$, the terms associated with the deviation from equilibrium magnetization will also be significant, since the quotient τ_{hydro}/τ_B always lead to a number greater than 1. That said, it is clear that hydrodynamic effects will effectively affect the magnetization field.

On the other hand, the only terms associated with magnetism in the equation of motion - Eq. (2.48) - are preceded by the relation:

$$Re_m^{-1} = \frac{3\phi\alpha}{PeRe} \tag{4.4}$$

In Equation, Re_m is the magnetic Reynolds number. For fixed ϕ and Re scenarios, this relation is reduced to α/Pe, described by the quotient of the hydrodynamic and magnetic timescales. Since $\tau_{mag} < \tau_{hydro}$ in usual applied magnetic fields under the simulated hydrodynamic conditions, this quotient will always lead to a positive number greater than 1. However, as this work deals with diluted ferrofluids ($\phi \sim 5\%$) in consistently large Reynolds numbers, the relation $\phi/Re = 10^{-5}$ for $\phi = 0.05$ and $Re = 5000$, so that Re_m^{-1} will always lead to a much smaller number

than the unit. Therefore, it is assumed that, although hydrodynamics plays a major role in non-equilibrium magnetization dynamics, magnetization effects would not lead to significant changes in hydrodynamic fields, since the magnetic effects are not numerically significant in the equation of motion due to the smallness of Re_m^{-1} under the simulated physical conditions.

4.1.2 Flow's entrance region

This work investigates the hydrodynamic-magnetic coupling in the context of a non-equilibrium ferrofluid flow, using as a case study a flow between two parallel plates. Such flows are divided into two basic regions: 1) The entrance region and 2) the fully developed region, as shown in Fig. (1.1).

The hydrodynamic entrance region is defined as the region in which the fluid entering the duct develops a non-uniform velocity profile due to the propagation of viscous forces that arise close to the walls. Its length L_h is determined as the section in which the hydrodynamic boundary layers - which appear on the walls and increase their thickness δ_h in the downstream direction - meet in the center of the duct, as indicated in Fig. (4.2a). After this region, the velocity profile remains unchanged. The mechanism for developing the velocity profile is well-known in the literature. Due to the diffusive nature of viscosity and the non-slip boundary condition, the fluid layers in contact with the walls gradually resist the movement of the adjacent ones. For mass conservation - $(\nabla \cdot \boldsymbol{v}) = 0$ -, the velocity of the layers in the center of the duct must increase as a way to balance the decrease in the velocities of the layers close to the walls, generating a velocity gradient [349, 222, 350].

Figures (4.2a) and (4.2b) represent typical velocity and magnetization fields, respectively. In Figure (4.2a), the aforementioned hydrodynamic entrance length L_h and the hydrodynamic boundary layer thickness δ_h are identified. The main feature of Fig. (4.2b) is the presence of a magnetization entrance region, characterized by a magnetization entrance length L_m and what we call an analogous magnetization boundary layer thickness δ_m. The presence of a magnetization entrance region is strictly linked to the hydrodynamic-magnetic coupling that governs the physics of the problem. As the velocity field develops due to a balance between advective and diffusive mechanisms, as in a classical boundary layer problem, it leads to a developing region in the vorticity field that is strictly linked to the dynamics of magnetization, ultimately leading to a magnetization

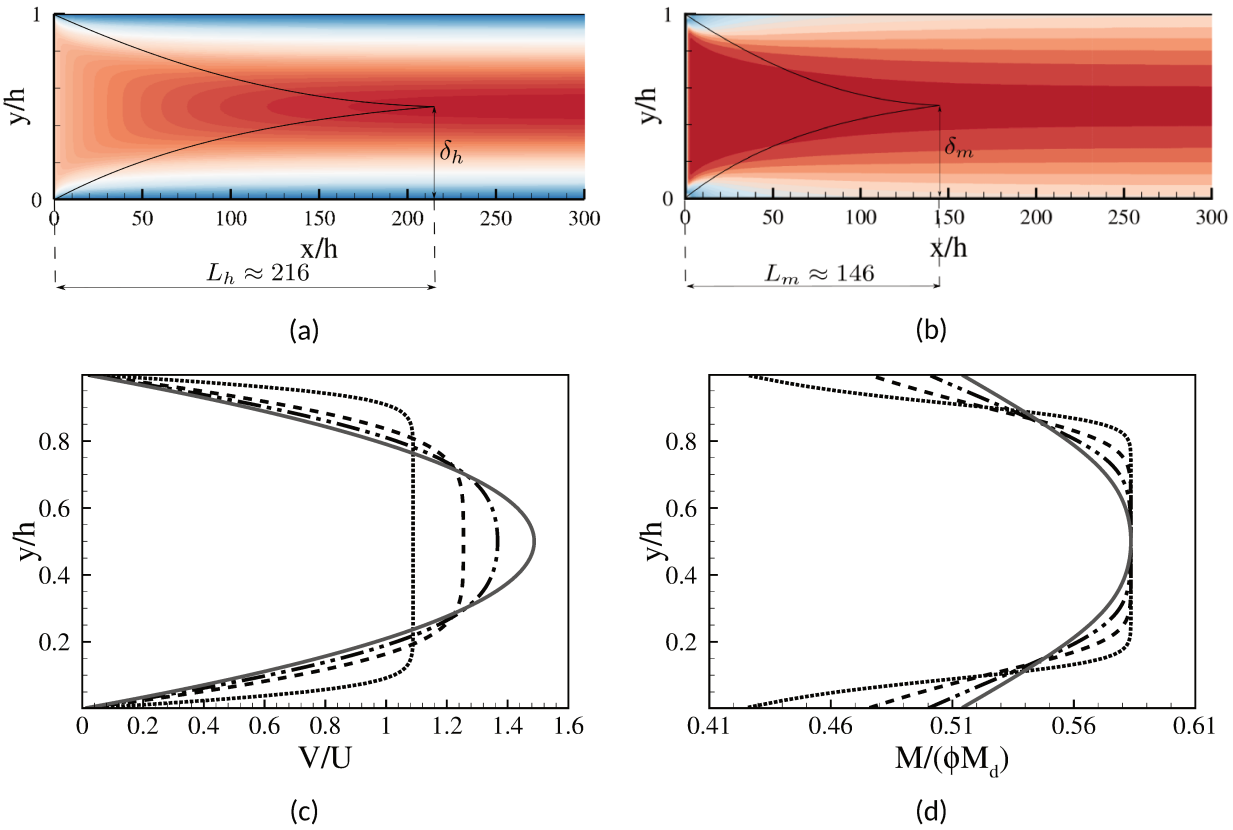

Figure. 4.2: (a) Velocity field. (b) Magnetization field. (c) Velocity profiles obtained for different sections in the duct. (d) Magnetization profiles obtained for different sections in the duct. For (c): The dotted line ·····, the dashed line - - -, the chain line -·-and the solid line —— represent sections x/d = 2.5, 30, 70 and 230, respectively. For (d): The dotted line ·····, the dashed line - - -, the chain line -·-and the solid line —— represent sections x/d = 10, 30, 70 and 160, respectively.. In all figures: α = 1, Pe = 0.5, Re = 5000, ϕ = 0.05 and λ = 2.9. In (a): δ_h and L_h represent the hydrodynamic boundary layer thickness and the hydrodynamic entrance length, respectively. In (b): δ_m and L_m represent the "magnetization boundary layer" thickness and the magnetization entrance length, respectively.

.

developing region. When comparing the differences between the length of the thermal and hydrodynamic entrance regions of a flow heated by the wall, it is noted that the relation L_h/L_T (L_T is the thermal entrance length) is associated with the Prandtl number, which is a dimensionless parameter that represents the ratio between two diffusive coefficients. This characteristic in particular led us to speculate the existence of an *equivalent diffusive coefficient of magnetization*. Generally, the diffusive coefficients are material dependent; however, in this context, this coefficient may be flow dependent. In this specific scenario, we speculate that the competition between vorticity and restorative magnetic torques would function as an equivalent diffusive mechanism,

leading to something analogous to a magnetization boundary layer, as indicated in Fig. (4.2b).

As indicated, the magnetization entrance region is developed by a balance of advective/diffusive physical mechanisms, which leads to the development of the magnetization boundary layer up to the entrance length. This indicates the existence of a diffusive magnetization mechanism. In an analogy to the purely hydrodynamic regime, in which the diffusion of momentum by viscous effects leads to a term of the type ($\nabla^2 \boldsymbol{v}$), we speculate the modeling of such diffusive terms in the magnetization relaxation equation in a form like:

$$\frac{\partial \boldsymbol{M}}{\partial t} + (\boldsymbol{v} \cdot \nabla)\boldsymbol{M} \sim \nu_{mag} \nabla^2 \boldsymbol{M} \tag{4.5}$$

In Equation (4.5), ν_{mag} is the equivalent diffusive coefficient of magnetization. It is important to mention that this term on the right side of Eq. (4.5) does not appear explicitly in any of the magnetization models studied in this work. However, it is important to note that the mechanisms of vorticity and restorative magnetic torques, present in the relaxation models, would combine and act as this equivalent diffusive mechanism.

For numerical purposes, the entrance length was defined as the non-dimensional distance from the entrance of the duct to the point where the maximum deviation between the fully developed profile of any variable and that of that specific section is less than 1%. For this specific choice of physical parameters, the hydrodynamic entrance length is $L_h \approx 216$ and the magnetization entrance length is $L_m \approx 146$, indicating that the magnetization field develops in smaller regions.

Figures (4.2c) and (4.2d) show velocity and magnetization profiles obtained in different sections of the duct, respectively. As expected, the velocity profiles are very flat close to the duct's entrance, as the inlet flow is uniform. As diffusive mechanisms begin to occur in the dynamics of the problem, a velocity gradient is formed until the velocity field remains unchanged in the fully developed region, assuming a parabolic shape, as indicated in the evolution of the velocity profiles in Fig. (4.2c). Similarly, the magnetization profiles are quite flat near the entrance of the duct, since the inlet fluid is demagnetized, in the absence of an applied magnetic field. When the fluid enters the duct, it begins to magnetize, since it is now subjected to the action of a magnetic field, causing the magnetic particles to begin to align in its direction. The magnetization then develops due to the speculated diffusive magnetic mechanism until it remains unchanged in the fully developed

magnetization region, as portrayed in Fig. (4.2d). In addition, it is possible to notice in Fig. (4.2d) that the magnetization values do not change in the center of the duct along the development region. As there are no hydrodynamic effects in the center of the duct, where vorticity is null - Fig. (4.10b) - , there will be no mechanisms that deviate magnetization from its equilibrium value, predicted by Eq. (2.22), which is the studied physical scenario ($\alpha = 1$, $\phi = 0.05$ and $\lambda = 2.9$) leads to $M/\phi M_d = 0.583$. This observation is best depicted in Fig. (4.5).

The functional dependency of four physical parameters of the problem was identified in this developing region, namely, the non-dimensional magnetic field α, the relaxation time of the particles, which is directly associated with the Péclet number Pe, the dipole's coupling parameter λ and the volume fraction of particles ϕ.

The developing region is associated with the interplay between hydrodynamic and magnetic effects. When the field is increased, the magnetic influence dominates magnetization dynamics and the particles are not able to efficiently perceive the effect of vorticity, since the magnetic torque works more efficiently, fixing the particles dipole moment in the direction of the field, which, as a result, leads to faster alignment in the direction of the field, leading to shorter entrance lengths. This behavior is seen in Fig. (4.3a) for $\alpha \gtrapprox 4$. For the interval $1 \lessapprox \alpha \lessapprox 4$, an interesting but unforeseen behavior is manifested, as a change in the figure's trend is observed. For $1 \lessapprox \alpha \lessapprox 3$, the expected response of a decrease in the entrance region is observed when the field intensity increases. However, when $3 \lessapprox \alpha \lessapprox 4$, the opposite behavior is observed, since L_m increases with α. This odd behavior confirms the complex nature of the problem and will be manifested in different ways in the next results. We assume that the unexpected change in behavior is associated with changes in the intensity of the dominant mechanisms that govern non-equilibrium magnetization, so that, in this specific physical scenario (when $3 \lessapprox \alpha \lessapprox 4$), the action of hydrodynamic effects would overcome the general damping action of the magnetic field and interparticle interactions -see Figs. (4.3c) and (4.3d) -, leading to larger developing regions.

On the other hand, changes in L_m under variations of Pe, ϕ and λ are not accompanied by changes in behavior, as shown in Figs. (4.3b), (4.3c) and (4.3d). When the Péclet number decreases, the physical scenario approaches equilibrium, which means that there is no space for an effective interaction between the physical mechanisms, leading to smaller development regions, as shown in Fig. (4.3b). In this case, the intensity of the hydrodynamic action in non-equilibrium magnetization dynamics is reduced, leading to an ineffective misalignment of the particles by the action of vorticity, which, in turn, evidences the response of the magnetic mechanism which, as

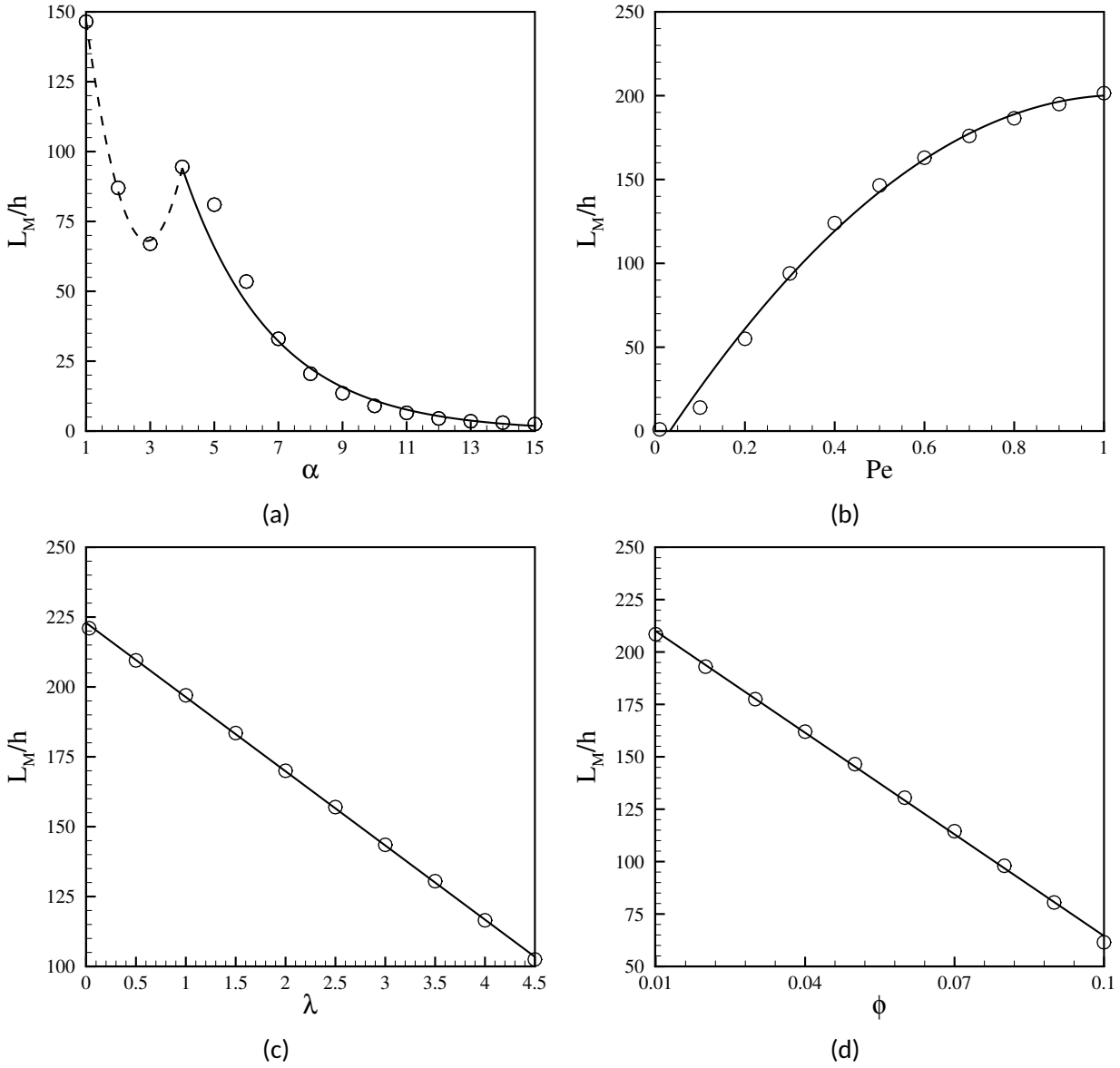

Figure. 4.3: Magnetization entrance length as a function of (a) α, (b) Péclet, (c) λ and (d) ϕ. In (a): Re = 5000, ϕ = 0.05, λ = 2.9 and Pe = 0.5. In (b): Re = 5000, ϕ = 0.05, λ = 2.9 and α = 1. In (c): Re = 5000, ϕ = 0.05, α = 1 and Pe = 0.5. In (d): Re = 5000, α = 1, λ = 2.9 and Pe = 0.5. The curve fits obtained are as follows: In (a): - - - L_m = 251.5 - 126.3α + 21.75α^2; —— $L_m = \exp(-0.3585\alpha + 5.979)$. In (b): —— L_m = -13.19 + 410.1Pe - 196.9Pe^2; In (c): —— L_m = 222.9 - 26.55λ; In (d): —— L_m = 226.1 - 1616ϕ.

.

generally observed in Fig. (4.3a), leads to smaller developing regions.

As for cases of variations in λ and ϕ, an increase in these parameters resulted in smaller developing regions. It is important to mention that both the volume fraction of particles ϕ and

the dipole's coupling parameter λ act to increase the intensity of the dipolar interactions between the particles. In many cases, real ferrofluids are composed by aggregates of magnetic grains, which are provided by the magnetic dipole-dipole interparticle interactions [16], described by the dipole's coupling parameter λ, which must be large enough to form long chains [16]. When in the absence of a magnetic field, the distribution of particles in ferrofluids is disordered. However, when the magnetic particles self-assemble, there is a tendency to align their magnetic dipole moments in the direction of the magnetic field due to neighboring particles or applied magnetic fields [15, 191, 192], resulting in anisotropy of the interactions, allowing the magnetic nanoparticles to form one-dimensional chains/wires, rings, two-dimensional aggregates or even three-dimensional super-lattices [67]. A ferrofluid represents a set of these flexible chains [16, 195, 198]. Many experiments and analysis show that forces of magnetic dipole-dipole interactions in strong magnetic fields cause large magnetic particles to form chains and aggregates. These, in turn, can greatly affect the macroscopic properties of ferrofluids, such as their viscosity, even in physical scenarios of low particle concentration [194, 195, 196, 197]. For instance, the presence of aggregates is used as a macroscopic approach to understand the strong magnetoviscous effect exhibited by ferrofluids. The intensity of the dipolar interactions also appears to have a huge effect on the magnetization entrance region, as indicated in Figs. (4.3c) and (4.3d). In this case, when the fluid concentration is increased (augmenting ϕ) or when the fluid possess particles with larger diameters (augmenting λ), the effect of the dipolar interactions in non-equilibrium magnetization is perceived as a way to replace the field's effect, since there is a general trend of an increase in the effect of the local field generated by the presence of the particle clusters. Thus, increases in both parameters lead to decreases in the developing region, in a result analogous to that generally seen in Fig. (4.3a), where increases in α generate decreases in L_m.

At this point, results on how the magnetization entrance length L_m behaves in other physical configurations of ϕ, Pe and λ as a function of α are presented.

First of all, it is interesting to note that, in all the cases presented in Fig. (4.4), for sufficiently strong fields, all curves present the same behavior of converging to the same magnetization entrance length L_m. As a general trend, when the field's effect on non-equilibrium magnetization dynamics becomes strong enough, it appears to dominate all other physical mechanisms leading to smaller developing regions. Making an analogy with the purely hydrodynamic case, where the hydrodynamic entrance length L_h is a direct function of the Reynolds number Re (i.e. for laminar pipe flow, $L_h/h = 0.05Re$ [351]), it is observed that that the lower the Re, the smaller the development region. Since Re is inversely proportional to the diffusion coefficient - Eq. (2.52) -,

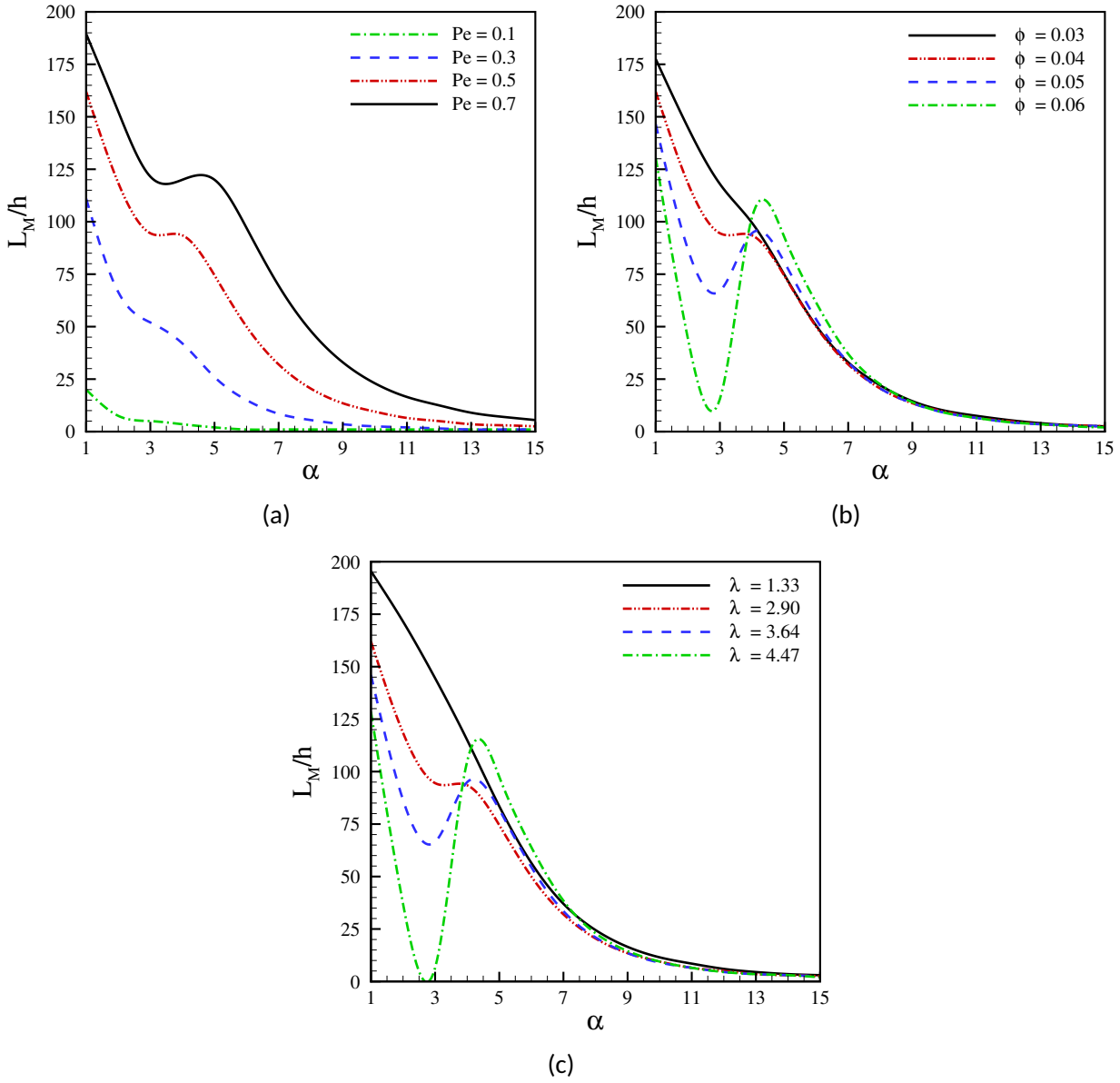

Figure. 4.4: Magnetization entrance length as a function of α under different physical configurations. (a) Different Péclet scenarios. In this figure: Re = 5000, ϕ = 0.04 and λ = 2.9. (b) Different ϕ scenarios. In this figure: Re = 5000, Pe = 0.5 and λ = 2.9. (c) Different λ scenarios. In this figure: Re = 5000, ϕ = 0.04 and Pe = 0.5.

the higher the diffusion coefficient, the smaller the entrance region. Therefore, the length of the entrance region is inversely associated with the diffusion coefficient. As indicated by the general trend observed in Fig. (4.4), the increase in field strength leads to reductions in the magnetization entrance length, so that increases in α are accompanied by increases in the equivalent magnetization diffusion coefficient ν_{mag}, making these two variables, in general, directly proportional to

each other.

Another trend observed in Fig. (4.4) is the presence of a change in the behavior of L_m in the regions of moderate fields ($\alpha \approx 3$), already observed in Fig. (4.3a), which becomes much more pronounced under physical conditions of intense hydrodynamic effects (greater Pe) and intense dipolar interactions (greater λ and ϕ). In these moderate field regions, the field effects are not strong enough to dominate non-equilibrium magnetization dynamics, and the effects of non-equilibrium flow can compete with the magnetic field-particle and particle-particle interaction mechanisms in order to substantially alter the equivalent magnetization diffusion field. On the other hand, when the field becomes strong enough, the other mechanisms become much less intense, and the field determines the behavior of the magnetization entrance region, bringing it to a fixed value, as already discussed.

Figure (4.4a) depicts L_m as a function of α in different Pe configurations. It is observed that for lower Pe configurations, in which a less pronounced magnetic-hydrodynamic coupling is present, the effects of the field are dominant and a tendency to decrease the entrance region is observed as the field is increased. This trend is generally observed in Fig. (4.4). For moderate Pe configurations, in which hydrodynamics has a more pronounced effect, it is observed that the hydrodynamic mechanism is able to compete effectively with the other mechanisms in non-equilibrium magnetization dynamics in the regions of moderate field ($\alpha \approx 3$). It is also observed that, in the same α configurations, increases in Pe lead to increases in L_m, as also shown in Fig. (4.3b). Therefore, it is concluded that the equivalent magnetization diffusion coefficient ν_{mag} is, in general, inversely proportional to the Péclet number.

Figures (4.4b) and (4.4c) show L_m as a function of α in different ϕ and λ configurations, respectively. Overall, both figures show very similar results. Both parameters work in a way to strengthen the intensity of the interparticles interactions when increased. In regimes of low dipolar interactions intensity (small ϕ and λ), non-equilibrium magnetization dynamics is effectively governed by field effects, in a way that increasing values of α lead to smaller values of L_m. This scenario is also the case for low intensity fields ($\alpha \lessapprox 3$) under intense dipolar interactions. Under intense dipolar interactions, the particles tend to form aggregates, which, in turn, generates an increase in the effect of the local field, which is manifested by the presence of particle's clusters, leading to a decrease in the entrance region. In regions of moderate fields ($3 \lessapprox \alpha \lessapprox 4$), there is an interplay between timescales in which dipolar interactions and particle-field interactions are somewhat replaced by the equivalent effect of hydrodynamics, which becomes the main

mechanism governing magnetization dynamics in the entrance region and, therefore, an increase in L_m is observed, similar to that observed in Fig. (4.3b). As soon as the magnetic field is increased, particle-field interactions gradually dominates all mechanisms and, although dipolar interactions and hydrodynamics can be intense, they become weak in relation to the field and, as a general trend, the curves converge towards a single value, as already discussed. It is also observed that, for a fixed value of α, increases in the intensity of dipolar interactions lead to smaller developing regions, similar to that shown in Figs. (4.3c) and (4.3d). Thus, increases in ϕ and λ lead to increases in the equivalent magnetization diffusion coefficient ν_{mag}.

The results obtained in Figs. (4.3) and (4.4) are indicatives of the characteristics of the non-linear equivalent magnetization diffusion coefficient ν_{mag} postulated in Eq. (4.5), in terms of how it varies and with what it varies. As there is no analogous magnetization diffusion material coefficient, we propose one whose functional dependence on the problem's parameters is given, in a first estimate, based on the results presented in Figs. (4.3) and (4.4), by:

$$\nu_{mag} \sim \frac{\lambda \phi \mathrm{e}^{\alpha}}{Pe^{C}} \tag{4.6}$$

In Equation (4.6), C is a constant.

Overall, these results seem to indicate the possibility of controlling the development of the flow's magnetization field through the applied magnetic field (affecting α), size distribution of the particles (affecting λ), the concentration of the fluid (affecting ϕ) and flow rate (affecting Pe), despite temperature T variations (affecting λ and Pe).

In the next sections, the results obtained for the fully developed flow are presented.

4.1.3 Fully developed flow

As observed, the physics of the analyzed problem is mainly altered by four main non-dimensional parameters, namely, the non-dimensional magnetic field α, the Péclet number Pe, the dipole's coupling parameter λ and the volume fraction of particles ϕ. In this section, analyzes of how changes in these parameters affect non-equilibrium magnetization dynamics for the fully

developed flow are presented. The first result presented corresponds to magnetization profiles obtained for the fully developed flow under different physical configurations.

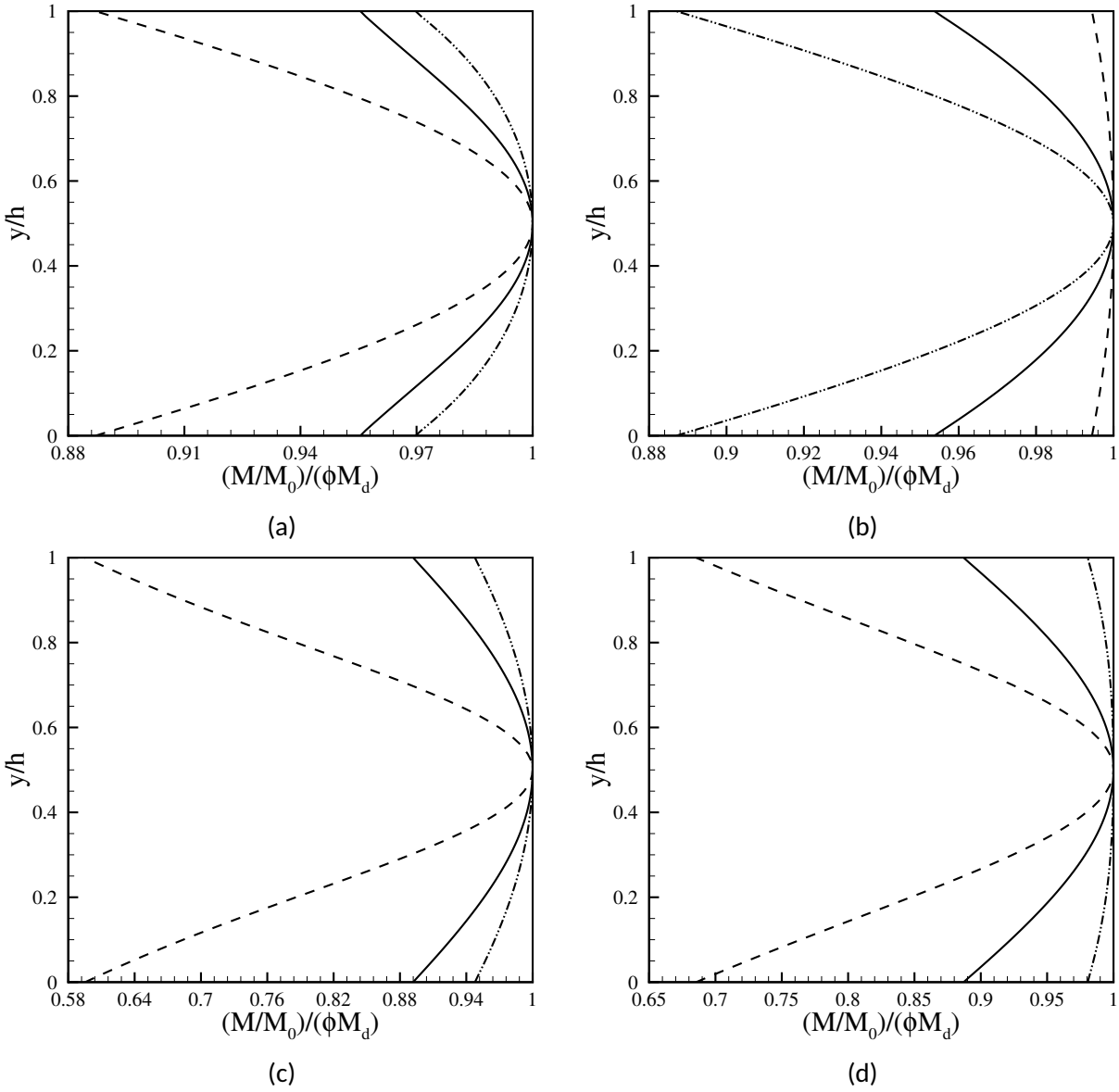

Figure. 4.5: Magnetization profiles for the fully developed flow normalized by their respective equilibrium magnetization values for different (a) α, (b) Péclet, (c) λ and (d) ϕ configurations. In (a): - - - , —— and -·-· represent $\alpha = 1$, $\alpha = 3$ and $\alpha = 5$, respectively. In (b): - - - , —— and -·-· represent $Pe = 0.1$, $Pe = 0.3$ and $Pe = 0.5$, respectively. In (c): - - - , —— and -·-· represent $\lambda = 0.03$, $\lambda = 3$ and $\lambda = 4.5$, respectively. In (d): - - - , —— and -·-· represent $\phi = 0.01$, $\phi = 0.05$ and $\phi = 0.1$, respectively. In (a): $Re = 5000$, $\phi = 0.05$, $\lambda = 2.9$ and $Pe = 0.5$. In (b): $Re = 5000$, $\phi = 0.05$, $\lambda = 2.9$ and $\alpha = 1$. In (c): $Re = 5000$, $\phi = 0.05$, $\alpha = 1$ and $Pe = 0.5$. In (d): $Re = 5000$, $\alpha = 1$, $\lambda = 2.9$ and $Pe = 0.5$.

Figures (4.5a), (4.5b), (4.5c) and (4.5d) depict total magnetization profiles for the fully developed flow normalized by their respective equilibrium magnetization M_0 under different α, Pe, λ and ϕ configurations, respectively. At first glance, Fig. (4.5) shows that variations in any of the four major physical parameters (α, Pe, λ and ϕ) lead to different magnetization profiles, showing the sensitivity of the problem to variations, however small. The obtained profiles are symmetric with respect to the center of the duct and variations do not occur after the development of the magnetization boundary layer. They also seem to be of parabolic nature, having similarity to the velocity profiles in classic Poiseuille flow, demonstrating a probable quadratic nature of the magnetization profiles in relation to the vertical y coordinate of the duct.

In all cases, deviations of the local magnetization are observed in relation to its respective equilibrium value, specially in the regions of greater vorticity (closer to the walls). As briefly described in section , in physical conditions of $Pe = 0.5$, which is the case of Figs. (4.5a), (4.5c) and (4.5d), hydrodynamics is capable of significantly disturbing magnetization dynamics, leading to a complex competition of physical mechanisms. As the particles' dipole moments are considered fixed (i.e. relaxation time is $\tau = \tau_B$), the torque produced by the interaction of the particles with the applied magnetic field $\boldsymbol{H}$ will tend to align them in the direction of the field as soon as it is applied. However, as the fluid is subjected to shear stresses, the torque due to viscous forces tends to rotate the particles in the direction of vorticity, generating a misalignment between the particles' dipole moments and the applied magnetic field [29]. As pointed out in de Carvalho and Gontijo [46], the physical mechanisms responsible for promoting the misalignment of the dipole moments in the direction of the field are weaker in regions of low vorticity (i.e closer to the center), leading to local magnetization values closer to equilibrium. In fact, right in the center, where vorticity is null, the local magnetization value is precisely the predicted equilibrium magnetization M_0, in all cases analyzed. de Carvalho and Gontijo [46] also points out that in regions where the interplay between hydrodynamics and magnetism is more prominent (i.e. regions of higher vorticity), the deviation of magnetization from the equilibrium magnetization is increased, as if the magnetic dipole moments of the particles were less aligned in the direction of the field due to the action of vorticity, leading to lower magnetization values.

Figure (4.5a) shows the influence of the non-dimensional magnetic field α on the magnetization profiles. Different α configurations lead to different polarization states in the ferrofluid, since particle-field interactions are modified according to the intensity of the field. Once the polarization of the ferrofluid is altered, associated with the degree of alignment of the magnetic particles suspended in the fluid, the fluid's magnetic response is significantly altered over the competition

of physical mechanisms, leading to different responses in different regions of the flow, since the intensity of these mechanisms is altered along the duct's cross section. This generates a magnetization profile, which tends to be modified according to the intensity of the physical mechanisms.

Figure (4.5b) depicts magnetization profiles in different Pe configurations. One of its main aspects is that, in low Pe configurations (i.e. $Pe = 0.1$), the magnetization profile obtained is almost linear, with values approximately equal to the predicted equilibrium magnetization M_0. Very small deviations are observed, the largest being around the fourth decimal place. As briefly described in section , in these physical conditions weakly non-equilibrium configurations are observed, as hydrodynamics is not able to significantly deviate local magnetization from its equilibrium value, due to the great nature of the hydrodynamic timescale when compared to the magnetic relaxation time of the particles. For instance, averaging the hydrodynamic and magnetic timescales for all ferrofluids presented in Tab. (4.1) under physical conditions of $Pe = 0.1$, $\alpha = 1$, $Re = 5000$, $\phi = 0.05$ and $\lambda = 2.9$, one obtains a hydrodynamic timescale ten times larger than the magnetic one ($\tau_{hydro} \approx 8.54 \times 10^{-3}$ and $\tau_{mag} \approx 8.54 \times 10^{-4}$). In such physical configurations, the disturbances produced by the flow's vorticity would take longer to manifest, so that they would not be perceived by the particles. At the approaching limit of very low Péclet numbers, magnetization dynamics is mainly governed by a linear magnetization relaxation. Thus, in the absence of perceptible hydrodynamic effects or in the impossibility of being perceived by the magnetic particles, weakly non-equilibrium results are expected. The other profiles presented, for higher Pe configurations present exactly the opposite, where greater deviations from equilibrium are observed. Under these conditions, hydrodynamics play an important role in magnetization dynamics, which means that hydrodynamic effects will manifest themselves most effectively in the complex physical nature of this problem. Once again, it is important to mention that low Péclet number regimes are more suitable for the applications of a large part of the commercially available ferrofluids presented in Rosensweig [3]. However, the objective of this work is to highlight a physical concept, predicted in the governing equations, of a competition of physical mechanisms (mainly magnetic and hydrodynamic ones) that lead to disturbances in non-equilibrium magnetization dynamics. These mechanisms would only manifest themselves clearly under large Péclet number configurations, as shown in Fig. (4.5b).

As modifications in the dipole's coupling parameter λ and in the volume fraction of particles ϕ lead to changes in the intensity of the interparticles' interactions, these modifications would lead to different responses in the competition of mechanisms that alter the fluid's magnetic response when in the presence of a magnetic field. Such changes would lead to modifications in the mag-

netization profiles, showing the importance of particles' aggregates in ferrofluids non-equilibrium magnetization dynamics, as indicated in Figs. (4.5c) and (4.5d), which portray magnetization profiles under different λ and ϕ configurations, respectively. Note that the greater the intensity of the dipolar interactions (higher λ and ϕ), the smaller the deviation from equilibrium magnetization. As already discussed, particles' aggregates tend to increase the local field, which, in turn, acts in conjunction with the particle-field interaction in order to overcome the hydrodynamic effect, causing the particles to become more aligned in the field's direction, resulting in a magnetic response closer to that of the predicted equilibrium magnetization $M_0/\phi M_d$ in Eq. (2.22).

As seen in Fig. (4.5), the closer to the walls, the greater the deviation between the local magnetization values and the predicted equilibrium values. Figure (4.6) shows the behavior of the maximum deviation $\Delta M_{max} = M_{center} - M_{wall}$ obtained, where M_{center} and M_{wall} are the magnetization values in the center of the duct and on the wall, respectively, as functions of the four main physical parameters (α, Pe, λ and ϕ).

Overall, Figure (4.6) shows that variations in any of the physical parameters of the problem affect the way the maximum deviation ΔM_{max} behaves. Under variations of α there are two distinct patterns. For Pe variations, it is noted that the greater the Pe, the greater is ΔM_{max} and, finally, for both increases in λ and ϕ, the maximum deviation is decreased.

Figure (4.6a) represents ΔM_{max} as a function of the non-dimensional magnetic field α. Different behaviors of ΔM_{max} are observed as α is increased. ΔM_{max} decreases with α when $1 \lessapprox \alpha \lessapprox 2$ and $\alpha \gtrapprox 4$ and it increases with α when $2 \lessapprox \alpha \lessapprox 4$. As the intensity of the non-dimensional field α is increased, field effects dominate magnetization dynamics, preventing any hydrodynamic perturbations due to vorticity gradients to be efficiently perceived. In this scenario, flow's vorticity would not be able to misalign the magnetic particles from the orientation of the magnetic field, leading to an equilibrium behavior of magnetization at the approaching limit of $\alpha \gg 1$. According to Eq. (4.3), α is defined as a ratio between the particle's relaxation timescale and the magnetic timescale; therefore, the higher this parameter, the less the relative importance of magnetic timescale. In this physical scenario, the magnetic effects are more noticeable in the magnetization dynamics, as they manifest themselves stronger or more quickly. For smaller values of α, vorticity is able to misalign the particles' dipole moments, leading to an interesting competition of physical mechanisms: the demagnetizing effect due to the action of vorticity and the external magnetic torque due to the applied field, which seeks to realign the dipoles in the direction of the field. When the field strength is decreased, there is more flexibility in these mechanisms, as

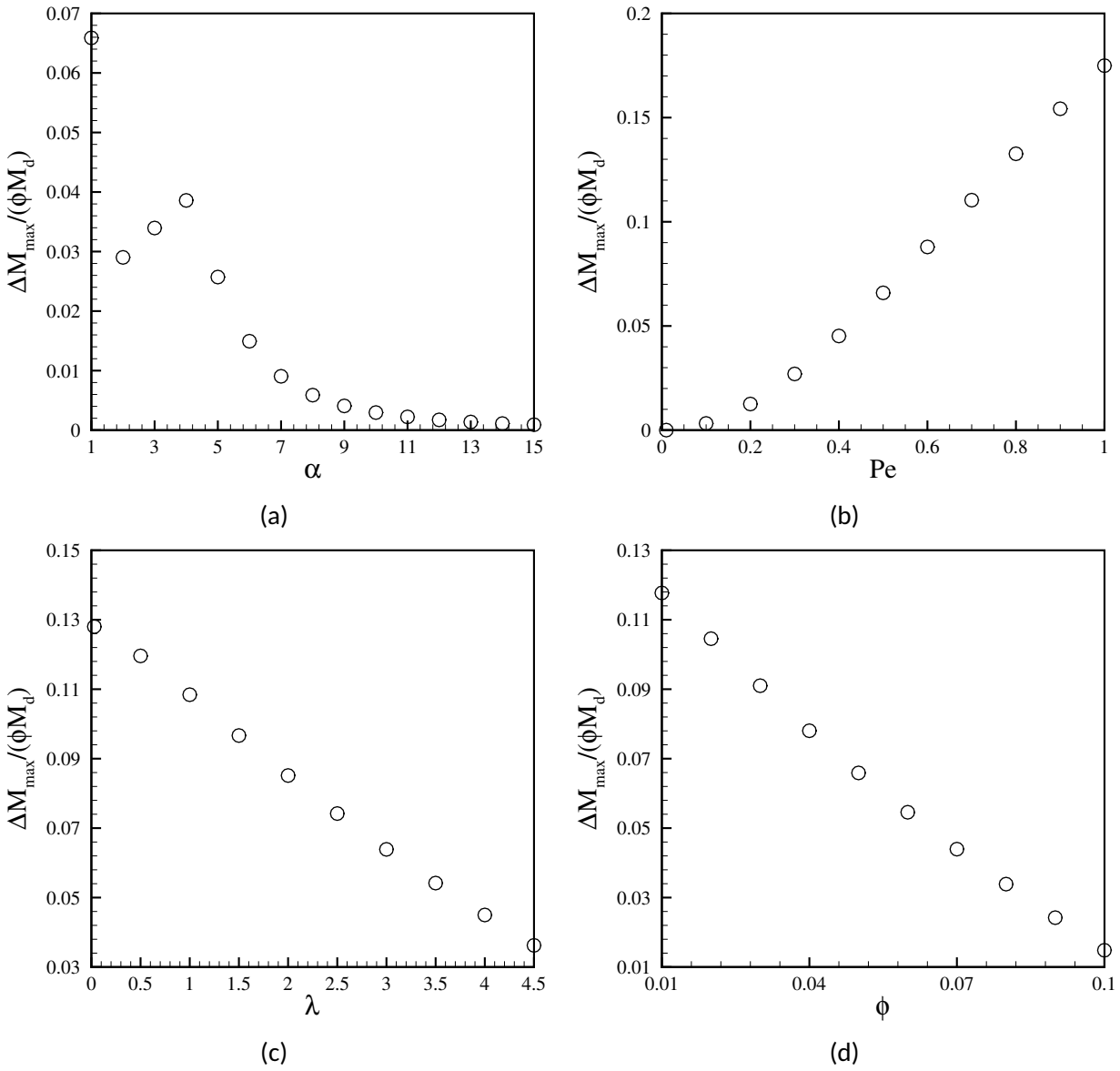

Figure. 4.6: Maximum magnetization deviation from the equilibrium magnetization M_0 as a function of (a) α, (b) Pe, (c) λ and (d) ϕ. In (a): $Re = 5000$, $\phi = 0.05$, $\lambda = 2.9$ and $Pe = 0.5$. In (b): $Re = 5000$, $\phi = 0.05$, $\lambda = 2.9$ and $\alpha = 1$. In (c): $Re = 5000$, $\phi = 0.05$, $\alpha = 1$ and $Pe = 0.5$. In (d): $Re = 5000$, $\alpha = 1$, $\lambda = 2.9$ and $Pe = 0.5$.

indicative of a deterministic mechanism associated with the field that is dominated by the effects of Brownian fluctuations.

As discussed above, a decrease in the value of ΔM_{max} with an increase in α is expected, because in these conditions the effects of the field dominate magnetization dynamics, making it

extremely difficult for vorticity to misalign vector fields $\boldsymbol{M}$ and $\boldsymbol{H}$. This trend was observed, in the simulated physical conditions, in the intervals $1 \lessapprox \alpha \lessapprox 2$ and $\alpha \gtrapprox 4$, however, when $2 \lessapprox \alpha \lessapprox 4$, the behavior is exactly the opposite. In the interval $2 \lessapprox \alpha \lessapprox 4$, hydrodynamics effects seem to dominate magnetization dynamics, so that ΔM_{max} increases with α. This very interesting behavior was also observed as a trend in Fig. (4.3a) and Fig. (4.4), confirming the complex nature of the analyzed problem. It becomes clear that not only the intensity of the magnetic field is primarily responsible for dictating the behavior of magnetization dynamics, but also an interplay between hydrodynamic, interparticle and magnetic effects. Under such conditions, the hydrodynamic effect through vorticity is more intense than that of the particle-particle and particle-field interactions, so that there is a greater deviation in the direction of the dipoles in relation to the field, resulting in a larger ΔM_{max}. The physical interplay is related to the problem's timescales, presented in section , where it was demonstrated that the combination (α;Pe) would result in a relation between the hydrodynamic and magnetic timescales $\alpha/Pe = \tau_{hydro}/\tau_{mag}$. Therefore, we postulate that there is a combination (α;Pe) in which an interaction between hydrodynamics and magnetism is present and is not subjugated to the intensity of the applied magnetic field. Under the studied physical configuration, when $2 \lessapprox \alpha \lessapprox 4$, the precession physical mechanism - more clearly observable as the term $\boldsymbol{M} \times (\boldsymbol{M} \times \boldsymbol{H})$ in Eq. (2.27) - is not strong enough to restore local values of magnetization to higher values, closer to those of equilibrium. As if only the precession mechanism were changed when the field strength varies and the Péclet number is kept constant.

When it comes to the behavior of ΔM_{max} as a function of Pe, it can be seen in Fig. (4.6b) that it increases with Pe. The magnitude of the Péclet number is related to the intensity of the hydrodynamic mechanism. When increased, the flow through vorticity is more likely to misalign the particles in the direction of the field, as if the particles were more permissive to rotate, resulting in greater demagnetization. This would lead to a decrease in ΔM_{max}. Therefore, it reaffirms the fact that, under conditions of greater Péclet number, the flow is able to disturb the magnetization more efficiently.

Increases in λ and ϕ causes ΔM_{max} to decrease, as portrayed in Figs. (4.6c) and (4.6d), respectively. In this case, when the interparticles' interactions are altered due to variations in ϕ and λ, the fluid's magnetic response is also altered. Increases in the the intensity of dipolar interactions result in particles forming aggregates, which are accompanied by increases in the local field, so that, in such scenarios, increases in ϕ and λ are perceived as a way for such physical mechanism to assume the role of particle-field interactions. As a general trend, a decrease in ΔM_{max} is observed in Fig. (4.6a) as α increases. The same behavior is observed in Figs. (4.6c) and (4.6d),

because, as already discussed, dipolar interactions act in the same way as the field's effect, causing the particles to become more aligned in the direction of the field, resulting in a closer magnetization response to that of the predicted equilibrium magnetization $M_0/\phi M_d$ in Eq. (2.22), a general trend observed for the entire magnetization profile, not only the response on the wall, as indicated in Figs. (4.5c) and (4.5d).

Different regions along the duct's section are subject to different intensities of the physical mechanisms that govern non-equilibrium magnetization dynamics. For instance, the magnitude of the hydrodynamic mechanism, which is strictly linked to vorticity, is clearly vertically dependent, in a way that the interplay of physical mechanisms behaves differently along the duct's section. In regions where vorticity is higher, closer to the walls, vectors $\boldsymbol{H}$ and $\boldsymbol{M}$ should be very misaligned, as the hydrodynamic mechanism acts to rotate the particles along the direction of vorticity. Similarly, where vorticity is null, right in the center of the duct, vectors $\boldsymbol{H}$ and $\boldsymbol{M}$ should be fully aligned, as no other physical mechanism act to misalign these vectors. This physical response of the particles' magnetic dipole moments according to the net intensity of the physical mechanisms, would also generate a profile for the angles θ between vectors $\boldsymbol{H}$ and $\boldsymbol{M}$ - Eq. (2.7) - along the duct's section. The expected behavior of larger angles in regions of higher vorticity and smaller ones in regions of lesser vorticity is confirmed in the profiles shown in Fig. (4.7), which depicts θ profiles for different Pe configurations.

As expected, right in the center, where vorticity is null, these vectors are completely aligned and $\theta = 0$. First, it is noticed that, for any position along the duct's section, the angles produced by configurations with the highest Pe are greater, again due to an increase in the intensity of the hydrodynamic mechanism that tends to misalign the particles in the applied magnetic field. For instance, at $y/h = 0.2$, under conditions of $Pe = 0.1$, $Pe = 0.3$ and $Pe = 0.5$, the obtained angles θ are respectively: $\theta = 0.088rad$, $\theta = 0.256rad$ and $\theta = 0.408rad$. It is also clearly observed a change from a linear behavior to a more complex and less linear behavior of the profiles as Pe is increased. This change in behavior reaffirms that, in configurations with higher Péclet number, the interplay of physical mechanisms responsible for governing non-equilibrium magnetization dynamics becomes much more complex. This higher response to disturbances at higher Pe configurations is also associated with the fact that the only term in the two-dimensional vorticity equation - Eq. (2.48) - associated with magnetism, when in the presence of a uniform applied magnetic field, is strictly related to the misalignment between vectors $\boldsymbol{M}$ and $\boldsymbol{H}$. Therefore, higher Péclet number scenarios are required for the vorticity to be significantly capable of disturbing the magnetization field.

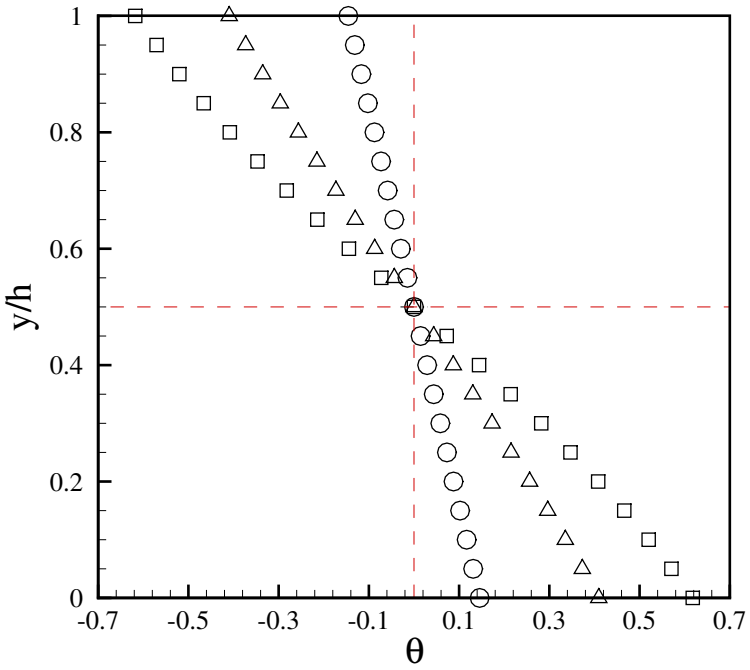

Figure. 4.7: Profiles for the fully developed flow of angles between vectors $\boldsymbol{M}$ and $\boldsymbol{H}$ for different Péclet number physical configurations. ○ , △ and ▫ represent $Pe = 0.1$, $Pe = 0.3$ and $Pe = 0.5$, respectively. For this figure: $\alpha = 1$, $Re = 5000$, $\phi = 0.05$ and $\lambda = 2.9$.

As seen in Fig. (4.7), the maximum angle θ between vectors $\boldsymbol{H}$ and $\boldsymbol{M}$ is obtained at the point of greatest vorticity, directly on the walls. Figure (4.8) shows how it behaves for changes in α, Pe, λ and ϕ. Figure (4.8a) displays the behavior of θ_{wall} as a function of α. It is possible to see two distinct behaviors of θ_{wall} as α is increased, in a similar way to that observed in Fig. (4.6a). For the interval $\alpha \gtrapprox 3$, θ_{wall} decreases with α, on the other hand, when $1 \lessapprox \alpha \lessapprox 3$, it increases. Ferrofluids are made of magnetic nanoparticles whose fixed magnetic dipole moments tend to align in the direction of the field as the field's magnitude is increased [3]. The aforementioned alignment would mean a decrease in θ_{wall}. This behavior is observed in the interval $\alpha \gtrapprox 3$. Under physical conditions of high intensity fields, the magnetic physical mechanism overcomes the hydrodynamic, leading to a minor misalignment between vectors $\boldsymbol{M}$ and $\boldsymbol{H}$ due to the action of vorticity. These results highlight the importance of the competition of physical mechanisms. Even if they are obtained under conditions of high Péclet number ($Pe = 0.5$), where vorticity is able to efficiently disturb the magnetization field, once the intensity of the field is increased and, therefore, the intensity of the magnetic mechanism, there will come a point where there will be no significant misalignment between vectors $\boldsymbol{M}$ and $\boldsymbol{H}$, and the main responsible for dictating non-equilibrium magnetization dynamics will be the magnetic mechanism, which acts to align vectors $\boldsymbol{M}$ and $\boldsymbol{H}$. In a limit case

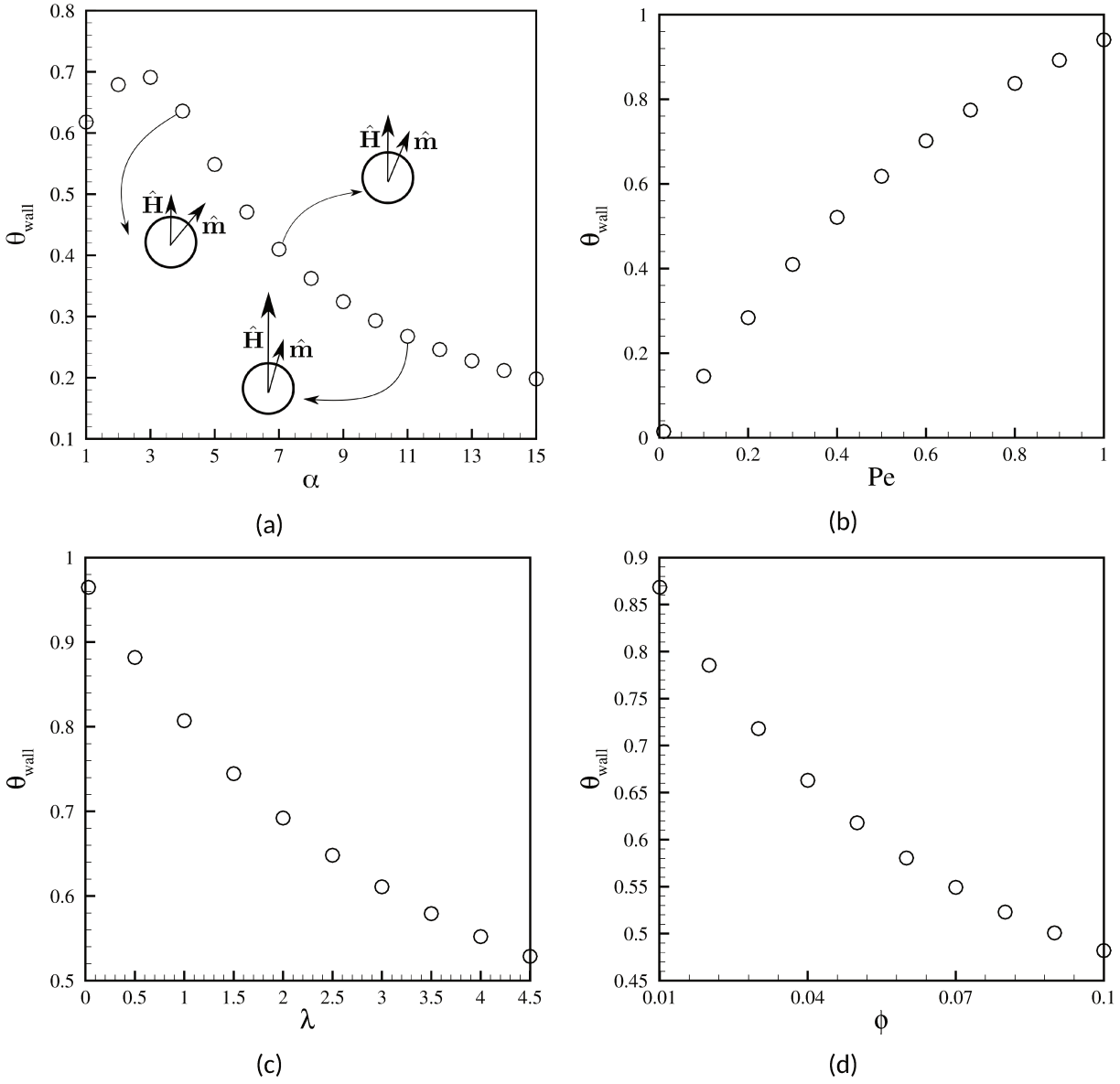

Figure. 4.8: Maximum angle θ (angle at the walls) between $\boldsymbol{M}$ and $\boldsymbol{H}$ along the angle profile as a function of (a) α, (b) Pe, (c) λ and (d) ϕ. In (a): $Re = 5000$, $\phi = 0.05$, $\lambda = 2.9$ and $Pe = 0.5$. In (b): $Re = 5000$, $\phi = 0.05$, $\lambda = 2.9$ and $\alpha = 1$. In (c): $Re = 5000$, $\phi = 0.05$, $\alpha = 1$ and $Pe = 0.5$. In (d): $Re = 5000$, $\alpha = 1$, $\lambda = 2.9$ and $Pe = 0.5$.

where $\alpha \gg 1$, Fig. (4.8a) seems to indicate that these vectors will be almost aligned, even in the regions of greatest vorticity. However, as was the case in the analysis of Fig. (4.6a), it appears that at some intervals of α, in this particular scenario when $\alpha \lessapprox 3$, due to the complex nature of the problem, the physical response of the problem to variations in α would behave differently, as it has already been postulated that there is a combination (α;Pe) in which an interaction between

hydrodynamics and magnetism is present and not subjugated to the intensity of the applied magnetic field and dipolar interactions. Under such conditions, hydrodynamics overcomes the effects of particle-particle and particle-field interactions, in order to misalign vectors $\boldsymbol{M}$ and $\boldsymbol{H}$, leading to larger magnetization entrance regions L_m - Fig. (4.3a) -, greater magnetization deviations ΔM_{max} - Fig. (4.6a), and, consequently, to smaller angles θ.

An increase in θ_{wall} is also observed when Pe is increased, as shown in Fig. (4.8b). As expected, the increase in Pe is accompanied by an increase in the intensity of the hydrodynamic physical mechanism, which acts to misalign the magnetic particles in the direction of the field, leading to greater angles θ. This result is in perfect agreement with what has been shown so far, especially with the direct correspondence with Fig. (4.6b). One of the key features of this figure is that in regimes of Low Péclet numbers, where most commercially available ferrofluids are suitable for use, the misalignment between vectors $\boldsymbol{M}$ and $\boldsymbol{H}$ is almost null, justifying, once again, the decision to explore regimes where a complex and quite interesting physical behavior of non-equilibrium magnetization dynamics happens, that is, higher Péclet number regimes.

As for the cases of variations in λ and ϕ, an increase in these parameters results in smaller angles on the walls, as indicated in Figs. (4.8c) and (4.8d). When the magnetic particles self-assemble, they tend to align their magnetic moments in the direction of the field due to neighboring particles or applied magnetic fields [15, 191, 192], allowing the magnetic nanoparticles to form aggregates. The formation of particles agglomerates is favored in higher λ and ϕ scenarios, since the intensity of dipolar interactions is increased in these cases. The increase in the intensity of such interactions leads to an increase in the magnetic restorative mechanisms, which tend to approximate vectors $\boldsymbol{H}$ and $\boldsymbol{M}$. The general trend of increase in the effective local field generated by the presence of particles aggregates manifested in decreases in both L_m and ΔM_{max} is also manifested here, so that dipolar interactions assume the role of field-particle interactions, causing the particles to become more aligned with the field, leading to minor deviations between vectors $\boldsymbol{H}$ and $\boldsymbol{M}$ and, consequently, smaller angles θ.

Since different regions of the flow are subject to different angular velocities, one would expect a profile of rotational viscosity in the duct's section, as it manifests when a difference appears between the angular velocities of the particle and the fluid. Figure (4.9) shows the rotational viscosity profile for the fully developed flow.

Closer to the walls, where vorticity is higher, the displayed values of η_r are lower, but closer

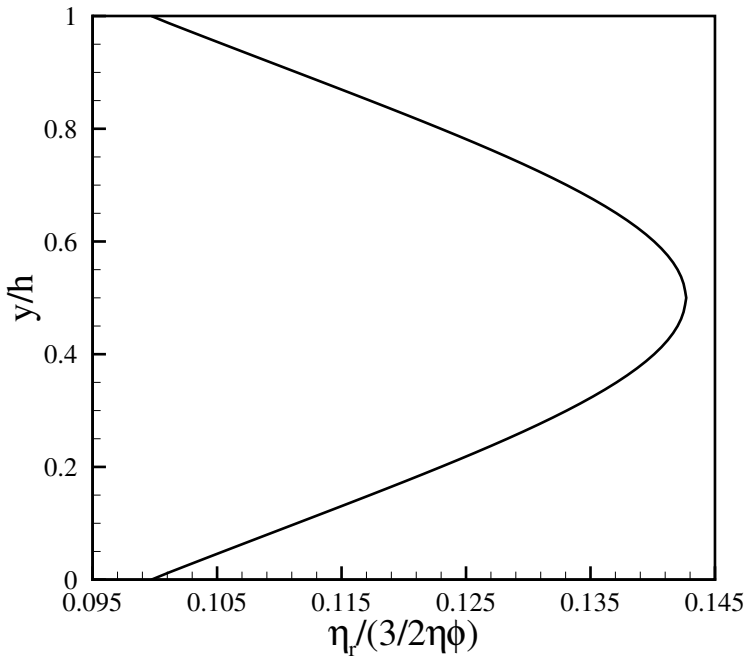

Figure. 4.9: Rotational viscosity profile for the fully developed flow. In this figure: $\alpha = 1$, $Pe = 0.5$, $Re = 5000$, $\lambda = 2.9$ and $\phi = 0.05$.

to the center, where the values of vorticity are lower, the values of η_r are higher, in a behavior analogous to shear thinning. In the regions of low vorticity, magnetic particles are highly aligned in the direction of the field, as already shown in Fig. (4.7). In such regions, the flow is more likely to spend more energy to deflect the particles from the direction of the field, in order to align them with the direction of vorticity, leading to an increase in energy dissipation, which manifests itself as an increase in the viscosity value. These observations are in agreement with those presented in Shliomis [40]. In a torque-free configuration, when particles are able to roll freely in the direction of vorticity (i.e. in the absence of a magnetic field), rotational viscosity is null. However, under high intensity magnetic fields, when the rolling of the particles is substituted by slipping, rotational viscosity reaches a saturation value equal to $\eta_r = \frac{3}{2}\eta\phi$ [21], as already depicted in Fig. (3.4). It is worthy mentioning that, for example, considering an ester based ferrofluid, as the one presented in Tab. (4.1), with density $\rho = 1400\text{kg}/\text{m}^3$ and viscosity $\eta = 0.035Pa.s$, this saturation value would reach for $\phi = 0.05\%$ approximately $\eta_r(\infty) = 0.0026Pa.s$, which corresponds to approximately 7.5% of the ferrofluid's viscosity. Therefore, even under extremely strong magnetic fields, the increase in fluid's viscosity corresponds to a small percentage of its original viscosity, indicating that the viscosity transport coefficient does not change noticeably [54].

The analogous shear thinning behavior is associated with the fact that, in diluted suspensions, shearing causes changes in the structure and arrangement of particles [233, 1]. The effect generated by the shear can orient the particles in the flow's direction. The particle's structures, formed previously due to magnetostatic forces, can break due to shear gradients, leading to a decrease in the amount of carrier liquid immobilized by the particles, which ends up generating a decrease in apparent viscosity [1]. Shear thinning behavior in various types of ferrofluids has been reported in Hong et al. [215], Pastoriza-Gallego et al. [234], Moeen et al. [235], Hezaveh et al. [220].

Up to this point, it has been demonstrated how hydrodynamics interact and disturb the magnetization field. At this point, results are presented on how hydrodynamics is disturbed by the presence of magnetic effects. Figures (4.10a) and (4.10b) display velocity and vorticity profiles obtained for the fully developed flow in comparison to the analytical profiles (solid lines) predicted for non-magnetic plane Poiseuille flow [301], given by Eqs. (3.5) and (3.7).

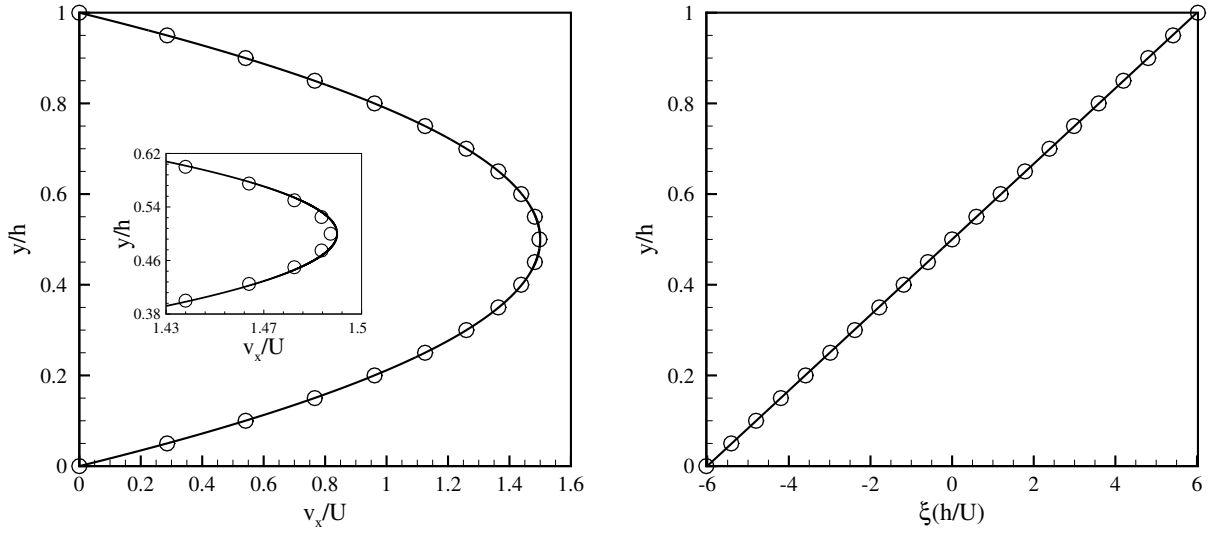

Figure. 4.10: (a) Velocity profile for the fully developed flow. (b) Vorticity profile for the fully developed flow. In both figures, ○ represent the numerical results and — represent the Poiseuille analytical results - Eqs. (3.5) and (3.7) - for velocity and vorticity, respectively. In all figures: $Pe = 0.5$, $Re = 5000$, $\phi = 0.05$, $\lambda = 2.9$ and $\alpha = 2$.

Although magnetization dynamics was strongly influenced by the effects of vorticity, especially in high Péclet number configurations, hydrodynamics has not been significantly influenced by magnetism. There is a slight deviation from the predicted non-magnetic Poiseuille profile - Eq. (3.5) - in the regions of low vorticity, close to the center. However, in general, the magnetic and non-

magnetic regimes profiles are very close to each other, the same is observed in the vorticity profile. The slight difference in profiles may be associated with non-Newtonian properties acquired by ferrofluids when in the action of magnetic fields, as shown in the the shear-dependent viscosity profile of Fig. (4.9).

For the simulated physical conditions presented in Fig. (4.10), Tab. (4.6) presents calculated values for both the hydrodynamic and magnetic timescales.

Table. 4.6: Hydrodynamic and magnetic timescales of different commercially available ferrofluids with diameter $d = 13nm$ at $T = 298K$. In this table: $Re = 5000$, $Pe = 0.5$ and $\alpha = 2$.

Carrier liquid	τ_{mag} (s)	τ_{hydro} (s)
Diester	3.15E-05	1.26E-04
Hydrocarbon	1.26E-06	5.03E-06
Hydrocarbon	2.52E-06	1.01E-05
Fluorocarbon	1.05E-03	4.19E-03
Ester	5.87E-06	2.35E-05
Ester	1.26E-05	5.03E-05
Ester	1.47E-05	5.87E-05
Water	2.94E-06	1.17E-05
Water	4.19E-06	1.68E-05
Polyphenylether	3.15E-03	1.26E-02

It is observed in Tab. (4.6) that in all cases the characteristic hydrodynamic timescale τ_{hydro} is larger than the magnetic timescale τ_{mag}. This means that the velocity changes much slowly than the magnetization, being subject to minor influences. Furthermore, under the simulated conditions of Fig. (4.10), $Re_m^{-1} = 1.2 \times 10^{-4}$, which is a very small term multiplying the magnetic effects in the equation of motion.

Parabolic velocity profiles in ferrofluid flows under the action of an applied magnetic field have also been reported in the literature, in the case of pipe flows with an imposed linearly polarized oscillating magnetic field [18] and under the effect of a steady magnetic field produced by a DC solenoid [58], also in the case of a planar duct subjected to a spatially uniform magnetic field along and transverse to the duct axis [52]. In such cases, the velocity profiles were similar to those of pure hydrodynamic flow, where the axial velocity profile is parabolic and the transverse velocity components are negligible. It is important to mention that this work is concerned with laminar flows, since turbulent profiles have been reported to be visually distinct [18]. Variations in the ve-

locity profile were present in cases of non-zero spin viscosity η' in Zahn and Greer [52], however the authors reported Poiseuille parabolic profiles in the case of null spin viscosity, which is the case of this present work, where the assumption that in ordinary ferrofluids η' becomes very small and may be neglected [70].

The similarity of the velocities profiles may be associated with the fact that only a small increase in ferrofluid's viscosity is present under extreme conditions of strong magnetic fields (i.e. 7.5% for the ester based ferrofluid in Tab. (4.1)), since little additional dissipation is present under such physical conditions. In this present context, the similarity in the velocity profiles occurred under a uniform field configuration where the only magnetic effect on the equation of motion is related to the term $Re_m^{-1}\nabla \times (\boldsymbol{M} \times \boldsymbol{H})$, where Re_m^{-1} is defined in Eq. (4.4).

Note that the alteration of the hydrodynamic field due to magnetic effects is proportional not only to the misalignment between $\boldsymbol{M}$ and $\boldsymbol{H}$, but also to the combination of physical parameters expressed by Re_m^{-1}. Although the angle formed between $\boldsymbol{M}$ and $\boldsymbol{H}$ is high for smaller values of α, spatial variations between the product $\boldsymbol{M} \times \boldsymbol{H}$ are very small in the asymptotic limit $\alpha \ll 1$, in addition to the small value of Re_m^{-1}. This occurs since in lower field configurations the suspension is weakly magnetized. Under non-uniform magnetic fields condition, the term that mainly affects the ferrofluid is the Kelvin force density. As reported in Papadopoulos et al. [58], the effect of the rotation of the magnetic torque only affected the flow characteristics in their numerical simulations when the magnetic field was approximately uniform.

Apart from the similarity in the velocity profile of the magnetic and pure hydrodynamic regimes, Papadopoulos et al. [58], Felderhof [54] claim that differences under such regimes will also occur in the axial pressure gradient [58] and in the flow rate [54]. The latter manifests through an increase in the viscosity (i.e. magnetoviscous effect) [26, 3, 39, 54]. The prior has been reported in Papadopoulos et al. [58], where the axial pressure drop varied significantly in the regions of strong magnetic field gradients, with its magnitude depending linearly on the volume fraction of particles ϕ.

4.2 Discrete results

In this section, the results obtained for the dynamic simulations of a suspension of particles interacting magnetically under the action of an external magnetic field are presented. The results were obtained following the numerical code described in section 3.2, which follows a dynamic Langevin scheme. First, some preliminary results are presented regarding the magnetization response of the magnetic particles when subjected to the field action, as well as to a local Couette flow. Subsequently, results are presented regarding the reconstruction of a continuous magnetization profile for the fully developed Poiseuille flow, obtained through the approach described in section 3.1. These results are partially published in de Carvalho and Gontijo [46].

When the simulation begins, the particles are randomly distributed in the simulation box, and no net magnetization is observed, as indicated in Fig. (4.11). As time goes by, the particles are subject to rotational and translational motions, due to dipole-dipole interactions, dipole-field interactions, flow field interactions and Brownian fluctuations. Dipole-dipole interactions, depending on their intensity (controlled by both λ and ϕ), tend to induce particle aggregates, which locally increase the magnetic field, resulting in the very interesting results observed in section 4.1. On the other hand, particle-field and particle-flow interactions are, in a way, more associated with the suspension's magnetization response, since both mechanisms are associated with the suspension's rotational dynamics, as well as with the so-called magnetoviscous effect, carefully described in section 1.3.1, in which the suspension's viscosity increases when in the presence of an applied magnetic field. Not only are the particles subject to the mentioned interactions, but also to random movements produced by Brownian thermal fluctuations, which tend to act to demagnetize the suspension. It is worth remembering that the simulation box of Fig. (4.11) is subsequently subject to a Couette flow, whose shear rate is provided by the continuous simulations, as discussed in section 3.2.5. The described complex physics governs the particle's dynamics, and some results regarding the suspension's magnetization response are presented below.

Magnetization is a suspension's property closely related to the rotation movement of the suspended magnetic particles, since it is defined as the average alignment of the particle's magnetic dipole moments in the direction of the applied field. Figure (4.12) depicts this rotation mechanism obtained from the numerical simulations developed here. These results are obtained under a null vorticity $\xi = 0$ configuration, indicating that the magnetization response obtained would correspond to the suspension's equilibrium magnetization M_0.

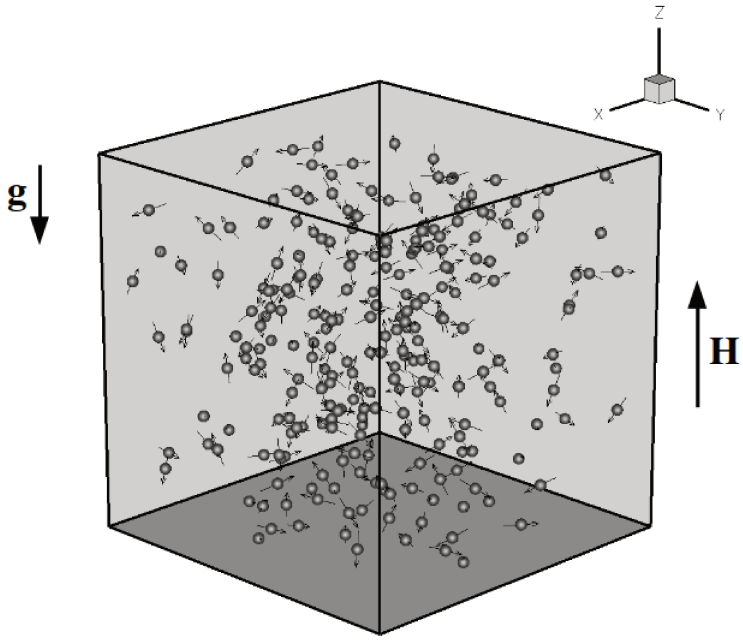

Figure. 4.11: Scheme of a three-dimensional initial configuration of the discrete simulation box.

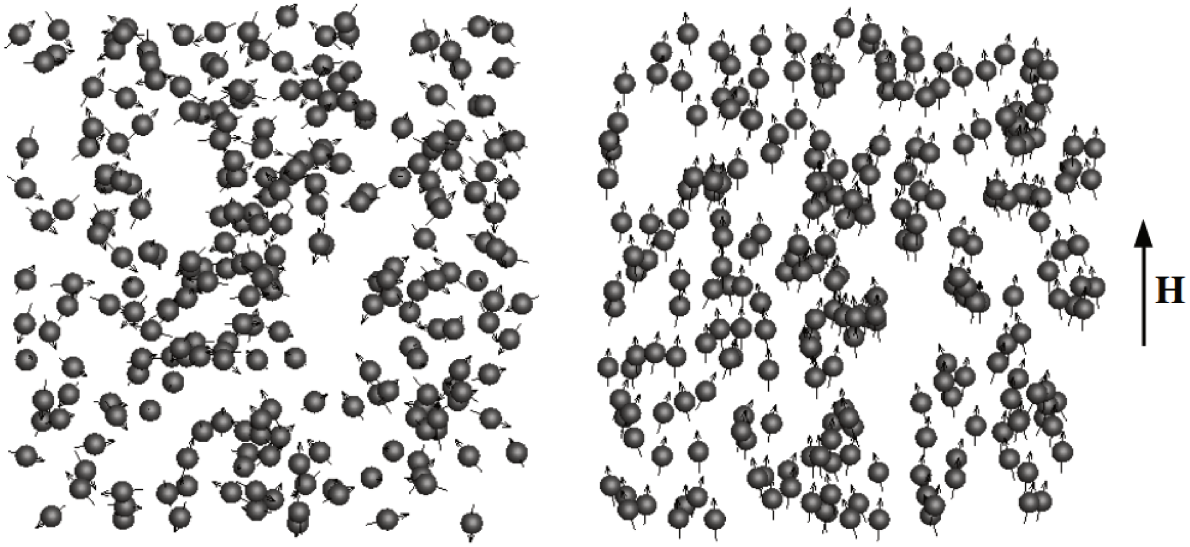

(a) (b)

Figure. 4.12: (a) Two-dimensional view of the initial configuration ($t = 0$) of the suspension's numerical box, in the absence of an applied magnetic field. (b) Later configuration ($t \neq 0$) of the suspension's numerical box, in the presence of an applied magnetic field. In all figures: $\alpha = 10$, $Pe = 0.7$, $\xi = 0$, $\phi = 0.04$ and $\tilde{\lambda} = 0.56$.

Figure (4.12) shows a typical dynamic response of the orientations of the dipole moments

when subjected to an applied magnetic field in two different configurations: when the suspension is numerically "generated" ($t = 0$, in the absence of field $\boldsymbol{H}$) and after some development time ($t \neq 0$, in the presence of field $\boldsymbol{H}$). Figure (4.12a) corresponds to the suspension's initial condition ($t = 0$) in the absence of an applied magnetic field. Note that each of the suspended particles is accompanied by a randomly oriented magnetic dipole moment. In this configuration, the suspension's net magnetization is null in the simulated volume, since the average orientation of the dipole moments over all particles is also zero. However, as soon as the suspension is subjected to an applied magnetic field, the particle's dipole moments respond to its presence, as indicated in Fig. (4.12b). This configuration is taken from the dynamic simulations at a later time, when $t \neq 0$. When the magnetic field is applied, a magnetic torque ($\boldsymbol{T_m} = \mu_0 \boldsymbol{m} \times \boldsymbol{H}$) is exerted on each of the suspended particles due to the interactions between the particles dipole moments with the external applied field. In all numerical simulations carried out in this work, it was assumed that the typical timescale of the magnetic relaxation mechanism is much smaller than the Néel relaxation - Eq. (1.10) -, so that the condition of fixed dipole moments in the particles (Brownian relaxation mechanism - Eq. (1.9) -) is considered. In this way, in the presence of the applied magnetic field, the magnetic torque also produces rotation movement of the particles and, thus, the fixed dipole moments tend to align in the direction of the field, generating a net magnetization. In a physical regime in which $\alpha > 1$, that is, the ratio between the magnetic and Brownian energies is sufficiently large, the net alignment of the particles appears to be in the field's direction, as Fig. (4.12b) clearly indicates.

With the magnetization response of the suspension analyzed in the absence of vorticity in Fig. (4.12), it is important to present now a typical response when in the presence of a local shear rate. As described in section 3.2.5, the vorticity values of a continuous flow field are extracted and used as an input for discrete simulations, which calculate the suspension's magnetization response in a local Couette flow subject to an applied magnetic field. In this scenario, another important physical mechanism is present in the suspension's dynamics: the hydrodynamic action by vorticity, which is a clear mechanism present in the magnetization ferrohydrodynamic relaxation equations. Here, the particles will also be subjected to a viscous torque, which tends to misalign the particles in the direction of the field, leading to lower values of magnetization and increases in the suspension's viscosity. That said, Fig. (4.13) shows extracts from the actual discrete simulations corresponding to three different regions in a vorticity field obtained through the continuous approach.

Three distinct regions of the flow field are represented in Fig. (4.13): one in the domain's center, where vorticity is null, another exactly on the wall, where vorticity is maximum and an-

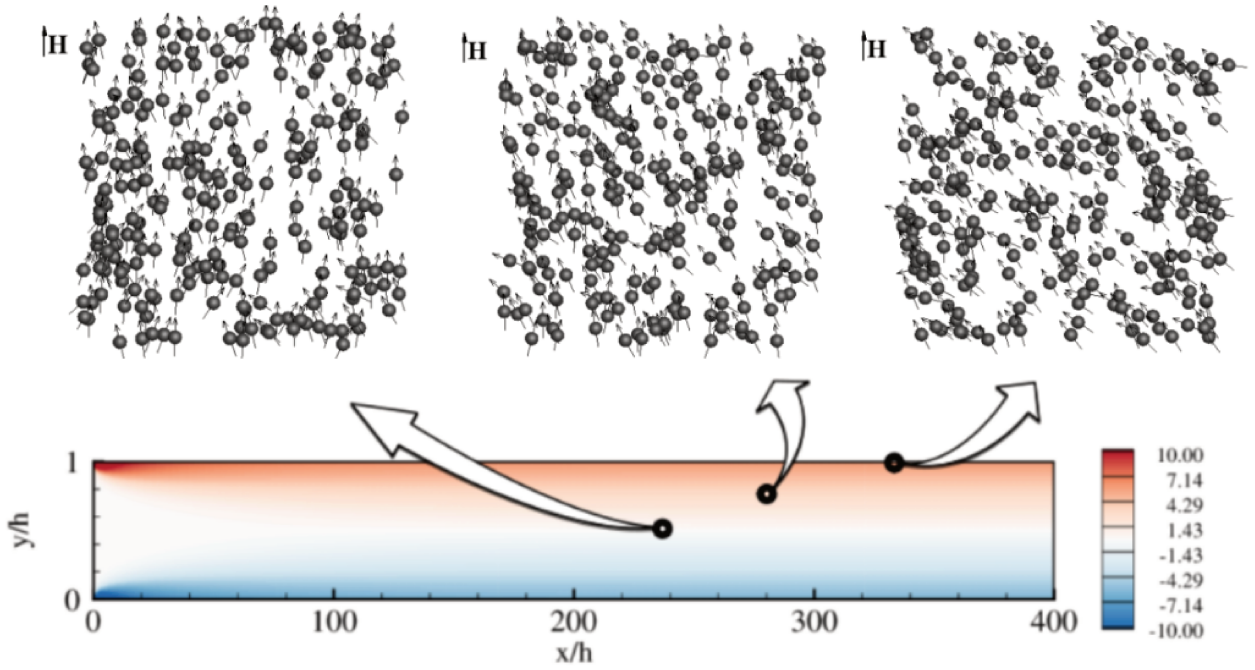

Figure. 4.13: Snapshots from the discrete simulations in three different regions of a vorticity field obtained through the continuous approach. For this figure: $\alpha = 5$, $Pe = 0.7$, $Re = 5000$, $\phi = 0.04$ and $\tilde{\lambda} = 0.56$.

other located in a position between them, where the value of vorticity is intermediate between the other two. In the central region, it is clear that an almost equilibrium behavior is observed, since there is no hydrodynamic effect acting to misalign the particles in the direction of the field, so that most of the particles are clearly aligned in the field's direction. The same scenario is observed in Fig. (4.12b). In the middle region, where the hydrodynamic action is present, there is still a tendency of alignment of the dipole moments with the field, however the particles do not seem as aligned in the vertical direction as they were in the previous image. In these regions, the shearing action clearly acts to misalign the particles and align them in vorticity's direction. Nevertheless, the hydrodynamic action is not strong enough to produce an intense misalignment, as the one observed in the walls. For the simulation on the wall under the maximum vorticity value obtained, there is a clear action of the shear that drives the particles' dipoles away from the vertical direction of the magnetic field, leading to lower magnetization values, as the particles are not clearly aligned in the field's direction as they were previously in the central region. These numerical results corroborate those obtained by the continuous approach, when vorticity and magnetization profiles were compared, indicating that regions of greater vorticity are associated with regions of less magnetization.

The previous results were qualitative when analyzing the suspension's magnetization response. Quantitatively speaking, these results have not yet been presented. Magnetization is numerically computed in this numerical code according to Eq. (3.17). As soon as the initial configuration is initialized, the time evolution process of the suspension dynamics begins, continuing until a convergent statistical property is reached. In the case of magnetization, the process begins with randomly oriented dipoles, which tend to orient themselves in the direction of the field as time passes. As soon as magnetization converges to a reliable statistical property, its value is extracted from the numerical routine. Figure (4.14) depicts the time evolution of the three magnetization components M_x, M_y and M_z until they reach statistical convergent values.

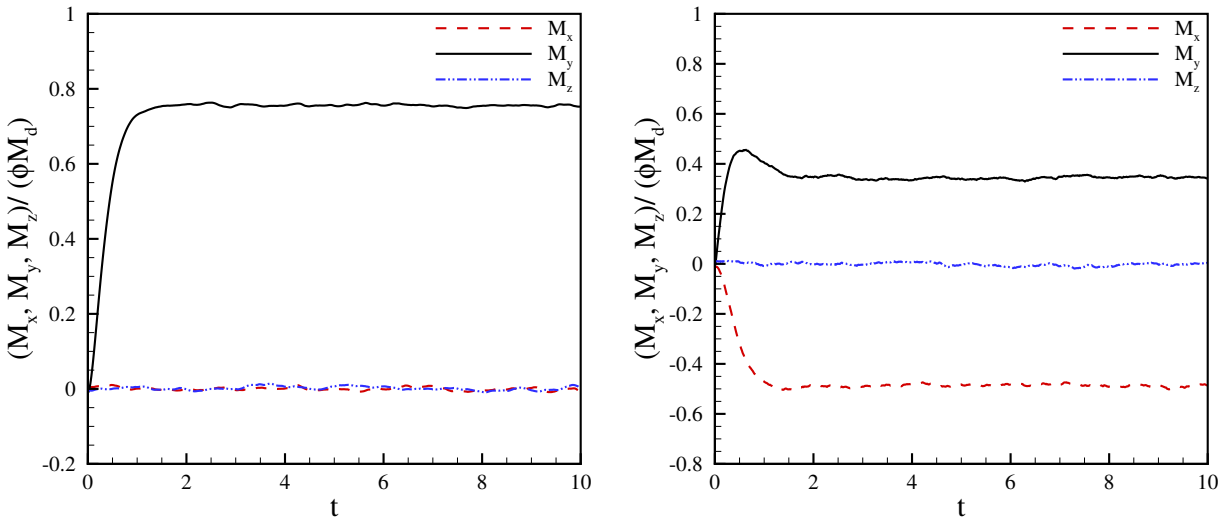

Figure. 4.14: Suspension's magnetization response as a function of the evolutive numerical time. In these figures: $\alpha = 4$, $Pe = 1.0$, $\phi = 0.04$ and $\tilde{\lambda} = 0.56$. (a) $\xi = 0$. (b) $\xi = 3.57$.

Two physical scenarios are presented in Fig. (4.14): 1) in the absence of vorticity (equilibrium scenario), where the only non-null magnetization component is that in the field's direction; 2) in the presence of hydrodynamic effects, where two distinct magnetization components are obtained. In Figure (4.14a), the value reached for the magnetization component in the field's direction is $M_y/\phi M_d \approx 0.75$, which is exactly the result predicted by Langevin's equilibrium model of Eq. (2.19). Figure (4.14b) depicts a physical scenario where hydrodynamic effects are present, leading to a magnetization response where two components are non-null. Under the simulated physical conditions, they read: $M_y/\phi M_d \approx 0.35$ and $M_x/\phi M_d \approx -0.49$.

With the magnetization response analyzed under the action of a local shear, the results ob-

tained for the reconstruction of the magnetization profiles of the fully developed Poiseuille flow are finally analyzed. In future works, not only magnetization profiles will be reconstructed, but the entire magnetization field. Figure (4.15) depicts the horizontal and vertical magnetization components obtained for the fully developed flow for the two magnetization models of Shliomis [26], Martsenyuk et al. [42], given respectively by Eqs. (2.50) and (2.49), along with the numerical results obtained from the numerical discrete scheme, in accordance to the procedure described in section 3.2. Two physical conditions were considered in these simulations: 1) $\alpha = 3$, $Pe = 0.7$, $Re = 5000$ and $\phi = 0.04$; 2) $\alpha = 4$, $Pe = 0.3$, $Re = 5000$ and $\phi = 0.04$. These parameters were carefully chosen to capture two very distinct regimes, one subject to intense hydrodynamic effects ($Pe = 0.7$) and other to weak/moderate hydrodynamic effects ($Pe = 0.3$). The particles were considered to be $d = 15nm$ in size, so that the dipole's coupling parameter is $\lambda = 4.47$, according to Eq. (1.14), under $T = 298K$ for magnetite particles. However, considering a surrounding coating thickness of $s = 7.5nm$ (s is generally $2nm < s < 8nm$) the modified dipole's coupling parameter $\tilde{\lambda}$, given in Eq. (1.14), reads $\tilde{\lambda} = 0.56$.

Figure (4.15) shows a very good agreement between the two continuous models in both magnetization components M_x and M_y. In addition, there is a behavior change in the horizontal magnetization component M_x when the system is subjected to higher hydrodynamic effects ($Pe = 0.3 \rightarrow Pe = 0.7$), which ceases to be linear to become non-linear. As for the discrete response, although the model proposed by Martsenyuk et al. [42] is more suitable for calculating magnetization in non-equilibrium regimes, it is noted that the discrete numerical simulation results are relatively closer to the magnetization response provided by the model of Shliomis [26]. For the horizontal M_x component, a very good agreement is observed between the discrete and continuous results predicted by the two models - Figs. (4.15a) and (4.15c) -. However, there appear to be greater discrepancies in the vertical magnetization component M_y, especially in the regime with the lowest Péclet number, as indicated in Fig. (4.15d). Under this regime, the discrete system is subjected to more intense Brownian effects, which acts in order to randomize the particles' orientations resulting in a lower magnetization response. Nevertheless, under conditions of greater hydrodynamic effects, the discrete code was able to capture the magnetization response satisfactorily, since the results obtained are in very good agreement with that proposed by the continuous models. The discrepancies observed between the results may be associated with the non-prediction of the dipolar interactions effects by the models studied in non-equilibrium physical regimes, since the equilibrium magnetization model considered in these continuous simulations is that of Langevin [3]. However, it is interesting to note that the shape of both profiles seems to be in accordance with the results captured by the numerical simulations. The largest discrepancies

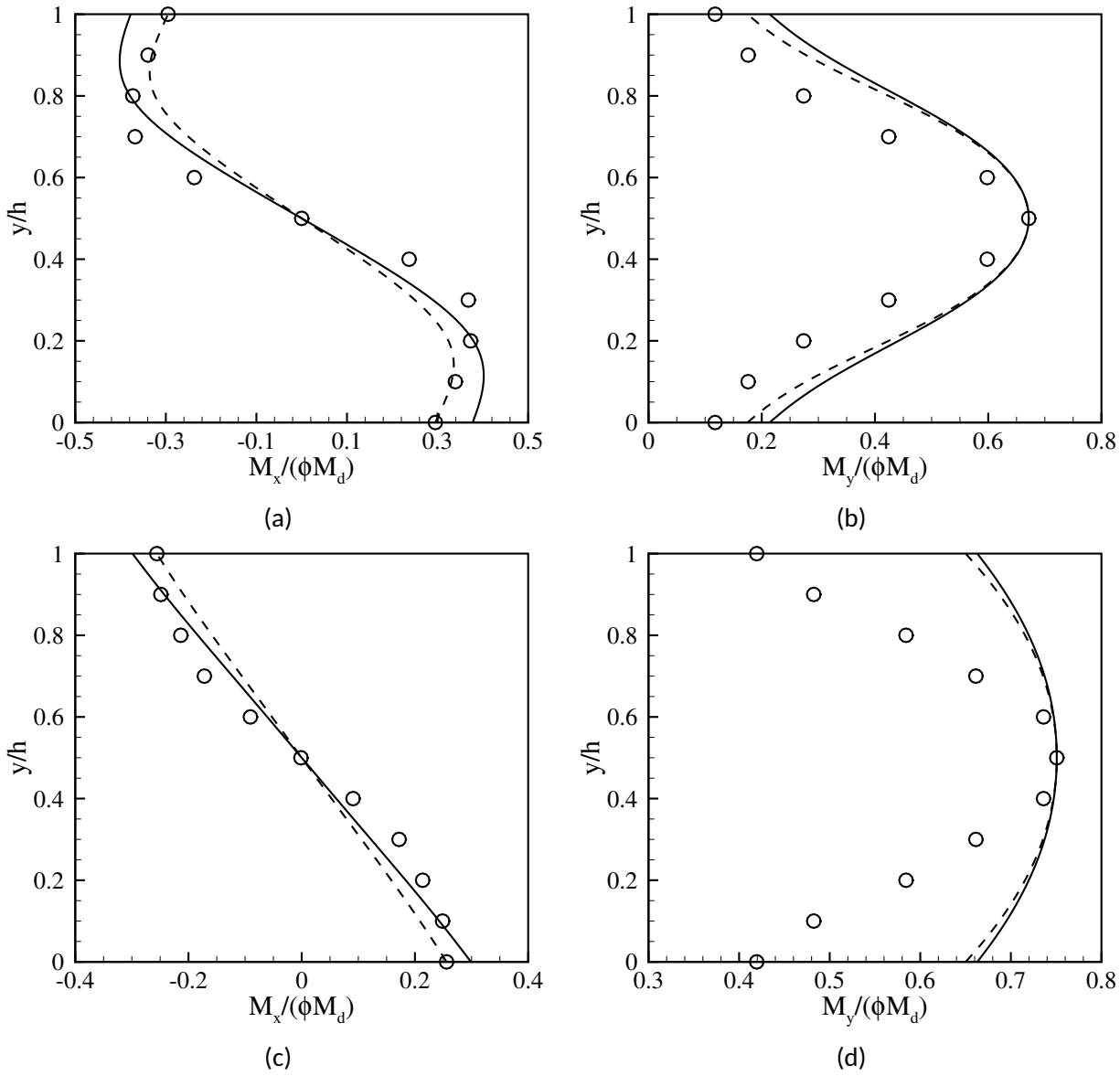

Figure. 4.15: Comparison between the profiles obtained for the fully developed flow for both magnetization components M_x and M_y. The lines corresponds to the results obtained through the continuous approach and ○ represents the results obtained through the discrete approach. The solid line ── represents the model of Martsenyuk et al. [42] from Eq. (2.31) and the dashed line - - - represents the model of Shliomis [26] from Eq. (2.27). For (a) and (b): $\alpha = 3$, $Pe = 0.7$, $Re = 5000$, $\phi = 0.04$ and $\tilde{\lambda} = 0.56$. For (c) and (d): $\alpha = 4$, $Pe = 0.3$, $Re = 5000$, $\phi = 0.04$ and $\tilde{\lambda} = 0.56$.

observed seem to occur in regions of greater vorticity, including the differences between the two continuous solutions. The obtained results are in accordance with the deviations firstly noted by Shliomis [40], where the authors clearly state that these differences could be relevant for testing

new magnetization models and for the interpretation of corresponding experiments. Nonetheless, further studies are needed to properly identify the physical mechanisms responsible for these discrepancies and to simulate new physical scenarios. In addition, not only the profiles for the fully developed flow will be reconstructed, but the entire magnetization field in future works.

Experimentally, small angle neutron scattering (SANS) can be used for the precise determination of magnetization profiles, since it distinguishes between magnetic and non-magnetic components of ferrofluids, also allowing for the determination of both density and ferrofluid's composition [352, 353, 70].

5 Concluding remarks

This work consisted of investigating the non-equilibrium magnetization dynamics of a ferrofluid's flow using two distinct tools: a continuous one, using Computational Fluid Dynamics (CFD) simulations of a plane Poiseuille flow of a ferrofluid flowing between two parallel plates under the action of an applied transverse magnetic field and a discrete one, using Langevin dynamics to simulate a suspension of particles interacting magnetically subject to the action of a magnetic field under a local Couette flow.

For the continuous part, the numerical developed code was validated by means of an asymptotic solution obtained by a regular perturbation method, by comparing the rotational viscosity obtained along the duct's cross section with the proposed theoretically and considering the limiting case of the absence of an applied magnetic field (purely hydrodynamic regime).

To mathematically modulate the problem, three different magnetization models (that of Shliomis [26], Martsenyuk et al. [42], Shliomis [40]) were used. A discussion regarding the different magnetization fields obtained for such models was also made. Overall, all considered magnetization models produced very similar results under physical conditions of low Péclet number (weak hydrodynamic action), but under high Péclet configurations, significant discrepancies were observed, specially between the magnetization response predicted by the models of Martsenyuk et al. [42], Shliomis [40] and that of Shliomis [26].

In addition, discussions regarding the flow identified timescales where made, in which it was observed that non-equilibrium magnetization dynamics is mainly governed by the Brownian diffusive timescale, a (convective) hydrodynamic timescale and a controllable magnetic timescale associated with the intensity of the applied field. Under low Péclet number scenarios, the hydrodynamic timescale is much larger than the magnetic one, justifying the almost equilibrium behavior observed in all results in such physical conditions.

An intricate balance between different physical mechanisms seemed to be responsible for a diffusive-like behavior of the magnetization field. This balance is governed by a competition between the flow's vorticity and magnetic relaxation mechanisms, which culminated in the postulation of the existence of an analogous magnetization diffusion coefficient ν_{mag}, which is directly proportional to the volume fraction of particles ϕ, the dipole's coupling parameter λ, the non-

dimensional magnetic field α and inversely proportional to the Péclet number Pe. It was proposed that this magnetization diffusion coefficient ν_{mag} could be associated with a non-existent term of the form ($\nu_{mag}\nabla^2\boldsymbol{M}$) in the magnetization relaxation equations. In addition, physical parameters responsible for this non-equilibrium magnetization dynamics were identified and interpreted using the problem's timescales. Overall, increases in both α, λ and ϕ led to decreases in the magnetization entrance region L_m, while increases in Pe led to increases in L_m. This particular part of the obtained results indicated towards the possibility of controlling the development of the flow's magnetization field by means of the applied magnetic field, the size distribution of the particles, ferrofluid's concentration and flow rate.

The wall magnetization and the angle between vectors $\boldsymbol{M}$ and $\boldsymbol{H}$ were also analyzed. In the regions of moderate field ($\alpha \approx 3$), a change in the behavior of the analyzed variables was always observed. This behavior was attributed to the complex nature of the problem's time scales, which under these conditions would lead to a more prominent hydrodynamic mechanism at the expense of the intensity of the particle-particle and field-particle interactions.

After extensive discussion of the magnetoviscous effect made in section 1.3.1, predictions of rotational viscosity along the duct's cross section were presented, where an analogous shear thinning behavior was observed, being attributed as associated with changes caused by shearing action on structures and particle's disposition.

Finally, even though magnetization dynamics was strongly influenced by hydrodynamic effects, especially in high Péclet number configurations, the hydrodynamic fields were not significantly influenced by magnetism.

As for the discrete part of this work, the effect of the hydrodynamic-magnetic coupling in non-equilibrium magnetization dynamics was clearly observed through the reconstruction of a continuous magnetization profile for the fully developed flow. The discrete simulations provided very good approximations of the continuous magnetization response, with the obtained discrepancies being attributed to the lack of predictions of particle-particle interactions by the continuous magnetization models. It has also been observed that in regions of higher vorticity, the particles tended to be less aligned in the direction of the field, resulting in regions of lower magnetization. The methodology proposed proved to be quite efficient when it comes to analyzing the magnetic response of a colloidal suspension of magnetic particles in the context of dynamic simulations.

Overall, this work presented physically consistent results regarding the magnetization field of a ferrofluid flowing between two parallel plates under different physical scenarios, in addition to a magnetization response obtained in the particle's scale.

Bibliography

[1] Seval Genc and Bora Derin. Synthesis and rheology of ferrofluids: a review. *Current Opinion in Chemical Engineering*, 3:118–124, 2014.

[2] Claudio Scherer and Antonio Martins Figueiredo Neto. Ferrofluids: properties and applications. *Brazilian Journal of Physics*, 35(3A):718–727, 2005.

[3] RE Rosensweig. *Ferrohydrodynamics*. Cambride University Press, 1985.

[4] Stefan Odenbach. *Ferrofluids: magnetically controllable fluids and their applications*, volume 594. Springer, 2008.

[5] Mohsen Sheikholeslami and Davood Domiri Ganji. Ferrohydrodynamic and magnetohydrodynamic effects on ferrofluid flow and convective heat transfer. *Energy*, 75:400–410, 2014.

[6] Mohsen Sheikholeslami, Davood Domiri Ganji, and Mohammad Mehdi Rashidi. Ferrofluid flow and heat transfer in a semi annulus enclosure in the presence of magnetic source considering thermal radiation. *Journal of the Taiwan Institute of Chemical Engineers*, 47:6–17, 2015.

[7] Mohsen Sheikholeslami Kandelousi and Rahmat Ellahi. Simulation of ferrofluid flow for magnetic drug targeting using the lattice boltzmann method. *Zeitschrift für Naturforschung A*, 70(2):115–124, 2015.

[8] Mohammad Goharkhah and Mehdi Ashjaee. Effect of an alternating nonuniform magnetic field on ferrofluid flow and heat transfer in a channel. *Journal of magnetism and magnetic materials*, 362:80–89, 2014.

[9] H Aminfar, M Mohammadpourfard, and S Ahangar Zonouzi. Numerical study of the ferrofluid flow and heat transfer through a rectangular duct in the presence of a non-uniform transverse magnetic field. *Journal of Magnetism and Magnetic materials*, 327:31–42, 2013.

[10] Jian Zeng, Yanxiang Deng, Pallavi Vedantam, Tzuen-Rong Tzeng, and Xiangchun Xuan. Magnetic separation of particles and cells in ferrofluid flow through a straight microchannel using two offset magnets. *Journal of Magnetism and Magnetic Materials*, 346:118–123, 2013.

[11] Do Kyung Kim and Jon Dobson. Nanomedicine for targeted drug delivery. *Journal of Materials Chemistry*, 19(35):6294–6307, 2009.

[12] Jon Dobson. Cancer therapy: Death by magnetism. *Nature materials*, 11(12):1006–1008, 2012.

[13] Ayse Rezzan Kose and Hur Koser. Ferrofluid mediated nanocytometry. *Lab on a Chip*, 12(1): 190–196, 2012.

[14] B Berkovski and V Bashtovoy. *Magnetic fluids and applications handbook*, volume 36. Begell House, New York, 1996.

[15] Stefan Odenbach and Steffen Thurm. Magnetoviscous effects in ferrofluids. In *Ferrofluids*, pages 185–201. Springer, 2002.

[16] Alexei P Krekhov, Mark I Shliomis, and Shinichi Kamiyama. Ferrofluid pipe flow in an oscillating magnetic field. *Physics of Fluids*, 17(3):033105, 2005.

[17] Mark I Shliomis and Konstantin I Morozov. Negative viscosity of ferrofluid under alternating magnetic field. *Physics of fluids*, 6(8):2855–2861, 1994.

[18] Kristopher R Schumacher, Inga Sellien, G Stuart Knoke, Tahir Cader, and Bruce A Finlayson. Experiment and simulation of laminar and turbulent ferrofluid pipe flow in an oscillating magnetic field. *Physical Review E*, 67(2):026308, 2003.

[19] Douglas Daniel de Carvalho, Francisco Ricardo Cunha, and Rafael Gabler Gontijo. Analysis of magnetic fluid displacement in capillaries. *Journal of the Brazilian Society of Mechanical Sciences and Engineering*, 42(1):32, 2020.

[20] MI Shliomis, TP Lyubimova, and DV Lyubimov. Ferrohydrodynamics: An essay on the progress of ideas. *Chemical Engineering Communications*, 67(1):275–290, 1988.

[21] Mark I Shliomis. Comment on “magnetoviscosity and relaxation in ferrofluids”. *Physical Review E*, 64(6):063501, 2001.

[22] Leidong Mao and Hur Koser. Ferrohydrodynamic pumping in spatially traveling sinusoidally time-varying magnetic fields. *Journal of magnetism and Magnetic materials*, 289:199–202, 2005.

[23] Carlos Rinaldi and Howard Brenner. Body versus surface forces in continuum mechanics: Is the maxwell stress tensor a physically objective cauchy stress? *Physical Review E*, 65(3): 036615, 2002.

[24] Hanns Walter Müller and Mario Liu. Structure of ferrofluid dynamics. *Physical Review E*, 64 (6):061405, 2001.

[25] Patrick Ilg, Martin Kröger, and Siegfried Hess. Magnetoviscosity of semidilute ferrofluids and the role of dipolar interactions: Comparison of molecular simulations and dynamical mean-field theory. *Physical Review E*, 71(3):031205, 2005.

[26] MI Shliomis. Effective viscosity of magnetic suspensions. *Zh. Eksp. Teor. Fiz*, 61(2411):s1971d–1971, 1971.

[27] RG Gontijo and FR Cunha. Dynamic numerical simulations of magnetically interacting suspensions in creeping flow. *Powder Technology*, 279:146–165, 2015.

[28] RG Gontijo and FR Cunha. Numerical simulations of magnetic suspensions with hydrodynamic and dipole-dipole magnetic interactions. *Physics of Fluids*, 29(6):062004, 2017.

[29] FR Cunha. Fundamentos da hidrodinâmica de fluidos magnéticos. *Turbulência*, 8:257–339, 2012. in Portuguese.

[30] Ronald E Rosensweig. Magnetic fluids. *Annual review of fluid mechanics*, 19(1):437–461, 1987.

[31] BM Berkovsky. Magnetic fluids. *Engineering Applications*, pages 171–213, 1993.

[32] Elmars Blums, Andrejs Cebers, and Mikhail Mikhailovich Maiorov. *Magnetic fluids*. Walter de Gruyter, 2010.

[33] Kalvis M Jansons. Determination of the constitutive equations for a magnetic fluid. *Journal of Fluid Mechanics*, 137:187–216, 1983.

[34] Alexey O Ivanov and Olga B Kuznetsova. Magnetic properties of dense ferrofluids: an influence of interparticle correlations. *Physical Review E*, 64(4):041405, 2001.

[35] John P McTague. Magnetoviscosity of magnetic colloids. *The Journal of Chemical Physics*, 51(1):133–136, 1969.

[36] MI Shliomis. Magnetic fluids. *Soviet Physics Uspekhi*, 17(2):153, 1974.

[37] S Kamiyama and A Satoh. Pipe-flow problems and aggregation phenomena of magnetic fluids. *Journal of magnetism and magnetic materials*, 85(1-3):121–124, 1990.

[38] Shinichi Kamiyama. Pipe flow problems of magnetic fluids. *JSME international journal. Ser. 2, Fluids engineering, heat transfer, power, combustion, thermophysical properties*, 35(2): 131–137, 1992.

[39] BU Felderhof. Magnetoviscosity and relaxation in ferrofluids. *Physical Review E*, 62(3):3848, 2000.

[40] Mark I Shliomis. Ferrohydrodynamics: Testing a third magnetization equation. *Physical Review E*, 64(6):060501, 2001.

[41] M. McCaig and A. G. Clegg. *Permanent Magnets in Theory and Practice*. Wiler, New York, second edition edition, 1987.

[42] MA Martsenyuk, Yu L Raikher, and MI Shliomis. On the kinetics of magnetization of suspensions of ferromagnetic particles. *Zh. Eksp. Teor. Fiz*, 65:834–841, 1973.

[43] BU Felderhof and HJ Kroh. Hydrodynamics of magnetic and dielectric fluids in interaction with the electromagnetic field. *The Journal of chemical physics*, 110(15):7403–7411, 1999.

[44] Mark I Shliomis. Comment on "structure of ferrofluid dynamics". *Physical Review E*, 67(4): 043201, 2003.

[45] AP Rosa and FR Cunha. The influence of dipolar particle interactions on the magnetization and the rotational viscosity of ferrofluids. *Physics of Fluids*, 31(5):052006, 2019.

[46] Douglas Daniel de Carvalho and Rafael Gabler Gontijo. Reconstructing a continuous magnetization field based on local vorticity cells, cfd and langevin dynamics: a new numerical scheme. *Journal of Magnetism and Magnetic Materials*, 514C:167135, 2020.

[47] R Moskowitz and RE Rosensweig. Nonmechanical torque-driven flow of a ferromagnetic fluid by an electromagnetic field. *Appl. Phys. Lett*, 11(301), 1967.

[48] V. M. Zaitsev and M. I. Shliomis. Entrainment of ferromagnetic suspension by a rotating field. *J. Appl. Mech. Tech. Phys.*, 10(696), 1969.

[49] RE Rosensweig, J Popplewell, and RJ Johnston. Magnetic fluid motion in rotating field. *Journal of Magnetism and Magnetic Materials*, 85(1-3):171–180, 1990.

[50] A Pshenichnikov, A Lebedev, and M Shliomis. On the rotational effect in nonuniform magnetic fluids. *Magnetohydrodynamics*, 36(4):275–281, 2000.

[51] A Chaves, C Rinaldi, S Elborai, X He, and M Zahn. Bulk flow in ferrofluids in a uniform rotating magnetic field. *Physical Review Letters*, 96(19):194501, 2006.

[52] Markus Zahn and Donald R Greer. Ferrohydrodynamic pumping in spatially uniform sinusoidally time-varying magnetic fields. *Journal of Magnetism and Magnetic Materials*, 149 (1-2):165–173, 1995.

[53] A Zeuner, R Richter, and I Rehberg. On the consistency of the standard model for magnetoviscosity in an alternating magnetic field. *Journal of magnetism and magnetic materials*, 201(1-3):191–194, 1999.

[54] BU Felderhof. Flow of a ferrofluid down a tube in an oscillating magnetic field. *Physical Review E*, 64(2):021508, 2001.

[55] BU Felderhof. Ferrohydrodynamic pumping of a ferrofluid or electrohydrodynamic pumping of a polar liquid through a planar duct. *Physics of Fluids*, 23(4):042001, 2011.

[56] J-C Bacri, R Perzynski, MI Shliomis, and GI Burde. "negative-viscosity" effect in a magnetic fluid. *Physical review letters*, 75(11):2128, 1995.

[57] A Zeuner, R Richter, and I Rehberg. Experiments on negative and positive magnetoviscosity in an alternating magnetic field. *Physical Review E*, 58(5):6287, 1998.

[58] PK Papadopoulos, P Vafeas, and PM Hatzikonstantinou. Ferrofluid pipe flow under the influence of the magnetic field of a cylindrical coil. *Physics of Fluids*, 24(12):122002, 2012.

[59] A O Cebers. Numerical experiments on the simulation of the rotational brownian motion of a ferromagnetic particle in a field. *Magnetohydrodynamics*, 20(4):343–348, 1985.

[60] Sachiko Kodama. Protrude, flow 2001. `http://sachikokodama.com/text/works/pf01/pf2.html`, 2001. Accessed: 04.03.2020.

[61] Papell Solomon Stephen. Low viscosity magnetic fluid obtained by the colloidal suspension of magnetic particles, November 2 1965. US Patent 3,215,572.

[62] Stefan Odenbach. Recent progress in magnetic fluid research. *Journal of physics: condensed matter*, 16(32):R1135, 2004.

[63] I Torres-Díaz and C Rinaldi. Recent progress in ferrofluids research: novel applications of magnetically controllable and tunable fluids. *Soft matter*, 10(43):8584–8602, 2014.

[64] E Auzans, D Zins, E Blums, and R Massart. Synthesis and properties of mn-zn ferrite ferrofluids. *Journal of materials science*, 34(6):1253–1260, 1999.

[65] H Bonnemann, W Brijoux, R Brinkmann, N Matoussevitch, and N Waldofner. Size selective synthesis of colloidal magnetic nanoparticles. *Magnetohydrodynamics*, 39:29–33, 2003.

[66] Modesto T López-López, Ana Gómez-Ramírez, Laura Rodríguez-Arco, Juan DG Durán, Larisa Iskakova, and Andrey Zubarev. Colloids on the frontier of ferrofluids. rheological properties. *Langmuir*, 28(15):6232–6245, 2012.

[67] Innocent Nkurikiyimfura, Yanmin Wang, and Zhidong Pan. Heat transfer enhancement by magnetic nanofluids—a review. *Renewable and Sustainable Energy Reviews*, 21:548–561, 2013.

[68] Inessa Bolshakova, M Bolshakov, A Zaichenko, and A Egorov. The investigation of the magnetic fluid stability using the devices with magnetic field microsensors. *Journal of magnetism and magnetic materials*, 289:108–110, 2005.

[69] G Bossis, O Volkova, S Lacis, and A Meunier. Magnetorheology: fluids, structures and rheology. In S. Odenbach, editor, *Ferrofluids, Magnetically Controllable Fluids and Their Applications*, pages 202–230. Springer, 2002.

[70] Carlos Rinaldi, Arlex Chaves, Shihab Elborai, Xiaowei Tony He, and Markus Zahn. Magnetic fluid rheology and flows. *Current Opinion in Colloid & Interface Science*, 10(3-4):141–157, 2005.

[71] MA Rahman and MZ Saghir. Thermodiffusion or soret effect: Historical review. *International Journal of Heat and Mass Transfer*, 73:693–705, 2014.

[72] E Blums. Heat and mass transfer phenomena. In S. Odenbach, editor, *Ferrofluids, Magnetically Controllable Fluids and Their Applications*, pages 124–142. Springer, 2002.

[73] Th Völker, E Blums, and S Odenbach. Thermodiffusion in magnetic fluids. *Journal of magnetism and magnetic materials*, 252:218–220, 2002.

[74] Adrian Lange. Magnetic soret effect: Application of the ferrofluid dynamics theory. *Physical Review E*, 70(4):046308, 2004.

[75] Andrey Ryskin and Harald Pleiner. Influence of a magnetic field on the soret-effect-dominated thermal convection in ferrofluids. *Physical Review E*, 69(4):046301, 2004.

[76] Thomas Völker and Stefan Odenbach. Thermodiffusion in magnetic fluids. *Journal of magnetism and magnetic materials*, 289:289–291, 2005.

[77] S Odenbach and Th Völker. Thermal convection in a ferrofluid supported by thermodiffusion. *Journal of magnetism and magnetic materials*, 289:122–125, 2005.

[78] AJ Silva, M Gonçalves, and Suhaila Maluf Shibli. Thermodiffusion study in ferrofluids through collinear mirage effect. *Journal of magnetism and magnetic materials*, 289:295–298, 2005.

[79] Elmars Blums. New transport properties of ferrocolloids: magnetic soret effect and thermomagnetoosmosis. *Journal of magnetism and magnetic materials*, 289:246–249, 2005.

[80] L.D. Landau and E.M. Lifshitz. *Fluid Mechanics*. Number v. 6. Elsevier Science, 1987. ISBN 9781483140506.

[81] Sandra Alvès, Gilles Demouchy, Agnes Bee, Delphine Talbot, Alain Bourdon, and AM Figueiredo Neto. Investigation of the sign of the soret coefficient in different ionic and surfacted magnetic colloids using forced rayleigh scattering and single-beam z-scan techniques. *Philosophical Magazine*, 83(17-18):2059–2066, 2003.

[82] Weili Luo, Tengda Du, and Jie Huang. Novel convective instabilities in a magnetic fluid. *Physical review letters*, 82(20):4134, 1999.

[83] SI Alves, Alain Bourdon, and AM Figueiredo Neto. Investigation of the soret coefficient in magnetic fluids using the z-scan technique. *Journal of magnetism and magnetic materials*, 289:285–288, 2005.

[84] J Lenglet, A Bourdon, JC Bacri, and G Demouchy. Thermodiffusion in magnetic colloids evidenced and studied by forced rayleigh scattering experiments. *Physical Review E*, 65(3): 031408, 2002.

[85] SIPMN Alves, A Bourdon, and AM Figueiredo Neto. Generalization of the thermal lens model formalism to account for thermodiffusion in a single-beam z-scan experiment: determination of the soret coefficient. *JOSA B*, 20(4):713–718, 2003.

[86] Markus Zahn. Magnetic fluid and nanoparticle applications to nanotechnology. *Journal of nanoparticle research*, 3(1):73–78, 2001.

[87] Carlos Rinaldi and Markus Zahn. Ferrohydrodynamic instabilities in dc magnetic fields. *Journal of Visualization*, 1(7):8–8, 2004.

[88] C Rinaldi, T Franklin, M Zahn, and T Cader. Magnetic nanoparticles in fluid suspension: Ferrofluid applications. In Marcel Dekker, editor, *Dekker encyclopedia of nanoscience and nanotechnology*, pages 1731–1748. Marcel Dekker, 2004.

[89] Sachiko Kodama. Dynamic ferrofluid sculpture: organic shape-changing art forms. *Communications of the ACM*, 51(6):79–81, 2008.

[90] MD Cowley and Ronald E Rosensweig. The interfacial stability of a ferromagnetic fluid. *Journal of Fluid mechanics*, 30(4):671–688, 1967.

[91] Holger Knieling, Ingo Rehberg, and Reinhard Richter. The growth of localized states on the surface of magnetic fluids. *Physics Procedia*, 9:199–204, 2010.

[92] G Reimers and S Khalafalla. Production of magnetic fluids by peptization techniques, October 22 1974. US Patent 3,843,540.

[93] Kandasamy Velmurugan, Vellaiyappan Sangli Karuppanan Venkatachalapathy, and Sechassalom Sendhilnathan. Synthesis of nickel zinc iron nanoparticles by coprecipitation technique. *Materials Research*, 13(3):299–303, 2010.

[94] Paveena Laokul, Vittaya Amornkitbamrung, Supapan Seraphin, and Santi Maensiri. Characterization and magnetic properties of nanocrystalline cufe2o4, nife2o4, znfe2o4 powders prepared by the aloe vera extract solution. *Current Applied Physics*, 11(1):101–108, 2011.

[95] Zhichuan Xu, Chengmin Shen, Yanglong Hou, Hongjun Gao, and Shouheng Sun. Oleylamine as both reducing agent and stabilizer in a facile synthesis of magnetite nanoparticles. *Chemistry of Materials*, 21(9):1778–1780, 2009.

[96] Ioan Bica. Nanoparticle production by plasma. *Materials Science and Engineering: B*, 68(1): 5–9, 1999.

[97] Samaila Bawa Waje, Mansor Hashim, Wan Daud Wan Yusoff, and Zulkifly Abbas. X-ray diffraction studies on crystallite size evolution of cofe2o4 nanoparticles prepared using mechanical alloying and sintering. *Applied Surface Science*, 256(10):3122–3127, 2010.

[98] Valérie Cabuil, Vincent Dupuis, Delphine Talbot, and Sophie Neveu. Ionic magnetic fluid based on cobalt ferrite nanoparticles: influence of hydrothermal treatment on the nanoparticle size. *Journal of Magnetism and Magnetic Materials*, 323(10):1238–1241, 2011.

[99] Linda J Cote, Amyn S Teja, Angus P Wilkinson, and Z John Zhang. Continuous hydrothermal synthesis and crystallization of magnetic oxide nanoparticles. *Journal of Materials Research*, 17(9):2410–2416, 2002.

[100] S. W. Charles and J. Popplewell. *Ferromagnetic Materials: A handbook on the properties of magnetically ordered substances*, volume 2, chapter Ferromagnetic Liquids. North Holland Publishing Company, Amsterdan, 1980.

[101] M Kroell, M Pridoehl, G Zimmermann, L Pop, S Odenbach, and A Hartwig. Magnetic and rheological characterization of novel ferrofluids. *Journal of magnetism and magnetic materials*, 289:21–24, 2005.

[102] Karina Donadel, Marcos DV Felisberto, Valfredo T Fávere, Mauricio Rigoni, Nelson Jhoe Batistela, and Mauro CM Laranjeira. Synthesis and characterization of the iron oxide magnetic particles coated with chitosan biopolymer. *Materials Science and Engineering: C*, 28(4):509–514, 2008.

[103] ME Khosroshahi and L Ghazanfari. Preparation and rheological studies of uncoated and pva-coated magnetite nanofluid. *Journal of magnetism and magnetic materials*, 324(24): 4143–4146, 2012.

[104] Ward Brullot, Naveen Krishna Reddy, Jelle Wouters, Ventsislav K Valev, Bart Goderis, Jan Vermant, and Thierry Verbiest. Versatile ferrofluids based on polyethylene glycol coated iron oxide nanoparticles. *Journal of Magnetism and Magnetic Materials*, 324(11):1919–1925, 2012.

[105] N Fauconnier, A Bee, J Roger, and JN Pons. Synthesis of aqueous magnetic liquids by surface complexation of maghemite nanoparticles. *Journal of Molecular Liquids*, 83(1-3):233–242, 1999.

[106] Rene Massart. Preparation of aqueous magnetic liquids in alkaline and acidic media. *IEEE transactions on magnetics*, 17(2):1247–1248, 1981.

[107] Jérôme Depeyrot, GJ Da Silva, Cleilton Rocha Alves, Eduardo Carvalho Sousa, Márcia Magalhães, Antônio Martins Figueiredo Neto, Marcelo Henrique Sousa, and Francisco Augusto Tourinho. Static magneto optical birefringence of new electric double layered magnetic fluids. *Brazilian journal of physics*, 31(3):390–397, 2001.

[108] MT López-López, JDG Durán, AV Delgado, and F González-Caballero. Stability and magnetic characterization of oleate-covered magnetite ferrofluids in different nonpolar carriers. *Journal of Colloid and Interface Science*, 291(1):144–151, 2005.

[109] Ajay Kumar Gupta and Mona Gupta. Synthesis and surface engineering of iron oxide nanoparticles for biomedical applications. *biomaterials*, 26(18):3995–4021, 2005.

[110] Sophie Laurent, Silvio Dutz, Urs O Häfeli, and Morteza Mahmoudi. Magnetic fluid hyperthermia: focus on superparamagnetic iron oxide nanoparticles. *Advances in colloid and interface science*, 166(1-2):8–23, 2011.

[111] P. C. Scholten. *Thermomechanics of the Magnetic Fluids*, chapter Colloid Chemistry of Magnetic Fluids. Hemisphere Publ. Corp., Bristol, 1978.

[112] Kyle JM Bishop, Christopher E Wilmer, Siowling Soh, and Bartosz A Grzybowski. Nanoscale forces and their uses in self-assembly. *small*, 5(14):1600–1630, 2009.

[113] Subrahmanyan Chandrasekhar. Stochastic problems in physics and astronomy. *Reviews of modern physics*, 15(1):1, 1943.

[114] RW Chantrell, A Bradbury, J Popplewell, and SW Charles. Agglomerate formation in a magnetic fluid. *Journal of Applied Physics*, 53(3):2742–2744, 1982.

[115] Karen Butter, PHH Bomans, PM Frederik, GJ Vroege, and AP Philipse. Direct observation of dipolar chains in iron ferrofluids by cryogenic electron microscopy. *Nature materials*, 2(2): 88–91, 2003.

[116] Jacob N Israelachvili. *Intermolecular and surface forces*. Academic press, 2015.

[117] Wei Huang and Xiaolei Wang. Study on the properties and stability of ionic liquid-based ferrofluids. *Colloid and Polymer Science*, 290(16):1695–1702, 2012.

[118] Dinesh Kumar, Prawal Sinha, and Peeyush Chandra. Ferrofluid squeeze film for spherical and conical bearings. *International Journal of Engineering Science*, 30(5):645–656, 1992.

[119] Dinesh Kumar, Peeyush Chandra, and Prawal Sinha. Ferrofluid lubrication of externally pressurized circular plates and conical bearings. *International journal of engineering science*, 31 (4):593–604, 1993.

[120] Anson Hatch, Andrew Evan Kamholz, Gary Holman, Paul Yager, and Karl F Bohringer. A ferrofluidic magnetic micropump. *Journal of Microelectromechanical systems*, 10(2):215–221, 2001.

[121] Lonnie J Love, John F Jansen, Tim E McKnight, Yul Roh, Tommy J Phelps, Lucas W Yeary, and Glen T Cunningham. Ferrofluid field induced flow for microfluidic applications. *IEEE/Asme Transactions on Mechatronics*, 10(1):68–76, 2005.

[122] Jonathan Denies, H Ben Ahmed, and Bruno Dehez. Design of a ferrofluid micropump using a topology optimization method. In *2009 8th International Symposium on Advanced Electromechanical Motion Systems & Electric Drives Joint Symposium*, pages 1–6. IEEE, 2009.

[123] Arnim Nethe, Thomas Schöppe, and Hanns-Dietrich Stahlmann. Ferrofluid driven actuator for a left ventricular assist device. *Journal of magnetism and magnetic materials*, 201(1-3): 423–426, 1999.

[124] Dong-Wook Oh, Jae Sik Jin, Jai Hyun Choi, Ho-Young Kim, and Joon Sik Lee. A microfluidic chaotic mixer using ferrofluid. *Journal of Micromechanics and Microengineering*, 17(10): 2077, 2007.

[125] S Engelmann, A Nethe, Th Scholz, and H-D Stahlmann. Force enhancement on a ferrofluid-driven linear stepping motor model. *Journal of magnetism and magnetic materials*, 272: 2345–2347, 2004.

[126] B Ando, A Ascia, S Baglio, and N Pitrone. Resonant ferrofluidic inclinometers: New sensing strategies. In *SENSORS, 2008 IEEE*, pages 1179–1182. IEEE, 2008.

[127] Ramya Bellamkonda, Tom John, Bobby Mathew, Mark DeCoster, Hisham Hegab, and Despina Davis. Fabrication and testing of a conicu/cu cpp-gmr nanowire-based microfluidic biosensor. *Journal of Micromechanics and Microengineering*, 20(2):025012, 2009.

[128] V Murariu and PJ Sergeant. Modelling of the separation process in a ferrohydrostatic separator using discrete element method. *Physical Separation in Science and Engineering*, 2007, 2007.

[129] Da-ming Lai, Li Deng, Jiang Li, Bing Liao, Qing-xiang Guo, and Yao Fu. Hydrolysis of cellulose into glucose by magnetic solid acid. *ChemSusChem*, 4(1):55–58, 2011.

[130] Ali Pourjavadi, Seyed Hassan Hosseini, Maliheh Doulabi, Seyed Mahmoud Fakoorpoor, and Farzad Seidi. Multi-layer functionalized poly (ionic liquid) coated magnetic nanoparticles: highly recoverable and magnetically separable brønsted acid catalyst. *ACS Catalysis*, 2(6): 1259–1266, 2012.

[131] Qiang Zhang, Hong Su, Jun Luo, and Yunyang Wei. A magnetic nanoparticle supported dual acidic ionic liquid: a "quasi-homogeneous" catalyst for the one-pot synthesis of benzoxanthenes. *Green Chemistry*, 14(1):201–208, 2012.

[132] Babak Kaboudin, Ramin Mostafalu, and Tsutomu Yokomatsu. Fe 3 o 4 nanoparticle-supported cu (ii)-β-cyclodextrin complex as a magnetically recoverable and reusable catalyst for the synthesis of symmetrical biaryls and 1, 2, 3-triazoles from aryl boronic acids. *Green Chemistry*, 15(8):2266–2274, 2013.

[133] Kuldip Raj, B Moskowitz, and R Casciari. Advances in ferrofluid technology. *Journal of magnetism and magnetic materials*, 149(1-2):174–180, 1995.

[134] Michaël De Volder and Dominiek Reynaerts. Development of a hybrid ferrofluid seal technology for miniature pneumatic and hydraulic actuators. *Sensors and Actuators A: Physical*, 152(2):234–240, 2009.

[135] Romain Ravaud, Marcos Pinho, Guy Lemarquand, Nicolas Dauchez, Jean-Michel Génevaux, Valérie Lemarquand, and Bruno Brouard. Radial stiffness of a ferrofluid seal. *IEEE Transactions on Magnetics*, 45(10):4388–4390, 2009.

[136] Romain Ravaud, Guy Lemarquand, and Valérie Lemarquand. Mechanical properties of ferrofluid applications: centering effect and capacity of a seal. *Tribology International*, 43(1-2): 76–82, 2010.

[137] AO Kuzubov and OI Ivanova. Magnetic liquids for heat exchange. *Journal de Physique III*, 4 (1):1–6, 1994.

[138] John Philip, PD Shima, and Baldev Raj. Evidence for enhanced thermal conduction through percolating structures in nanofluids. *Nanotechnology*, 19(30):305706, 2008.

[139] Qiang Li, Yimin Xuan, and Jian Wang. Experimental investigations on transport properties of magnetic fluids. *Experimental Thermal and Fluid Science*, 30(2):109–116, 2005.

[140] KS Hong, Tae-Keun Hong, and Ho-Soon Yang. Thermal conductivity of fe nanofluids depending on the cluster size of nanoparticles. *Applied Physics Letters*, 88(3):031901, 2006.

[141] RY Hong, SZ Zhang, YP Han, HZ Li, J Ding, and Y Zheng. Preparation, characterization and application of bilayer surfactant-stabilized ferrofluids. *Powder Technology*, 170(1):1–11, 2006.

[142] John Philip, PD Shima, and Baldev Raj. Enhancement of thermal conductivity in magnetite based nanofluid due to chainlike structures. *Applied physics letters*, 91(20):203108, 2007.

[143] Maryam Abareshi, Elaheh K Goharshadi, Seyed Mojtaba Zebarjad, Hassan Khandan Fadafan, and Abbas Youssefi. Fabrication, characterization and measurement of thermal conductivity of fe3o4 nanofluids. *Journal of Magnetism and Magnetic Materials*, 322(24):3895–3901, 2010.

[144] Wei Yu, Huaqing Xie, Lifei Chen, and Yang Li. Enhancement of thermal conductivity of kerosene-based fe3o4 nanofluids prepared via phase-transfer method. *Colloids and surfaces A: Physicochemical and engineering aspects*, 355(1-3):109–113, 2010.

[145] Tae-Keun Hong, Ho-Soon Yang, and CJ Choi. Study of the enhanced thermal conductivity of fe nanofluids. *Journal of Applied Physics*, 97(6):064311, 2005.

[146] Anwar Gavili, Fatemeh Zabihi, Taghi Dallali Isfahani, and Jamshid Sabbaghzadeh. The thermal conductivity of water base ferrofluids under magnetic field. *Experimental Thermal and Fluid Science*, 41:94–98, 2012.

[147] Innocent Nkurikiyimfura, Yanmin Wang, Zhidong Pan, and Dawei Hu. Enhancement of thermal conductivity of magnetic nanofluids in magnetic field. In *2011 International Conference on Materials for Renewable Energy & Environment*, volume 2, pages 1333–1337. IEEE, 2011.

[148] Jacob Eapen, Roberto Rusconi, Roberto Piazza, and Sidney Yip. The classical nature of thermal conduction in nanofluids. *Journal of heat transfer*, 132(10), 2010.

[149] Raj K. *Magnetic fluids and applications handbook*, chapter Magnetic Fluids and Devices: a Commercial Survey. Begell House, New York, 1996.

[150] AM Figueiredo Neto and MMF Saba. Determination of the minimum concentration of ferrofluid required to orient nematic liquid crystals. *Physical Review A*, 34(4):3483, 1986.

[151] Antônio M Figueiredo Neto, Silvio RA Salinas, et al. *The physics of lyotropic liquid crystals: phase transitions and structural properties*, volume 62. Oxford University Press on Demand, 2005.

[152] JC Bacri and AM Figueiredo Neto. Dynamics of lyotropic ferronematic liquid crystals submitted to magnetic fields. *Physical Review E*, 50(5):3860, 1994.

[153] T Kroin, AJ Palangana, and AM Figueiredo Neto. Determination of the bend elastic constant and the anisotropy of diamagnetic susceptibility of lyotropic nematic calamitic liquid crystals. *Physical Review A*, 39(10):5373, 1989.

[154] Pierre-Gilles De Gennes and Jacques Prost. *The physics of liquid crystals*, volume 83. Oxford university press, 1993.

[155] I.C. Khoo. *Liquid Crystals: Physical Properties and Nonlinear Optical Phenomena*. A Wiley-Interscience publication. Wiley, 1987.

[156] Quentin A Pankhurst, J Connolly, Stephen K Jones, and JJ Dobson. Applications of magnetic nanoparticles in biomedicine. *Journal of physics D: Applied physics*, 36(13):R167, 2003.

[157] Andreas S Lübbe, Christoph Alexiou, and Christian Bergemann. Clinical applications of magnetic drug targeting. *Journal of Surgical Research*, 95(2):200–206, 2001.

[158] Ch Alexiou, R Schmid, R Jurgons, Ch Bergemann, W Arnold, and FG Parak. Targeted tumor therapy with "magnetic drug targeting": Therapeutic efficacy of ferrofluid bound mitoxantrone. In *Ferrofluids*, pages 233–251. Springer, 2002.

[159] Keon Mahmoudi, Alexandros Bouras, Dominique Bozec, Robert Ivkov, and Constantinos Hadjipanayis. Magnetic hyperthermia therapy for the treatment of glioblastoma: a review of the therapy's history, efficacy and application in humans. *International Journal of Hyperthermia*, 34(8):1316–1328, 2018.

[160] Donald W McRobbie, Elizabeth A Moore, Martin J Graves, and Martin R Prince. *MRI from Picture to Proton*. Cambridge university press, 2017.

[161] Nikolai A Brusentsov, Lev V Nikitin, Tatiana N Brusentsova, Anatoly A Kuznetsov, Felix S Bayburtskiy, Leonid I Shumakov, and Nikolai Y Jurchenko. Magnetic fluid hyperthermia of the mouse experimental tumor. *Journal of Magnetism and Magnetic Materials*, 252:378–380, 2002.

[162] U.S. National Library of Medicine. Mononuclear phagocyte system. `https://meshb.nlm.nih.gov/record/ui?name=Mononuclear%20Phagocyte%20System`, 1999. Accessed: 03.26.2020.

[163] Yasushi Takeda. Velocity profile measurement by ultrasonic doppler method. *Experimental thermal and fluid science*, 10(4):444–453, 1995.

[164] H Kikura, Y Takeda, and Tatsuo Sawada. Velocity profile measurements of magnetic fluid flow using ultrasonic doppler method. *Journal of magnetism and magnetic materials*, 201 (1-3):276–280, 1999.

[165] Tatsuo Sawada, H Nishiyama, and T Tabata. Influence of a magnetic field on ultrasound propagation in a magnetic fluid. *Journal of magnetism and magnetic materials*, 252:186–188, 2002.

[166] Hiroshige Kikura, Masanori Aritomi, and Yasushi Takeda. Velocity measurement on taylor–couette flow of a magnetic fluid with small aspect ratio. *Journal of magnetism and magnetic materials*, 289:342–345, 2005.

[167] Masaaki Motozawa and Tatsuo Sawada. Influence of magnetic field on ultrasonic propagation velocity in magnetic fluids. *Journal of magnetism and magnetic materials*, 289:66–69, 2005.

[168] Y Takeda et al. Ultrasonic doppler method for velocity profile measurement in fluid dynamics and fluid engineering. *Experiments in fluids*, 26(3):177–178, 1999.

[169] Markus Zahn and Peter N Wainman. Effects of fluid convection and particle spin on ferrohydrodynamic pumping in traveling wave magnetic fields. *Journal of magnetism and magnetic materials*, 122(1-3):323–328, 1993.

[170] Markus Zahn and Loretta L Pioch. Ferrofluid flows in ac and traveling wave magnetic fields with effective positive, zero or negative dynamic viscosity. *Journal of Magnetism and Magnetic Materials*, 201(1-3):144–148, 1999.

[171] Leidong Mao and Hur Koser. Towards ferrofluidics for μ-tas and lab on-a-chip applications. *Nanotechnology*, 17(4):S34, 2006.

[172] BU Felderhof. Ferrohydrodynamic pumping of a ferrofluid or electrohydrodynamic pumping of a polar liquid through a circular tube. *Physics of Fluids*, 23(9):092002, 2011.

[173] J. M. Ginder. *Encyclopedia of Applied Physics*, chapter Rheology controlled by magnetic fields. VCH, New York, 1996.

[174] Ronald E Rosensweig. “negative viscosity” in a magnetic fluid. *Science*, 271(5249):614–614, 1996.

[175] A Pérez-Madrid, T Alarcon, JMG Vilar, and JM Rubı. A mesoscopic approach to the “negative” viscosity effect in ferrofluids. *Physica A: Statistical Mechanics and its Applications*, 270(3-4): 403–412, 1999.

[176] RE Rosensweig, R Kaiser, and G Miskolczy. Viscosity of magnetic fluid in a magnetic field. *Journal of Colloid and Interface Science*, 29(4):680–686, 1969.

[177] D Soto-Aquino and C Rinaldi. Magnetoviscosity in dilute ferrofluids from rotational brownian dynamics simulations. *Physical Review E*, 82(4):046310, 2010.

[178] Abdel-Fatah Lehlooh, Sami H Mahmood, and John M Williams. On the particle size dependence of the magnetic anisotropy energy constant. *Physica B: Condensed Matter*, 321(1-4): 159–162, 2002.

[179] Robert Krauß, Bert Reimann, Reinhard Richter, Ingo Rehberg, and Mario Liu. Fluid pumped by magnetic stress. *Applied Physics Letters*, 86(2):024102, 2005.

[180] Cory Lorenz and Markus Zahn. Hele-shaw ferrohydrodynamics for rotating and dc axial magnetic fields. *Physics of Fluids*, 15(9):S4–S4, 2003.

[181] Scott Rhodes, Juan Perez, Shihab Elborai, Se-Hee Lee, and Markus Zahn. Ferrofluid spiral formations and continuous-to-discrete phase transitions under simultaneously applied dc axial and ac in-plane rotating magnetic fields. *Journal of magnetism and magnetic materials*, 289:353–355, 2005.

[182] S Elborai, D-K Kim, X He, S-H Lee, S Rhodes, and M Zahn. Self-forming, quasi-two-dimensional, magnetic-fluid patterns with applied in-plane-rotating and dc-axial magnetic fields. *Journal of applied physics*, 97(10):10Q303, 2005.

[183] Adam D Rosenthal, Carlos Rinaldi, Thomas Franklin, and Markus Zahn. Torque measurements in spin-up flow of ferrofluids. *J. Fluids Eng.*, 126(2):198–205, 2004.

[184] Carlos Rinaldi, Fernando Gutman, Xiaowei He, Adam D Rosenthal, and Markus Zahn. Torque measurements on ferrofluid cylinders in rotating magnetic fields. *Journal of magnetism and magnetic materials*, 289:307–310, 2005.

[185] MI Shliomis and VI Stepanov. Theory of the dynamic susceptibility of magnetic fluids. *Advances in Chemical Physics: Relaxation Phenomena in Condensed Matter*, 87:1–30, 1994.

[186] Claudio Scherer and Hans-Georg Matuttis. Rotational dynamics of magnetic particles in suspensions. *Physical Review E*, 63(1):011504, 2000.

[187] S Thurm and S Odenbach. Magnetic separation of ferrofluids. *Journal of Magnetism and Magnetic Materials*, 252:247–249, 2002.

[188] Loredana Mirela Pop, Stefan Odenbach, Albrecht Wiedenmann, Nina Matoussevitch, and Helmut Bönnemann. Microstructure and rheology of ferrofluids. *Journal of Magnetism and Magnetic Materials*, 289:303–306, 2005.

[189] Stéphane Mornet, Sébastien Vasseur, Fabien Grasset, and Etienne Duguet. Magnetic nanoparticle design for medical diagnosis and therapy. *Journal of materials chemistry*, 14 (14):2161–2175, 2004.

[190] Robert Müller, Rudolf Hergt, Matthias Zeisberger, and Wolfgang Gawalek. Preparation of magnetic nanoparticles with large specific loss power for heating applications. *Journal of magnetism and magnetic materials*, 289:13–16, 2005.

[191] Valentin S Mendelev and Alexey O Ivanov. Ferrofluid aggregation in chains under the influence of a magnetic field. *Physical Review E*, 70(5):051502, 2004.

[192] Christian Holm and J-J Weis. The structure of ferrofluids: A status report. *Current Opinion in Colloid & Interface Science*, 10(3-4):133–140, 2005.

[193] Steffen Thurm and Stefan Odenbach. Particle size distribution as key parameter for the flow behavior of ferrofluids. *Physics of Fluids*, 15(6):1658–1664, 2003.

[194] Andrey Zubarev. Statistical physics of non-dilute ferrofluids. In S. Odenbach, editor, *Ferrofluids, Magnetically Controllable Fluids and Their Applications*, pages 143–161. Springer, 2002.

[195] Konstantin I Morozov and Mark I Shliomis. Magnetic fluid as an assembly of flexible chains. In S. Odenbach, editor, *Ferrofluids, Magnetically Controllable Fluids and Their Applications*, pages 162–184. Springer, 2002.

[196] A Yu Zubarev and L Yu Iskakova. On the theory of structural transformations in magnetic fluids. *Colloid Journal*, 65(6):703–710, 2003.

[197] AO Ivanov and SS Kantorovich. Structure of chain aggregates in ferrocolloids. *Colloid Journal*, 65(2):166–176, 2003.

[198] Konstantin I Morozov and Mark I Shliomis. Ferrofluids: flexibility of magnetic particle chains. *Journal of Physics: Condensed Matter*, 16(23):3807, 2004.

[199] Hamid Shahnazian and Stefan Odenbach. Rheological investigations of ferrofluids with a shear stress controlled rheometer. *Journal of Physics: Condensed Matter*, 20(20):204137, 2008.

[200] M Reindl and S Odenbach. Effect of axial and transverse magnetic fields on the flow behavior of ferrofluids featuring different levels of interparticle interaction. *Physics of Fluids*, 23(9): 093102, 2011.

[201] John Philip, PD Shima, and Baldev Raj. Nanofluid with tunable thermal properties. *Applied physics letters*, 92(4):043108, 2008.

[202] Ravi Prasher, William Evans, Paul Meakin, Jacob Fish, Patrick Phelan, and Pawel Keblinski. Effect of aggregation on thermal conduction in colloidal nanofluids. *Applied Physics Letters*, 89(14):143119, 2006.

[203] Pei Tillman and James M Hill. A new model for thermal conductivity in nanofluids. In *2006 International Conference on Nanoscience and Nanotechnology*. IEEE, 2006.

[204] Pawel Keblinski, Ravi Prasher, and Jacob Eapen. Thermal conductance of nanofluids: is the controversy over? *Journal of Nanoparticle research*, 10(7):1089–1097, 2008.

[205] Bu-Xuan Wang, Wen-Yan Sheng, and Xiao-Feng Peng. A novel statistical clustering model for predicting thermal conductivity of nanofluid. *International Journal of Thermophysics*, 30 (6):1992, 2009.

[206] Haitao Zhu, Canying Zhang, Shiquan Liu, Yaming Tang, and Yansheng Yin. Effects of nanoparticle clustering and alignment on thermal conductivities of fe 3 o 4 aqueous nanofluids. *Applied Physics Letters*, 89(2):023123, 2006.

[207] Innocent Nkurikiyimfura, Yanmin Wang, and Zhidong Pan. Effect of chain-like magnetite nanoparticle aggregates on thermal conductivity of magnetic nanofluid in magnetic field. *Experimental Thermal and Fluid Science*, 44:607–612, 2013.

[208] S Odenbach and K Raj. The influence of large particles and agglomerates on the magnetoviscous effect in ferrofluids. *Magnetohydrodynamics*, 36(4):312–319, 2000.

[209] Zuowei Wang, Christian Holm, and Hanns Walter Müller. Molecular dynamics study on the equilibrium magnetization properties and structure of ferrofluids. *Physical Review E*, 66(2): 021405, 2002.

[210] Zuowei Wang and Christian Holm. Structure and magnetic properties of polydisperse ferrofluids: A molecular dynamics study. *Physical Review E*, 68(4):041401, 2003.

[211] Patrick Ilg and Martin Kröger. Magnetization dynamics, rheology, and an effective description of ferromagnetic units in dilute suspension. *Physical Review E*, 66(2):021501, 2002.

[212] LM Pop, J Hilljegerdes, S Odenbach, and A Wiedenmann. The microstructure of ferrofluids and their rheological properties. *Applied organometallic chemistry*, 18(10):523–528, 2004.

[213] A Yu Zubarev, Stefan Odenbach, and J Fleischer. Rheological properties of dense ferrofluids. effect of chain-like aggregates. *Journal of magnetism and magnetic materials*, 252:241–243, 2002.

[214] F Gazeau, C Baravian, J-C Bacri, R Perzynski, and MI Shliomis. Energy conversion in ferrofluids: Magnetic nanoparticles as motors or generators. *Physical Review E*, 56(1):614, 1997.

[215] RY Hong, ZQ Ren, YP Han, HZ Li, Y Zheng, and J Ding. Rheological properties of water-based fe3o4 ferrofluids. *Chemical Engineering Science*, 62(21):5912–5924, 2007.

[216] Albert Einstein. *Investigations on the Theory of the Brownian Movement*. Courier Corporation, 1956.

[217] HC Brinkman. The viscosity of concentrated suspensions and solutions. *The Journal of Chemical Physics*, 20(4):571–571, 1952.

[218] GK Batchelor. The effect of brownian motion on the bulk stress in a suspension of spherical particles. *Journal of fluid mechanics*, 83(1):97–117, 1977.

[219] Jozef Bicerano, Jack F. Douglas, and Douglas A. Brune. Model for the viscosity of particle dispersions. *Journal of Macromolecular Science, Part C*, 39(4):561–642, 1999. doi: 10.1081/MC-100101428.

[220] Hadi Hezaveh, Alireza Fazlali, and Iman Noshadi. Synthesis, rheological properties and magnetoviscos effect of fe2o3/paraffin ferrofluids. *Journal of the Taiwan Institute of Chemical Engineers*, 43(1):159–164, 2012.

[221] Praveen K Namburu, Devdatta P Kulkarni, Debasmita Misra, and Debendra K Das. Viscosity of copper oxide nanoparticles dispersed in ethylene glycol and water mixture. *Experimental Thermal and Fluid Science*, 32(2):397–402, 2007.

[222] Frank M White and Isla Corfield. *Viscous fluid flow*, volume 3. McGraw-Hill New York, 2006.

[223] D Yu Borin and S Odenbach. Magnetic measurements on frozen ferrofluids as a method for estimating the magnetoviscous effect. *Journal of Physics: Condensed Matter*, 21(24): 246002, 2009.

[224] Stefan Odenbach and H Störk. Shear dependence of field-induced contributions to the viscosity of magnetic fluids at low shear rates. *Journal of magnetism and magnetic materials*, 183(1-2):188–194, 1998.

[225] To S Lundgren. Slow flow through stationary random beds and suspensions of spheres. *Journal of Fluid Mechanics*, 51(2):273–299, 1972.

[226] Stefan Odenbach. *Colloidal magnetic fluids: basics, development and application of ferrofluids*, volume 763. Springer, 2009.

[227] Loredana Mirela Pop and Stefan Odenbach. Investigation of the microscopic reason for the magnetoviscous effect in ferrofluids studied by small angle neutron scattering. *Journal of Physics: Condensed Matter*, 18(38):S2785, 2006.

[228] A Yu Zubarev and L Yu Iskakova. Rheological properties of ferrofluids with drop-like aggregates. *Physica A: Statistical Mechanics and its Applications*, 376:38–50, 2007.

[229] O Volkova, G Bossis, M Guyot, V Bashtovoi, and A Reks. Magnetorheology of magnetic holes compared to magnetic particles. *Journal of Rheology*, 44(1):91–104, 2000.

[230] John P Friend and Robert J Hunter. Plastic flow behavior of coagulated suspensions treated as a repeptization phenomenon. *Journal of Colloid and Interface Science*, 37(3):548–556, 1971.

[231] Christopher W Macosko and Ronald G Larson. Rheology: principles, measurements, and applications. 1994.

[232] John R. Wagner, Eldridge M. Mount, and Harold F. Giles. In *Extrusion*, Plastics Design Library, page xvi. William Andrew Publishing, Oxford, second edition edition, 2014. ISBN 978-1-4377-3481-2. doi: https://doi.org/10.1016/B978-1-4377-3481-2.09001-3.

[233] Ronald G Larson. *The structure and rheology of complex fluids*, volume 150. Oxford university press New York, 1999.

[234] María Jose Pastoriza-Gallego, Luis Lugo, José Luis Legido, and Manuel M Piñeiro. Rheological non-newtonian behaviour of ethylene glycol-based fe 2 o 3 nanofluids. *Nanoscale research letters*, 6(1):560, 2011.

[235] S Jebelli Moeen, MR Vaezi, AA Yousefi, and E Ghasemi. Synthesis and rheological properties of nickel-zinc ferrite polymer nanocomposites. *Journal of applied polymer science*, 123(4): 2534–2539, 2012.

[236] RE Rosensweig. Directions in ferrohydrodynamics. *Journal of Applied Physics*, 57(8):4259–4264, 1985.

[237] Robert H Davis and Andreas Acrivos. Sedimentation of noncolloidal particles at low reynolds numbers. *Annual Review of Fluid Mechanics*, 17(1):91–118, 1985.

[238] P Ilg and Stefan Odenbach. Ferrofluid structure and rheology. In *Colloidal Magnetic Fluids*, pages 1–77. Springer, 2009.

[239] FR Da Cunha and EJ Hinch. Shear-induced dispersion in a dilute suspension of rough spheres. *Journal of fluid mechanics*, 309:211–223, 1996.

[240] FR Cunha and HLG Couto. Transverse gradient diffusion in a polydisperse dilute suspension of magnetic spheres during sedimentation. *Journal of Physics: Condensed Matter*, 20(20): 204129, 2008.

[241] FR Cunha and HLG Couto. On the influence of the hydrodynamic interactions on the aggregation rate of magnetic spheres in a dilute suspension. *Journal of magnetism and magnetic materials*, 323(1):77–82, 2011.

[242] RG Gontijo and FR Cunha. Magnetic-induced migration in a sedimenting suspension of magnetic spherical particles. *Journal of nanoscience and nanotechnology*, 12(12):9286–9294, 2012.

[243] FR Cunha, RG Gontijo, and YD Sobral. Symmetry breaking of particle trajectories due to magnetic interactions in a dilute suspension. *Journal of magnetism and magnetic materials*, 326:240–250, 2013.

[244] FR Cunha, YD Sobral, and RG Gontijo. Stabilization of concentration waves in fluidized beds of magnetic particles. *Powder technology*, 241:219–229, 2013.

[245] M Bahiana, JP Pereira Nunes, D Altbir, P Vargas, and M Knobel. Ordering effects of the dipolar interaction in lattices of small magnetic particles. *Journal of magnetism and magnetic materials*, 281(2-3):372–377, 2004.

[246] Rogelio Díaz-Méndez and Roberto Mulet. Monte carlo simulations of the equilibrium and non-equilibrium properties of low-dimensional magnetic systems with long-range dipolar interactions. *Journal of Magnetism and Magnetic Materials*, 294(2):e21–e25, 2005.

[247] Lorenzo Rovigatti, John Russo, and Francesco Sciortino. Structural properties of the dipolar hard-sphere fluid at low temperatures and densities. *Soft Matter*, 8(23):6310–6319, 2012.

[248] Philip J Camp, Ekaterina A Elfimova, and Alexey O Ivanov. The effects of polydispersity on the initial susceptibilities of ferrofluids. *Journal of Physics: Condensed Matter*, 26(45):456002, 2014.

[249] XZ Cheng, MBA Jalil, Hwee Kuan Lee, and Yutaka Okabe. Mapping the monte carlo scheme to langevin dynamics: a fokker-planck approach. *Physical review letters*, 96(6):067208, 2006.

[250] Julien O Sindt, Philip J Camp, Sofia S Kantorovich, Ekaterina A Elfimova, and Alexey O Ivanov. Influence of dipolar interactions on the magnetic susceptibility spectra of ferrofluids. *Physical Review E*, 93(6):063117, 2016.

[251] G Bossis and A Cebers. Effects of the magnetodipolar interactions in the alternating magnetic fields. *Journal of magnetism and magnetic materials*, 201(1-3):218–221, 1999.

[252] DV Berkov, L Yu Iskakova, and A Yu Zubarev. Theoretical study of the magnetization dynamics of nondilute ferrofluids. *Physical Review E*, 79(2):021407, 2009.

[253] John Happel and Howard Brenner. *Low Reynolds number hydrodynamics: with special applications to particulate media*, volume 1. Springer Science & Business Media, 2012.

[254] Sangtae Kim and Seppo J Karrila. *Microhydrodynamics: principles and selected applications*. Courier Corporation, 2013.

[255] Elisabeth Guazzelli and Jeffrey F Morris. *A physical introduction to suspension dynamics*, volume 45. Cambridge University Press, 2011.

[256] Francisco Ricardo da Cunha. *Hydrodynamic dispersion in suspensions*. PhD thesis, University of Cambridge, 1995. PhD thesis.

[257] Robert H Davis. Hydrodynamic diffusion of suspended particles: a symposium. *Journal of Fluid Mechanics*, 310:325–335, 1996.

[258] Russel E Caflisch and Jonathan HC Luke. Variance in the sedimentation speed of a suspension. *The Physics of fluids*, 28(3):759–760, 1985.

[259] Donald L Koch and ESG Shaqfeh. Screening in sedimenting suspensions. *Journal of fluid mechanics*, 224:275–303, 1991.

[260] Donald L Koch. Anomalous diffusion of momentum in a dilute gas–solid suspension. *Physics of Fluids A: Fluid Dynamics*, 4(7):1337–1346, 1992.

[261] Hélene Nicolai and Elisabeth Guazzelli. Effect of the vessel size on the hydrodynamic diffusion of sedimenting spheres. *Physics of Fluids*, 7(1):3–5, 1995.

[262] FR Cunha, GC Abade, AJ Sousa, and EJ Hinch. Modeling and direct simulation of velocity fluctuations and particle-velocity correlations in sedimentation. *J. Fluids Eng.*, 124(4):957–968, 2002.

[263] Shang-You Tee, PJ Mucha, MP Brenner, and DA Weitz. Velocity fluctuations in a low-reynolds-number fluidized bed. *Journal of Fluid Mechanics*, 596:467–475, 2008.

[264] Elisabeth Guazzelli and John Hinch. Fluctuations and instability in sedimentation. *Annual review of fluid mechanics*, 43:97–116, 2011.

[265] Paul A Durbin and Gorazd Medic. *Fluid dynamics with a computational perspective*, volume 10. Cambridge university press New York, 2007.

[266] P Ewald. Evaluation of optical and electrostatic lattice potentials. *Ann. Phys.*, 64:253–287, 1921.

[267] Hidenori Hasimoto. On the periodic fundamental solutions of the stokes equations and their application to viscous flow past a cubic array of spheres. *Journal of Fluid Mechanics*, 5(2): 317–328, 1959.

[268] Jens Rotne and Stephen Prager. Variational treatment of hydrodynamic interaction in polymers. *The Journal of Chemical Physics*, 50(11):4831–4837, 1969.

[269] CWJ Beenakker. Ewald sum of the rotne–prager tensor. *The Journal of chemical physics*, 85 (3):1581–1582, 1986.

[270] AJC Ladd. Effects of container walls on the velocity fluctuations of sedimenting spheres. *Physical review letters*, 88(4):048301, 2002.

[271] Gustavo Coelho Abade and Francisco Ricardo Cunha. Computer simulation of particle aggregates during sedimentation. *Computer methods in applied mechanics and engineering*, 196(45-48):4597–4612, 2007.

[272] RG Gontijo. *Micromechanics and microhydrodynamics of magnetic suspensions*. PhD thesis, PhD Thesis, University of Brasília, 2013.

[273] RG Gontijo, S Malvar, and FR Cunha. Magnetic particulate suspensions from the perspective of a dynamical system. *Powder Technology*, 297:165–182, 2016.

[274] Ashok Shantilal Sangani and A Acrivos. Slow flow through a periodic array of spheres. *International Journal of Multiphase Flow*, 8(4):343–360, 1982.

[275] JT Padding and AA Louis. Hydrodynamic and brownian fluctuations in sedimenting suspensions. *Physical review letters*, 93(22):220601, 2004.

[276] David Saintillan, Eric Darve, and Eric SG Shaqfeh. A smooth particle-mesh ewald algorithm for stokes suspension simulations: The sedimentation of fibers. *Physics of Fluids*, 17(3): 033301, 2005.

[277] Andrew Crosby and John R Lister. Hydrodynamic diffusion of sedimenting point particles in a vertical shear flow. *Journal of Fluid Mechanics*, 730:699–732, 2013.

[278] J Liam McWhirter and GN Patey. Nonequilibrium molecular dynamics simulations of a simple dipolar fluid under shear flow. *The Journal of chemical physics*, 117(6):2747–2761, 2002.

[279] Zuowei Wang, Christian Holm, and Hanns Walter Müller. Boundary condition effects in the simulation study of equilibrium properties of magnetic dipolar fluids. *The Journal of chemical physics*, 119(1):379–387, 2003.

[280] Dmitri V Berkov and Natalia L Gorn. Stochastic dynamic simulations of fast remagnetization processes: recent advances and applications. *Journal of magnetism and magnetic materials*, 290:442–448, 2005.

[281] NA Usov and Yu B Grebenshchikov. Superparamagnetic relaxation time of a single-domain particle with a nonaxially symmetric double-well potential. *Journal of Applied Physics*, 105 (4):043904, 2009.

[282] Hao Zhenghua, Li Xiang, Lu Huilin, Liu Guodong, He Yurong, Wang Shuai, and Xu Pengfei. Numerical simulation of particle motion in a gradient magnetically assisted fluidized bed. *Powder Technology*, 203(3):555–564, 2010.

[283] Ph Depondt, J-CS Lévy, and FG Mertens. Vortex polarity in 2-d magnetic dots by langevin dynamics simulations. *Physics Letters A*, 375(3):628–632, 2011.

[284] Xiaoliang Deng, James V Scicolone, and Rajesh N Davé. Discrete element method simulation of cohesive particles mixing under magnetically assisted impaction. *Powder technology*, 243: 96–109, 2013.

[285] Shuyan Wang, Ze Sun, Xin Li, Jinsen Gao, Xingying Lan, and Qun Dong. Simulation of flow behavior of particles in liquid–solid fluidized bed with uniform magnetic field. *Powder technology*, 237:314–325, 2013.

[286] David J Griffiths. *Introduction to electrodynamics*. American Association of Physics Teachers, 2005.

[287] James R Melcher. *Continuum electromechanics*, volume 2. MIT press Cambridge, MA, 1981.

[288] W He, SJ Lee, David C Jiles, DH Schmidt, Marc D Porter, and Ruth Shinar. Design of high-magnetic field gradient sources for controlling magnetically induced flow of ferrofluids in microfluidic systems. *Journal of applied physics*, 93(10):7459–7461, 2003.

[289] Yevgen Melikhov, SJ Lee, David C Jiles, DH Schmidt, Marc D Porter, and Ruth Shinar. Micro-electromagnetic ferrofluid-based actuator. *Journal of applied physics*, 93(10):8438–8440, 2003.

[290] Norihiko Saga and Taro Nakamura. Elucidation of propulsive force of microrobot using magnetic fluid. *Journal of Applied Physics*, 91(10):7003–7005, 2002.

[291] W Drenckhan, F Elias, S Hutzler, D Weaire, E Janiaud, and J-C Bacri. Bubble size control and measurement in the generation of ferrofluid foams. *Journal of applied physics*, 93(12): 10078–10083, 2003.

[292] MI Shliomis. Hydrodynamics of a liquid with intrinsic rotation. *JETP*, 24:173, 1967.

[293] HOWARD Brenner. Rheology of two-phase systems. *Annual Review of Fluid Mechanics*, 2(1): 137–176, 1970.

[294] Howard Brenner. Rheology of a dilute suspension of dipolar spherical particles in an external field. *Journal of Colloid and Interface Science*, 32(1):141–158, 1970.

[295] Arlex Chaves, Markus Zahn, and Carlos Rinaldi. Spin-up flow of ferrofluids: Asymptotic theory and experimental measurements. *Physics of Fluids*, 20(5):053102, 2008.

[296] Arlex Chaves, Isaac Torres-Diaz, and Carlos Rinaldi. Flow of ferrofluid in an annular gap in a rotating magnetic field. *Physics of Fluids*, 22(9):092002, 2010.

[297] Isaac Torres-Díaz and Carlos Rinaldi. Ferrofluid flow in the annular gap of a multipole rotating magnetic field. *Physics of Fluids*, 23(8):082001, 2011.

[298] I Torres-Diaz and C Rinaldi. Ferrofluid flow in a spherical cavity under an imposed uniform rotating magnetic field: Spherical spin-up flow. *Physics of Fluids*, 24(8):082002, 2012.

[299] I Torres-Diaz, A Cortes, Y Cedeno-Mattei, O Perales-Perez, and C Rinaldi. Flows and torques in brownian ferrofluids subjected to rotating uniform magnetic fields in a cylindrical and annular geometry. *Physics of Fluids*, 26(1):012004, 2014.

[300] Carlos Rinaldi and Markus Zahn. Effects of spin viscosity on ferrofluid flow profiles in alternating and rotating magnetic fields. *Physics of Fluids*, 14(8):2847–2870, 2002.

[301] GK Batchelor. An introduction to fluid dynamics, 1967.

[302] R Chantrell, J Popplewell, and Stuart Charles. Measurements of particle size distribution parameters in ferrofluids. *IEEE Transactions on Magnetics*, 14(5):975–977, 1978.

[303] Peter Kopčanskỳ, Milan Timko, Ivana Potočová, Martina Koneracká, Alena Juríková, Natália Tomašovičová, Július Štelina, Ctibor Musil, and Juraj Braciník. The determination of the hydrodynamic diameter of magnetic particles using frs experiment. *Journal of magnetism and magnetic materials*, 289:97–100, 2005.

[304] P Debye. Polar molecules, the chemical catalog company. *Inc., New York*, pages 77–108, 1929.

[305] AC Levi, RF Hobson, and FR McCourt. Magnetoviscosity of colloidal suspensions. *Canadian Journal of Physics*, 51(2):180–194, 1973.

[306] B U Felderhof. Steady-state magnetoviscosity of a dilute ferrofluid. *Magnetohydrodynamics*, 36(4):329–334, 2000.

[307] BU Felderhof. Reply to "comment on 'magnetoviscosity and relaxation in ferrofluids'". *Physical Review E*, 64(6):063502, 2001.

[308] Mark I Shliomis. Ferrohydrodynamics: Retrospective and issues. In S. Odenbach, editor, *Ferrofluids, Magnetically Controllable Fluids and Their Applications*, pages 85–111. Springer, 2002.

[309] Rajesh Patel, RV Upadhyay, and RV Mehta. Viscosity measurements of a ferrofluid: comparison with various hydrodynamic equations. *Journal of colloid and interface science*, 263(2): 661–664, 2003.

[310] A Zeuner, R Richter, and I Rehberg. Weak periodic excitation of a magnetic fluid capillary flow. *Journal of magnetism and magnetic materials*, 201(1-3):321–323, 1999.

[311] Patrick Ilg, Martin Kröger, and Siegfried Hess. Magnetoviscosity and orientational order parameters of dilute ferrofluids. *The Journal of chemical physics*, 116(20):9078–9088, 2002.

[312] Martin Kröger, Patrick Ilg, and Siegfried Hess. Magnetoviscous model fluids. *Journal of Physics: Condensed Matter*, 15(15):S1403, 2003.

[313] Juha Pyrhonen, Tapani Jokinen, and Valeria Hrabovcova. *Design of rotating electrical machines*. John Wiley & Sons, 2013.

[314] Stefan Odenbach and Hanns Walter Müller. Stationary off-equilibrium magnetization in ferrofluids under rotational and elongational flow. *Physical review letters*, 89(3):037202, 2002.

[315] PM Hatzikonstantinou and P Vafeas. A general theoretical model for the magnetohydrodynamic flow of micropolar magnetic fluids. application to stokes flow. *Mathematical Methods in the Applied Sciences*, 33(2):233–248, 2010.

[316] Stefan Odenbach. Ferrofluids and their applications. *MRS bulletin*, 38(11):921–924, 2013.

[317] Pijush Kundu Ira Cohen David Dowling. *Fluid mechanics*. Elsevier Academic Press, 2015.

[318] Richard H Pletcher, John C Tannehill, and Dale Anderson. *Computational fluid mechanics and heat transfer*. CRC press, 2012.

[319] Duane W Condiff and John S Dahler. Fluid mechanical aspects of antisymmetric stress. *The Physics of Fluids*, 7(6):842–854, 1964.

[320] P Brunn. The velocity slip of polar fluids. *Rheologica Acta*, 14(12):1039–1054, 1975.

[321] Kenneth A Kline. Predictions from polar fluid theory which are independent of spin boundary condition. *Transactions of the society of rheology*, 19(1):139–145, 1975.

[322] SC Cowin. A note on the predictions from polar fluid theory which are independent of the spin boundary condition. *Transactions of the society of rheology*, 20(2):195–202, 1976.

[323] P Brunn. The hydrodynamic wall effect for a disperse system. *International Journal of Multiphase Flow*, 7(2):221–234, 1981.

[324] Kenneth A Kline. Discussion of predictions from polar fluid theory which are independent of spin boundary conditions. *Journal of Rheology*, 26(3):317–319, 1982.

[325] NP Migun. On hydrodynamic boundary conditions for microstructural fluids. *Rheologica acta*, 23(6):575–581, 1984.

[326] PN Kaloni. Some remarks on the boundary conditions for magnetic fluids. *International journal of engineering science*, 30(10):1451–1457, 1992.

[327] Olga Aleksandrovna Ladyzhenskaya. *The mathematical theory of viscous incompressible flow*, volume 2. Gordon and Breach New York, 1969.

[328] DJ Jeffrey and Y Onishi. Calculation of the resistance and mobility functions for two unequal rigid spheres in low-reynolds-number flow. *Journal of Fluid Mechanics*, 139:261–290, 1984.

[329] Larry C Andrews. *Special functions of mathematics for engineers*, volume 49. Spie Press, 1998.

[330] Carl Wilhelm Oseen. Uber die stokes' sche formel und uber eine verwandte aufgabe in der hydrodynamik. *Arkiv Mat., Astron. och Fysik*, 6:1, 1910.

[331] Alfred Barnard Basset. *A treatise on hydrodynamics: with numerous examples*, volume 2. Deighton, Bell and Company, 1888.

[332] YD Sobral, TF Oliveira, and FR Cunha. On the unsteady forces during the motion of a sedimenting particle. *Powder Technology*, 178(2):129–141, 2007.

[333] DA McQuarrie. *Statistical Mechanics*. Harper & Row Publishers, 1976.

[334] John F Brady and Georges Bossis. Stokesian dynamics. *Annual review of fluid mechanics*, 20 (1):111–157, 1988.

[335] JM Nitsche and GK Batchelor. Break-up of a falling drop containing dispersed particles. *Journal of Fluid Mechanics*, 340:161–175, 1997.

[336] A Salih. Streamfunction-vorticity formulation. *Department of Aerospace Engineering Indian Institute of Space Science and Technology*, 2013.

[337] H Lamb. *Hydrodynamics*. Dover Publications Inc., New York, 6 edition, 1945.

[338] Ercan Erturk. Numerical solutions of 2-d steady incompressible flow over a backward-facing step, part i: High reynolds number solutions. *Computers & Fluids*, 37(6):633–655, 2008.

[339] AP Rosa, RG Gontijo, and FR Cunha. Laminar pipe flow with drag reduction induced by a magnetic field gradient. *Applied Mathematical Modelling*, 40(5-6):3907–3918, 2016.

[340] Anthony JC Ladd. Dynamical simulations of sedimenting spheres. *Physics of Fluids A: Fluid Dynamics*, 5(2):299–310, 1993.

[341] Anthony JC Ladd. Numerical simulations of particulate suspensions via a discretized boltzmann equation. part 2. numerical results. *Journal of fluid mechanics*, 271:311–339, 1994.

[342] Richard L Burden and J Douglas Faires. *Análise numérica*. Cengage Learning, 2008.

[343] Adriano Possebon Rosa. *Microestrutura e magneto-reologia de ferrofluidos em cisalhemento: teoria e simulação*. PhD thesis, Universidade de Brasília, 2018. PhD thesis.

[344] AW Lees and SF Edwards. The computer study of transport processes under extreme conditions. *Journal of Physics C: Solid State Physics*, 5(15):1921, 1972.

[345] Douglas Daniel de Carvalho and Rafael Gabler Gontijo. Magnetization diffusion in duct flow: The magnetic entrance length and the interplay between hydrodynamic and magnetic timescales. *Physics of Fluids*, 32(7):072007, 2020.

[346] Lloyd N Trefethen. *Spectral methods in MATLAB*, volume 10. Siam, 2000.

[347] Hermann Schlichting and Klaus Gersten. *Boundary-layer theory*. Springer, 2016.

[348] Christopher Charles Finlay, Stefan Maus, CD Beggan, TN Bondar, A Chambodut, TA Chernova, A Chulliat, VP Golovkov, B Hamilton, Mohamed Hamoudi, et al. International geomagnetic reference field: the eleventh generation. *Geophysical Journal International*, 183(3):1216–1230, 2010.

[349] R.B. Bird, W.E. Stewart, and E.N. Lightfoot. *Transport Phenomena*. Wiley International edition. Wiley, 2006. ISBN 9780470115398.

[350] Yunus A Cengel. *Fluid mechanics*. Tata McGraw-Hill Education, 2010.

[351] Theodore L Bergman, Frank P Incropera, David P DeWitt, and Adrienne S Lavine. *Fundamentals of heat and mass transfer*. John Wiley & Sons, 2011.

[352] Albrecht Wiedenmann. Magnetic and crystalline nanostructures in ferrofluids as probed by small angle neutron scattering. In *Ferrofluids*, pages 33–58. Springer, 2002.

[353] F Gazeau, E Dubois, J-C Bacri, F Boué, A Cebers, and R Perzynski. Anisotropy of the structure factor of magnetic fluids under a field probed by small-angle neutron scattering. *Physical Review E*, 65(3):031403, 2002.

[354] Vusala Ambethkar and Manoj Kumar. Numerical solutions of 2-d unsteady incompressible flow with heat transfer in a driven square cavity using streamfunction-vorticity formulation. *International Journal of Heat and Technology*, 35(3):459–473, 2017.

[355] Tom M Apostol. *Calculus, volume II: multi-variable calculus and linear algebra, with applications to differential equations and probability*. John Wiley & Sons, 1969.

[356] EJ Hinch. *Perturbation methods*. Cambridge University Press, 1991.

APPENDIX A – Discretized governing equations

In this Appendix, the discretized mathematical form of the problem's governing equations is presented. A finite difference method was employed to discretize the governing equations due to its compatibility with the regularly shaped geometry of our problem. A forward-differencing scheme was used to approximate the time derivatives and central differences were used to approximate the spatial derivatives [354]. To make a clear presentation of the discretized equations, the finite difference operators δ was used, which is defined by the relations in Eq. (A.1) [318]. The forward-differencing scheme for the time derivatives is shown in Eq. (A.2) [318].

$$\begin{aligned} &\delta_x(\iota) = \frac{\iota_{i+1,j} - \iota_{i-1,j}}{2\Delta x}; \qquad \delta_{xx}(\iota) = \frac{\iota_{i+1,j} - 2\iota_{i,j} + \iota_{i-1,j}}{\Delta x^2}; \qquad \delta_y(\iota) = \frac{\iota_{i,j+1} - \iota_{i,j-1}}{2\Delta y}; \\ &\delta_{yy}(\iota) = \frac{\iota_{i,j+1} - 2\iota_{i,j} + \iota_{i,j-1}}{\Delta y^2}; \qquad \delta_{xy}(\iota) = \frac{\iota_{i+1,j+1} - \iota_{i+1,j-1} - \iota_{i-1,j+1} + \iota_{i-1,j-1}}{4\Delta x \Delta y} \end{aligned} \tag{A.1}$$

$$\frac{\partial \iota_{i,j}}{\partial t} = \frac{\iota_{i,j}^{n+1} - \iota_{i,j}^{n}}{\Delta t} \tag{A.2}$$

In Equations (A.1) and (A.2) ι is an arbitrary variable, Δx and Δy are the horizontal and vertical dimensionless steps, respectively, Δt is the dimensionless time step, n represents the property in a time t and $n+1$ represents the property in a time $t + \Delta t$.

The convective terms of the governing equations were modelled using a first-order upwind scheme, as described in Eq. (A.3) [318].

$$
\begin{aligned}
u\frac{\partial \iota}{\partial x} &= u\left(\frac{\iota_{i,j}-\iota_{i-1,j}}{\Delta x}\right), \quad for \quad u>0\\
u\frac{\partial \iota}{\partial x} &= u\left(\frac{\iota_{i+1,j}-\iota_{i,j}}{\Delta x}\right), \quad for \quad u<0\\
u\frac{\partial \iota}{\partial y} &= u\left(\frac{\iota_{i,j}-\iota_{i,j-1}}{\Delta y}\right), \quad for \quad u>0\\
u\frac{\partial \iota}{\partial y} &= u\left(\frac{\iota_{i,j+1}-\iota_{i,j}}{\Delta y}\right), \quad for \quad u<0
\end{aligned}
\tag{A.3}
$$

In Equation (A.3), u stands for a component of the velocity field, v_x or v_y. The discretized equations are presented in below.

- Discretized Poisson streamfunction equation

$$\delta_{xx}(\psi)+\delta_{yy}(\psi)=-\xi_{i,j} \tag{A.4}$$

- Discretized vorticity equation in two-dimensional flow

$$
\begin{aligned}
&\frac{\partial \xi_{i,j}}{\partial t}+v_x\frac{\partial \xi}{\partial x}+v_y\frac{\partial \xi}{\partial y}=\frac{1}{Re}\Big[\delta_{xx}(\xi)+\delta_{yy}(\xi)\Big]+\frac{3\phi\alpha}{PeRe}\Bigg[\delta_x(M_x)\delta_x(H_y)+\delta_x(M_y)\delta_y(H_y)\\
&+M_x\delta_{xx}(H_y)+M_y\delta_{xy}(H_y)-\delta_y(M_x)\delta_x(H_x)-\delta_y(M_y)\delta_y(H_x)-M_x\delta_{xy}(H_x)-M_y\delta_{yy}(H_x)\\
&-\frac{1}{2}\delta_{xx}(M_xH_y-M_yH_x)-\frac{1}{2}\delta_{yy}(M_xH_y-M_yH_x)\Bigg]
\end{aligned}
\tag{A.5}
$$

- Discretized magnetization equations

  - First model - Phenomenological equation:

Horizontal direction:

$$\frac{\partial M_{x_{i,j}}}{\partial t} + v_x \frac{\partial M_x}{\partial x} + v_y \frac{\partial M_x}{\partial y} = -\frac{1}{2}(\xi M_y)_{i,j} - \frac{1}{Pe}(M_x - M_{0x})_{i,j} - \frac{1}{2}\frac{\alpha}{Pe}\Big[M_y(M_x H_y - M_y H_x)\Big]_{i,j} \quad \text{(A.6)}$$

,

Vertical direction:

$$\frac{\partial M_{y_{i,j}}}{\partial t} + v_x \frac{\partial M_y}{\partial x} + v_y \frac{\partial M_y}{\partial y} = \frac{1}{2}(\xi M_x)_{i,j} - \frac{1}{Pe}(M_y - M_{0y})_{i,j} + \frac{1}{2}\frac{\alpha}{Pe}\Big[M_x(M_x H_y - M_y H_x)\Big]_{i,j} \quad \text{(A.7)}$$

· Second model - EFM equation:

Horizontal direction:

$$\frac{\partial M_{x_{i,j}}}{\partial t} + v_x \frac{\partial M_x}{\partial x} + v_y \frac{\partial M_x}{\partial y} = -\frac{1}{2}(\xi M_y)_{i,j} - \frac{1}{Pe}\frac{\Big[\alpha_e^2 - (\boldsymbol{\alpha}\cdot\boldsymbol{\alpha_e})\Big]}{\alpha_e^2} M_{x_{i,j}} - \frac{1}{2}\frac{\alpha}{Pe}\frac{\Big[\alpha_e - \mathcal{L}(\alpha_e)\Big]}{\alpha_e \mathcal{L}^2(\alpha_e)}\Big[M_y(M_x H_y - M_y H_x)\Big]_{i,j} \quad \text{(A.8)}$$

Vertical direction:

$$\frac{\partial M_{y_{i,j}}}{\partial t} + v_x \frac{\partial M_y}{\partial x} + v_y \frac{\partial M_y}{\partial y} = \frac{1}{2}(\xi M_x)_{i,j} - \frac{1}{Pe}\frac{\Big[\alpha_e^2 - (\boldsymbol{\alpha}\cdot\boldsymbol{\alpha_e})\Big]}{\alpha_e^2} M_{y_{i,j}} + \frac{1}{2}\frac{\alpha}{Pe}\frac{\Big[\alpha_e - \mathcal{L}(\alpha_e)\Big]}{\alpha_e \mathcal{L}^2(\alpha_e)}\Big[M_x(M_x H_y - M_y H_x)\Big]_{i,j} \quad \text{(A.9)}$$

· Third model - Phenomenological equation:

Horizontal direction:

$$\frac{\partial H_{ex_{i,j}}}{\partial t} + v_x \frac{\partial H_{ex}}{\partial x} + v_y \frac{\partial H_{ex}}{\partial y} = -\frac{1}{2}(\xi H_{ey})_{i,j} - \frac{1}{Pe}(H_{ex} - H_x)_{i,j} - \frac{1}{2}\frac{\alpha}{Pe}\Big[H_{ey}(M_x H_y - M_y H_x)\Big]_{i,j} \quad \text{(A.10)}$$

Vertical direction:

$$\begin{aligned}\frac{\partial H_{ey_{i,j}}}{\partial t} + v_x\frac{\partial H_{ey}}{\partial x} + v_y\frac{\partial H_{ey}}{\partial y} &= \frac{1}{2}(\xi H_{ex})_{i,j} \\ -\frac{1}{Pe}(H_{ey} - H_y)_{i,j} - \frac{1}{2}\frac{\alpha}{Pe}&\Big[H_{ex}(M_xH_y - M_yH_x)\Big]_{i,j}\end{aligned} \tag{A.11}$$

In Equations (A.10) and (A.11), H_{ex} and H_{ey} stand for the horizontal and vertical components of the effective field $\boldsymbol{H_e}$, respectively.

- Discretized velocity field relations

$$v_{x_{i,j}} = \delta_y(\psi); \qquad v_{y_{i,j}} = -\delta_x(\psi) \tag{A.12}$$

APPENDIX B – Magnetic boundary conditions

The magnetic boundary conditions come from the Ampère and Gauss magnetism laws, being determined as follows:

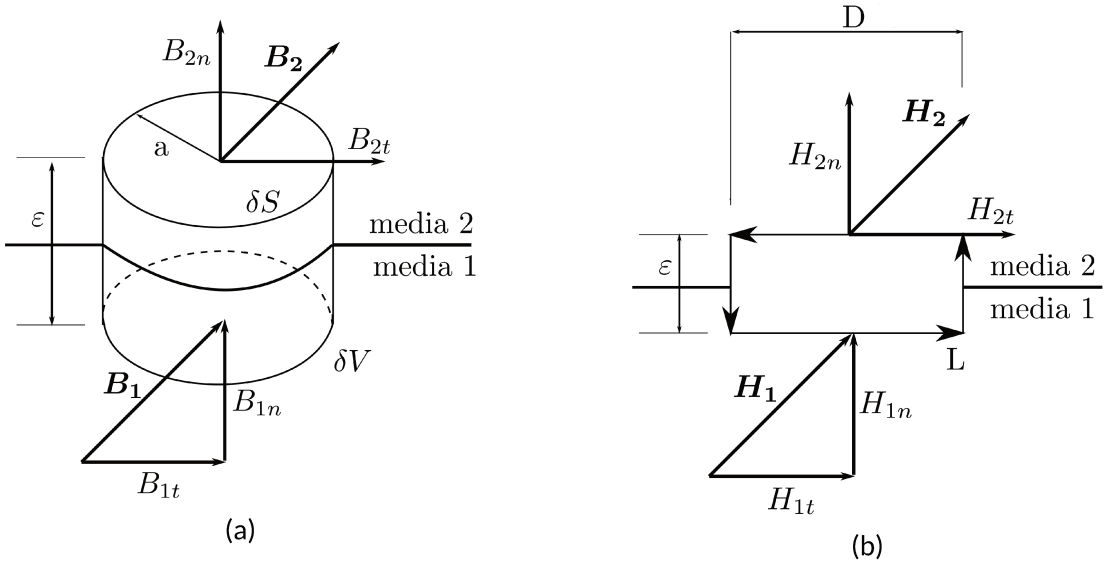

Figure. B.1: Scheme for the magnetic boundary conditions between media 1 and media 2. In (a): Magnetic induction field $\boldsymbol{B}$. In (b): Applied magnetic field $\boldsymbol{H}$. Image adapted from Ref. [29].

The boundary condition for the magnetic induction field $\boldsymbol{B}$ is a direct consequence of Gauss' law of magnetism $(\nabla \cdot \boldsymbol{B}) = 0$ - Eq. (2.1) -. For its calculation, consider the infinitesimal volume δV presented in Fig. (B.1a), with radius $a = D/2$ and height ε, which is placed between two different continuous media 1 and 2. Integrating Gauss magnetism law into the referred volume and applying Gauss divergence theorem [355] one arrives at [3, 29]:

$$\iiint \nabla \cdot \boldsymbol{B} dV = \iint \boldsymbol{B} \cdot \boldsymbol{n} dS = 0. \tag{B.1}$$

Equation (B.1) indicates that the magnetic induction's net flow through any closed surface is null. When the volume's height ε is diminished in order to ensure $\varepsilon \ll D$, the total magnetic induction flow over the δS disk's surface will have significant contributions coming only from the upper A_2 (out) and lower A_1 (in) areas, since $\varepsilon \ll a$, or $|\boldsymbol{B}|\pi a^2 \gg |\boldsymbol{B}|2\pi a\varepsilon$. Therefore, the surface integral in Eq. (B.1) is reduced to:

$$\iint_{A_1} B_{1n} dS = \iint_{A_2} B_{2n} dS. \tag{B.2}$$

Since $A_1 = A_2$, the condition presented in Eq. (B.2) is only satisfied if the normal component of $\boldsymbol{B}$ is continuous along the interface between medias 1 and 2 [29]. Which leads to:

$$B_{1n} = B_{2n}. \tag{B.3}$$

Thus, Equation (B.3) indicates that the normal component of the magnetic induction field $\boldsymbol{B}$ is continuous across any interface.

As for the applied field's $\boldsymbol{H}$ boundary conditions, they are readily obtained from Ampère's circuit law in the magnetostatic limit $\nabla \times \boldsymbol{H} = \boldsymbol{0}$ - Eq.(2.1) - with the aid of Fig. (B.1b). By integrating the applied field's $\boldsymbol{H}$ irrotationality condition into the regular surface S limited by the outline L and by applying Stokes' theorem [355], one obtains [29]:

$$\iint (\nabla \times \boldsymbol{H}) \cdot \boldsymbol{n} dS = \oint \boldsymbol{H} \cdot \boldsymbol{t} dL = 0. \tag{B.4}$$

In Equation (B.4), $\boldsymbol{t}$ is the unit tangent vector to path L. One notices in the integrating path indicated in Fig.(B.1b) that $D \gg \varepsilon$, in a way that the first species line integrals in ε considering the path L are much smaller than those in D. Thus, the integral along the closed path L of Eq. (B.4) reduces to:

$$\oint_{D_1} \boldsymbol{H} \cdot \boldsymbol{t} dL = \oint_{D_2} \boldsymbol{H} \cdot \boldsymbol{t} dL. \tag{B.5}$$

Which leads to:

$$\boldsymbol{H}_2 \cdot \boldsymbol{t} - \boldsymbol{H}_1 \cdot \boldsymbol{t} = 0 \rightarrow H_{2t} = H_{1t} \tag{B.6}$$

This way, Eq. (B.6) indicates that the tangential component of the applied field $\boldsymbol{H}$ is continuous throughout the interface of medias 1 and 2.

Altogether, the field's boundary conditions, given by Eqs. (B.3) and (B.6), indicate that the normal components of the induction field $\boldsymbol{B}$ and the tangential components of the applied field $\boldsymbol{H}$ are continuous through an interface [3].

APPENDIX C – Asymptotic solution for code validation purposes

In this Appendix, the asymptotic solution used to validate the numerical code is derived. This solution was developed taking inspiration from the pioneer work of Rosa et al. [339]. In the present context, a ferrofluid laminar flow is held between two horizontal flat plates with unitary spacing $h = 2a$ and aspect ratio $L/h = 100$. The flow is subjected to a stationary magnetic field gradient with linear decay applied in the horizontal direction as well as a pressure gradient. The derivation process of this solution is now briefly described.

For the present asymptotic solution, the working magnetic fluid is considered symmetrical. The condition of symmetry of the stress tensor is met when there are no internal torques per unit volume acting on the fluid. Under the symmetry hypothesis, the resulting magnetic torque - Eq. (1.11) - is null $\boldsymbol{T} = \mu_0(\boldsymbol{M} \times \boldsymbol{H}) = \boldsymbol{0}$, leading to the collinearity of the magnetization $\boldsymbol{M}$ and magnetic field $\boldsymbol{H}$ vectors in all points of the fluid domain. Physically, this means that the relaxation time τ is so short that as soon as the magnetic field is applied, the magnetic dipole moments instantly line up in the field's direction[339].

The magnetic stress tensor for a symmetric magnetic fluid is given by [3, 39]:

$$\boldsymbol{\Sigma} = -\frac{1}{2}\mu_0 H^2 \boldsymbol{I} + \frac{1}{2}\mu_0(\boldsymbol{HM} + \boldsymbol{MH}) \tag{C.1}$$

For symmetric fluids, the equation of motion - Eq. (2.16) - is modified to:

$$\rho\left[\frac{\partial \boldsymbol{v}}{\partial t} + (\boldsymbol{v}\cdot\nabla)\boldsymbol{v}\right] = -\nabla p + \eta\nabla^2\boldsymbol{v} + \mu_0(\boldsymbol{M}\cdot\nabla)\boldsymbol{H} \tag{C.2}$$

This asymptotic solution is developed for regimes close to equilibrium; therefore, the magnetization model used is that of Eq. (2.27)[26]. With the symmetry hypothesis, Eq. (2.27) takes the form:

$$\frac{\partial \boldsymbol{M}}{\partial t} + (\boldsymbol{v} \cdot \nabla)\boldsymbol{M} = \frac{1}{2}\boldsymbol{\xi} \times \boldsymbol{M} - \frac{(\boldsymbol{M} - \boldsymbol{M_0})}{\tau} \tag{C.3}$$

Since $\boldsymbol{M}$ and $\boldsymbol{H}$ collinear, the last term in Eq. (C.2), associated with the magnetic force density - Eq. (2.2) -, can be written in the horizontal coordinate x as:

$$\left[\mu_0(\boldsymbol{M} \cdot \nabla)\boldsymbol{H}\right]_x = \mu_0\left(M_x\frac{\partial H_x}{\partial x} + M_y\frac{\partial H_x}{\partial y}\right) \tag{C.4}$$

Note that the horizontal component of the term $\mu_0 M \nabla H$ is given by:

$$\left[\mu_0(M\nabla H)\right]_x = \mu_0\left(\sqrt{M_x^2 + M_y^2}\frac{\partial}{\partial x}\sqrt{H_x^2 + H_y^2}\right) \tag{C.5}$$

Due to the small aspect ratio $a \ll L$ associated with the problem's geometry, it is possible to consider that $H_y \ll H_x$ and $M_y \ll M_x$, thus, it is noticed that $\boldsymbol{M} \cdot \nabla \boldsymbol{H} = M\nabla H$ in the horizontal direction.

To make Eqs. (C.2) and (C.3) non-dimensional, reference scales presented in Eq. (2.46) were used, with a slight modification f the pressure reference scale, which was made non-dimensional using a normalized volume rate $\tilde{p} = \frac{p}{12\rho U^2}$. Thus, the non-dimensional linear momentum and magnetization equations are given, respectively, by:

$$\frac{\partial \boldsymbol{v}}{\partial t} + (\boldsymbol{v} \cdot \nabla)\boldsymbol{v} = -12\nabla p + \frac{1}{Re}\nabla^2\boldsymbol{v} + \frac{1}{Re_m}(\boldsymbol{M} \cdot \nabla)\boldsymbol{H} \tag{C.6}$$

$$\frac{\partial \boldsymbol{M}}{\partial t} + (\boldsymbol{v} \cdot \nabla)\boldsymbol{M} = \frac{1}{2}\boldsymbol{\xi} \times \boldsymbol{M} - \frac{1}{Pe}(\boldsymbol{M} - \boldsymbol{M_0}) \tag{C.7}$$

In this particular case, the Péclet number indicates the tendency of magnetization to change in time and space compared to a flow characteristic timescale[339]. The magnetic Reynolds number Re_m is defined as $Re_m = \frac{\rho U^2}{\mu_0 M_s H_0}$.

In addition, the variations produced in magnetization $\boldsymbol{M}$ due to its advective transport are considered to be much smaller than those produced by flow's vorticity. In mathematical notation, it means that $|\boldsymbol{v} \cdot \nabla \boldsymbol{M}| \ll |\frac{1}{2}\boldsymbol{\xi} \times \boldsymbol{M}|$, reducing Eq. (C.7) to:

$$\frac{\partial \boldsymbol{M}}{\partial t} = \frac{1}{2}\boldsymbol{\xi} \times \boldsymbol{M} - \frac{1}{Pe}(\boldsymbol{M} - \boldsymbol{M_0}) \tag{C.8}$$

With all the restrictions discussed so far, and also considering a stationary magnetic field with linear decay in the horizontal (streamwise) direction in a fully developed steady state flow, Eq. (C.6) can be written, in the horizontal direction, as:

$$\frac{d^2 v_x}{dy^2} + \frac{Re}{Re_m} M \frac{dH}{dx} = -12ReG \tag{C.9}$$

In Equation (C.9), $\frac{dH}{dx}$ is the dimensionless constant magnetic field gradient and G is a dimensionless constant pressure gradient, given by:

$$G = -\left(\frac{h}{l}\right)\frac{\Delta p}{12\rho U^2} \tag{C.10}$$

In Equation (C.10), Δp is the pressure difference between two points in the fully developed flow domain. In steady state, Eq. (C.8) is rewritten as:

$$\frac{Pe}{2}\boldsymbol{\xi} \times \boldsymbol{M} = \boldsymbol{M} - \boldsymbol{M_0} \tag{C.11}$$

Equation (C.11) makes it clear that the developed analytical solution deals only with the deviation of the magnetization from its equilibrium value due to the vorticity of the flow. Components

of Eq. (C.11) in the horizontal x and vertical y directions are presented below.

$$\frac{dv_x}{dy}M_y = \frac{2}{Pe}(M_x - M_{x0}) \tag{C.12}$$

$$\frac{dv_x}{dy}M_x = -\frac{2}{Pe}(M_y - M_{y0}) \tag{C.13}$$

In Equations (C.12) and (C.13), M_{y0} and M_{x0} represent the vertical and horizontal equilibrium magnetization components, respectively. If it is assumed that the initial magnetization is aligned with the applied magnetic field, it leads to $M_{y0} = 0$. Therefore, Eq. (C.13) is reduced to:

$$M_y = -\frac{Pe}{2}\frac{dv_x}{dy}M_x \tag{C.14}$$

Substituting Eq. (C.14) in Eq. (C.12), and after performing some algebraic manipulations, it yields:

$$M_x = M_{x0}\left[\frac{1}{4}Pe^2\left(\frac{dv_x}{dy}\right)^2 + 1\right]^{-1} \tag{C.15}$$

In this way, the absolute value of the the magnetization vector $\boldsymbol{M}$ present in Eq. (C.9) can be calculated, leading to:

$$M = \sqrt{M_x^2 + M_y^2} = M_{x0}\left[\frac{1}{4}Pe^2\left(\frac{dv_x}{dy}\right)^2 + 1\right]^{-\frac{1}{2}} \tag{C.16}$$

The term in brackets in Eq. (C.16) can be expanded using binomial expansion. Taking only the

highest order term, it yields:

$$M \approx M_{x0}\left[1 - \frac{1}{8}Pe^2\left(\frac{dv_x}{dy}\right)^2\right] \tag{C.17}$$

The substitution of Eq. (C.17) in Eq. (C.9) results in a nonlinear ordinary differential equation - Eq. (C.18) - that governs the laminar flow of a diluted magnetic fluid between two horizontal flat plates with small aspect ratio under the action of a horizontal constant magnetic field gradient, that takes into consideration the coupling between flow's vorticity and fluid's magnetization.

$$\frac{d^2v_x}{dy^2} + \frac{Re}{Re_m}\frac{dH}{dx}M_{x0}\left[1 - \frac{1}{8}Pe^2\left(\frac{dv_x}{dy}\right)^2\right] + 12ReG = 0 \tag{C.18}$$

Equation (C.18) is best visualized with the aid of some constants, defined in Eq. (C.20).

$$\frac{d^2v_x}{dy^2} - \epsilon\left(\frac{dv_x}{dy}\right)^2 = -\gamma \tag{C.19}$$

$$\begin{aligned} \beta &= \frac{Re}{Re_m}M_{0x}\frac{dH}{dx} \\ \gamma &= 12ReG + \beta \\ \epsilon &= \frac{Pe^2\beta}{8} \end{aligned} \tag{C.20}$$

It is difficult to perform a direct integration of Eq. (C.19) due to the presence of the term $\left(\frac{dv_x}{dy}\right)^2$, responsible for its non-linearity. However, if one assumes that the ϵ parameter is small enough ($\epsilon \ll 1$), Eq. (C.19) can be solved by a regular perturbation method[356].

The $\mathcal{O}(\epsilon^2)$ asymptotic expansion for $v_x(y)$ is given by:

$$v_x(y) = v_{x0}(y) + \epsilon v_{x1}(y) + \epsilon^2 v_{x2}(y) \tag{C.21}$$

Substituting Eq. (C.21) in Eq. (C.19) yields:

$$\left[\frac{d^2 v_{x0}}{dy^2} + \gamma\right] + \epsilon\left[\frac{d^2 v_{x1}}{dy^2} - \left(\frac{dv_{x0}}{dy}\right)^2\right] + \epsilon^2\left[\frac{d^2 v_{x2}}{dy^2} - 2\left(\frac{dv_{x0}}{dy}\right)\left(\frac{dv_{x1}}{dy}\right)\right] = 0 \tag{C.22}$$

Therefore, it is necessary to solve a system of linear differential equations given by:

$$\begin{aligned}
&\frac{d^2 v_{x0}}{dy^2} + \gamma = 0 \\
&\frac{d^2 v_{x1}}{dy^2} - \left(\frac{dv_{x0}}{dy}\right)^2 = 0 \\
&\frac{d^2 v_{x2}}{dy^2} - 2\left(\frac{dv_{x0}}{dy}\right)\left(\frac{dv_{x1}}{dy}\right) = 0
\end{aligned} \tag{C.23}$$

To solve the system of linear equations shown in Eq. (C.23), the classic no-slip boundary condition on the walls is used. This leads to:

$$\begin{aligned}
v_{x0}(y) &= \frac{\gamma}{2}\left(y - y^2\right) \\
v_{x1}(y) &= \frac{\gamma^2}{24}\left(2y^4 - 4y^3 + 3y^2 - y\right) \\
v_{x2}(y) &= \frac{\gamma^3}{6}\left(\frac{-2}{15}y^6 + \frac{2}{5}y^5 - \frac{1}{2}y^4 + \frac{1}{3}y^3 - \frac{1}{8}y^2 + \frac{1}{40}y\right)
\end{aligned} \tag{C.24}$$

Finally, the asymptotic velocity profile is obtained.

$$v_x(y) = \frac{\gamma}{2}\left(y - y^2\right) + \epsilon\frac{\gamma^2}{24}\left(2y^4 - 4y^3 + 3y^2 - y\right) + \epsilon^2\frac{\gamma^3}{6}\left(\frac{-2}{15}y^6 + \frac{2}{5}y^5 - \frac{1}{2}y^4 + \frac{1}{3}y^3 - \frac{1}{8}y^2 + \frac{1}{40}y\right) \tag{3.8 revisited}$$

The velocity profile in Eq. (3.8) represents a parabolic profile only in the absence of magnetic effects, resulting in non-Newtonian behavior of the magnetic fluid when in the presence of an external magnetic field.